Structure of ^{25}Na measured using $d(^{24}\mathrm{Na}, p)^{25}\mathrm{Na}$ with a radioactive ^{24}Na beam

Andrew Knapton

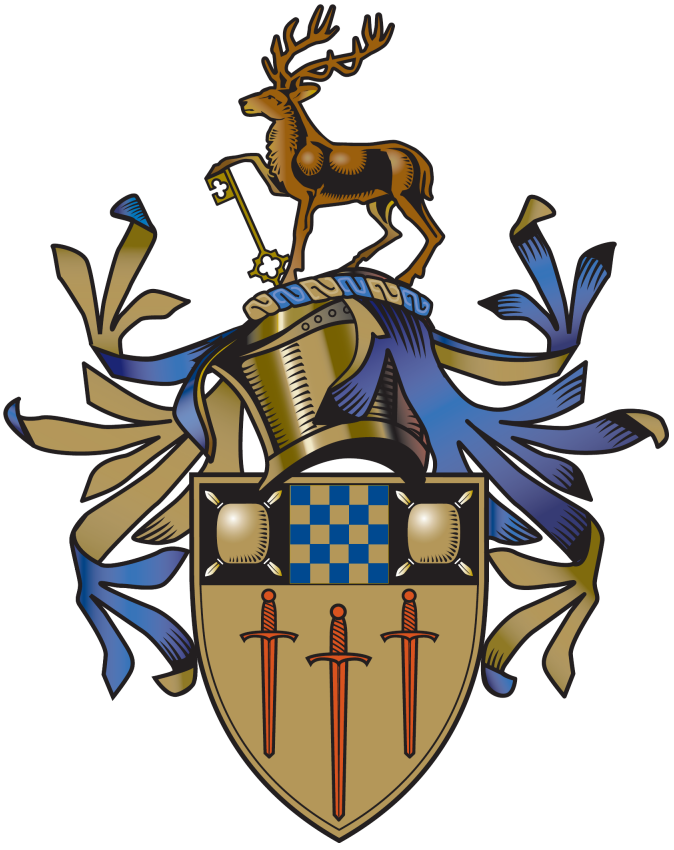

Submitted for the Degree of Doctor of Philosophy

Department of Physics
Faculty of Engineering and Physical Sciences
University of Surrey
Guildford, GU2 7XH

August 2017

Declaration of Authorship

I, Andrew Knapton, declare that this thesis titled, 'Structure of ^{25}Na measured using $d(^{24}\mathrm{Na}, p)^{25}\mathrm{Na}$ with a radioactive ^{24}Na beam' and the work presented in it are my own. I confirm that:

- This work was done wholly or mainly while in candidature for a research degree at this University.
- Where any part of this thesis has previously been submitted for a degree or any other qualification at this University or any other institution, this has been clearly stated.
- Where I have consulted the published work of others, this is always clearly attributed.
- Where I have quoted from the work of others, the source is always given. With the exception of such quotations, this thesis is entirely my own work.
- I have acknowledged all main sources of help.
- Where the thesis is based on work done by myself jointly with others, I have made clear exactly what was done by others and what I have contributed myself.

Signed: _____

Date: _____

Abstract

The structure of ^{25}Na is studied using the (d, p) transfer reaction using the ISAC-II accelerator at TRIUMF, Canada. An 8 MeV per nucleon beam of ^{24}Na, incident onto a 1.0 mg CD_2 target was used to populate excited states in ^{25}Na. The target was surrounded by the SHARC and TIGRESS arrays, which were used to detect the ejected protons, and coincident γ-rays emitted from the excited ^{25}Na nuclei respectively. The angular distribution of the protons has been analysed for each state observed and compared to the theoretical distributions generated using TWOFNR to get a value of the spectroscopic factors. Data were compared to WBC shell-model calculations in order to assign spin and parities to each observed state. States at 2.788 MeV and 3.455 MeV are strongly populated and show a strong s-wave contribution to the wave functions.

In addition, the structure of the astrophysically relevant mirror nucleus ^{25}Si is commented on. The reaction $^{24}\mathrm{Al}(p,\gamma)^{25}\mathrm{Si}$ reaction is thought to occur in hot stellar environments, but little to no experimental data exist that confirm reaction rates calculated for this reaction. The spectroscopic factors found in this work for ^{25}Na are used as a point of comparison and used to determine the validity of theoretical reaction rate calculations used for the astrophysical reaction. The relevant energy region in the reaction $^{24}\mathrm{Al}(p,\gamma)^{25}\mathrm{Si}$ is between the proton separation energy of 3.414 and 4 MeV. Two states are observed in this energy range in ^{25}Na at 3.455 and 3.995 MeV, though the 3.455 MeV state is expected to be Thomas-Ehrman shifted below the 3.414 MeV threshold in the mirror ^{25}Si. The state at 3.995 MeV was found to have an s-wave component that matched the predicted value from literature. No other states were observed within the relevant energy region in ^{25}Na.

Acknowledgements

Working towards my Ph.D will likely be one of the biggest challenges that I am ever going to face. I would therefore like to take this opportunity to acknowledge the people who helped my reach this point in which I am hopefully about to finally achieve this academic qualification.

I would first like to thank Dr Adrien Matta, who I think was the person most pivotal person on my journey to completing this thesis. I cannot stress enough how helpful he was in teaching me the coding skills that were required to analyse the data and explaining the physics that I didn't understand. I am of the firm belief that if he hadn't been around, then I would not have been able to complete my studies. If it were appropriate, I would put a big picture of Adrien with arrows pointing at it to emphasise how crucial I think he was to my work! I would also like to thank my supervisor, Professor Wilton Catford aka The King, without whom I wouldn't even have had a chance to try and get this Ph.D. He provided me with a lot of helpful advice, and directed me when I had no idea what was going on (which I feel was all the time).

I'd also like to acknowledge all the people I met whilst living in Canada, whether they were the staff at the TRIUMF Laboratory who gave me lots of experience with the practical part of nuclear physics, or my housemates and friends I met whilst living there who made me feel welcome when I was so far away from everyone else I knew.

To my office mates Dr Zena Patel, Dr Callum Shand, Riley Ilieva, Ryan Wilkinson, Lisa Morison, Laila Gurgi, Tom Berry, Sam Hallam, Rob Shearman, Chantal Nobs, Dr Rob Carroll, Dr Terver Daniel, Dr Emma Wilson, Dr Tom Alexander, Dr Ilker Celik and Dr Vytas Astromskas. I am very grateful for you all being there to help me out when I needed it, and for providing me with some stress relief when we had days out and trips to the pub. This last point also extends to my friends and family who made my life outside of the university even more enjoyable.

A special thanks to Rosanna Fish, who I think played a key part in helping me realise that learning new things in order to improve myself is a huge part of who I am. I like learning new things so that I can tell her about them. My sister, Julia, also deserves a mention because it was she who, through sibling rivalry, pushed me to stay in education for longer than she did so that I could legitimately say that I was smarter than her!

Contents

List of Figures

List of Tables

Chapter 1

Introduction

1.1 Motivation

The use of a particle detector and a γ-ray detector in conjunction with each other when studying a (d, p) transfer reaction was first used to investigate the disappearance of the magic number at $N = 20$ in neutron rich isotopes in favour of a magic number at $N = 16$ [1] [2]. These experiments have demonstrated how successful this experimental set up is for studying the structure of a nucleus. References [1], [2] andv[3] are two of a series of three experiments performed at TRIUMF designed to study the evolution of shell structure of sodium as it becomes increasingly neutron rich. The third experiment of this set is described in this work, and looks at the shell structure of ^{25}Na via the $d(^{24}\mathrm{Na}, p)^{25}\mathrm{Na}$ transfer reaction.

In addition to gaining an insight to the structure of ^{25}Na, the (d, p) transfer reaction can also provide an indirect measurement of the astrophysical reaction $^{24}\mathrm{Al}(p, \gamma)^{25}\mathrm{Si}$. It has been shown [4] that the astrophysical spectroscopic factor of a proton capture on a nucleus of proton number, Z, and neutron number, N, can be related to the spectroscopic factor of its mirror nucleus (proton number, N, and neutron number, Z) for a neutron capture. This means that by measuring the spectroscopic factors for different states in ^{25}Na, which has eleven protons and fourteen neutrons, it is possible to evaluate the spectroscopic factors of ^{25}Si, which has fourteen protons and eleven neutrons.

The $^{24}\mathrm{Al}(p, \gamma)^{25}\mathrm{Si}$ reaction is thought to be part of the rp-process that takes place in novae [5] and has a small affects on the nucleosynthesis of ^{28}Si, ^{29}Si, ^{30}Si, ^{33}S, ^{34}S and ^{36}Ar [6]. The rp-process is modelled using vairous parameters that are not currently experimentally confirmed causing variations in theory that attempts to model it. Attempts to quantify the the variations in different models have been conducted [6], but are only capable of revealing the uncertainties of modern theory.

1.2 Current Knowledge of ^{25}Na

The low lying states of ^{25}Na have been determined experimentally through various methods prior to this experiment. A paper published in 1956 studied the structure of low lying states in ^{25}Mg using β^- decay from ^{25}Na. The experiment was able to determine that the ground-state of ^{25}Na was most likely to have a spin/parity of $3/2^+$ or $5/2^+$ [7]. Later, in 1962, Hinds et al. examined some excited energy levels of ^{25}Na using the ^{23}Na$(t,p)^{25}$Na and the ^{25}Mg$(t,\alpha)^{25}$Na reactions [8]. Twenty nine excited energies where identified between 0.09 and 5.749 MeV using each reaction. Each reaction yielded results that varied from each other by a few keV. No information was available regarding the spin and parity of the states, though Hinds et al. speculated that the ground and first excited state of ^{25}Na is a 90 keV doublet due to the similarities between ^{25}Na and ^{19}O, which both have three effective particles in the $0d_{5/2}$ shell. Oxygen-19 has a $5/2^+$ ground-state with a $3/2^+$ excited state at 0.096 MeV [9]. This doublet structure is well known to be caused by the coupling of the three particles in the $0d_{5/2}$ shell [10].

In 1969 the spin assignments of some of the low lying states were established by examining the yield of γ-rays detected at different angles during a ^{26}Mg$(t,\alpha)^{25}$Na reaction [11]. Spin assignments have been built up by examining the angular distributions measured using reactions such as $^{26}Mg(d,t)^{25}Na$, and $^{23}Na(t,p)^{25}Na$ [12] [13] [14]. The current knowledge of the states of ^{25}Na that also have associated γ-rays or information regarding the spin of the state is shown in Table 1.1.

Sodium-24 consists of 11 protons and 13 neutrons which completely fill up the nuclear shells according to the Pauli exclusion principle to produce a core of ^{16}O. The remaining three protons and five neutrons occupy the first three and five spaces in the $0d_{5/2}$ shell respectively. The occupancy of the $0d_{5/2}$ shell is $(2 \times l) + 1 = 6$ and so there would be three holes in the proton shell and a single hole left in the neutron shell as shown schematically in Figure 1.1. During a (d,p) reaction, a single neutron is deposited into the neutron shell structure and, due to the direct nature of the reaction, leaves the structure of the protons unchanged. The way that these three protons' spins couple together in ^{23}Na and ^{24}Na can therefore provide initial estimates of how they will couple in ^{25}Na.

Three protons in the $0d_{5/2}$ shell can couple together to form a total spin of $9/2^+$, $5/2^+$ and $3/2^+$. In the ground-state of ^{23}Na, the even number of neutron holes couple together to 0, only leaving the three proton configurations listed as possible ground-state spins. It turns out that for ^{23}Na, the ground-state has a $3/2^+$ spin with the $5/2^+$ appearing as the first excited state at 440 keV. The first $9/2^+$ state does not appear until 2.703 MeV. The ground-state of ^{24}Na is 4^+ which can be made by coupling the odd neutron in

Energy (MeV)	Spin/Parity	E_γ (MeV)	Final Level (MeV)
0	5/2+		
0.08953 (10)	3/2+	0.08953	0
1.06932 (19)	1/2+	0.97977	0.08953
		1.06930	0
2.202 (1)	3/2+	1.1328 (10)	1.06932
		2.1125 (10)	0.08953
		2.2020 (10)	0
2.416 (3)		2.416 (3)	0
2.788 (3)	(1/2+,3/2,5/2−)	2.788 (2)	0
2.914 (4)	5/2+	2.825 (3)	0.08953
3.353 (3)		3.263 (3)	0.08953
		3.353 (3)	0
3.455 (4)		1.043 (2)	2.416
3.687 (2)	(3/2)+	3.599 (3)	0.08953
		3.688 (3)	0
3.928 (7)	(1/2+)	3.928 (7)	0
3.950 (5)	(1/2+,3/2,5/2+)	2.887 (3)	1.06932
		3.861 (5)	0.08953
		3.950 (5)	0
3.995 (5)	1/2−	1.207 (3)	2.788
4.132 (5)		4.132 (5)	
4.289 (3)	1/2+	3.220 (3)	1.06932
5.190 (9)	3/2−		
5.690 (12)	3/2−		
6.005 (22)	(1/2,3/2)−		
6.549 (19)	3/2−		
7.603 (17)	3/2−		
8.052	(1/2,3/2)−		

TABLE 1.1: Current known energy states for ^{25}Na which have had measured spins or γ-rays associated with them.

the $0d_{5/2}$ shell to any of these proton orientations, though because there is such a large energy difference between the 9/2 spin state and the 5/2 and 3/2 spin states in ^{23}Na, it can be expected that the 9/2 component is small in the ground-state wave function.

As with ^{23}Na, ^{25}Na has an even number of neutrons and three proton holes. For this reason, the ground-state is expected to have a spin of either $9/2^+$, $5/2^+$ or $3/2^+$. The ground-state and first excited state are already known to be $5/2^+$ and $3/2^+$ respectively, but the first $9/2^+$ state has not yet been found. As stated above for ^{24}Na, the $9/2^+$ state is expected to have a small contribution to the wave function to the ground-state. Making the assumption that this remains true for ^{25}Na means, and that the core of the nucleus is undisturbed by the transfer reaction, it is assumed that this first $9/2^+$ state will be weakly populated during the (d, p) reaction described in this text.

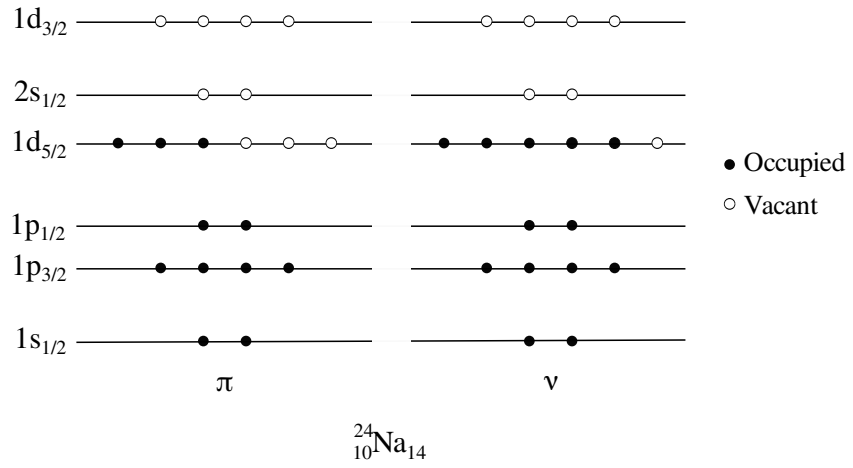

FIGURE 1.1: Schematic of the shell structure of ^{24}Na. After the (d,p) reaction, a neutron is transferred to one of the vacant orbitals.

In addition to a neutron being added into the $1d_{5/2}$ shell and completing that orbital, which will result in the excited states caused by the coupling of the protons as described above, a neutron may be deposited into the $2s_{1/2}$ state. Since the ground-state spin of ^{24}Na is 4^+, and acting under the assumption that the the transfer into this state does not interfere with this ground-state, we can see that the spin of unpaired $2s_{1/2}$ neutron couples to the ground-state and produces either a $7/2^+$ or a $9/2^+$ state. The $2s_{1/2}$ level is also completely unoccupied prior to the reaction, as opposed to the $1d_{5/2}$ level, which only has one available occupancy. As a result, the excited $7/2^+$ and $9/2^+$ states are expected to be strongly populated by the (d,p) reaction.

Chapter 2

Theory

2.1 The Shell Model

In analogy to the structure of the atom, the atomic nucleus can be described using the idea of orbitals and energy levels. A nuclear energy level can be filled according to the Pauli exclusion principle to obtain a core of largely inert filled energy states and some valence nucleons. Each energy level has an associated integer value of angular momentum which is given by the quantum number, l. The term "shell" is given to a state of a particular l. Each shell has a potential occupancy, which is the number of nucleons that can be found at a particular l which is given by $2l + 1$. Filling a shell with $2l + 1$ nucleons leads to the idea of shell closures; a point at which there is no more room available for occupation by a nucleon, and it must instead occupy a higher shell. The case in which there is a particularly large gap between a filled energy level and the next vacant one indicates the closure of a major shell. The number of nucleons at which all shells below this large gap are fully coupled is referred to as a "magic number" and occurs at 2, 8, 20, 28, 50, 82 and 126.

The shell-model deals with the filling of these various shells as the nucleon number, A, is increased as well as the energies of each of these states. To a simple approximation, the quantised energy levels of a nucleon in this shell structure can be calculated by solving the Schrödinger equation for a particle represented by the wave function, $\Psi(r)$,

$$H\Psi(r)_i = \epsilon_i \Psi(r)_i, \tag{2.1}$$

where ϵ_i is the ith energy eigenvalue corresponding to the ith state represented by the wave function $\Psi(r)_i$ and H is an operator known as the Hamiltonian and is given by

$$H = \left[\frac{-\hbar^2}{2m}\nabla^2 + V(r)\right], \tag{2.2}$$

in which m is the mass of the nucleon and $V(r)$ is the potential of the system as a function of the distance, r, from the centre of the potential. The potential chosen in this model has an affect on the energies predicted. The following subsections describe the evolution of the shell-model potential that correctly recreates the shell structure seen by experiment.

2.1.1 Wood-Saxon Potential

The shell-model, and in particular, the splitting of the energy levels is strongly dependent on the potential well used to define the nucleus. A three-dimensional infinite potential well and a simple harmonic oscillator potential both do an adequate job in describing the energies of the first states in a nucleus and also does admirably in predicting the first few magic numbers as seen for experimental variables, but fails to explain these values at higher energies. Part of the solution to these short comings is to try and pick a potential that is physically realistic.

The infinite potential well fails for a number of reasons: an infinite amount of energy is required in order to separate a proton or neutron from the nucleus, implying that nucleons are forever trapped in this potential, and therefore not allowing processes such as fission or alpha decay to occur. In addition, the edges of the potential are extremely sharp, whereas it would be expected that the nuclear forces contributing to the potential will decrease smoothly as the distance from the nucleus becomes greater than the average radius. The harmonic oscillator reduces these problems, but still inaccurately represents the asymptotic behaviour as the potential increases with radius. It would be expected that the potential would closely approximate the charge and matter distribution of the nucleus, since the potential is created through interactions between nucleons, and would decrease as the surface of the nucleus is approached.

The potential that is chosen to approximate these parameters is known as the Woods-Saxon potential, which is of the form [15]

$$V(r) = \frac{-V_0}{1 + \exp[(r - R)/a]}, \tag{2.3}$$

were V_0 is the depth of the potential, R is the mean nuclear radius, and a is a measure of diffuseness of the nuclear surface [16].

As can be seen in Figure 2.1, the potential described by Equation 2.3 is an improvement over the simple harmonic oscillator, but is still not adequate at creating the magic numbers found through experiment.

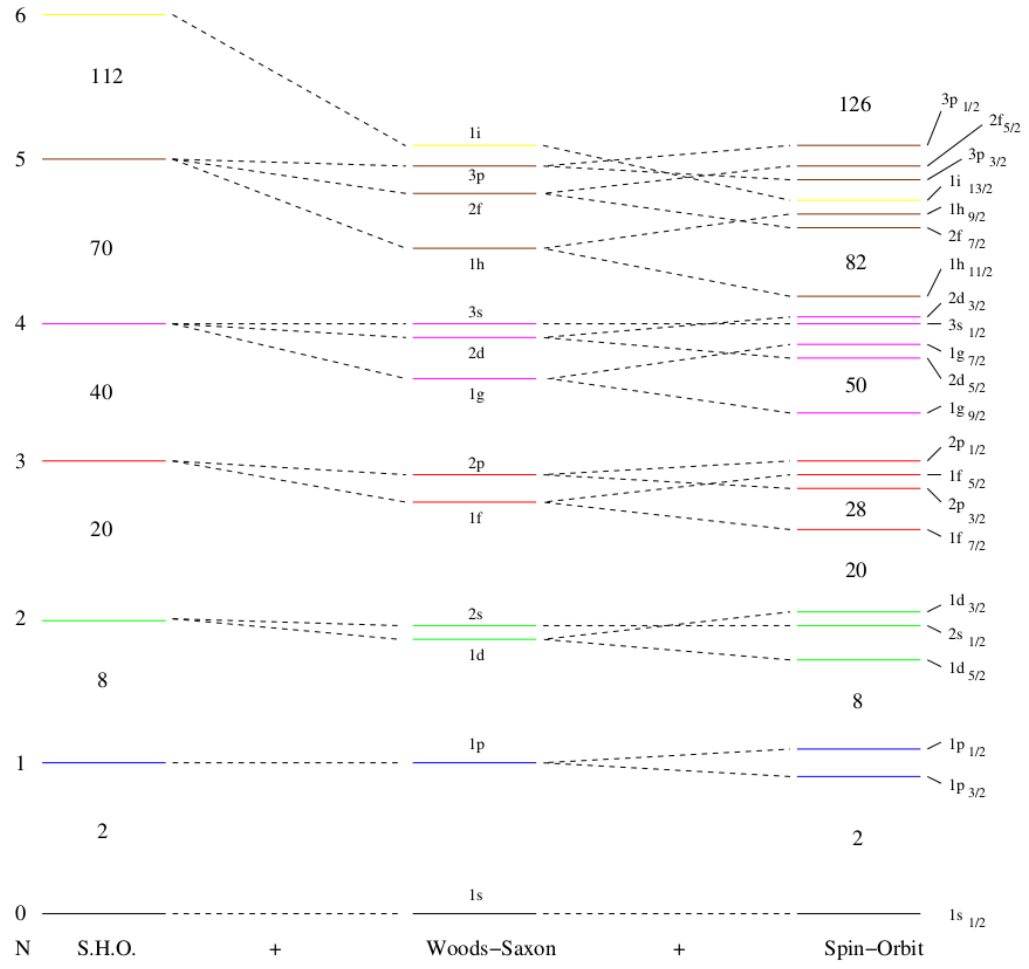

FIGURE 2.1: The evolution of the shell-model as the potential used in the Schrödinger equation becomes more complex.

2.1.2 Spin-Orbit Interaction

In 1949, MG Mayer [17] showed that the correct magic numbers could be obtained by considering a spin-orbit interaction between nucleons. The spin-orbit force only exists when the spin of the two interacting nucleons are parallel ($S = 1$), and is attractive when the spin of a particle is parallel to the relative angular momentum of the interacting particles, and repulsive when they are anti-parallel [16]. The effect that the spin orbit interaction has on the potential of the nucleus is shown in Figure 2.2.

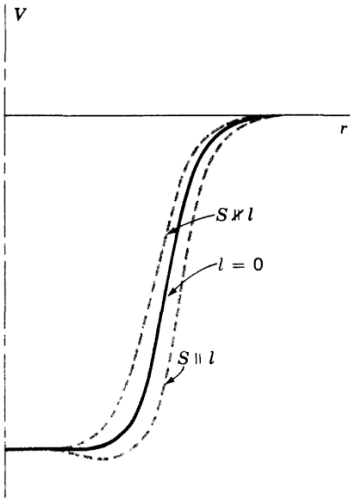

FIGURE 2.2: The effect of the spin-orbit interaction on the Woods-Saxon potential [18].

This interaction has the form $-V_{SO}(r)\mathbf{l}\cdot\mathbf{s}$ where $\mathbf{l}$ and $\mathbf{s}$ are the angular momentum and the spin of the nucleons respectively. The value of the $-V_{SO}(r)$ form is not important in the re-ordering of the shell structure, it is the $\mathbf{l}\cdot\mathbf{s}$ term that causes this shift. The quantum number j is used to describe the total angular momentum of a particle: $j = l + s$. Since $s = \pm 1/2$, $j = l \pm 1/2$ (unless $l = 0$ in which case only $j = 1/2$ is allowed), meaning that a particle is in a different state depending on whether its spin is parallel or anti parallel with its angular momentum.

The amount which this coupling effects the splitting of the energy levels is simple since

$$j^2 = (l+s)^2 = l^2 + s^2 + 2l\cdot s, \tag{2.4}$$

$$l\cdot s = \frac{1}{2}\left(j^2 - l^2 - s^2\right). \tag{2.5}$$

Using the expectation values of j, l and s, which are $\hbar^2 j\,(j+1)$, $\hbar^2 l\,(l+1)$ and $\hbar^2 s\,(s+1)$ respectively, it is seen that

$$\langle l\cdot s\rangle = \frac{1}{2}\left[j\,(j+1) - l\,(l+1) - s\,(s+1)\right]\hbar^2, \tag{2.6}$$

and, hence, that $\langle l\cdot s\rangle = \frac{1}{2}l\hbar^2$ for $j = l + s$ and $\langle l\cdot s\rangle = -\frac{1}{2}\,(l+1)\,\hbar^2$ for $j = l - s$. This gives the final result that each energy state is split by an amount proportional to $2l + 1$ [19].

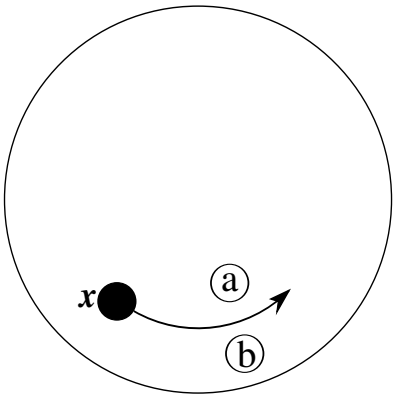

FIGURE 2.3: Semi-classical explanation of how the spin-orbit interaction works.

The spin-orbit interaction can be explained with a semi-classical picture of a nucleon orbiting inside a nucleus, as shown in Figure 2.3 There is only an interaction when the spins of each particle are aligned. In this example, lets assume that the particles each have a spin that is pointing out of the page. As nucleon x orbits the nucleus, it interacts with the nucleons a and b. The relative angular momentum between x and a is out of the page, and therefore x and a experience an attractive force. Conversely, the relative momentum between x and b is into the page and is therefore repulsive since it is anti-parallel with the spin of the nucleon. In the interior of the nucleus, this effect is small since nucleon x passes an approximately equal number of nucleons with the parallel and anti-parallel relative spins and the forces cancel out. Close to the surface, however, there are many more nucleons like a (i.e. with a smaller radius) than there are like b, and so the spin-orbit force with be attractive at the surface of the nucleus. If x reverses its direction, then the force will be repulsive at the surface [16] [18].

The addition of the attractive or repulsive spin-orbit interaction splits the energy levels of shell-model, as shown in Figure 2.1, with the states with $j = l + s$ being decreased in energy and $j = l - s$ increasing in energy. Tweaking the spin orbit potential, $V_{SO}(r)$ can then reproduce the desired values of the magic numbers, as required.

2.1.3 Perturbations and Diagonalising Matrices

The value of Ψ given in Equation 2.1 can be giving by a super position of the wave functions of different states, and so can be expressed as

$$\Psi = \sum_i c_i \phi_i \tag{2.7}$$

where ϕ_i is the wave function describing the state at a particular angular momentum, l, and c_i^2 is the probability of being observed in that state. The implication of this is that the wave function Ψ is actually made up of a mixing of particles in different states with different probabilities, the amplitude of which depends on the energy contained within the system. Consider the nucleus ^{18}O as an example; assuming that the nucleus has been filled according to the Pauli exclusion principle, this nucleus will contain two neutrons in the sd-shell depicted in the far right of Figure 2.1. For the purpose of simplicity, let us assume that these two neutrons' spins are always coupled to a 0+ state. In the sd-shell, there are three possible ways for two particles to couple to a 0^+; two neutrons found in the $d_{5/2}$ shell, two neutrons found in the $s_{1/2}$ shell, and two neutrons found in the $d_{3/2}$ shell. This means that Equation 2.7 can be written as

$$\Psi\left(0^+\right) = c_1\phi_1 + c_2\phi_2 + c_3\phi_3, \tag{2.8}$$

where ϕ_1, ϕ_2, and ϕ_3 refer to the wave functions of the states at $d_{5/2}$, $s_{1/2}$, and $d_{3/2}$ respectively. If there are no residual interactions between the neutrons (there is no way for scattering nucleons to cause a transition from, say, $(d_{5/2})$ to $(s_{1/2})$) then these states are the eigenstates of the Hamiltonian, and so H in Equation 2.1 can be expressed as the matrix:

$$H = \begin{bmatrix} \epsilon_1 & 0 & 0 \\ 0 & \epsilon_2 & 0 \\ 0 & 0 & \epsilon_3 \end{bmatrix}, \tag{2.9}$$

the basis of which is comprised by the wave functions Ψ_1, Ψ_2, and Ψ_3. For Equation 2.1 to be true given 2.9, it is clear that

$$\Psi_1 = \begin{bmatrix} 1 \\ 0 \\ 0 \end{bmatrix}, \Psi_2 = \begin{bmatrix} 0 \\ 1 \\ 0 \end{bmatrix} \text{ and } \Psi_3 = \begin{bmatrix} 0 \\ 0 \\ 1 \end{bmatrix}. \tag{2.10}$$

The values in the column matrices in 2.10 correspond to the values of c_i in Equation 2.8 and so it is obvious that a particle has a 100% chance of being observed in state ϕ_i and having an energy ϵ_i. Now consider a system in which residual interactions are allowed and it is possible for the two neutrons to collide and cause a transition between one state and another. Allowing this type of interaction in the model requires a perturbation potential, V' to be included in Equation 2.1 so that it now becomes,

$$\left(H + V'\right)\Psi_i = E\Psi_i, \tag{2.11}$$

where V' can be given by

$$V' = \begin{bmatrix} v_{11} & v_{12} & v_{13} \\ v_{21} & v_{22} & v_{23} \\ v_{31} & v_{32} & v_{33} \end{bmatrix}, \tag{2.12}$$

and $v_{ij} = \int \phi_j^* V' \phi_i dr$ gives the likelihood of the transition from state ϕ_i to ϕ_j occurring when being operated on by V'. In 2.9 only elements in which $i = j$ have non-zero values due to the assumption that particles do not feel a residual interaction with each other. However, the matrix element v_{ij} in 2.12 can be a non-zero term meaning that the eigenvalue of Equation 2.11 is not simply the diagonal matrix element of the matrix $H + V'$, as it was for H. The addition of the perturbing potential also causes the eigenfunctions of H, Ψ_i given in 2.10, not to be eigenfunctions of the new $H' = H + V'$ matrix.

It is possible to diagonalise H' by performing a similarity transformation in which the basis state of the matrix is given in terms of its eigenfunctions [20]. This diagonal matrix, D, is obtained by multiplying H' by some matrix, X such that

$$D = X^{-1} H' X \tag{2.13}$$

where X has the form

$$X = \begin{bmatrix} |\Psi_1'\rangle & |\Psi_2'\rangle & |\Psi_3'\rangle \end{bmatrix} \tag{2.14}$$

and $|\Psi_i'\rangle$ are the column vectors corresponding to the eigenvectors of H' in the original basis. The values contained within $|\Psi_i'\rangle$ provide the new coefficients, c_i, given in Equation 2.8. The values of the diagonal elements of D are the eigenvalues of the perturbed H' matrix.

The description above detailing the digonalisation of the H' matrix gives a simplified example of how to find the energy eigenvalues and eigenfunctions of the three 0^+ states in ^{18}O. The calculation becomes more complicated when trying to calculate the energies for all spin states within the sd-shell. The 'universal' sd (USD) Hamiltonian is often used to find the energies of states in the sd-shell. The USD value for v_{ij} was found by comparing the energy calculations from initial wave functions using an appropriate N-N

interaction, and performing a least-squares fit to the experimental energies of 447 excited states in the sd-shell. This produces an effective residual interaction between nucleons in that shell [21] [22]. The USD is valid for nuclei in the range $A = 21 - 35$. Outside of this range, sd excited states become fewer in number, and intruder states from other shells become more important. However, the USD Hamiltonian was proposed in the 1980 when computing power was more limited, and so an improved USD-A Hamiltonian was proposed in 2006 which used a fit to 77 nuclei to find the effective interaction to a complete set of 608 states within the sd-shell [23].

Both the USD and USD-A shell-model calculations are truncated so that they only allow for excitations in the sd-shell and so only positive parity states are calculated. Negative parity states are much harder to calculate because particles can be excited into the pf-shell. Let us use the example of ^{18}O described above and allow the two neutrons outside of the closed shells to be excited into the $f_{7/2}$ state in the pf-shell (this state is the lowest in energy in the pf-shell, as shown in Figure 2.1). Including this extra state in the calculation means that instead of diagonalising a 3×3 matrix, as was shown above, we are now diagonalising a 4×4 matrix (since the state 4^-, for instance, can be made by placing one of the two neutrons in either the $d_{5/2}$, $s_{1/2}$, $d_{3/2}$ or the $f_{7/2}$ state, and putting the second neutron into the $f_{7/2}$ state), which requires more computing power to solve. The WBP and WBC Hamiltonians [24][25] calculate the energy eigenvalues and eigenfunctions using USD and USD-A Hamiltonians respectively as a starting point.

2.2 Reaction Mechanisms

There are two main nuclear reaction types that occur at low energies; compound reactions and direct reactions. The reaction of interest in this work is the (d, p) transfer reaction, which is a type of direct reaction and is the reaction type that allows the probing of nuclear energy states. However, the experiment performed here is not able to select which reaction takes place; there is no guarantee that the (d, p) reaction will occur over a compound reaction in which the deuteron is fully absorbed, and then evaporates a proton. It is therefore important to be able to understand each of the reaction types in order to properly analyse the results.

2.2.1 Compound Reactions

A reaction may occur in which the target nucleus and the projectile combine to form a nucleus made up of the constituents of the two original nuclei. The simplest case would be where a single proton (or neutron), is incident onto a larger nucleus made up of several

nucleons. The incident proton can interact with a single nucleon through scattering, for example, and impart some of its energy. The struck nucleon and the incident particle can then each go on onto make successive collisions with other nucleons and therefore share the energy of the original incident particle amongst multiple other nucleons. On average, the energy imparted to each nucleon in this process is not enough to allow it to break free of the nuclear potential, however, a small number of particles do receive enough energy and are able to escape and "evaporate" from the nucleus.

Such reactions have an intermediate state after the absorption of the nucleus, but before the emission of any particles. This intermediate form is called a compound nucleus. A general reaction of this type can be written as

$$a + X \rightarrow C^* \rightarrow Y + b, \tag{2.15}$$

were C^* indicates the compound nucleus [19]. The process that forms the intermediate C^* nucleus interrupts the internal structure of the target nucleus and so C^* is left in a highly excited state made up of several nucleons occupying excited states.

Due to this intermediate stage, the nucleus is said to have lost its memory of the incident $a+X$ channel from which it was formed and that the probability of creating $Y+b$ will be independent of the incident reaction channel. The cross section of a particular reaction will be the product of the cross section of $a + X$ to create C at a particular energy, $\sigma^C_{a+X}(E)$ and a relative probability for C^* to decay into $Y + b$, $P^C_{Y+b}(E)$:

$$\sigma = \sigma^C_{a+X}(E) P^C_{Y+b}(E). \tag{2.16}$$

The significance of this is that if another process produces C^* at the same energy, E, it will have the same probability of producing $Y + b$ [26]. As a result, it is not possible to infer much about the structure of a nucleus that was created in this type of reaction.

2.2.2 Direct Reactions

The term "direct reactions", so called because they do not form a compound nucleus, is a very broad term referring to several different types of reaction, the three described here are the ones relevant to this work.

Elastic scattering is the simplest reaction, in which the structure of the target and incident particle remain unchanged after the collision. Inelastic scattering is more important since the nucleus of one or both the incident and target nucleus emerge in an

excited state whilst retaining the same type and number of nucleons in each. Stripping and pick-up reactions (collectively called transfer reactions) exchange nucleons between the incident and target nuclei, potentially leaving one of the participating nuclei in an excited state.

Whereas compound reactions are generally head-on collisions between nuclei, direct reactions tend to be glancing blows that only make contact for a short time. The time scale for a reaction to occur turns out to be an important point that plays a large role defining which category it falls into. Direct reactions happen in a time less than (or approximately equal to) the time it takes for a nucleon to orbit the nucleus, which is typically around $2R/v_p$ [27]. This short interaction time means that there is not enough time for energy to be shared between nucleons and form a compound nucleus, and a nucleus will, in the case of inelastic or transfer reactions, be left in a low lying excited state composed of an inert core plus one excited nucleon.

2.2.3 Transfer Reactions

The peripheral nature of direct reactions make them useful in studying the low-lying states in a nucleus because only a small number of nucleons are affected by the reaction. In the instance where the recoil nucleon is left in an excited state, it can be considered to be made up of an inert core of a particular spin and parity plus one excited nucleon. The general form of transfer reactions can be shown symbolically as

$$a + X_A \rightarrow Y_{A+i} + b, \tag{2.17}$$

where nucleus X consists of A nucleons and nucleus Y consists of a core made of the same A nucleons plus i transferred nucleons. An example of this would be in the (d, p) transfer reaction where nucleus 'a' is a deuteron, nucleus 'b' is a proton and $i = 1$ (referring to one neutron being transferred).

The energy, spin and parity of the final nucleus is determined by which state the transferred nucleon is occupying after the reaction. For example, if nucleus X in Equation 2.17 has a ground-state of 0^+, nucleus Y might have a spin and parity of $3/2^+$ if a nucleon is placed into the first $d_{3/2}$ state (since the spin of a nucleus can be $j_1 + j_2 \rightarrow |j_1 - j_2|$ which can couple to be $3/2$).

The cross section of this reaction can be calculated theoretically by considering the overlap between the ingoing channel of the nucleus of nucleon number A, and outgoing channels of $A + i$

$$\mathscr{T}_{A+i,A}(r) = \langle \Psi^{A+i} | a^{\dagger} | \Psi^{A} \rangle, \tag{2.18}$$

where $a^{\dagger}$ is the creation operator creating a particle at position r and $\mathscr{T}_{A+i,A}$ is the transition matrix (or $\mathscr{T}$-matrix) element between the initial and final states. This overlap function, referred to as the spectroscopic amplitude, will give the probability distribution as a function of r that the $A+i$ nucleus will be formed. The normalisation of Equation 2.18 gives the probability of the particle being created at a given r,

$$\sigma \equiv \int |\mathscr{T}(r)|^2 d^3r, \tag{2.19}$$

where σ is the total cross section of the reaction. Equation 2.19, however, is only correct if Ψ^{A} and Ψ^{A+i} in Equation 2.18 are exact eigenstates of a Hamiltonian that describe the system completely. In a single particle model, Ψ^{A}_{SPM} and Ψ^{A+i}_{SPM} describe a state in which a nucleon is considered to be independent of the core of the nucleus; as is the case for transfer reactions. This model neglects to take the internal structure of the nucleus' core into account which results in $\sigma < \sigma_{SPM}$ [28, 29]. The total cross section of the reaction is then

$$\sigma = C^2 S \sigma_{SPM}, \tag{2.20}$$

where C^2S is the spectroscopic factor and is a measure of how much the wave function of a pure single particle state overlaps with that of a given state.

2.3 Theoretical Analysis of Transfer Reactions

The description of transfer reactions given in the previous section gives an overview of the process, but does not take into account that transfer reactions are complex many-body problems that require many approximations to solve. The assumption that during a transfer reaction, the outgoing reaction channel can be described as an inert core plus a transferred nucleon has already been noted in section 2.2.3, and will be built upon in order to reduce the many-body problem into a simpler three-body problem as shown in Figure 2.4, which shows a nucleus, X which is made up of a core, labelled "b" and one valence neutron, ν, which is separated from b by a distance, r, and X is a distance, R, away from nucleus a. During the reaction, ν is transferred from X to a to form Y. This is the same as the reaction shown in Equation 2.17.

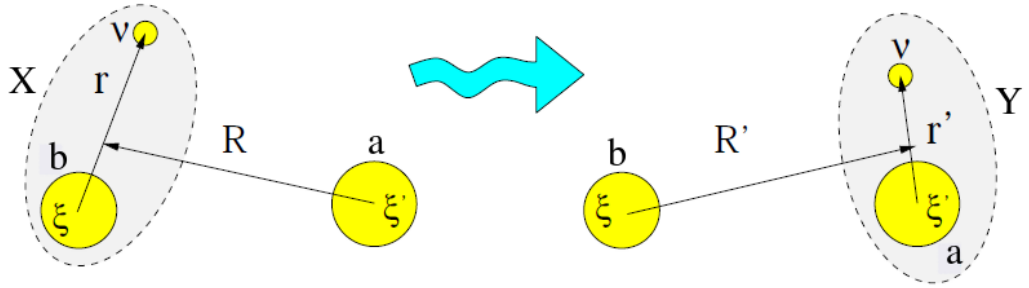

FIGURE 2.4: Schematic of a transfer reaction in a three-body problem where one neutron is transferred from nucleus X to nucleus Y (Adapted from reference [30]).

Equation 2.18 can then be re-written using the notation that for a reaction $a(X,Y)b$, the initial partition $a+X$ is denoted by α, and the outgoing partition $b+Y$ by β

$$\mathcal{T}_{\beta\alpha} = \langle \chi^{(-)}_{Yb}(R')\psi_{bv}(r')|V_\beta|\Psi^{(+)}(R,r)\rangle, \tag{2.21}$$

where the superscripts $^+$ and $^-$ refer to the incoming and outgoing channels respectively, $\chi_{Yb}(R')$ describes the relative motion between Y and b, and $\psi_{bv}(r')$ is the internal wave function of Y, and the potential of the system post reaction is V_β. Here $\Psi^{(+)}(R,r)$ is the exact solution of a many body problem for all open incoming channels available in the reaction. This value is an unknown since it is too complicated to calculate. It can. however, be reduced in complexity by using assumptions that will be described below. The potential used is dependent on the model describing the interaction.

2.3.1 The Plane Wave Born Approximation

A simple approximation of a transfer reaction is known as the Plane Wave Born Approximation (PWBA), which makes the assumption that the exact wave function, $\Psi^{(+)}$, given in Equation 2.21 for the incoming beam particle has the form

$$\Psi^{(+)}(R) \simeq Ae^{iKR}, \tag{2.22}$$

where Ψ is propagating in the positive R-direction, A is a constant, and K in the wave number. Post reaction, the scattered wave is in the form of a spherical plane wave propagating away from the scattering potential, $V(R)$. Note that using this simplest approximation, $\Psi^{(+)}$ is only a function of R, unlike in Equation 2.21, where it was a function of both R and r. This is because historically, the PWBA was proposed as a

model to explain elastic scattering and so the the wave function describing the internal structure of particle X, $\psi(r)$ is not required in the model. The fact that the PWBA was intended to describe elastic scattering is also the reason for the choice of the potential, $V(R)$. The Woods-Saxon potential, given in Equation 2.3, is used since it describes the interaction experienced between a nucleus and a projectile target [27].

The probability of an incident particle being scattered by $V(R)$ is dependent on the strength of the potential. In the case that $V(R)$ is not too strong, it can be considered as a perturbation problem; the potential may perturb an incoming beam particle of an associated eigenstate such that the outgoing eigenstate is associated with a particle travelling in a different direction. The rate at which the potential induces a change from the incoming to out going eigenstate can be converted to a differential scattering cross section, $d\sigma/d\Omega$, which, when integrated over the area surrounding the initial potential is the Born approximation for the cross section, σ.

The use of a plane wave to describe the incoming and outgoing particles has an effect on the profile of the cross section at different angles. Particles being scattered at different sides of the same scattering potential produce an interference pattern, creating minima and maxima at certain angles. PWBA can reproduce some basic features of transfer reactions such as these minima and maxima, but the model only describes the scattering of incident particles by a nucleus.

2.3.2 The Distorted Wave Born Approximation

The PWBA provides the first step in understanding direct reactions by using the Woods-Saxon potential as a scattering potential. The Woods-Saxon potential describes elastic scattering very well, but does not describe a situation in which scattered particles lose some of their energy, nor does it describe transfer. Using an optical potential, rather than a scattering potential can describe the reaction much more fully. The optical potential is sometimes referred to as the "cloudy crystal ball" [31], so called because the calculations describing it are very similar to those describing light incident on a semi-opaque glass sphere. This model represents scattering by considering a medium in which the wave function of the incident particle can be attenuated as well as scattered. In this model, the scattering is represented in terms of a complex potential, $U(R)$,

$$U(R) = V(R) + iW(R), \tag{2.23}$$

where $V(R)$ is the Woods-Saxon potential as seen in Equation 2.3 and describes the elastic scattering of the nucleus, and $W(R)$ describes the absorption in the medium. This

distortion of the outgoing wave provides an improvement over the PWBA and is referred to as the Distorted Wave Born Approximation (DWBA). The following discussion of the distorted wave approximation is largely adapted from the review from reference [32].

The form of $W(R)$ is often chosen as being proportional to $dV(R)/dr$ since this has a form that is only large at the surface of the sphere; at low energies only the valence nucleons can absorb incident particles, nucleons in the inert core of the nucleus do not participate in the absorption due to the Pauli exclusion principle. At high energies, $W(R)$ may be chosen to more closely resemble $V(R)$. In addition to these two terms, a spin-orbit term is also introduced (which also peaks near the surface of the nucleus due to the mean-field effect in which the spin density is cancelled out by the inert nuclear core), and a Coulomb term if the incident particle is charged.

The addition of this optical potential distorts the outgoing ($\Psi^{(-)}$) waves in Equation 2.21. The incoming wave, $\Psi^{(+)}$, can be approximated by

$$\Psi^{(+)}(R,r) \simeq \chi^{(+)}_{Xa}(R)\psi_{b\nu}(r), \tag{2.24}$$

where $\chi^{(+)}_{Xa}(R)$ is the wave function describing the relative motion between X, a and $\psi_{b\nu}(r)$ is the bound wave function between b and ν.

Substituting this into Equation 2.21 yields:

$$\mathcal{T}_{\beta\alpha} \simeq \langle \chi^{(-)}_{Yb}(R')\psi_{a\nu}(r')|V_\beta|\chi^{(+)}_{Xa}(R)\psi_{b\nu}(r)\rangle, \tag{2.25}$$

which is a far simpler equation than considering the wave function for the many-body bound state that would be needed to fully describe the interaction shown in Figure 2.4.

2.3.3 The Adiabatic Distorted Wave Approximation

The incoming wave, $\Psi^{(+)}$, is made up of all possible incoming channels. However, Equation 2.24 makes the approximation that only the elastic channel is open in the reaction. Using the DWBA therefore results in the assumption that the elastic channel is the dominant channel in the reaction. The DWBA, then, approximates the reaction as a two-body problem in which the scattered probability of a particle is reduced by an absorbing potential.

Since the DWBA is a two-body approximation, it fails to take into account the relative motion between b and ν prior to the reaction. This is an important consideration to make

when examining a reaction such as (d, p) because the relatively low binding energy of a deuteron (2.22 MeV [33]) means that it is liable to break apart. A new approximation is therefore made that describes the incoming wave function as a three-body problem:

$$\Psi^{(+)}(R, r) \simeq \chi^{(+)}_{Xa}(R, r)\psi_{b\nu}(r). \tag{2.26}$$

This value of $\chi^{(+)}_{Xa}$ differs from that of Equation 2.24 because $\chi^{(+)}_{Xa}$ is dependent on both R and r and so is the solution to a two-body scattering problem.

The Adiabatic Distorted Wave Approximation (ADWA) is an approximation developed by Johnson and Soper [34] that simplifies this three-body problem for cases where collision energies are comparatively high in comparison to the binding energy of the colliding particle (as is the case for a deuteron). The assumption here is that the internal motion of a deuteron is much slower than that of the motion of a deuteron as a whole. The positions of the neutron and proton can therefore be considered to be 'frozen' with respect to each other. This allows the interaction potential between the proton, p, neutron, n, and target particle, T, to be treated separately:

$$U_{dT} = U_{pT} + U_{nT}, \tag{2.27}$$

where U_{dT} is the total optical potential experienced between the target and the deuteron as a whole.

2.4 Nuclear Astrophysics

As described in Chapter 1, the experiment described in the current work has some astrophysical motivations. Even though the actual astrophysical process is not being directly addressed in this work, a brief theoretical description of the relevant physics will be given.

2.4.1 The rp-process and the reaction ^{24}Al$(p, \gamma)^{25}$Si

The $rp-$process ('rapid proton' capture process) is an astrophysical process used to describe the nucleosynthesis of elements via proton capture. It occurs in hot stellar environments in which a lot of hydrogen is available to undergo fusion. Unlike the analogous r-process, which describes rapid neutron capture, the reaction pathway undertaken by the rp-process is determined by the size of the Coulomb barrier of the

nucleus in the reaction, which increases as more protons are added. When the Coulomb barrier is sufficiently high, β^+-decay competes favourably with proton capture, which reduces the barrier and potentially allows proton capture to occur once again. This β^+-decay helps close a loop and create a reaction cycle such as the CNO or hot-CNO cycles which produce energy in stars depending on the temperature. If the temperature is sufficiently high, and the density of hydrogen is sufficient, then the Coulomb barrier is easily overcome and the β^+-decay that closes the loop is no longer competitive. This opens up the pathway to successive proton captures via the *rp*-process.

The reaction rate of a resonant reaction, $\langle\sigma\nu\rangle_r$, depends upon the resonance energy, E_R, of the resonant state [35]:

$$\langle\sigma\nu\rangle_r \propto \exp\left(\frac{-11.605E_R}{T_9}\right), \tag{2.28}$$

where T_9 is the temperature on the system expressed in 10^9K. The relationship between $\langle\sigma\nu\rangle_r$ and E_R given in Equation 2.28 requires that the value of E_R must be known very precisely because a small error of a few keV can greatly alter the reaction rate [35].

There are very few experimental results for proton capture rates in reactions of astrophysical significance [35]. This is because of the effect of the Coulomb barrier, which reduces the yield of reactions as energy decreases, thus making it difficult to study reactions at astrophysical energies [35]. Low yields inevitably result in low statistics which means a higher uncertainty in results. Equation 2.28 also suggests that the higher E_R, the lower the reaction rate is.

The reaction rates for the ^{24}Al$(p,\gamma)^{25}$Si reaction have been calculated by Herndl *et al.* [5] in relation to its potential importance in various astrophysical environments. This was part of a wide ranging study of many reactions in the early stages of the *rp*-process pathways. Herndl *et al* used large-basis shell-model calculations in order to provide information about the internal structure of the largely unknown ^{25}Si nucleus [5]. These calculations were benchmarked against calculations for the much better studied ^{25}Na nucleus, and the formalism of Ormand and Brown [36] was used to account for the different Coulomb effects in ^{25}Si. The ^{25}Si results where then used to find a theoretical value of the resonance strengths, $\omega\gamma$, of the states close to the Coulomb barrier

$$\omega\gamma = \frac{2J+1}{2\,(2J_T+1)}\frac{\Gamma^{(+)}\Gamma^{(-)}}{\Gamma^{(+)}+\Gamma^{(-)}} \tag{2.29}$$

where $J_T = 4$ is the spin of the ground-state of ^{24}Al, J is the spin of the excited state in ^{25}Si and $\Gamma^{(+)}$ and $\Gamma^{(-)}$ are the partial widths of the incoming and outgoing reaction

J^π	Ex_{exp} (^{25}Na) (MeV)	Ex_{exp} (^{25}Si) (MeV)	δE (MeV)	E_R
$5/2^+_3$	3.69	3.60	-0.09	0.19
$5/2^+_3$	3.95	3.82	-0.16	0.41
$5/2^+_3$	3.93	3.91	-0.04	0.50
$5/2^+_3$	4.14	3.92	-0.22	0.51
$5/2^+_3$	4.34	4.14	-0.20	0.73

TABLE 2.1: Comparison of excited states in ^{25}Na and calculated excited states in ^{25}Si. The resonance energy of the proton, E_R for each state is also shown. These data were taken from reference [5].

E_R (MeV)	Γ_p (eV)	Γ_γ (eV)	$\omega\gamma$ (eV)	$C^2S_{5/2}$	$C^2S_{1/2}$	$C^2S_{3/2}$
0.19	3.99×10^{-2}	5.66×10^{-7}	1.89×10^{-7}	0.02		0.01
0.41	1.31×10^{-2}	7.47×10^{-1}	7.2×10^{-3}	0.03	0.02	0.14
0.50	1.51×10^{-2}	2.38	6.7×10^{-3}	0.04	0.01	0.16
0.51	7.27×10^{-2}	0.1	1.4×10^{-2}	0.04		0.00
0.73	1.22×10^{-1}	5.3×10^{-2}	1.23×10^{-2}	0.001	0.00	

TABLE 2.2: Reaction strength for different excited states in ^{25}Si. The calculated spectroscopic factors for the $d_{5/2}$, $s_{1/2}$ and $d_{3/2}$ states. These data were taken from reference [5].

channels respectively. In the case of a (p, γ) reaction, the widths are $\Gamma^{(+)} = \Gamma_p$ and $\Gamma^{(-)} = \Gamma_\gamma$. The reaction rate is proportional to this reaction strength, therefore states with a large $\omega\gamma$ will be the most important when estimating a reaction rate. The relevant states calculated in reference [5] are given in Table 2.1 and are compared to the known states in ^{25}Na. Table 2.2 shows the reaction strengths and the spectroscopic factors for these states. Shown in both of these tables are the resonance energies of the proton, E_R, for these states.

Using the reaction rates obtained for these states, and performing the same analysis on other reactions in the the mass range $A = 23 - 43$, a reaction path for the *rp*-process was established for different temperatures. The reaction rate varies with temperature and depends on the state populated. This variation is shown in Figure 2.5.

2.4.2 Novae and X-ray Bursters

Consider a close binary star system that consists of a main sequence star, and a much denser white dwarf star. There is a point, referred to as the inner Lagrangian point, between the two stars at which the gravitational potential is equal. If the main sequence star is close enough to the white dwarf, or the main sequence star enters its red giant stage of stellar evolution, its outer radius may surpass the Lagrangian point, that is some of its mass is affected more by the white dwarf than the host star.

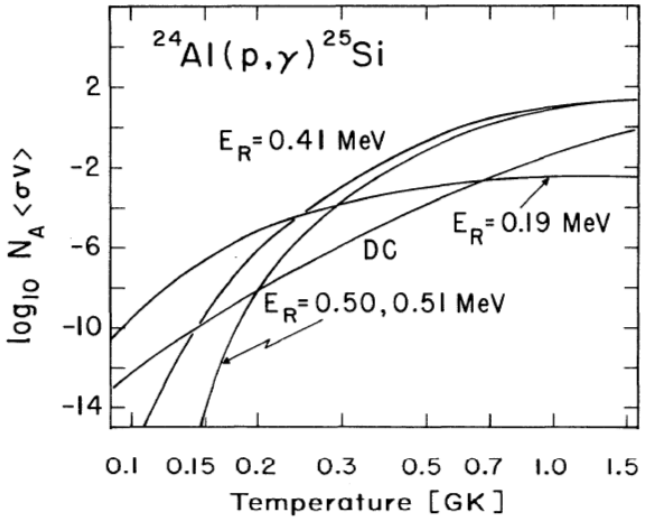

FIGURE 2.5: Variation of reaction rates with temperature [5].

This results in matter being transferred from the main sequence star to the white dwarf, forming an accretion disk around it as the matter accelerates towards the surface of the star. The stolen mass is drawn from the surface of the main sequence star, meaning that it contains high levels of hydrogen. As this hydrogen is pulled in by the high gravitational force created by the white dwarf, it is heated and compressed. At some point as it falls, the matter becomes electron degenerate, and so it cannot cool via expansion, and a temperature of $\sim 20 \times 10^6$ K is reached that allows fusion to begin on the surface of the white dwarf [35].

The hydrogen-rich matter transferred from the main sequence star is mixed with material, made up from heavier elements, from the top layer of the white dwarf. Due to the degeneracy of the transferred material, expansion cannot occur to control the energy being released from the hydrogen burning that is taking place. As a result, temperature increases, causing more thermonuclear reactions to occur at a higher rate in a process referred to as themornuclear runaway, which results in an eruption of material into the interstellar medium [6].

Reaction rates in novae are very sensitive to temperature and so the abundance of different elements seen from novae events can be used to determine the peak temperature reached during the event. Of course, the accuracy of this deduction depends on how well the reactions involved in the process are understood experimentally. The range of temperature predicted by different models is $T_{peak} = 0.145 - 0.418$ GK [6], which is in the temperature range required for the CNO cycle to begin.

X-ray bursts are caused by similar circumstances as novae, though are created in much more extreme environments. Both occur in binary star systems containing a main sequence star. The difference is in the second star involved; whereas an accretion disk is formed around a white dwarf star in novae, it is instead formed around a neutron star (or possibly a black hole) for X-ray bursts. The increased density of the neutron star creates a much stronger gravitational field, which allows for higher temperatures to be reached before the degeneracy is lifted within the accretion disk material, resulting in a mass ejection explosion that is characterised by its X-ray activity.

2.5 Inverse Kinematics

The kinematics of an experiment can greatly affect the set-up of the apparatus used. In a classic experiment, measuring the elastic scattering of a reaction, and where a light projectile nucleus is incident on a heavy target nucleus, one might expect both the ejected and the recoil particles to be detected at angles forward of the target, whereas in a reaction with a positive Q-value, some particles would be expected to be found at backward angles. The reasons for this will be discussed in this section.

Due to the half-life of ^{24}Na being so short (approx. 15 hours [37]), it is infeasible to create a target to be used for the duration of the experiment. Because of this factor, the work described here was performed in inverse kinematics, where the heavy, radioactive ^{24}Na nuclei were created via the ISOL technique (described further in section 3.2) in a cyclotron and accelerated to the experimental hall to collide with the deuteron atoms in the target. The derivation of the kinematics seen in the experiment is purely classical, but serves well in explaining the expected kinematics of the experiment.

Consider a reaction $m_1(m_2, m_3)m_4$ in which a light particle is incident on a heavy target as shown in Figures 2.6 and 2.7 for the lab frame and centre-of-mass frame respectively. In the lab frame, m_2 is stationary, and hence $T_2 = \overrightarrow{p_2} = 0$, therefore, $\overrightarrow{p_1} = \overrightarrow{p_3} + \overrightarrow{p4}$. In the centre of mass frame, $\overrightarrow{p_1'} + \overrightarrow{p'2} = \overrightarrow{p_3'} + \overrightarrow{p_4'} = 0$, where primed quantities represent the values in the centre-of-mass frame. A tilde in an equation represents a quantity after a reaction has occurred.

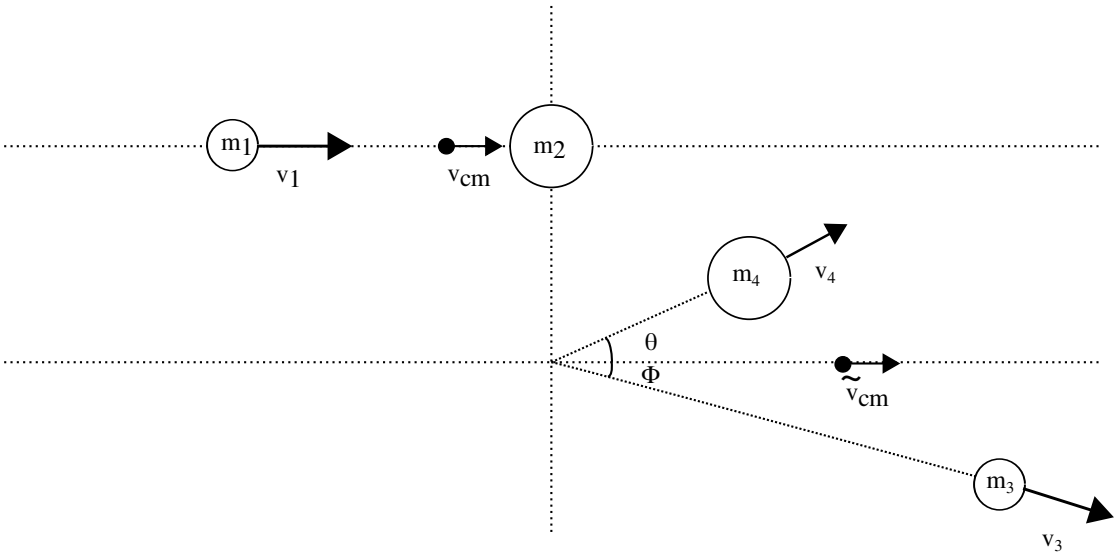

FIGURE 2.6: The trajectories of two particles before(top) and after (bottom) a reaction in the laboratory frame.

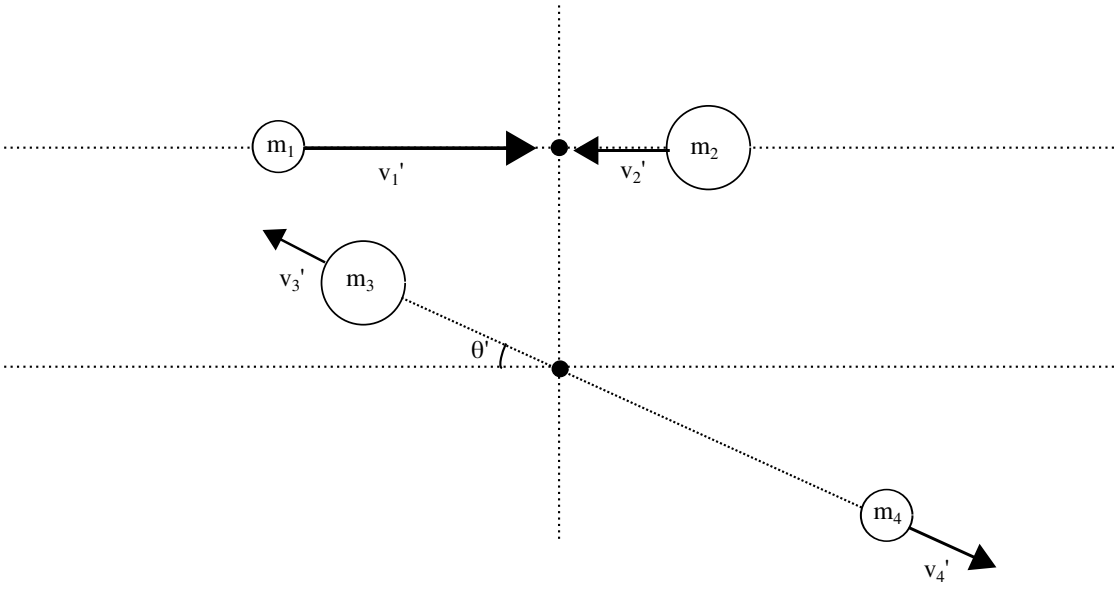

FIGURE 2.7: The trajectories of two particles before(top) and after (bottom) a reaction in the centre-of-mass frame.

Due to conservation of momentum:

$$v_2' = \frac{m_1}{m_2} v_1' \tag{2.30}$$

$$v_4' = \frac{m_3}{m_4} v_3'. \tag{2.31}$$

From Figure 2.6, it can be shown that the velocity vectors of the particles can be given as:

$$\overrightarrow{v_1}' = \overrightarrow{v}_1 - \overrightarrow{v}_{cm} \tag{2.32}$$

and

$$\overrightarrow{v}_{cm} = \frac{m_1 \overrightarrow{v}_1}{m_1 + m_2}. \tag{2.33}$$

Implying

$$\begin{aligned} \overrightarrow{v_1}' &= \overrightarrow{v}_1 - \frac{m_1 \overrightarrow{v}_1}{m_1 + m_2} \\ &= \overrightarrow{v}_1 \left(1 - \frac{m_1}{m_1 + m_2}\right) \\ &= \overrightarrow{v}_1 \left(\frac{m_2}{m_1 + m_2}\right). \end{aligned} \tag{2.34}$$

Therefore, substituting Equation 2.30 into equation Equation 2.34 gives:

$$\overrightarrow{v}_{cm} = -\overrightarrow{v'}_2. \tag{2.35}$$

Rearranging Equation 2.33 to make v_1 the subject and substituting into 2.32 provides an expression for v_1' in terms of m_1, m_2 and v_{cm}:

$$\begin{aligned} \overrightarrow{v_1'} &= \left(\frac{m_1 + m_2}{m_1}\right) \overrightarrow{v}_{cm} - \overrightarrow{v}_{cm} \\ &= \overrightarrow{v}_{cm} \left(\frac{m_1 + m_2}{m_1} - 1\right) \\ &= \overrightarrow{v}_{cm} \left(\frac{m_2}{m_1}\right) \end{aligned} \tag{2.36}$$

The energy of the centre-of-mass frame before the reaction is equal to the sum of the kinetic energy of the beam m_1 plus the kinetic energy of the target m_2. Similarly, the energy of the centre-of-mass frame after the reaction is equal to the kinetic energy of the products m_3 and m_4. Using this information and using Equations 2.30 and 2.31 gives:

$$E_{cm} = \frac{1}{2} m_1 v_1'^2 \left(\frac{m_1 + m_2}{m_2} \right) \tag{2.37}$$

and

$$\tilde{E}_{cm} = \frac{1}{2} m_3 v_3'^2 \left(\frac{m_3 + m_4}{m_4} \right). \tag{2.38}$$

Substituting Equation 2.36 into 2.37,

$$\begin{aligned} E_{cm} &= \frac{1}{2} m_1 \left(\frac{m_2}{m_1} \right)^2 \overrightarrow{v}_{cm}^{\,2} \left(\frac{m_1 + m_2}{m_2} \right) \\ &= \frac{1}{2} \frac{m_2^2}{m_1} \overrightarrow{v}_{cm}^{\,2} \left(\frac{m_1 + m_2}{m_2} \right) \\ &= \frac{1}{2} \frac{m_2}{m_1} \left(m_1 + m_2 \right) \overrightarrow{v}_{cm}^{\,2}, \end{aligned} \tag{2.39}$$

since $\overrightarrow{v}_{cm}$ is related to $\overrightarrow{\tilde{v}}_{cm}$ via,

$$\begin{aligned} \left(m_1 + m_2 \right) \overrightarrow{v}_{cm} &= \left(m_3 + m_4 \right) \overrightarrow{\tilde{v}}_{cm} \\ \overrightarrow{v}_{cm} &= \frac{m_3 + m_4}{m_1 + m_2} \overrightarrow{\tilde{v}}_{cm} \\ \Rightarrow E_{cm} &= \frac{1}{2} \frac{m_2}{m_1} \frac{\left(m_3 + m_4 \right)^2}{m_1 + m_2} \overrightarrow{\tilde{v}}_{cm}^{\,2} \end{aligned} \tag{2.40}$$

The center-of-mass energy post reaction, $\tilde{E}_{cm}$ is equal to the center-of-mass energy prior to the reaction plus the Q-value of the excited state, E_x, of the recoil particle, Q^*:

$$\tilde{E}_{cm} = E_{cm} + Q^*, \tag{2.41}$$

where Q^* equals the ground-state Q-value minus the excitation energy, E_x. Let us define a quantity, q, that describes the ratio between $\tilde{E}_{cm}$ and E_{cm}:

$$\frac{\tilde{E}_{cm}}{E_{cm}} = 1 + \frac{Q^*}{E_{cm}} \equiv q \tag{2.42}$$

Using Equation 2.42 and substituting values for $\tilde{E}_{cm}$ and E_{cm} from Equations 2.38 and 2.40 respectively, it is possible to get a value for $v_3'/\tilde{v}_{cm}$:

$$\begin{aligned} q &= \frac{\frac{1}{2}m_3 v_3'^2 \left(\frac{m_3+m_4}{m_4}\right)}{\frac{1}{2}\frac{m_2}{m_1}\frac{(m_3+m_4)^2}{m_1+m_2}\tilde{v}_{cm}^2} \\ &= \frac{m_3}{m_2}\frac{m_1}{m_4}\frac{(m_1+m_2)}{(m_3+m_4)}\left(\frac{v_3'}{\tilde{v}_{cm}}\right)^2 \\ \Rightarrow \frac{v_3'}{\tilde{v}_{cm}} &= \sqrt{q\frac{m_2}{m_3}\frac{m_4}{m_1}\frac{(m_3+m_4)}{(m_1+m_2)}} \end{aligned} \tag{2.43}$$

This value is important when describing the vector diagram of the reaction. Consider the scenario shown in Figure 2.7. In the lab frame, the centre-of-mass frame is travelling along at a velocity $\tilde{v}_{cm}$ in the direction of the beam, as shown in Figure 2.6. Figure 2.8 shows how the trajectories seen in the lab relate to those seen in the centre-of-mass frame. The possible orientations of v_3' and v_4' trace out a circle around the centre-of-mass. It can be seen that θ reaches a maximum when v_3 and v_3' are perpendicular to each other. Hence the maximum angle, θ_{max}, at which particle 3 can be detected is:

$$\begin{aligned} \theta_{max} &= \arcsin\left(\frac{v_3'}{\tilde{v}_{cm}}\right) \\ &= \arcsin\sqrt{q\frac{m_2}{m_3}\frac{m_4}{m_1}\frac{(m_3+m_4)}{(m_1+m_2)}} \end{aligned} \tag{2.44}$$

Now consider the reaction studies in this work; the $d(^{24}\mathrm{Na}, p)^{25}\mathrm{Na}$ reaction is performed in inverse kinematics and so m_1, m_2, m_3 and m_4 refers to ^{24}Na, d, p and ^{25}Na respectively. Since m_1 and m_4 have comparable masses in this reaction, and the quantity q deviates from 1 by a factor of less than 10% [38], Equation 2.44 reduces to:

$$\theta_{max} \approx \arcsin\sqrt{\frac{m_2}{m_3}} \tag{2.45}$$

For a (d, p) reaction, $m_2/m_3 = 2$ and so θ_{max} is undefined meaning that the light proton ejectile has no maximum angle. In other words, $v_3' > \tilde{v}_{cm}$ in Figure 2.8. In this scenario,

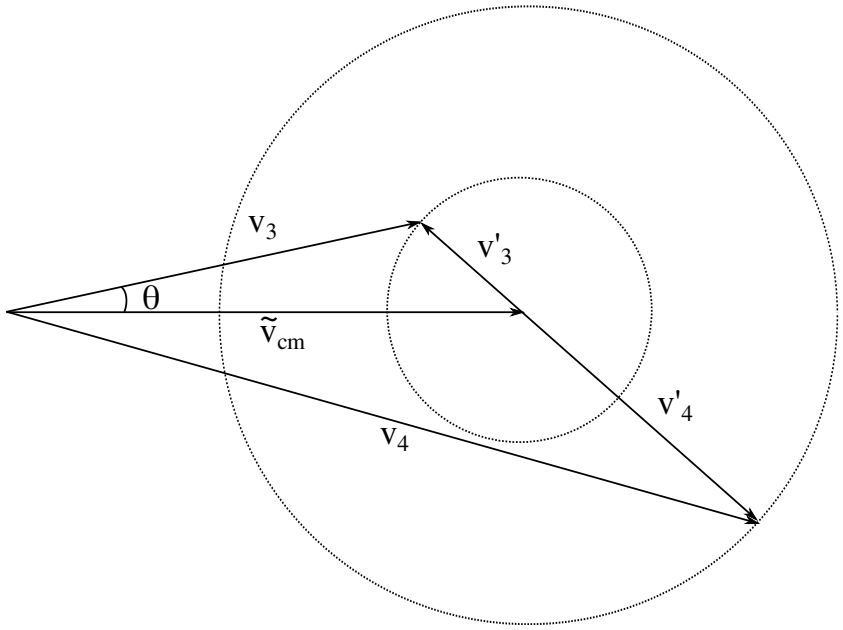

FIGURE 2.8: Velocity diagram for a $m_1(m_2, m_3)m_4$ reaction. The transformation between the lab frame and the centre-of-mass frame.

the value of the heavy recoil nucleus' velocity, v_4' is small, and so the ^{24}Na nucleus is focused into a cone in the direction of $\tilde{v}_{cm}$.

2.6 Energy Loss in Matter

2.6.1 Charged Particle Energy Loss in Matter

A charged particle, as it passes through a medium, will interact with the Coulomb field created by the atoms in that medium. This force is felt simultaneously by many electrons as the charged particle passes by. In most cases, nearly all of the energy of the charged particle is lost to electrons as opposed to the nucleus of atoms in the absorbing medium. The impulse given to the electron transfers momentum and so the lighter mass of an electron means that it will carry away more energy than the nucleus. Nuclear interactions are also rare unless the interacting charged particle has a high energy. Because of these facts, a particle is not affected much by the nucleus of the absorbing material [16]. The attractive forces felt by an individual electron as the charged particle passes by might excite it into a higher energy state, or separate it from its atom depending on its distance from the charged particle. It is this ionisation process that creates the charge that is used to detect the charged particle as it passes through a detector [39].

These interactions gradually slow down the particle as it passes through a material until it is completely stopped. The rate of energy loss per unit of distance travelled in a material is referred to as the stopping power of that material [39],

$$S = -\frac{\mathrm{d}E}{\mathrm{d}x}, \tag{2.46}$$

where $\mathrm{d}E/\mathrm{d}x$ is negative because energy is being lost as a particle passes through a material. The formula used to predict the stopping power of a particular material was derived in 1930 and is known as the Bethe-Bloch formula:

$$-\frac{\mathrm{d}E}{\mathrm{d}x} = \left(\frac{ze^2}{4\pi\varepsilon_0}\right)^2 \frac{4\pi Z\rho N_A}{Amv^2}\left[\ln\left(\frac{2mv^2}{I}\right) - \ln\left(1-\beta^2\right) - \beta^2\right], \tag{2.47}$$

where Z, A and ρ are the atomic number, atomic mass and density of the absorbing material respectively, m is the mass of an electron, ze is the charge of the ion, and v is its velocity. The mean energy required to ionize an atom in the stopping material is given by I, and is generally considered to be equal to $11Z$ eV. Equation 2.47 reveals several things about the stopping power of a material: it is directly proportional to the density of electrons in the stopping material ($Z\rho N_A/A$), and it is dependent on $1/v^2$ (and therefore m/E) of the charged particle [16].

As the ion travels through the absorber material and loses energy, it spends more time interacting with surrounding electrons. As a result, its rate of loss of energy reaches a maximum at low energies. The Bethe-Bloche formula is not valid at very low energies since the possibility of electron capture in the ion increases and so it can no longer be assumed that the z of the particle is the same as it was when it first entered the absorbing material.

2.6.2 Gamma-ray Interactions in Matter

There are three main contributing effects to the absorption of a photon in matter: the photoelectric effect, Compton scattering, and pair production. The frequency of photon interactions of a particular type is dependent on the energy of the photon and the Z of the absorbing medium. Figure 2.9 shows the relative importance of each interaction method as Z of the absorbing material, and energy of the photon changes.

The first way in which photons are absorbed by a material is the photoelectric effect, which dominates when the photon has an energy of a few hundred keV. The photon is completely absorbed by the bound electron in the absorbing material and excites it

enough to escape the atom with the energy of the absorbed photon minus the binding energy of the electron. This interaction only occurs between an atom and a photon, and so will create an ionised atom with and electron vacancy in one of its shells. This hole is quickly filled by the re-arrangement of electrons in higher shells de-exciting and emitting a characteristic X-ray in the process, or through the capture of a free electron. The characteristic X-ray emitted could then also be absorbed by its surroundings via the same process. Auger electrons may be emitted instead of a characteristic X-ray [39].

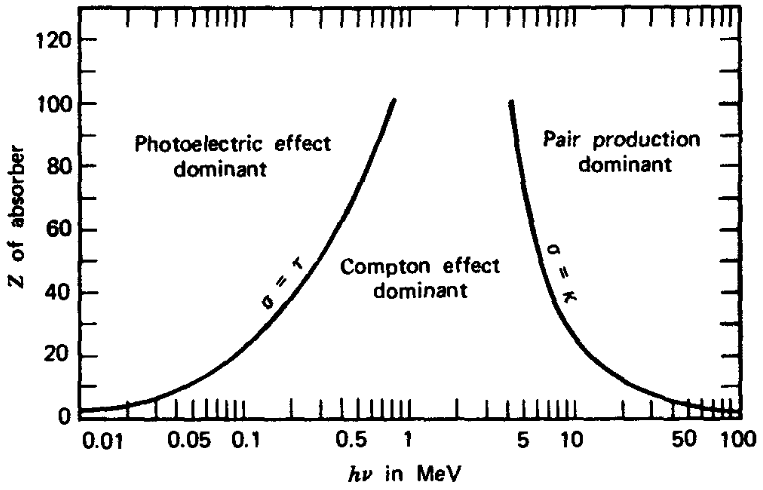

FIGURE 2.9: Relative importance between the three main methods of photon absorption at different energies and different atomic masses [39].

The second interaction method is Compton scattering, which is typically the most relevant interaction for photons of a few MeV. During the scattering process, the γ-ray imparts a fraction of its energy to the recoil electron that is proportional to its scattering angle, θ relative to its original direction. The expression relating the final energy of the γ-ray post scattering event, $h\nu'$, to the scattering angle is

$$h\nu' = \frac{h\nu}{1 + \frac{h\nu}{m_0c^2}\left(1 - \cos\theta\right)}, \tag{2.48}$$

where $h\nu$ is the energy of the γ-ray before scattering, and m_0c^2 is the rest-mass energy of the electron (511 keV).

A scattering angle of 180° equates to the maximum energy given to the recoil electron. A γ-ray can not lose all of its energy via Compton scatter since the only solution for $h\nu' = 0$ in Equation 2.48 is for $h\nu$ to also equal 0. This means that the only way to detect the full energy of a γ-ray is for it to first scatter and lose enough energy to then be absorbed via the photoelectric effect. Photons that scatter inside a detector, but

are not fully absorbed, will contribute to the Compton continuum in the final energy spectra.

The final mechanism that describes how photons interact with matter is pair production. This can start to occur when the energy of a photon is greater than the rest-mass energy of two electrons. Practically, however, the processes only becomes relevant at energies of several MeV. The interaction takes place in the Coulomb field of a nucleus where the γ-ray photon disappears and is replaced by an electron-positron pair. Any extra energy the γ-ray had is carried away by the pair in the form of kinetic energy. The positron then loses energy and comes to rest, and is annihilated, producing two secondary γ-rays at 0.511 MeV each [39].

These mechanisms for photon interaction with matter all depend on the absorber atomic mass, Z and energy of the γ-ray, E_γ. The probability of an interaction occurring per nucleus for photoelectric absorption, τ, is approximately

$$\tau \cong \text{constant} \times \frac{Z^n}{E_\gamma^{3.5}} \tag{2.49}$$

were n varies between 4 and 5 depending on what E_γ range is being examined. Compton scattering is more likely to occur if there are more electrons to scatter off, the probability of the γ-ray being absorbed via this method per atom is therefore linearly dependent on Z. There is no simple relationship between the probability of pair production and the atomic mass of the absorber, but an approximation is that it varies as a function of Z^2 [39].

Chapter 3

Experimental Details

3.1 Experimental Overview

The experiment described in this work looks to populate excited states in ^{25}Na via a (d, p) reaction using a beam provided by the ISAC-II facility. The beam used consisted of the radioactive element ^{24}Na and had an energy of 8 MeV per nucleon which was incident on a target made of deuterated carbon (CD_2). The intensity of the beam was initially expected to be 10^6 pps, but was reduced to 10^4 pps early in the experiment. As a result of this, the decision was made to increase the the target thickness from 0.5 mg/cm^2 to 1.0 mg/cm^2 to ensure that good statistics were still gathered.

The experiment was performed in inverse kinematics meaning that the beam particle is heavier than the target particle, unlike the traditional experimental procedure where the target contains the heavy particle. After collision, the produced ^{25}Na particles' trajectories remain reasonably unaltered due to the fact that they contain most of the mass of the system. There was no zero detector available during the experiment that was able to determine the energy of the reacted ^{25}Na particles. Instead, the light ejected proton was detected since they were emitted at all angles around the target (as described in section 2.5).

The protons were detected by the SHARC (Silicon Highly-segmented Array for Reactions and Coulex) detector array. This was made up of a total of twelve double-sided silicon strip detectors (DSSSDs) which cover an angular range between 35° and 172°. Elastically scattered protons and deuterons were detected at angles less than 90° which are used in the normalisation of the cross section. Protons detected from the (d, p) reaction can be emitted at all angles, but were only expected to be seen above 90°. The angle of detection and energy of the protons are required to establish the energy of the populated

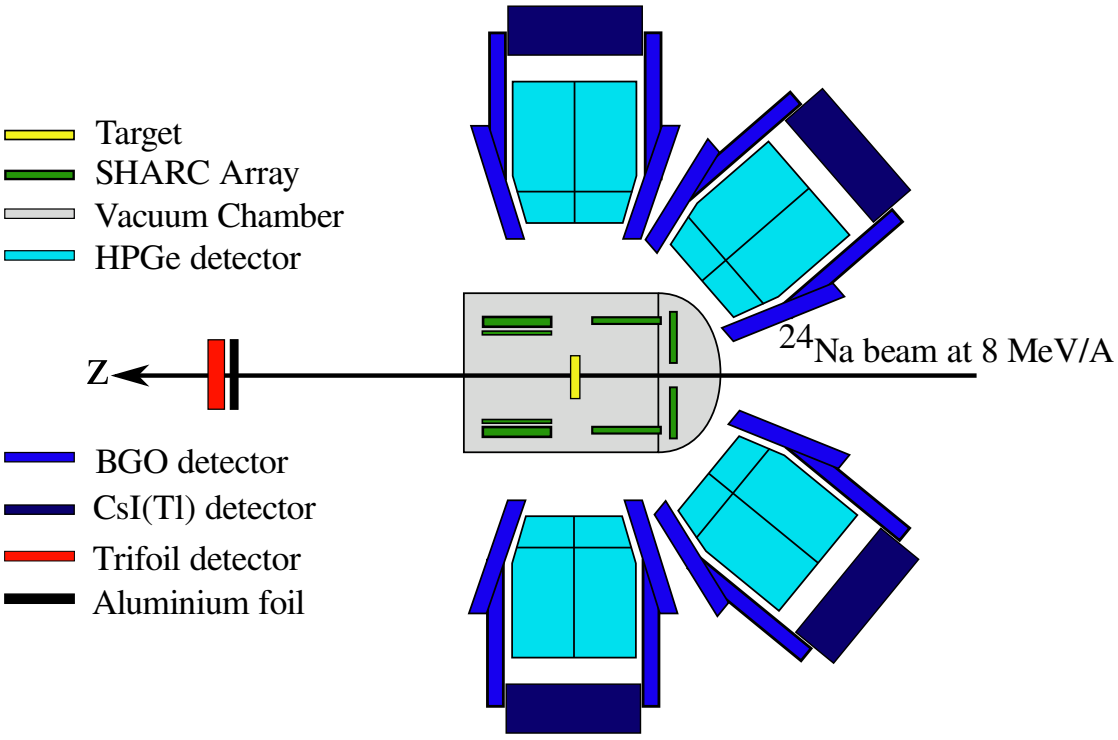

FIGURE 3.1: Schematic of the experimental set-up.

state in ^{25}Na. As a result, SHARC is designed to have a very high angular resolution (section 4.2.3). The whole detector is housed within a vacuum chamber in order to prevent emitted protons form imparting some of their energy to air molecules.

Post reaction, if a neutron has been placed in a bound excited state of ^{25}Na then it will de-excite via γ-ray emission. These γ-rays are detected by the TIGRESS (TRIUMF-ISAC Gamma Ray Escape Suppressed Spectrometer) array, which surrounds the vacuum chamber housing SHARC. It is made up of up to sixteen high purity germanium detectors (HPGe) that are placed in rings of $\theta = 45°, 90°$ and $135°$ around SHARC, though only twelve were used in this experiment at $\theta \geq 90°$ in order to make room for the SHARC electronics to be mounted. TIGRESS also has the option of utilising bismuth-gemanate (BGO) and thallium-drifted caesium iodide (CsI(Tl)) scintillator detectors in order to decrease the signal-to-noise ratio of the γ-ray data.

Due to the target used in the experiment containing carbon as well as deuterium, it is possible for a compound reaction to occur in which ^{12}C fuses with the beam particles. These particles are discriminated against using the Trifoil; a scintillator detector placed in the beam line. The Trifoil has an aluminium foil placed in front of it which prohibits the transmission of fusion evaporation products while simultaneously allowing the transmission of beam-like particles, thus giving a way to determine when protons from the (d, p) reaction have been detected.

The Data Acquisition (DAQ) is triggered when a particle is detected in SHARC at which point data from every other electrical channel is read out and recorded. The thresholds in the DSSSD detectors are set at 2 MeV (with the exception of one which has a threshold of 1.5 MeV). The overall set-up of the experiment is shown schematically in Figure 3.1, which shows the main attributes of the detector array.

3.2 The TRIUMF Facility

Traditionally the heavier of the two particles involved in a reaction is located in the target of the experiment, which is bombarded by a beam made up of the lighter particles. This becomes impractical when studying unstable nuclei because the particle being examined will decay away during the manufacture and transportation of the target to the experimental hall and during the experiment itself. The use of a radioactive beam is therefore utilised so that the unstable particle of interest can be created on site and transported directly to the experimental hall.

Radioactive beams can be produced using two methods: in-flight fragmentation and Isotope Separation On-Line (ISOL). In-flight fragmentation is performed by accelerating heavy ions into a thin target material, causing fragmentation. This produces a secondary beam made up of various different types of particle that are separated out before being transported to the experiment [40]. This technique is advantageous when a high energy secondary beam is required because the secondary beam carries a lot of the forward momentum of the primary beam after its collision with the target, thus eliminating the need to re-accelerate the beam. However, at relatively low energies, secondary beam is scattered much more by the target, resulting in a less focused beam spot.

In comparison to this, the ISOL technique uses a light particle primary beam on a heavy production target. This creates the particles that will be used in the secondary beam through spallation, fragmentation, fission and various other reaction channels [41]. The produced particles are completely stopped in the thick target, unlike in-flight separation, preventing them from being taken directly to the experimental hall to be used within the experiment. The production target is heated to assist the diffusion of the stopped radioactive particles to its surface where they are ionised, electromagnetically separated from other products produced in the target, and re-accelerated to the experimental hall. The advantage of this technique is that it allows for a relatively low energy beam due to the fact that the beam particles were completely stopped in the production target, then re-accelerated. This allows for experiments to be performed at energies just above the Coulomb barrier.

The TRIUMF (Tri-University Meson Facility) cyclotron in Vancouver, Canada, utilises the ISOL technique to create the radioactive beam. The primary beam of protons with an energy and intensity of up to 500 MeV and 100μA are produced by accelerating negatively charged hydrogen atoms through the six-sector magnetic field of the cyclotron. The magnetic field bends the H^- ions, causing them to follow a spiral trajectory as they are accelerated. When the hydrogen atoms have been accelerated to the desired speed, they pass through a graphite stripping foil which removes the electrons in the atom (and therefore creating positively charged ions). This change in charge causes the ions to change direction and are steered out of the cyclotron and into the beam line and taken to the rest of the Isotope Separator and Accelerator (ISAC) experimental hall.

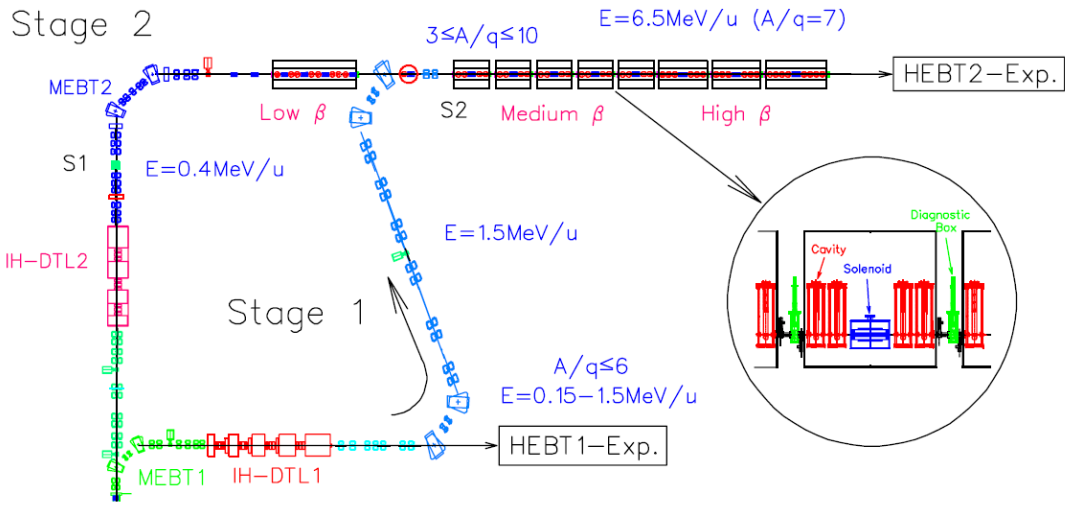

FIGURE 3.2: Schematic of the beamline in the ISAC facility [42].

There are two ISAC halls within TRIUMF. ISAC-I is is used for experiments where the required beam energies range between 0.153 and 1.53 MeV/u [43]. The beam is bunched within the Low Energy beam transport (LEBT) using an 11.8 MHz multi-harmonic pre-buncher, which increases the beam quality. The initial acceleration is created by a Radio Frequency Quadrupole (RFQ), operating at 35.36 MHz, which accelerates the beams with a mass to charge ratio of $A/q \leq 30$ from 2 keV/u to 153 keV/u. The use of a the 35.36 MHz RFQ after the 11.8 MHz pre-buncher creates small satellite bunches around the primary bunches of the beam. A chopper is used to clean up these small satellites so that only the primary bunch is passed into the Interdigital H-mode Drift Tube Linac (IH-DTL) to be accelerated further [43][44]. At this stage, the beam is either directed to be used within the ISAC-I (labelled as HEBT1-Exp in Figure 3.2) hall, or is transferred to the ISAC-II hall.

ISAC-II is an extension of ISAC-I in which the beam is deflected north using an S-bend transfer line as depicted in Figure 3.2. This bend allows further separation of particles with a different mass-to-charge ratio, (A/q), compared to the desired beam particle. The beam was accelerated further to between 5 to 11 MeV [45] towards the experimental hall (labelled as HEBT2-Exp) using the ISAC-II linear accelerator.

TIGRESS is situated at the end of the HEBT2-Exp beam line. A stable beam of ^{24}Mg was used for beam tuning. A 2 mm aperture transmitted 86% of the stable beam. The radioactive ^{24}Na beam was re-tuned using a 3 mm aperture at the target position to ensure that it was correctly focused and centred for the experiment. The tuning managed to achieve a transmission of 100% in this case.

3.3 SHARC

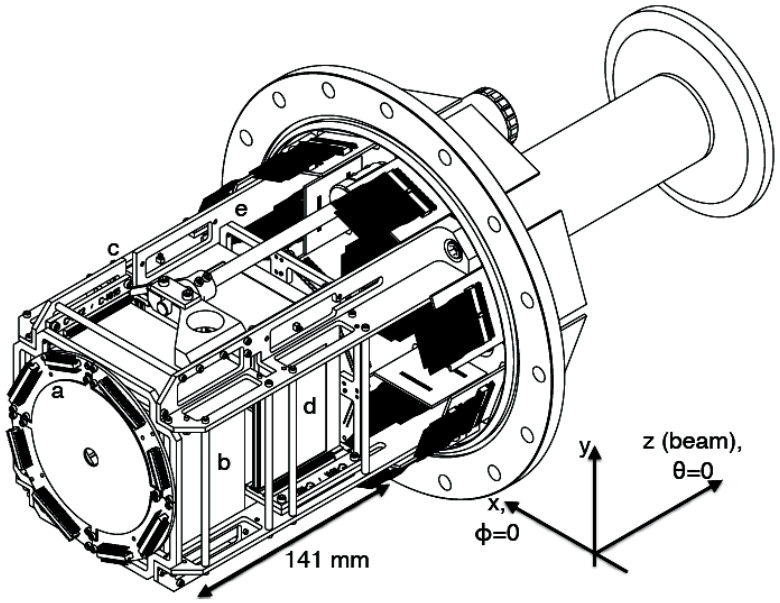

FIGURE 3.3: Schematic of the full SHARC array[46].

SHARC (Silicon Highly-segmented Array for Reactions and Coulex) is a highly advanced array consisting of up to sixteen DSSSD detectors. Its purpose is to be used for detecting particles from transfer reactions in inverse kinematics. It has been designed so that its components can be removed and re-arranged depending on the detection requirements and the kinematics expected for the experiment being undertaken. Figure 3.3 shows the frame of the array and that the array consists of two box detectors, one downstream of the target, and one upstream (labelled b and d respectively), and two CD detectors, so called because of the physical resemblance to a compact disk (labelled a and e, where

e is actually positioned behind the box detector). Each DSSSD described here, with the exception of the PAD detectors found in the downstream box, are segmented into pixels. The nature of this segmentation will be described in more detail in the following subsections, however, it is noted here due to it being a common feature for all DSSSD detectors that there is an aluminium strip running along the front and back face of the detectors. This strip is used to collect and carry away the electronic signal from the detector.

The inclusion of two box detectors, rather than one larger detector that covers a greater angular range allows for the insertion of the target through the gap between the detectors. The target holder consists of a rotating fan that rotates through the beam path. The fan has space for four targets to be placed on it at any one time, which allows the experimenters to quickly switch between targets as required quickly and without having to vent the chamber housing the array. The hinge for this fan is labelled "c" in Figure 3.3.

The cuboid shape of the SHARC array makes it convenient to define a co-ordinate system that uses Cartesian co-ordinates where z is in the direction of the beam, and y points in the direction of the ceiling.

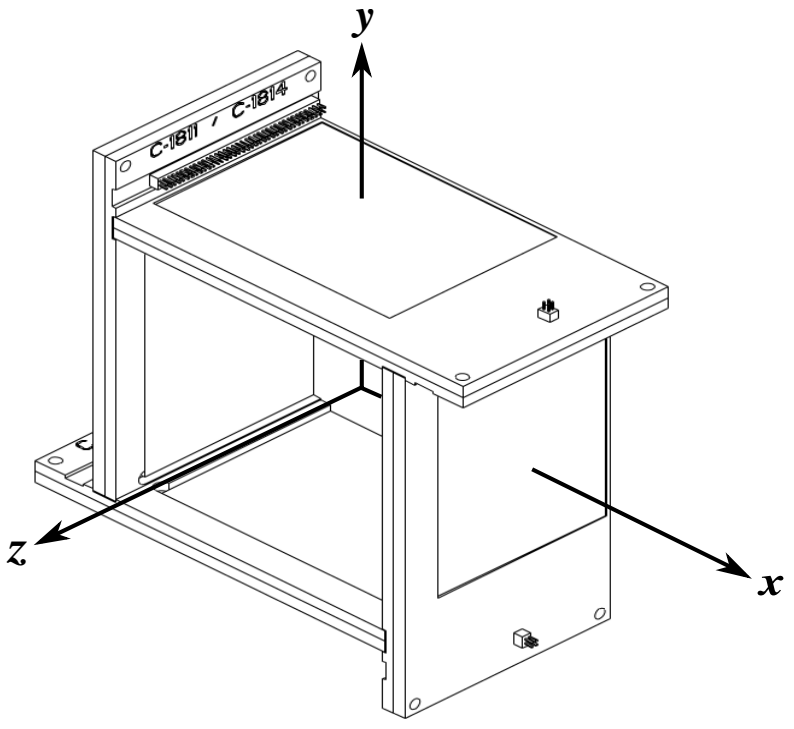

FIGURE 3.4: Drawing of the downstream box of SHARC including the $\Delta E-E$ detector.

3.3.1 Box Detectors

Each box detector is made up of four DSSSD detectors. These detectors are arranged in a windmill orientation where the edge of one detector slots into a groove in the edge of the adjacent detector. This construction allows for the detectors to only be supported by the frame at one point each, whist still being stable, and allows for the active area of each PCB to cover as much of the solid angle as possible because the detector is able to extend right up to the edge of the next detector. This windmill configuration is shown in Figure 3.4 for the upstream box detector.

This windmill set-up also allows for some flexibility in the angular coverage of the box detectors as it is possible to invert the PCBs so that the active area of the detector covers angles closer to 90°. The decision to do this or not is dependent on what is expected to be seen in the experiment at hand and which angles are predicted to be important. For this work, the downstream box is inverted relative to the upstream box so that both boxes have the best angular coverage close to 90°.

There is a slight difference in size between the upstream and downstream box: the exposed area of each PCB in the downstream box is 80.0×61.1 mm^2 compared to 83.4×61.1 mm^2 per PCB in the upstream box. The difference in size is caused by the use of a $E - \Delta E$ telescope in the downstream detector. This consists of a thin 140 μm thick ΔE DSSSD, which was segmented into pixels in the same way as the downstream box, followed by a much thicker 1500 μm PAD detector placed behind, which had no segmentation, but was used to stop particles that punched through the ΔE detector.

The upstream box detector consists of four highly segmented DSSSDs of a thickness of 1000 μm. The dimensions of the active area are 72×48 mm^2. The detector is divided into pixels using conductive strips along the front and back of the detector which are used to determine the position of the interaction point within the detector. The front strips have a pitch width of 3 mm, and run parallel along the z-axis of the array, whereas the back strips have a pitch width of 1 mm, and run perpendicular to the z-axis. The gap between each strip is 0.1 mm for both front and back strips as shown in Figure 3.5.

The electronics channels coming from each PCB are numbered so that the position of each detection can be documented. Front strips are numbered from 1 to 24 and back strips are numbered 1 to 48. This numbering system can be used to work out the position along the active area corresponding to the centre of each front strip. This position, defined as l, is given by

$$l = \frac{P}{2} + (n-1)\,P, \tag{3.1}$$

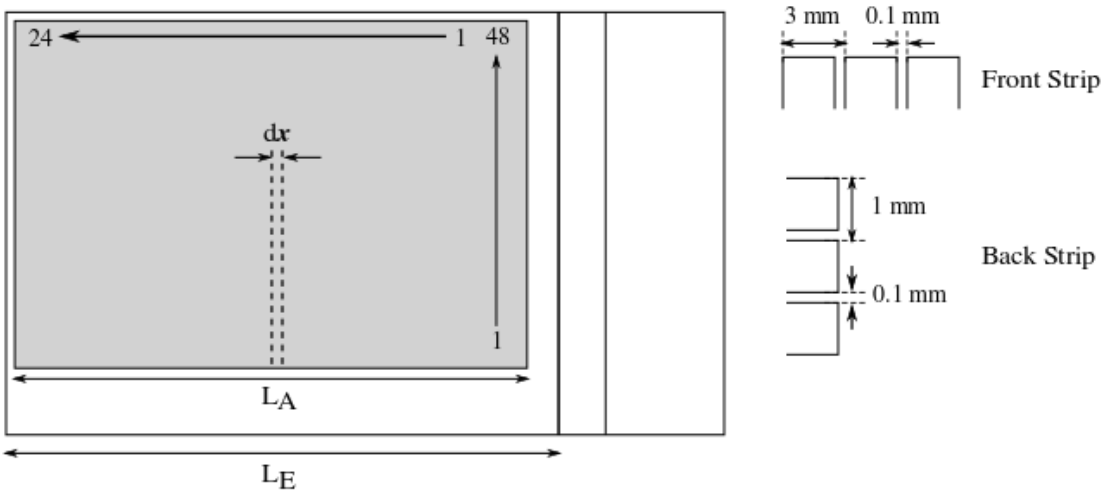

FIGURE 3.5: Schematic of a PCB in one of the SHARC box detectors. The shaded area represents the active area. The difference between the centre of the active length, L_A, and the exposed length L_E is given by dx.

where $P = 3$ is the pitch of the front strip and n is the strip number.

Due to the inversion of the box detectors relative to each other as described above, the numbering system of the back strips are reversed for each detector in the downstream box relative to the upstream box. The asymmetry of the PCB's design means that the centre of the length of the active area, L_A, of the detector is not simultaneously the centre of the length of the PCB that is exposed to the protons that are detected in the experiment, L_E, as shown in Figure 3.5. The centre of the exposed length is relevant because it matches a co-ordinate (the x or y co-ordinate depending on which side of the box detector the PCB is placed on) with the target position. The position of each strip relative to the target should therefore be known in order to work out the angle it covers relative to the target. The difference between the centre of the active length is given by half the difference between the two lengths, $dx = (L_E - L_A)/2$. The translation between the position along the active area given by Equation 3.1 and the position relative to the target, L_R, can therefore be given by

$$L_R = \pm \left(l - \frac{L_A}{2} + dx \right). \tag{3.2}$$

Here, the $\pm$ occurs due to the fact that the PCB is rotated by 90 degrees for each side of the box and so the geometry of the strips is flipped along the imaginary line showing the centre of the exposed length. The value of dx is different between the upstream and downstream box due to their difference in size:

$$dx = \begin{cases} 4.0mm & \text{for downstream DSSSDs} \\ 5.7mm & \text{for upstream DSSSDs.} \end{cases} \tag{3.3}$$

3.3.2 CD Detectors

The CD detectors, so called because they form a disk that resembles a Compact Disk, each consist of four QQQ detectors of a thickness of 400 μm which are mounted together on one frame. A 9 mm hole at the centre of the detector allows the beam through to the target. An aluminium shield is mounted behind the DSSSDs in the direction of the beam in order to protect the detector from being hit by the beam directly if the beam were to be incorrectly focused onto the target. SHARC is designed to use two CD detectors in total, one upstream of the target, and one downstream. However, due to being limited in the number of electronics channels available for the experiment, only the upstream CD detector was used to collect these results.

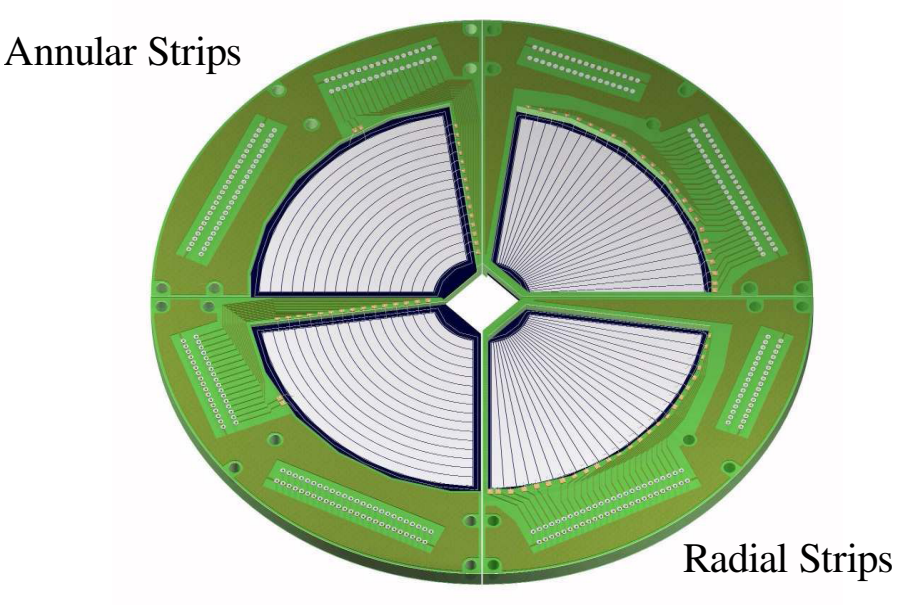

FIGURE 3.6: A fully assembled CD detector displaying the front and back segmentation [47].

Each quadrant of the CD detector is segmented into twenty-four radial and sixteen annular sections as depicted in Figure 3.6. Each radial strip covers an angle in ϕ of 3.4° each, with each quadrant covering 81.6° in ϕ. The width of each annular strip is 2 mm. The entire upstream CD detector covers a range of $\theta = 148.0°$ to 171.7°.

3.4 TIGRESS

The TIGRESS array is a Hyper Pure Germanium (HPGe) detector array situated at the end of the beam line in the ISAC II facility at TRIUMF. It consists of up to sixteen clover detectors placed around a target in three separate rings at $\theta = 45°, 90°$ and $135°$, which can hold four, eight and four clover detectors respectively. When fully assembled, the faces of the detector fit together to form a rhombicuboctahedron [48], as shown in Figure 3.7. The distance of each face of the detectors from the target can be adjusted between 11.0 cm "high efficiency" configuration, and 14.5 cm "suppressed" depending on the purpose of the experiment [49]. When in its suppressed configuration, the detectors are drawn back far enough to allow compton suppression shields to be placed around them, as will be discussed later in the chapter.

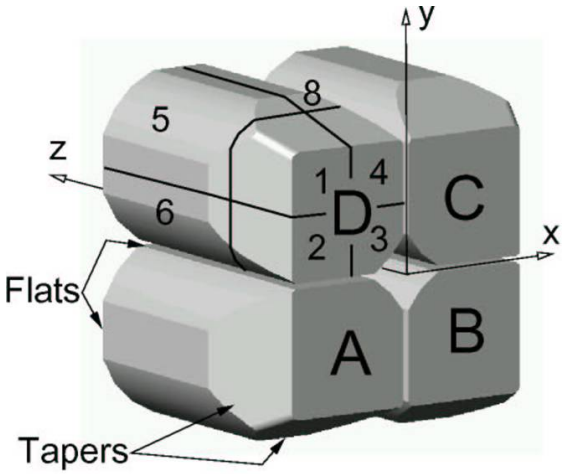

FIGURE 3.7: Three-dimensional model of a TIGRESS clover [50]. The labeling system described in text.

Each clover contains four closed-ended, coaxial HPGe crystals, initially 60 mm in diameter and 90 mm in length, which are cut to have four flat lengths along their sides to allow for efficient packing into a square. The front 30 mm of each crystal is tapered at 22.5° in order to allow for close packing with neighbouring clovers. These measurements are shown in Figure 3.10.

TIGRESS uses a Cartesian co-ordinate system to describe the internal position of each component making up the detector (see section 3.4.1), but uses a polar co-ordinates (r, θ, ϕ) to describe the position of each clover relative to the target. Theta, $\theta = 0$, corresponds to a positive z direction using SHARCs co-ordinate system. The co-ordinate ϕ points due north and increases anti-clockwise around the z-axis as shown in Figure 3.8.

During this work, the clovers at 45° were removed in order to make room for the SHARC electronics, meaning that only twelve clover detectors were used in this experiment.

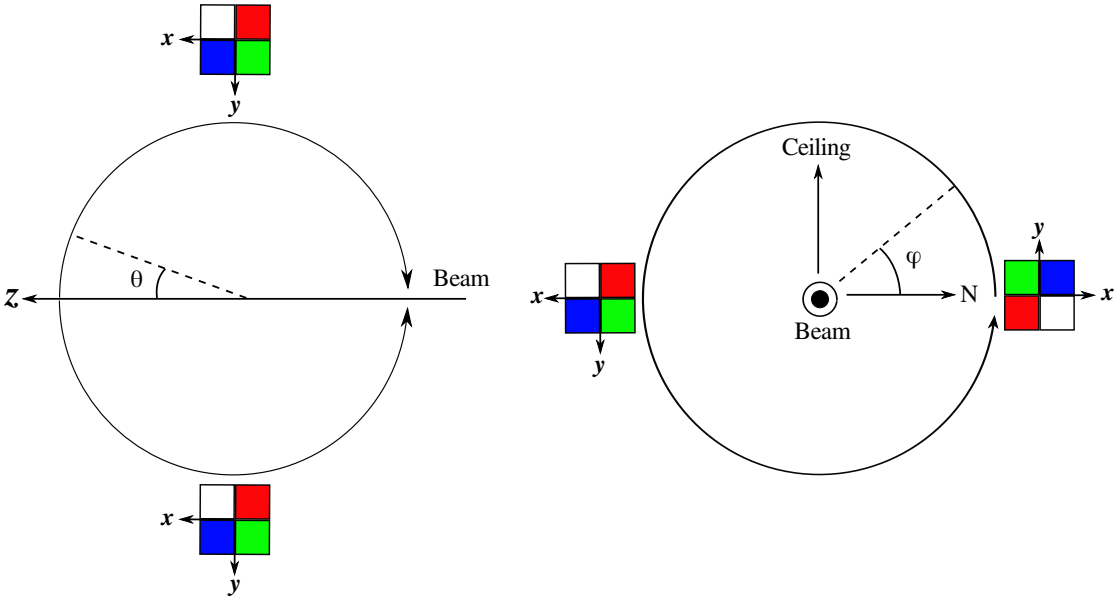

FIGURE 3.8: Schematic of the TIGRESS co-ordinate system.

3.4.1 Clover Geometry

Each clover in TIGRESS is made up of four co-axial crystals of high purity germanium. Germanium is used as a solid-state semi-conductor detector, the physics of which is described in detail in reference [39]. Briefly, an incident γ-ray on a semi-conductor detector can excite an electron into the conduction band of the detector material, creating an electron-hole pair. The reverse bias voltage across the detector sweeps the excited electron away towards the positively charged n^+ contact and the 'positively' charged hole towards the negatively charged p^+ contact, thus creating two signals from the same event: a current from both the conducting electron, and the valence hole. The crystals within TIGRESS are n-type semi-conductors, as shown in Figure 3.9, and are originally cylindrical before being cut to fit next to three other crystals within one cryostat. The central point of this cylinder contains the n^+ contact, which is hereafter referred to as the "core" of the crystal. The outer contacts of the crystal collect the charge of the holes.

The outer contact for each crystal in TIGRESS is actually divided into eight different contacts, the geometry of which is described later in this section. This separation gives a TIGRESS crystal a greater angular resolution since a hole produced by an interacting γ photon will be attracted to the closest contact, thus providing information about the position in the crystal at which a γ-ray was detected. The precision of the localisation of

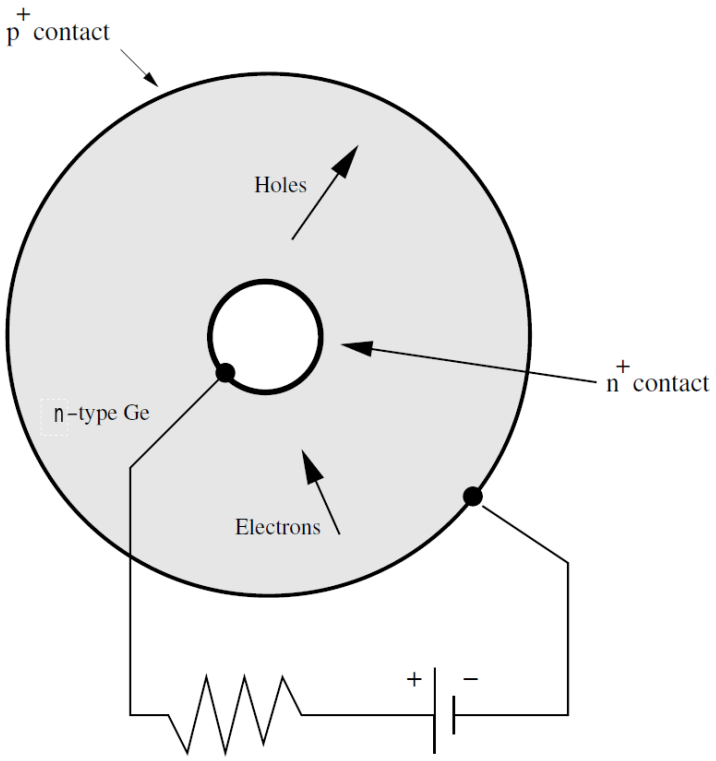

FIGURE 3.9: An n-type coaxial germanium detector [39].

the γ-ray interactions can be further improved by analysing the waveform of the collected charge at the outer contact [51], however, this level of precision was not required during this experiment. The segmentation also helps to reduce Doppler broadening, described in section 4.1.6.

The crystals are colour coded with blue, green, red and white for ease of cabling and for use as a co-ordinate system. The face of each clover represents a value of $z = 0$ with z increasing further into the detector. The centre of the clover corresponds to the origin of the $x - y$ plane as shown in Figure 3.11. The crystal labelled "blue" is the only crystal found in the positive x and y direction, the other crystals progress in alphabetical order (blue, followed by green, followed by red, followed by white) in an anti-clockwise direction.

The position of the clovers with respect to the target are described using polar co-ordinates r, θ and ϕ where the target is positioned at $(0, 0, 0)$. TIGRESS was used in its "suppressed" mode during this experiment so the value of r, relating to the centre of the face of the target, is set to 14.5 mm for every clover. The value of θ is either 90° or 135° depending on which detector ring the clover is housed in. As is shown in Figure 3.8, the red and white crystals have a lower ϕ value relative to the centre of the clover,

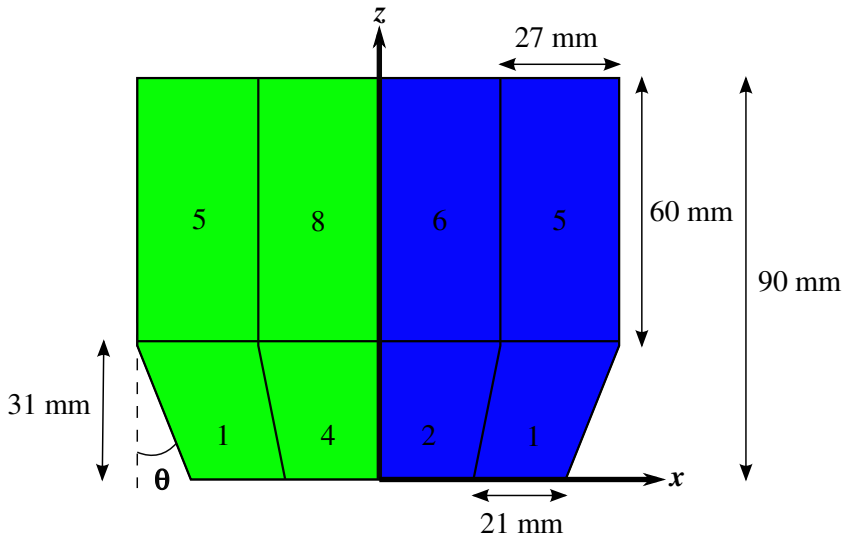

FIGURE 3.10: Schematic of the side of a clover within TIGRESS. Displayed are the physical dimensions of the detector as well as the numbering system of each segment.

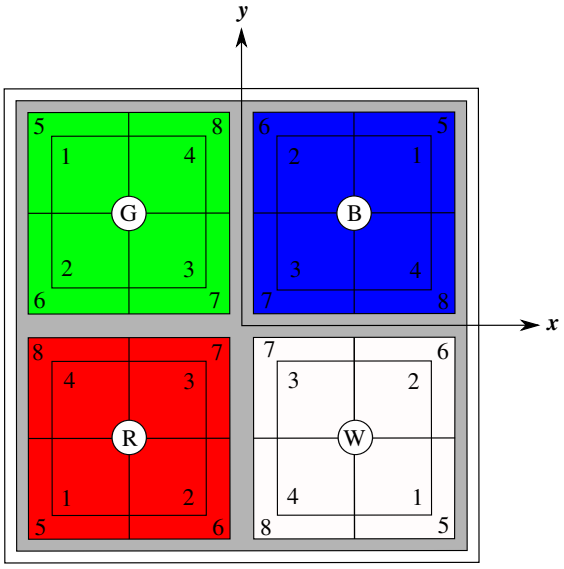

FIGURE 3.11: Schematic of the front of a clover within TIGRESS. Displayed is the numbering system of each segment as well as the colour coding of each crystal.

and so clovers in opposite hemispheres are rotated 180° relative to each other. It is also the case that the blue and white crystals are found at lower values of θ.

Each crystal is further divided in to eight segments as shown in Figures 3.10 and 3.11. These segments of the crystal are labelled 1 to 8, and are positioned to follow an internal pattern common to all crystals in the array. Segments $1-4$ is always located on the face of the detector and extends 31 mm into the clover. The widths of these segments of these segments increases from 21mm to 27 mm as z increases. Segments $5-8$ begin at $z = 31$ mm and extend to the back of the crystal ($z = 90$ mm see Figure 3.10). The position of

segment 1 is always located at the outer most corner of a clover for each crystal. The numbering of each segment the progresses in ascending order anti-clockwise such that segment 3 is always the segment that is closest to the centre of the clover. This pattern is the same for segments $5-8$, with 5 being located at the outer most corner of the detector, and 7 being closest to the centre. This therefore means that the co-ordinates of each segment for each crystal is a rotation of the previous crystal rotated by 90° about the centre of the clover.

3.4.2 Compton Suppression

TIGRESS has the capability of working in two modes: high efficiency mode, where the clovers are packed close together and close to the target chamber in order to increase the solid angle covered by each clover, and Compton suppression mode. In this latter mode, each clover in TIGRESS is surrounded by scintillation detectors used to tag γ-rays that are Compton scattered out of the clover. Titanium collimators are positioned at the front of the clover to ensure that direct hits to the front BGOs do not occur. Two types of scintillator are used: $Bi_4Ge_3O_{12}$ or BGOs, and thallium-drifted caesium iodide (CsI(Tl)). This is shown in Figure 3.12.

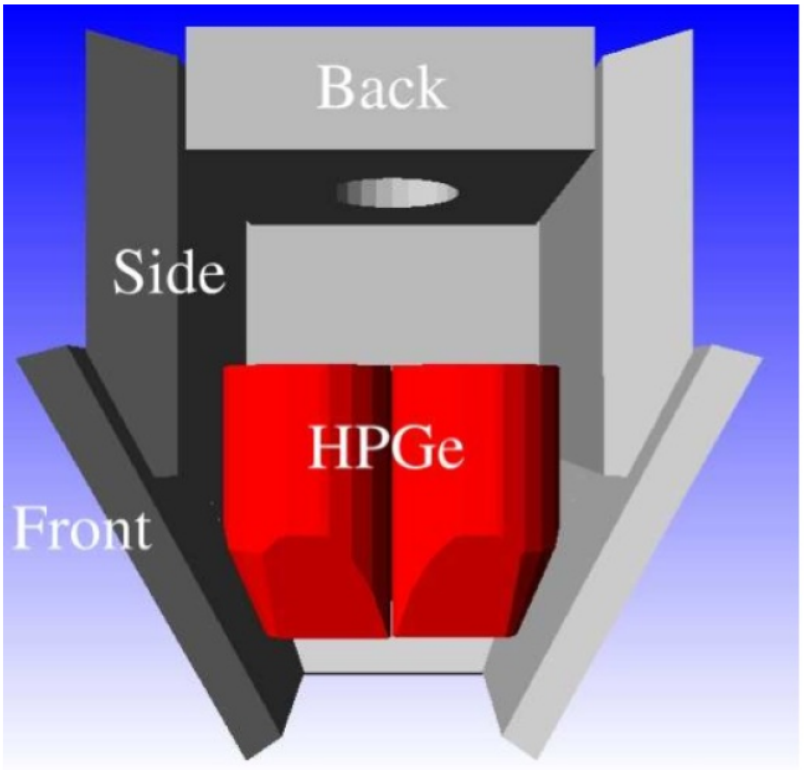

FIGURE 3.12: Cross section of a clover in Compton suppression mode [52].

As discussed in section 2.6.2, the probability of a γ-ray interacting with matter is proportional to the Z of the absorbing material. Bismuth has a much higher Z in comparison to germanium (83 for bismuth compared to 32 for germanium) making the BGOs effective at detecting escaping photons that do not interact with the matter in the clover detector. The energy resolution of the BGOs is not as good as that for germanium, meaning that they are not useful in helping to determine the energy of the γ-ray detected. This, however, is not the purpose of the BGO shields. Their purpose is to tag photons escaping from the germaniums and eliminate events arriving in coincidence from the analysis. The cheaper CsI(Tl) scintillator is used at the back of the detector due to the small chance of a γ-ray proceeding through the thick clover without being absorbed.

Like the HPGe clovers, the scintillator suppression shields are segmented in order to track the position around the clovers at which a γ-ray escapes. This segmentation is shown schematically in Figure 3.13. Each crystal has four BGO detectors adjacent to it: two at the front of the clover, one on each side, and two along the side of the clover (Figure 3.12). The back CsI(Tl) scintillator detector is also separated into quarters; one for each crystal. Each clover is therefore surrounded by a total of twenty scintillator detectors.

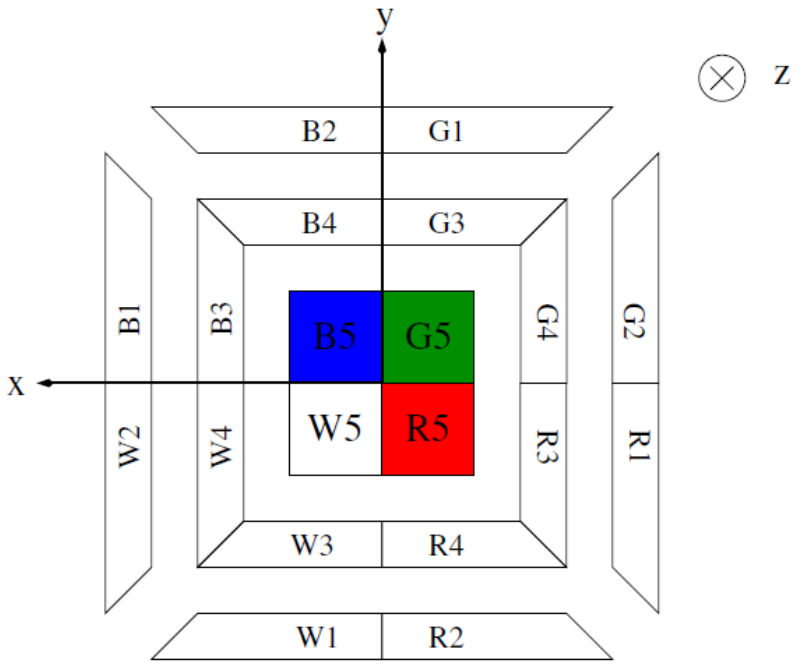

FIGURE 3.13: A schematic of the scintillator detectors and their positions in comparison to the different crystals. Viewed from the back of the detector [52].

3.5 The Trifoil

Due to the need to use inverse kinematics in this experiment, the reacted ^{25}Na particles emerge from the target travelling in a small cone of trajectories around the beam axis. A zero-degree detector would therefore be ideal for this form of experiment. Ideally, a detector of this type would be required to be able to identify the particles it has detected so that a distinction between un-reacted particles, reacted particles, and fusion-evaporation products can be made. This is advantageous as it allows for a closer look at events that may otherwise be lost in noise by discriminating between useful and un-useful events. Being able to detect with high precision, the energy and angle at which these reacted particles emerge at would be ideal since it would allow the excitation energies of the particles of interest to be calculated directly; however, this perhaps is too much to ask in an experiment performed in inverse kinematics since the detected particle will be the heavier of the two reaction products and will therefore be diverged from the beam axis by a very small degree.

A sophisticated zero-degree detector such as a mass spectrometer, which incorporates the use of magnetic and electrostatic separation in order to effectively achieve the separation of masses of particles is currently being constructed in the form of EMMA (ElectroMagnetic Mass Analyzer)[53] at TRIUMF, but was unavailable at the time of this experiment. Instead, the Trifoil detector, a small scintillator detector was positioned behind the SHARC array in the beam line.

The Trifoil (Figure 3.14), so named because it uses three photomultiplier tubes on one side of the scintillator plastic in order to create a signal to be analysed, was originally developed at LPC Caen for the use of providing a time signal for experiments involving secondary beams produced by projectile fragmentation [54]. It was re-purposed for this experiment to tag the recoil particles, which consisted mostly of fusion evaporation products produced by the compound reaction between ^{24}Na in the beam and ^{12}C in the target, and ^{25}Na nuclei from (d, p) transfer. A 50 μm aluminium foil is placed before the scintillator foil that acts as a stopper to the slower moving, higher Z particles produced as a result of fusion-evaporation. This thickness was chosen so as to still allow particles of $A \approx 25$ to pass through, thus allowing the recoils to be tagged and gated on, while stopping the compound nuclei which contained no information relevant to this experiment. This will be explained further in Chapter 4. The stopper foil also allows non-reacted beam particles to pass through, which can cause problems since the scintillator's performance can degrade if exposed to a high flux of radiation. When exposed to a beam produced by projectile fragmentation, as was the trifoil's original purpose, this is not a problem since the beam spot is less focused. However, the ISAC-II

facility beam is produced via the ISOL method and has a beam spot of order 1.5 mm [3] in diameter which can lead to a dead spot in the detector.

This dead spot is not a problem in and of itself as it will be localised to the diameter of the beam and will contain mostly non-reacted beam particles which are of no interest to this experiment. However, the dead spot is opaque to light and so can effect the detector efficiency since the PMTs are only located on one side. The particles that are of interest are the recoil nuclei after the (d, p) reaction, which emerge from the target in a narrow cone around the beam axis.

The waveform of the signal picked up by the PMTs are passed through a Constant Fraction Discriminator (CFD) in order to acquire timing information about the pulse. A CFD interprets the amplitude of the pulse and calculates a threshold at which the pulse raises above a constant predetermined fraction of the pulses amplitude. The pulse is then delayed by a time greater than the original rise time, and the signal is compared to the calculated threshold and a linear extrapolation of the points just above and below the lines is performed in order to gain a higher precision of the time that this threshold is crossed. This technique gives a value of time that is independent of the amplitude of the peak [39]. The time passed to the DAQ is in units of 1/16th of the Front End Field-Programmable Gate Array (FE FPGA) clock cycle in the Tig-10 front-end cards where one cycle equals 10 ns [55].

A signal from the Trifoil is only recorded and analysed if two PMTs signals are in coincidence with each other. This was determined with a NIM coincidence module with a resolving time of 6.5 ns [56]. The signal is then sent to the DAQ to be recorded.

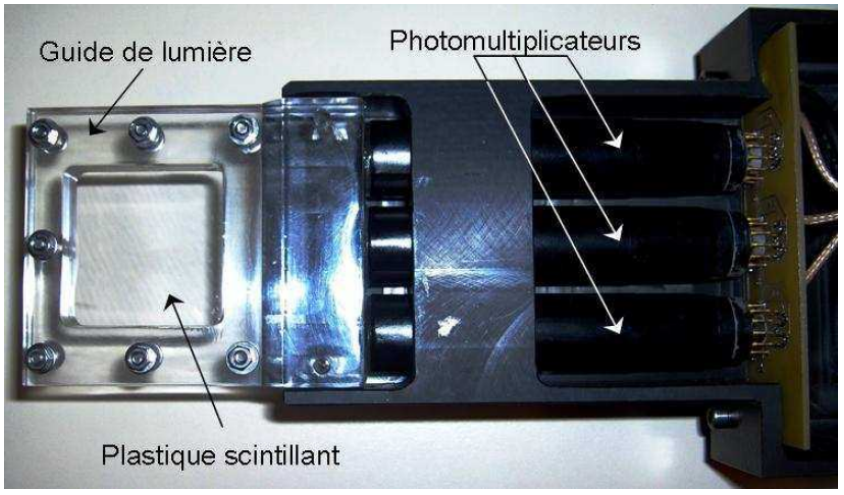

FIGURE 3.14: The Trifoil detector with the scintilator foil and photomultiplier tubes labelled [57].

Chapter 4

Analysis

4.1 Calibrations

4.1.1 Alpha Calibrations

A triple α source consisting of ^{239}Pu, ^{241}Am and ^{244}Cm was used to calibrate the SHARC array. The calibrated spectrum obtained from these sources for all pixels is shown in Figure 4.1. The main contributors to the spectrum, including the intensities of each energy, are given in Table 4.1. Three peaks are observable in this plot, whereas there are eight listed in Table 4.1. This is due to the energy resolution of SHARC being too poor to be able to distinguish some of the energy peaks in the source; SHARC has a 250-300 keV FWHM energy resolution [46], compared to the peaks in the spectrum which are never more than 50 keV apart. Due to this observation, each peak has a distribution that is not entirely Gaussian, but is actually slightly skewed. This affects the calibration because the fit that is required must also account for these smaller peaks.

The calibration of the silicon detectors is not a simple matter of finding the difference between the detected value for energy and comparing this to the known energies from the α source to find a scaling factor, as is the case for the germanium detectors described below. This is because of the dead-layer associated with each strip which could result in a systematic error in the results if not taken into account.

As described in Chapter 3, each DSSSD has an aluminium strip running across the length of the detector. The function of these strips is to carry away the collected charge that produces the signal for the DAQ to process, however, their position on the face of the detector results in the active area being shielded, and thus any energy detected in the DSSSDs will be an energy that is reduced due to the energy loss in the aluminium strips.

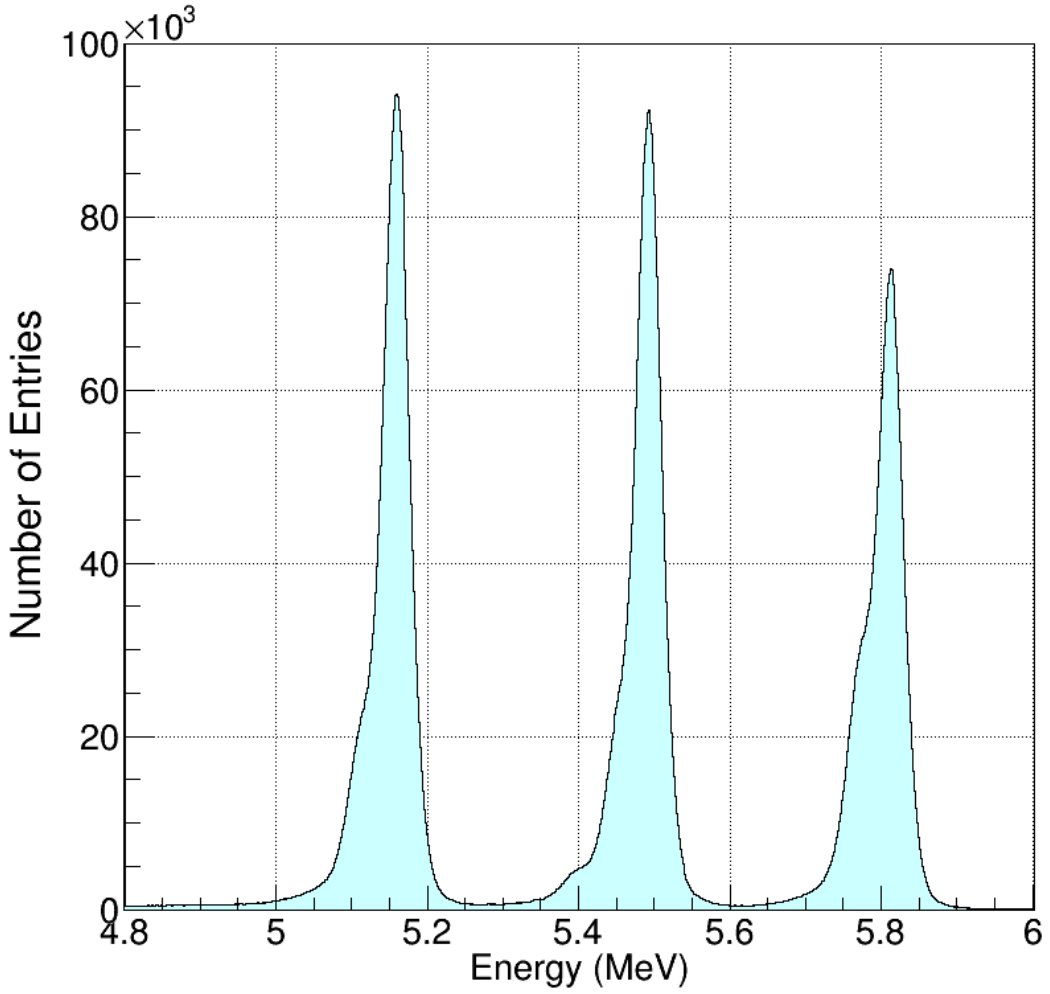

FIGURE 4.1: The triple-α calibration spectrum obtained over the entire SHARC array.

This effect is reduced for the box detectors because the average thickness of the aluminium strips are reduced to maximise the detector efficiency at low energies. The strips on the CD detector, however, have a much greater thickness, and so the energy loss can have a much greater impact on the energy. The detected energy of the particles in the CD detector will be lower than particles of the same energy detected in the Box detectors due to the greater amount of aluminium covering the strips.

In addition to the aluminium dead-layer, there is also a layer of inert silicon. The loss of energy in both the aluminium and silicon dead-layers must be corrected in order for the true energy of the detected particle to be recorded. The thickness of the aluminium and silicon did not need to be calculated separately in order to find the total energy lost in the dead-layers. Energy loss was calculated using a function in the software NPTool [58], which in turn used a table generated by SRIM. NPTool assumes the dead-layer to be given in aluminium, and so an effective thickness for a dead-layer of pure aluminium

Source	Energy (MeV)	Relative Intensity (%)	$T_{1/2}$ (years)
^{239}Pu	5.15659(14)	70.77(14)	2.144×10^4
	5.11443(8)	17.11(14)	
	5.1055(8)	11.94(7)	
^{241}Am	5.48556(12)	84.8(5)	432.6
	5.44280(13)	13.1(3)	
	5.388	1.660(20)	
^{244}Cm	5.80477(5)	76.90(10)	18.11
	5.76264(3)	23.10(10)	

TABLE 4.1: Main contributing energies see from the triple α source [33].

was found using this software. SRIM is a collection of software packages which can be used to calculate the range of particles in a material using a combination of experimental data and various models [59] [60].

The actual thickness of the dead-layer that must be accommodated was computed separately for each pixel, since the thickness of the dead-layer is dependent on the the angle at which the particle enters the detector. It is not, therefore, a simple case of assuming that each pixel has the same dead-layer thickness.

Plotting a graph of known energy peaks (Table 4.1) against peak channel from the data files and extrapolating the linear line of best fit to find the intercept of the x-axis demonstrates the possible error associated with ignoring the dead-layer thickness; in a linear detector, the extrapolated line should intersect the origin since an energy of zero should result in getting a zero signal. If this is not the case, then the implication is that the energy that is detected is not actually the energy displayed in Table 4.1, but an energy that has been reduced by the dead-layer. The dead-layer can then be determined using the following iterative process:

1. An initial value of 0 for the dead-layer thickness was assumed. Using the NPTool function to determine energy loss for this thickness, the energy loss of the α particle was found, and the energy of a particle after the dead-layer was calculated.

2. A graph of the calibrated energy post dead-layer correction was plotted against channel energy, and a linear fit $E_{Calibrated} = c + mE_{channel}$ was plotted.

3. The Zero point energy $E_{Channel} = (E_{Calibrated} - c)/m$ was calculated for $E_{Calibrated} = 0$, i.e. $E_{Channel} = -c/m$, for each pixel, and the difference between E_0 and 0, δ_0 was evaluated.

4. If δ_0 was within 0.1 keV of the origin, then the dead-layer thickness was recorded for the pixel. Otherwise, the dead-layer thickness was modified and the process was repeated.

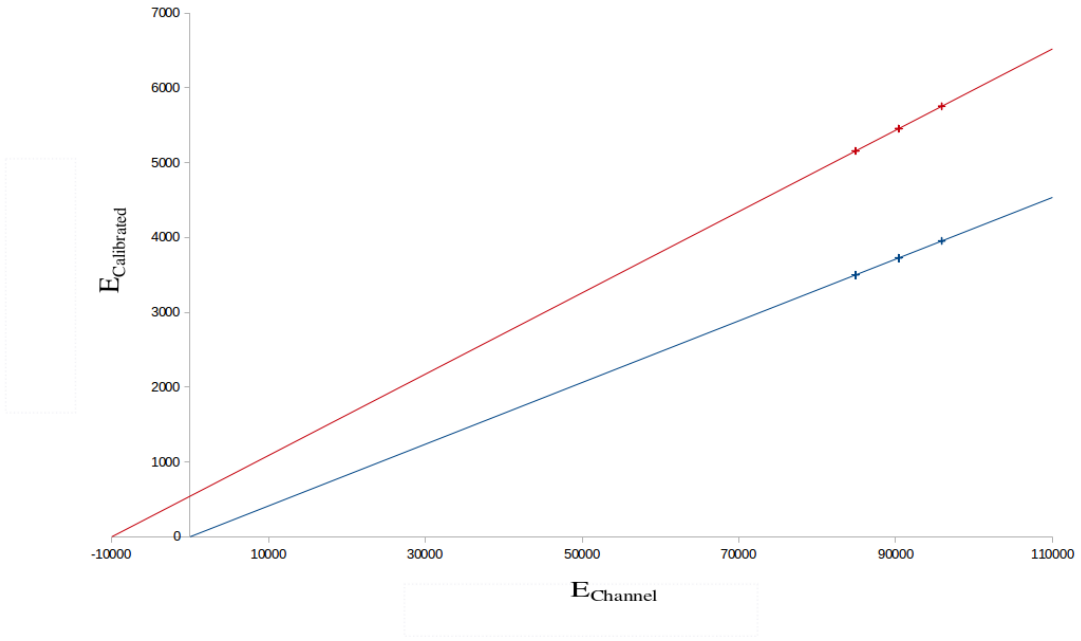

FIGURE 4.2: Illustration of how the dead-layer can affect the energy of the α calibrations. Before dead-layer corrections, $E_{Calibrated}$ equal the points for the three largest peaks listed in Table 4.1 (red line). After dead-layer corrections, $E_{Calibrated}$ is less and creates a line that passes through the origin (blue line). This figure is exaggerated in order to make this effect clear.

This process is illustrated in Figure 4.2.

The thickness found for each pixel was plotted in order to clearly see if there were any pixels that where giving a false reading. These plots are shown in Figure 4.3 and reveal that some pixels close to 90° are calculated to have an extremely high dead-layer thickness. This is likely due to the source frame or parts of the SHARC frame hindering the α particle's journey to the detector. Strips displaying this high large thickness characteristic were removed from further analysis. The average thickness over all the box detectors after the exclusion of the anomalous strips is 0.5×10^{-3} mm with a standard deviation of 0.2×10^{-3} mm.

4.1.2 PAD Calibrations

Due to the DSSSDs of the downstream box being very thin, it is possible that the protons and deuterons can punch through and only deposit a fraction of their original energy. As described in Chapter 3, thicker PAD detectors were placed behind the ΔE telescopes so as to be able find the total energies of the particles.

The PAD detectors are shielded from the source by the ΔE DSSSDs detectors , making them impossible to calibrate using an α emitter as described above. The α particles

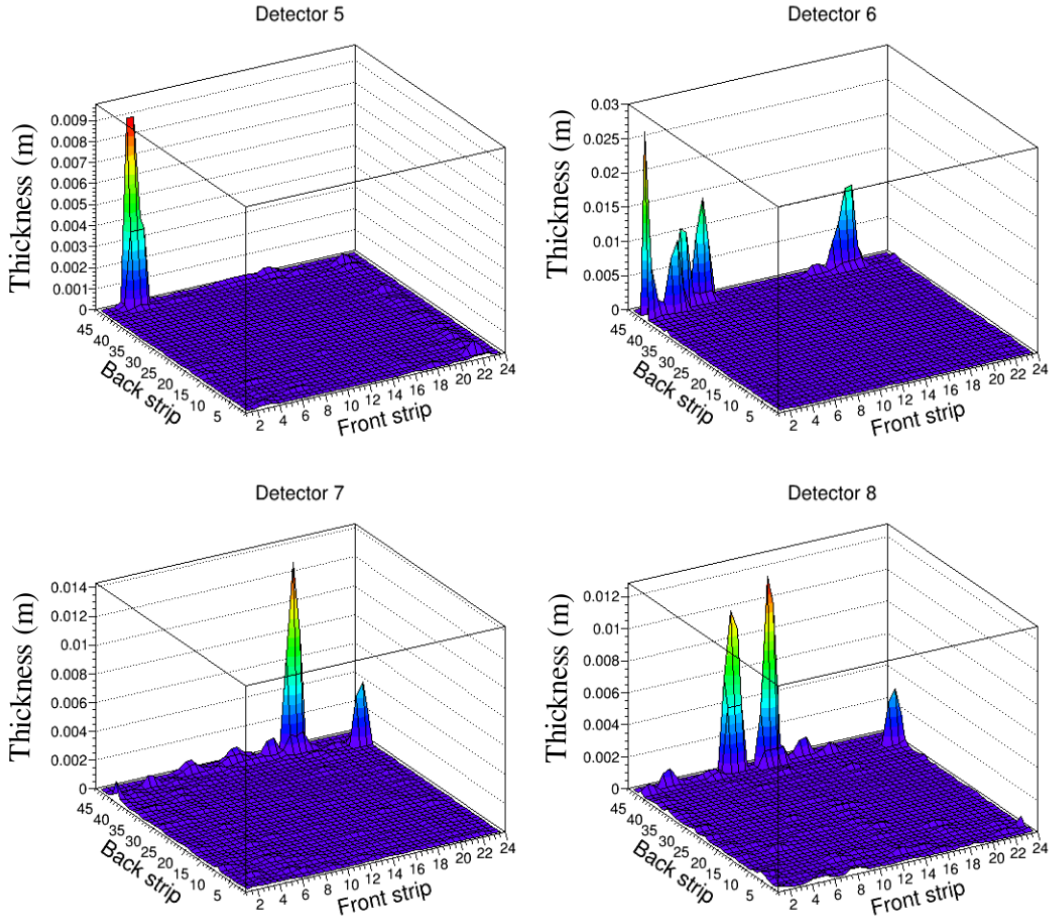

FIGURE 4.3: Dead-layer thickness of each pixel for the Upstream Box detectors.

from the triple α source are completely absorbed by the silicon in the ΔE strip detectors housed in front, meaning that any events that are detected will be as a result of background noise. A different technique must therefore be deployed in order to calibrate these detectors. The adopted method used the data from the experiment and calibrated values from the DSSSD punch-through events as explained below.

PAD calibrations in principle can be performed using one of two methods. The first possibility would be to take the angle at which the event was detected, and work out the energy that should be detected in the PAD detector after the energy loss in the $\Delta E - E$ telescope. The other method is to take the energy detected in the $\Delta E - E$ detector and deduce the energy that is required to be found in the PAD in order to match the predicted energy of the kinematic line. The former method assumes the detected angle to be accurate, whereas the latter requires the measured energy to be correctly calibrated. This work uses the latter method due to initial problems in aligning the detectors, as described in section 4.2.3.

The first step in this process is to distinguish between the punch-through protons and deuterons. Each of these types of particles can be used to calibrate the detector, however, they lose energy at a different rate when travelling through a medium and this difference will affect the calculation of the expected energy in the PADs given the energy deposited in the DSSSDs. As such, each event must first be identified as either a proton or a deuteron. Once this is complete, the calibration can be found with either type of particle.

Particle identification is done by examining the energy lost in the ΔE telescopes compared to the (un-calibrated) energy in the PADs, as shown in Figure 4.4. It does not matter that the PADs are not calibrated in this stage, since the goal is simply to distinguish particle types.

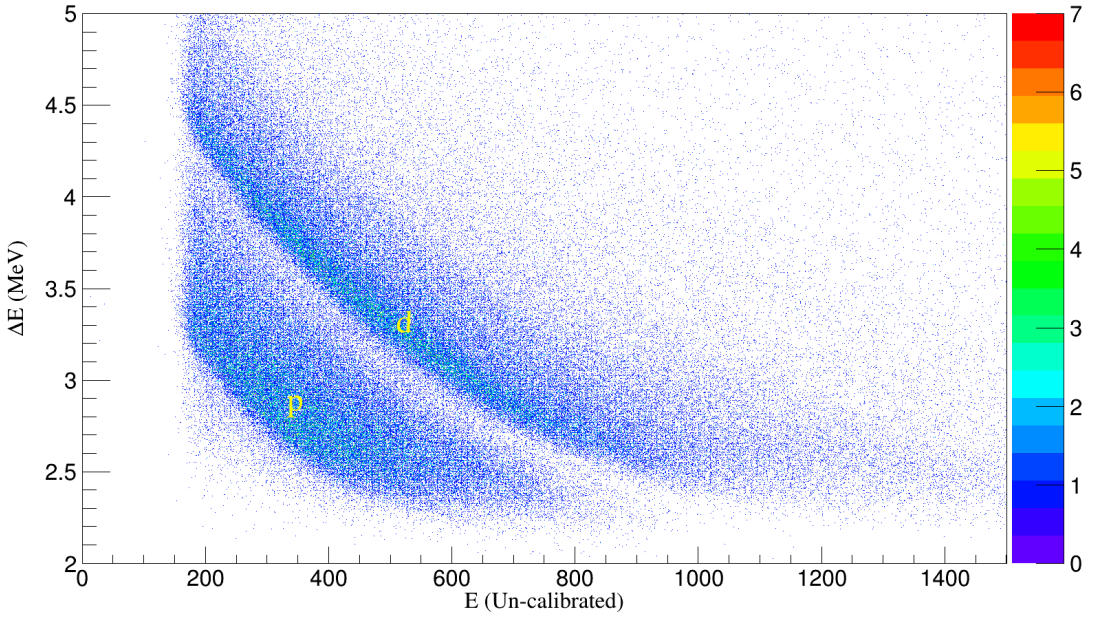

FIGURE 4.4: Particle identification of protons (lower band) and deuterons (upper band) for the downstream box.

The separation of the different particles is important not only because of the difference in the rate at which particles lose energy when travelling through a medium, but also because of the difference in the kinematics of each particle. An elastically scattered deuteron emerges from the target at a different angle than an elastically scattered proton of the same energy. Therefore a proton and a deuteron of the same energy will lose different amounts of energy travelling through the ΔE detector because they have to travel through a different thickness of material. A cut was created around the deuteron band in Figure 4.4. The calibration of the PAD detectors was performed by comparing the events within this cut and the deuteron elastic kinematic line. Using a 2D graph of predicted PAD energy (i.e. the kinematic energy minus the threshold energy of the pad

detector) against the un-calibrated energy in the PAD detector, and drawing a line of best fit, the calibrated energy could be found.

In order to check how successful the calibrations were, a new plot showing ΔE against the calibrated E was created where the values of ΔE were normalised to the nominal thickness of the ΔE telescope (140 μm), i.e. the energy lost in the ΔE telescope if each particle passes through 140 μm of silicon vs total detected energy, was created.

For this process, the values of energy after being normalised will be marked with a prime symbol, for example, in E'_{PAD} represents the energy of a particle detected in the PAD detector after it has passed through 140 μm of silicon. The total energy detected, E_{Total} is equal to the total energy after the value for ΔE has been normalised, hence:

$$E_{Total} = \Delta E + E_{PAD} = \Delta E' + E'_{PAD}, \tag{4.1}$$

$$\Delta E' = \Delta E \cos\theta_D \tag{4.2}$$

and

$$E'_{PAD} = \left(\Delta E - \Delta E'\right) + E_{PAD} \tag{4.3}$$

where θ_D is the detector angle which is the angle at which the particle passes through the detector with respect to the normal of the detector. This angle is defined by the dot product of the vector path taken by the particle to the detector face, $\hat{r}$, and the unit vector of the face of the detector, $\hat{a}$:

$$\cos\theta_D = \frac{\hat{r}\cdot\hat{a}}{|\hat{r}||\hat{a}|}. \tag{4.4}$$

Equation 4.3 originates from the condition shown in Equation 4.1; because $\Delta E'$ is ΔE reduced by a factor of $\cos\theta_D$, E'_{PAD} must equal E_{PAD} plus the difference between ΔE and $\Delta E'$.

Figure 4.5 shows the particle identification after calibrations and the normalisation described above have been performed. It can be seen here that the proton and deuteron lines are more pronounced than in Figure 4.4. This figure also reveals a clear band of ^{3}H that was detected in the experiment.

4.1.3 Solid Angle

The solid angle of the SHARC array is required in order to get the differential cross sections of the reaction. The solid angle in the centre-of-mass frame, Ω_{CM}, was used in

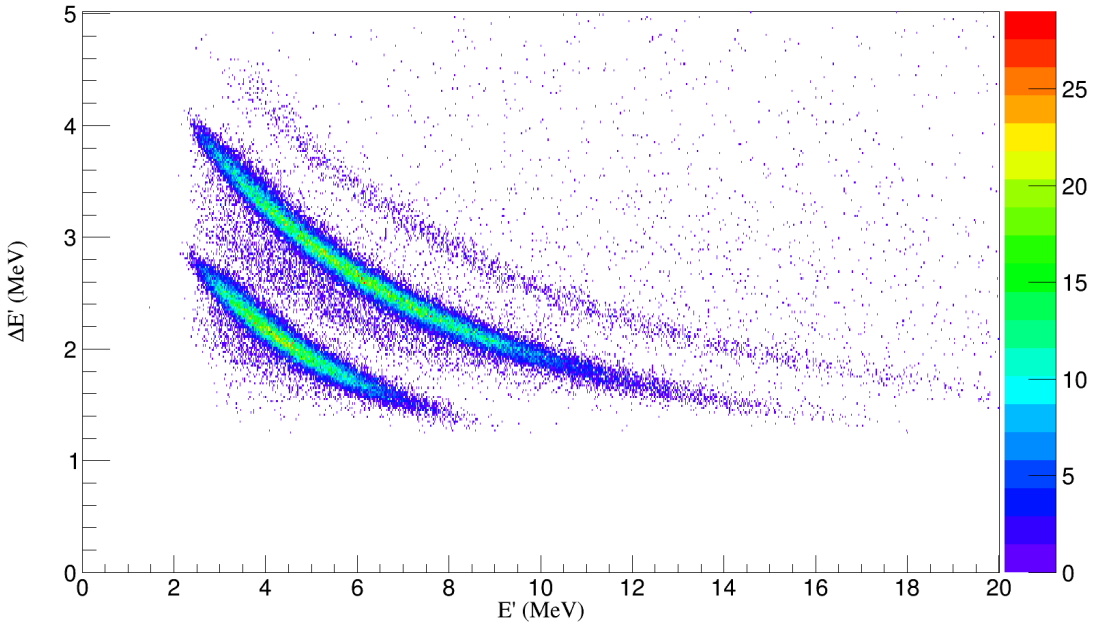

FIGURE 4.5: Particle identification of protons and deuterons for the downstream box after calibrations and normalisation to passing through 140 μm.

order to normalise the elastic scatter in the downstream box detector in order to find the beam current and the number of target nuclei, and the solid angle in the lab frame, Ω_{Lab}, was used to find the angular distribution of protons.

For a detector array that is cylindrically symmetric around ϕ, the solid angle can be found by

$$\mathrm{d}\Omega = \int_{\theta_{min}}^{\theta_{max}} \int_{\phi} \sin\theta \mathrm{d}\theta \mathrm{d}\phi = 2\pi \int_{\theta_{min}}^{\theta_{max}} \sin\theta \mathrm{d}\theta. \tag{4.5}$$

Equation 4.5 gives the case in which the coverage in ϕ is total and that there are no gaps in the detector. It therefore gives the maximum solid angle coverage possible by a detector array. Any θ-independent gaps in a cylindrical detector results in reducing the dΩ by a scaling factor between 0 and 1. The rectangular cuboid shape of SHARC means that each detector is constant in one of the x, y, or z co-ordinates, and so the ϕ coverage in each angle bin in the SHARC array is not constant since each corner of a single pixel corresponds to a different value of θ and ϕ.

The solid angle covered by each pixel can be calculated using

$$\mathrm{d}\Omega = \frac{\mathrm{d}\overrightarrow{A} \cdot \hat{r}}{\mathrm{r}^2} = \frac{\mathrm{d}\overrightarrow{A} \cdot \overrightarrow{r}}{\mathrm{r}^3} \tag{4.6}$$

and

$$\mathrm{d}\overrightarrow{A} = \begin{cases} (\mathrm{dx})(\mathrm{dz})\hat{n} & \text{if } y \text{ is constant} \\ (\mathrm{dy})(\mathrm{dz})\hat{n} & \text{if } x \text{ is constant.} \end{cases} \tag{4.7}$$

Here $\mathrm{d}\overrightarrow{A}$ is the area of an individual pixel and $\hat{n}$ is a vector normal to the plane of the pixel.

Figure 4.6 includes a sinusoidal curve that depicts the solid angle of a detector with a 100% efficiency as given in Equation 4.5. The actual solid angle of SHARC follows this line, but has a reduced height due to the geometry of the detector. As described in section 3.3.1, the active area of each DSSSD does not extend all the way to the corner of the box. This reduces the efficiency of the detector for each value of θ. This inherent loss is exacerbated if the detector has a dead front strip (running parallel with the beam axis), which causes the profile of the solid angle for SHARC to become jagged.

A sharp decrease in solid angle is seen on the occasion that there is a gap in the active area of a detector that runs perpendicular to the z-axis, for instance, when there is a dead strip on the back side of the DSSSD, or due to the edges of the detector being reached. An example of this can be seen in Figure 4.6 around 140°, which is caused by a gap between the upstream box and the CD detector.

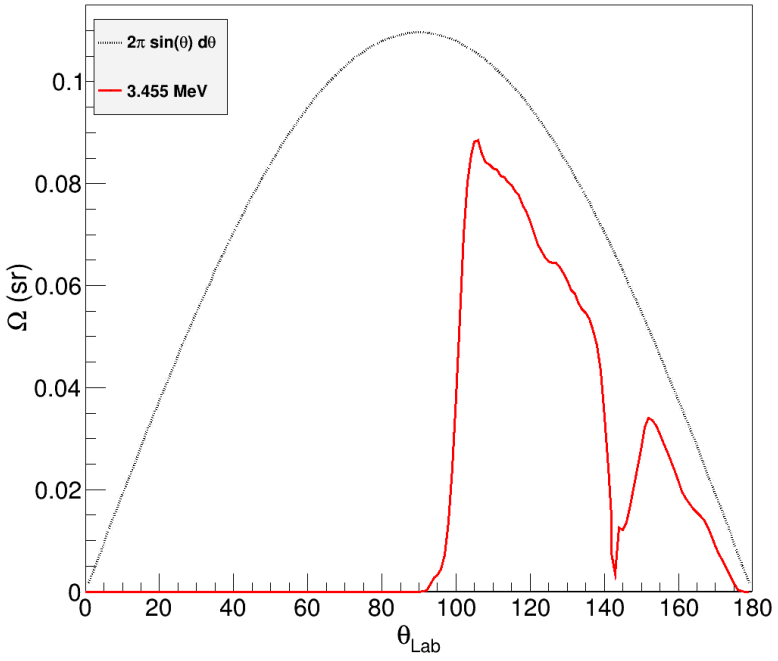

FIGURE 4.6: Solid angle for the upstream detectors for the 3.455 MeV excited state in ^{25}Na.

The solid angle in the upstream box was calculated using NPTool [58] which used a Monte-Carlo simulation with a flat cross section to simulate the number of detected events found at each value of θ and ϕ, namely $N_{detected}(\mathrm{d}\Omega_{CM}, C)$, where C refers to the input conditions i.e. cuts, threshold values, dead detector strips etc. The value of the centre-of-mass solid angle, $\mathrm{d}\Omega_{CM}$, was then calculated using Equation 4.8 by comparing $N_{detected}(\mathrm{d}\Omega_{CM}, C)$ and the number of particles emitted, $N_{emitted}$ [61],

$$\mathrm{d}\Omega_{CM} = \frac{N_{detected}(\mathrm{d}\Omega_{CM}, C)}{N_{emitted}} 4\pi. \tag{4.8}$$

Subsequently, $\mathrm{d}\Omega_{CM}$ can be converted into $\mathrm{d}\Omega_{Lab}$ using the method described in section 4.2.5.

Using a flat cross section Monte-Carlo simulation is advantageous because it allows the input of other factors which might have an effect on the solid angle. The threshold of the detectors, for example, causes a drop off in solid angle at higher energy levels; energy levels populated in the (d, p) reaction are associated with lower energy protons. This became a major factor in the analysis of the experiment as it affects the angular distributions found for each excited energy state (see section 4.4). The way that the solid angle drops off as excitation energy increases is shown in Figure 4.7.

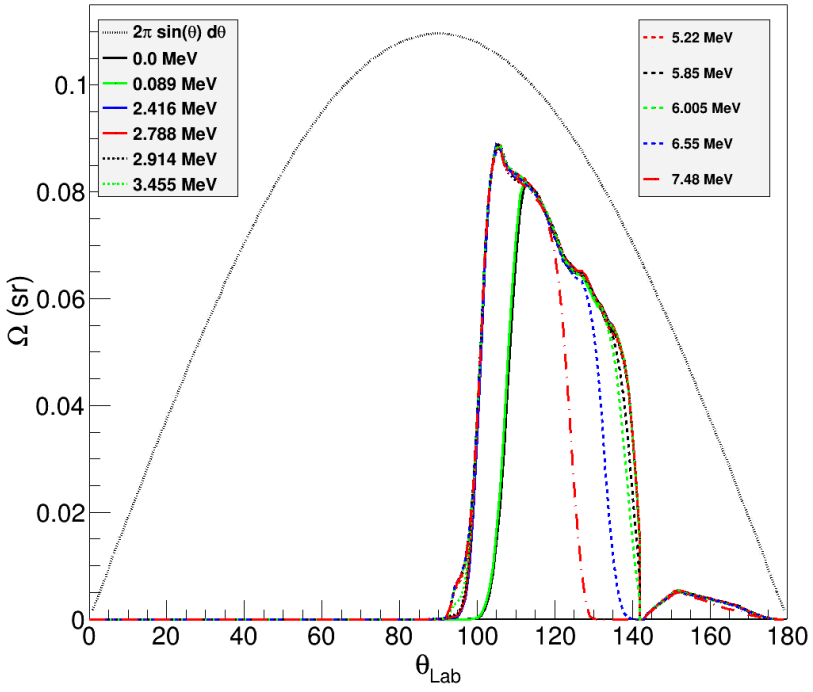

FIGURE 4.7: Solid angle drop-off as energy increases as a result of the energy threshold in the detectors.

4.1.4 Germanium Calibrations

The well known γ-ray energy transitions from ^{152}Eu, ^{133}Ba and ^{56}Co sources were used to calibrate the germanium detectors in TIGRESS. The energies in Table 4.2 gives the γ-ray energies of the radioactive sources used in the calibration. Using Root, a histogram of the energy spectrum for each source was produced and the peak for each energy listed was found. The values of the uncalibrated peaks where then plotted against the energy values obtained from the literature. A linear line of best fit was plotted and the gradient and intercept along the y-axis of this line was found and used to calibrate the spectra.

The peaks that were used in the calibration have been marked with an arrow in Figures 4.8 and 4.9. Also observable in Figure 4.8 is a γ-ray at 511 keV. This peak is produced when ^{56}Co β^+ decays and the produced positron annihilates with an electron. Europium-152 decays primarily through electron capture, and so no 511 keV peak is seen in Figure 4.9, though a characteristic X-ray is observed at < 100 keV. The peaks used in the calibration were chosen due to how uniformly they were spread throughout their spectrum. This was done so that the line of best fit was not weighted around one spot and thus able to alter the values of the gradient and intercept.

Figures 4.8 and 4.9 show the calibrated spectra for each of the calibration sources. To obtain these histograms, the add-back over one detector was calculated using the methods described in Section 4.1.5.

4.1.5 Add-back

The majority of γ-rays detected during this experiment fall within the range of 0.1 MeV to 5.0 MeV. Figure 2.9 shows that the most likely interaction process for γ-rays at this energy (at $Z = 32$, which is the atomic number of the germanium detector) is Compton scattering. This means that it is likely that a γ-ray detected in TIGRESS will deposit a fraction of its energy in one segment before being scattered to another interaction point, which may be in another segment. A schematic of three possible γ-ray paths is shown in Figure 4.10 where the asterisk represents a point at which energy is deposited in the detector.

BGO shields are used to detect when a γ-ray exits a clover without depositing all of its energy, as described in Chapter 3. If this occurs, the γ-ray is rejected and not used in further analysis. The γ-rays that remain within the detector, but are Compton scattered between crystals do not contribute to the Full Energy Peak (FEP) in the final spectrum for an individual crystal, but instead contribute 2 or more counts to the

Source	Energy (keV)	Relative Intensity (%)
^{56}Co	846.770	99.94
	1037.843	14.05
	1238.288	66.46
	1771.357	15.41
	2034.791	7.77
	2598.500	16.97
	3253.503	7.92
^{133}Ba	80.9979	32.9
	276.3989	7.16
	302.8508	18.34
	356.0129	62.05
	383.8485	8.94
^{152}Eu	121.78	28.67
	244.70	7.61
	344.28	26.6
	778.90	12.93
	964.079	14.65
	1112.069	13.69
	1408.006	21.07

TABLE 4.2: Energies of the peaks used to calibrate the TIGRESS array and their relative intensities.

Compton continuum at lower energies, effectively increasing the background of other peaks. The event can be recovered using an add-back procedure described below.

Each crystal in a clover has a central core readout of energy for each event. This means that if a γ-ray is scattered, but is later absorbed in an adjacent segment in the same crystal, the total energy of that clover can be read out without the need for any further analysis, however, no such system can be used for inter-crystal scattering events. In this case, Compton scattering is reduced by implementing add-back between γ-rays detected in different crystals in the same clover. If two photons are detected simultaneously in the same clover (and nothing is detected in the BGO adjacent to any of these events) then the two energies are added back together to get the full energy of the γ-ray. Only those photons that are detected in adjacent crystals are added together. This is because of the geometry of the HPGe detectors; for a γ-ray to have been detected travelling diagonally across a detector, it must have first travelled through at least one other segment without being detected. It is considered that two γ-rays originate from different sources if they are detected diagonally across from each other. Of course, this allows for the situation in which two unrelated γ-rays are added together. This situation is rare because events with a multiplicity greater than two only happen 4.2% of the time.

The angle of emission is taken to be that of the γ-ray interaction which deposits the highest energy [62] because particles that deposit large energies correspond to γ-rays

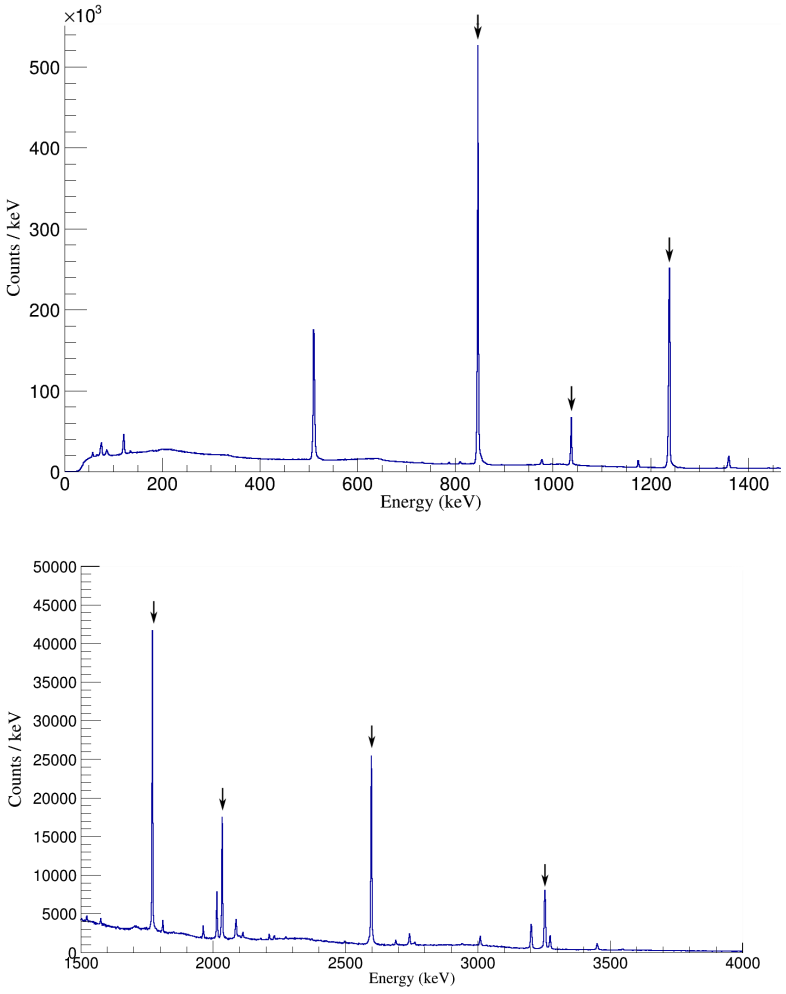

FIGURE 4.8: Calibrated γ source data for cobalt-56 below 1500 keV (top) and above 1500 keV (bottom). The energies of the peaks shown in Table 4.2 are marked with an arrow.

that are scattered at high angles (Equation 2.48) and are therefore more likely to enter a different segment or clover in the detector.

4.1.6 Doppler Corrections

Post reaction, a ^{25}Na nucleus in an excited state will be travelling at modestly relativistic speeds of order 0.1c. The γ-ray emitted as the nucleus de-excites will be subjected to a Doppler shift,

$$E_0 = \gamma E_\gamma \left(1 - \beta \cos\theta\right), \tag{4.9}$$

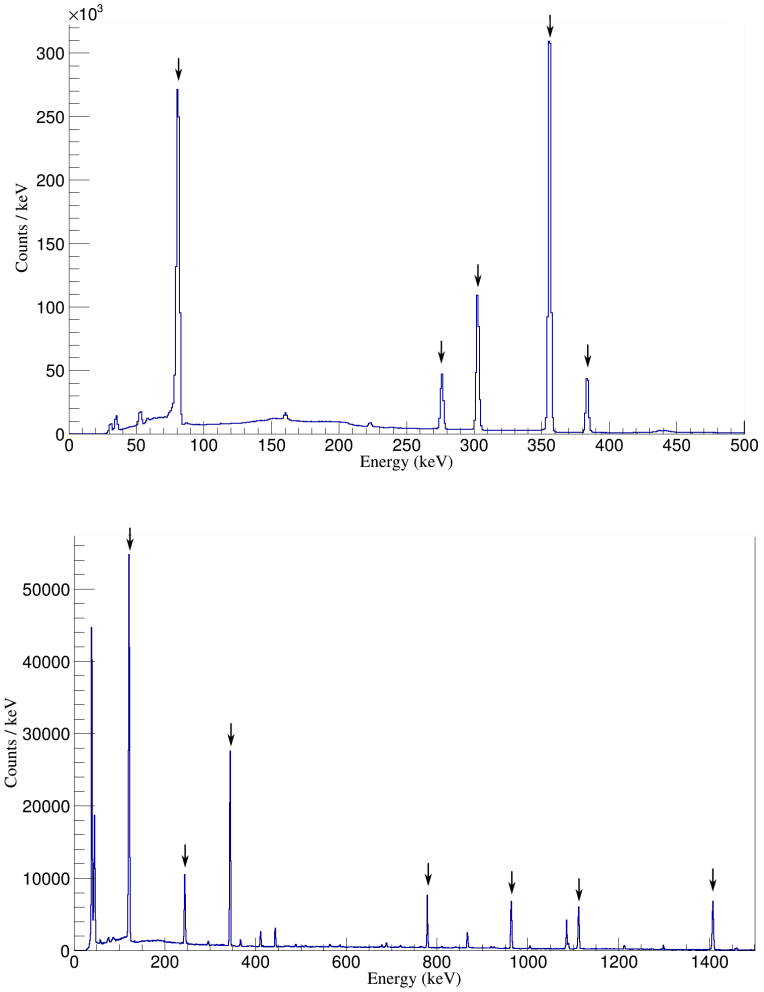

FIGURE 4.9: Calibrated γ source data for barium-133 (top) and europium-152 (bottom). The energies of the peaks shown in Table 4.2 are marked with an arrow.

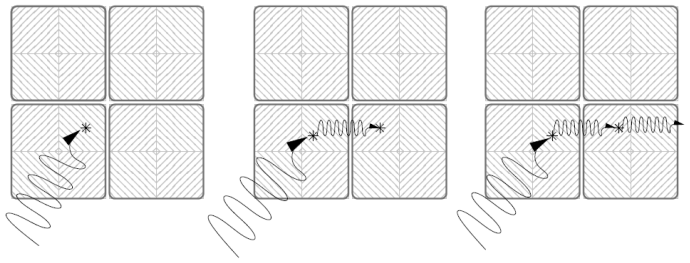

FIGURE 4.10: Possible paths taken by a γ-ray through a detector. A γ-ray enters the detector and is absorbed via the photoelectric effect (left). A γ-ray is Compton scattered in one segment of a detector before being completely absorbed in the adjacent segment (middle). A γ-ray is Compton scattered twice before managing to escape the detector completely (right) [57].

where E_0 is the energy of the detected γ-ray if it were emitted from the nucleus at rest, E_γ is the energy detected in the lab, β is the ratio between the velocity of the emitting source and the speed of light, v/c, and

$$\gamma = \frac{1}{\sqrt{1-\beta^2}}, \tag{4.10}$$

is the relativistic γ factor and equals 1.00856 here. The dependence E_0 has on angle means that if the particle is travelling towards the detector, E_0 will be shifted to a higher energy than that at which it was emitted; if the particle is travelling away, the γ-ray will be detected at a lower energy. The segmentation of TIGRESS becomes useful here, as it allows for a more accurate measurement to be made of the the γ-ray by being able to identify its angle to within 9°, which is the angle covered by one segment.

The segmentation of TIGRESS also helps to reduce the effect known as Doppler broadening. A γ source could emit a photon in any direction as it passes the detector. If a photon is emitted at a forward angle relative to its direction of travel, then it will be detected with an energy shifted by an amount determined by Equation 4.9. If the photon is emitted at backwards angles, then the γ-ray will be detected at an energy lower than its true value. Therefore, it is possible for one photon of a single energy to be detected as a continuum of energies. This effect is reduced if the angular acceptance of the detector is reduced, which is achieved in segmented detector arrays.

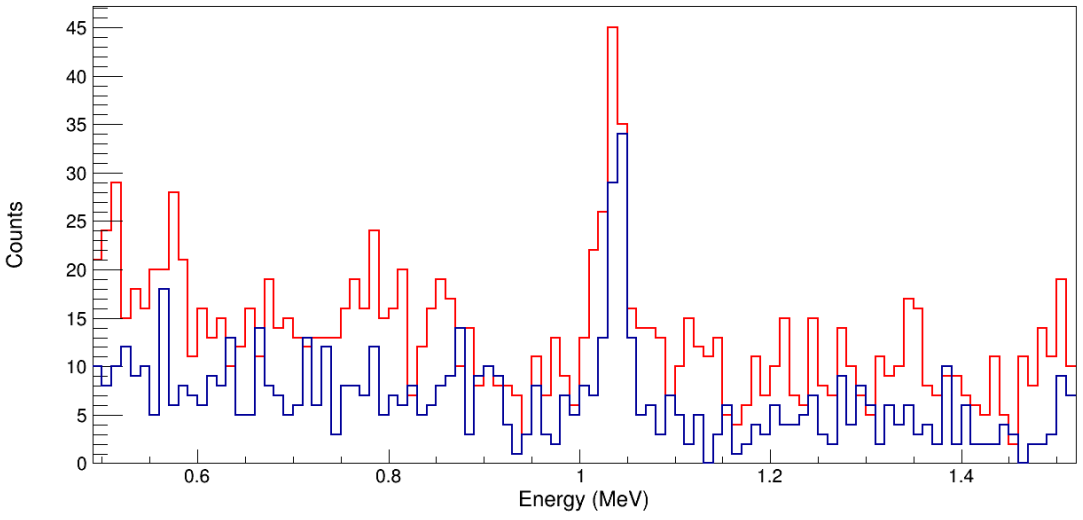

FIGURE 4.11: Full energy peak at 1.043 MeV as seen for both the 90° detector ring (red) and the 135° detector ring

.

The value of β used in Equations 4.9 and 4.10 were obtained by comparing the difference between the centroid position of a γ peak detected in the 90° and 135° detector rings.

The β value for the beam was $\beta = 0.13$ according to kinematic calculations, so this was used as an initial estimate of the β value for the reacted ^{25}Na nuclei, however, this resulted in a discrepancy between the two detector rings. In order to refine the effective value of β, the centroid for the γ peaks were fitted for each detector ring to gain the centroid positions, which were then averaged. Equation 4.9 was then equated to this averaged peak at different angles to find $\beta = 0.127$. The agreement between peaks at different values of θ can be seen in Figure 4.11.

4.1.7 Relative Efficiency Calibrations

The ways in which γ-rays interact with matter are different to those of charged particles. Charged particles are deflected by the change in electromagnetic potential created by atoms in the stopping material which causes them to slow down as they pass through. A γ-ray, however, has a chance of passing through the active area of a detector without losing any energy. This means that γ-ray detectors may not detect some γ-rays at all, even when they cover the full solid angle. The absolute efficiency, ε_{abs}, of a detector is defined as the ratio between the number of detected events in the detector, $N(E_\gamma)$ and the number of γ-rays emitted, which is the product of the intensity of the decay, $I(E_\gamma)$, the activity of the source, A, and the time over which the calibration was run, t,

$$\varepsilon_{abs} = \frac{N\left(E_\gamma\right)}{I\left(E_\gamma\right) A t}. \tag{4.11}$$

The value for $N(E_\gamma)$ in Equation 4.11 is expressed as a function of energy since it is more likely for a high energy γ-ray to pass through the detector undetected. This then means that the absolute efficiency is dependent on energy and as such it is necessary to use the radioactive sources listed in Table 4.2 to measure the efficiency over a range comparable to the expected range of γ energies found in the experiment. These sources were supplied with a value for activity measured on the date of their creation. Using this value of activity would allow for the calculation of the sources' current activity which would then allow for the absolute efficiency to be calculated.

This standard method for measuring the efficiency is impossible to achieve with the TIGRESS array due to difficulty in measuring the dead time of the Data AcQuisition system (DAQ). When a γ-ray is detected in a clover, it will be rendered dead, but the remaining clovers remain live and capable of detecting a photon. This has the effect of making the array more efficient, but means that there is no direct measurement of dead time to be made in the DAQ. If the activity of a source is small then the effect of dead time is also small because the detectors have time to become live again before another

γ-ray enters the clover. Previous experiments performed with the same set-up as this experiment have quoted that using Equation 4.11 to find the efficiency of TIGRESS is inconsistent, likely because of this issue with the dead time [57] [63]. As a result Equation 4.11 could not be used.

Instead, the counts under the Full Energy Peak of each energy in the spectra of ^{56}Co, ^{133}Ba and ^{152}Eu where measured using a Gaussian plus a second order polynomial in RadWare [64]. RadWare then fitted the measured counts at each energy for each spectrum to Equation 4.12, where values A, B, C, D, E, F and G are constants found by the software.

$$\varepsilon_r = \exp\left\{\left(A + Bx + Cx^2\right)^{-G} + \left(D + Ey + Fy^2\right)^{-G}\right\}^{-1/G}, \tag{4.12}$$

where

$$x = \ln\left(\frac{E_\gamma}{100keV}\right) \text{ and } y = \ln\left(\frac{E_\gamma}{1MeV}\right). \tag{4.13}$$

Here ε_r is the relative efficiency. The relative efficiency curve for ^{133}Ba was produced first. Each other efficiency curve was then scaled to fit. This was done separately for both the 90° and the 135° clovers. This produced the shape of the efficiency curve as shown in Figure 4.12 but does not yield the absolute efficiency.

4.1.8 Absolute Efficiency Calibrations

A technique that is not dependent on the dead time of a system is required to find the efficiency. A new approach was developed in previous experiments [57] that uses γ cascades seen in the decay of ^{56}Co to determine the efficiency of the detectors.

In a γ cascade, there will be a certain probability that a γ-ray, γ_2, will be emitted after another γ-ray, γ_1. The probability of this occurring is equal to the branching ratio (BR) of that decay. It follows, then, that the efficiency of the detector at the energy of γ_2, namely the efficiency ε_2, will be equal to the ratio of detected γ_2-rays (given that γ_1 is also detected), to the number of γ_1-rays detected multiplied by the branching ratio,

$$\varepsilon_2 = \frac{N\left(\gamma_2|\gamma_1\right)}{N\left(\gamma_1\right) \times BR}. \tag{4.14}$$

The level scheme for ^{56}Co (Figure 4.13) is appropriate in order to utilise Equation 4.14 because it has two γ decays that have a branching ratio of 100% ($BR = 1$): 1238 keV

and 847 keV. The energy states that produce these γ-rays also have several states feeding into them. This latter characteristic means that several measurements for efficiency can be performed by gating on each of the energies that are feeding either the 2085 keV or 847 keV energy states. For instance, $N(\gamma_{1238}|\gamma_i)$ can be found by gating on $\gamma_i = 2035$ keV, 1771 keV or 1038 keV γ-rays.

This measurement does not take into account any random coincidences that may occur. There is a small chance that a γ-ray associated with a cascade is detected in coincidence, but was not actually emitted as part of the same cascade. The chance of this occurring was investigated by finding $N(\gamma_2|\gamma_1)$ in the case that $\gamma_1 = \gamma_2$. The probability of a random coincidence, $p(r)$ is therefore

$$p(r) = \frac{N(\gamma_1|\gamma_1)}{N(\gamma_1)} \tag{4.15}$$

The counts found that are random coincidences must be removed in order to find the correct efficiency, hence,

$$\varepsilon_2 = \frac{N\left(\gamma_2|\gamma_1\right) - N\left(\gamma_2|\gamma_1\right)p(r)}{N\left(\gamma_1\right) \times BR}. \tag{4.16}$$

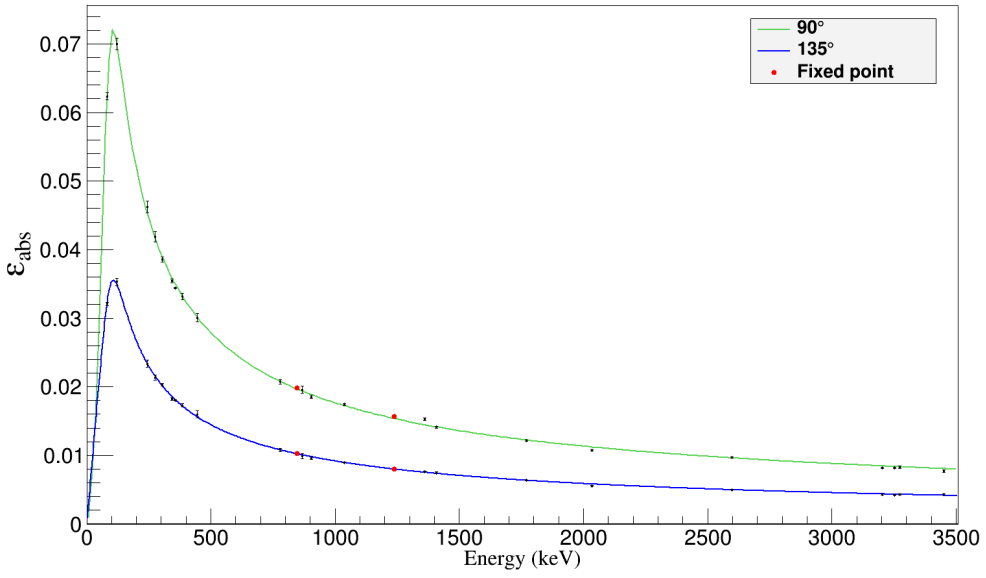

FIGURE 4.12: The efficiencies of the 90° and 135° γ-ray detector rings. The calibration points are the γ energies that were used to determine ε_{abs} (described in text) and provided the factor to which all other points were scaled. The values of the absolute efficiency calibration data are listed in Table 4.4.

The clover that detects γ_1 will be will be dead to any other γ-ray that may be emitted in its direction. This will again result in dead time affecting the efficiency calculations of

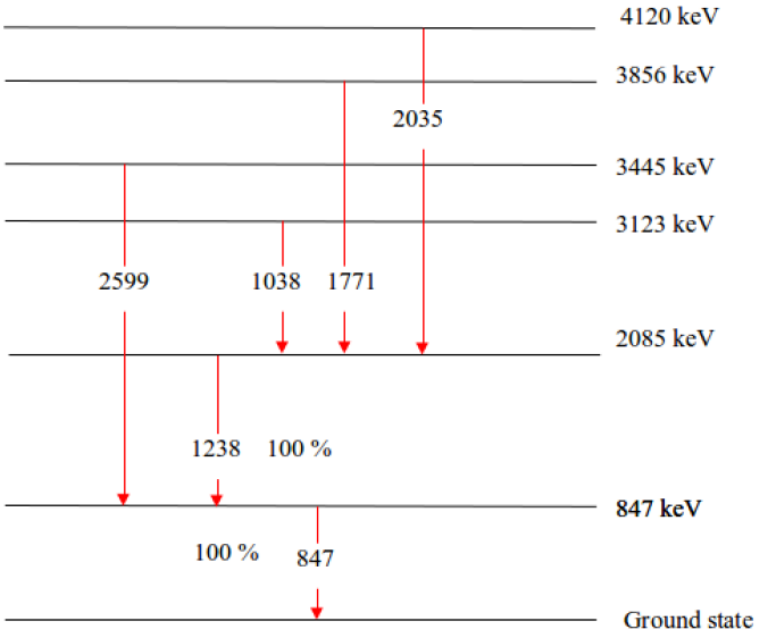

FIGURE 4.13: The level scheme for ^{56}Co. Gamma-decay cascades are shown for each of the states [63] [33].

γ_2 (keV)	Gated Energies, γ_1 (keV)	ε_2	
		90°	135°
847	1038	0.0199 (6)	0.0108 (3)
	1238	0.0195 (3)	0.0100 (1)
	1771	0.0197 (7)	0.0116 (4)
	2035	0.0187 (9)	0.0110 (5)
	2599	0.0211 (7)	0.0010 (4)
1238	1038	0.0148 (5)	0.0078 (3)
	1771	0.0163 (6)	0.0082 (3)
	2035	0.0146 (8)	0.0074 (4)

TABLE 4.3: Absolute efficiencies of TIGRESS at 847 keV and 1238 keV when gated on γ-rays that are seen in the same γ cascade for the 90° and 135° detector rings.

the array. This problem is avoided by partitioning the TIGRESS array into individual rings of detectors. By doing this, it is possible to find the efficiency of the 90° detector ring by gating on γ_1 in the 135° detector ring and measuring the number of γ_2 detected in the 90° ring. The efficiencies found using each γ-ray in the cascade using each detector ring is listed in Table 4.3

Using different values for γ_1 to perform the efficiency measurement gives different values for efficiency with varying precision. The results from each measurement where combined using a weighted average given in Equation 4.17,

γ_2 (keV)	ε_2	
	90°	135°
847	0.0197 (2)	0.0103 (1)
1238	0.0153 (4)	0.0079 (2)

TABLE 4.4: Absolute efficiencies of TIGRESS at 847 keV and 1238 keV for the 90° and 135° detector rings.

$$\bar{\varepsilon}_{weigted} = \frac{\sum_{\gamma} \varepsilon_\gamma / \sigma_\gamma^2}{\sum_{\gamma} 1/\sigma_\gamma^2}, \tag{4.17}$$

with an error of

$$\sigma_{\bar{\varepsilon}} = \sqrt{\frac{1}{\sum_{\gamma} 1/\sigma_\gamma^2}} \tag{4.18}$$

were ε_γ is the efficiency calculated for a particular γ-ray energy and σ_γ is the error in that efficiency. Equation 4.17 gives a single averaged value for efficiency for the energy of γ_2 used. These values are shown in Table 4.4 and are the final results used to scale the relative efficiency curves found in section 4.1.7. The absolute efficiency curves are displayed in Figure 4.12. It can be seen here that the 135° detectors are approximately 50% less efficient than the detectors at 90°.

During the experiment, the particles that emit the detected γ-rays are moving at $0.127c$, and so any γ-rays that are detected will have to be Doppler corrected in order to establish their true energies. The efficiency curves of the 135° detector ring must therefore be Doppler shifted using the process described in Section 4.1.6 in order to show the detector efficiency at the emitted γ-ray energy, and not the detected energy. The effect this shift has on the efficiency curve at 135° is shown in Figure 4.14. These curves are used by reading off the efficiency at the Doppler corrected energy.

4.2 Position of the SHARC Array

4.2.1 Aligning the z axis

All the data recorded for this experiment relies upon knowing the angle at which the particle is detected. It is therefore very important to make sure that the SHARC array is aligned correctly with the target position and that the particle position is known.

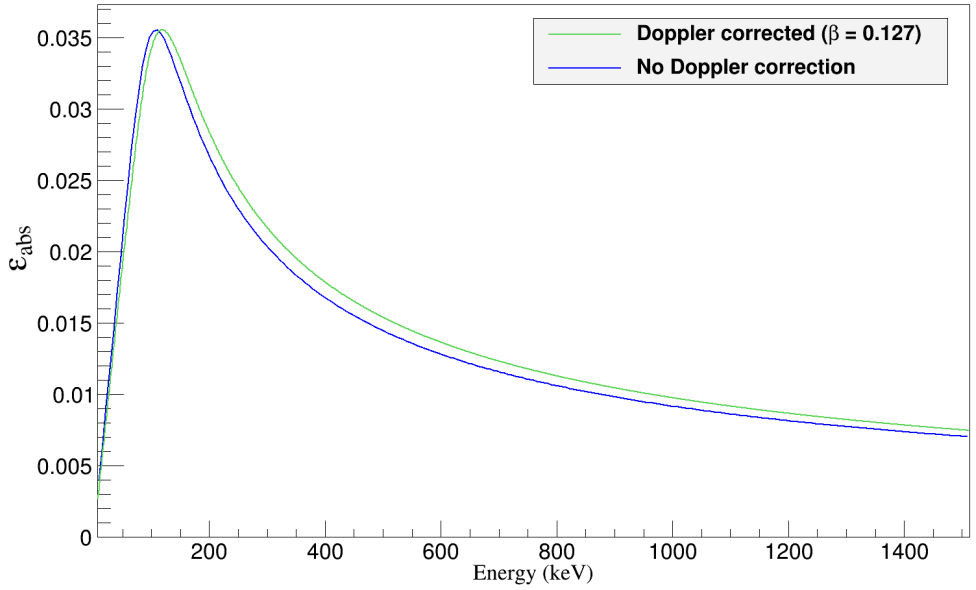

FIGURE 4.14: Efficiency curves before and after Doppler corrections for the TIGRESS detectors at 135°. The corrected curve is used by looking up the efficiency at the Doppler corrected energy.

Due to the design of SHARC, it is possible for each box detector and each CD detector to move independently of each other during the construction of the array. It is, however, unlikely for each DSSSD to shift relative to the others in the detector that are holding it in position. Therefore, the alignment of the array was treated by looking at the three separate sections of the array: upstream and downstream box detectors, and the upstream CD detector.

The z-alignment is the most critical as it is this co-ordinate that has the greatest effect on the θ of the detected particle, which in turn has an effect on the calculated excited state of the final nucleus. The z-alignment was checked by comparing the kinematic lines seen in the plotted data against the calculated kinematics. Due to the well defined lines seen for (d, d) elastic reactions, it is very easy to see if the data stray from the known values.

To estimate the shift required to ensure that the data fit with the calculated kinematic lines, θ was plotted with a gate on a narrow band of energy. The energy band chosen for the gate was arbitrary as long as it was within the energy range of the detected particle of interest. The peak that was seen using this gate occurred at a θ that was different from the angle predicted by the kinematic line.

A shift in θ is related to a shift in the z-position of the box as shown in Figure 4.15. Since $\Delta z = z_2 - z_1$, then clearly

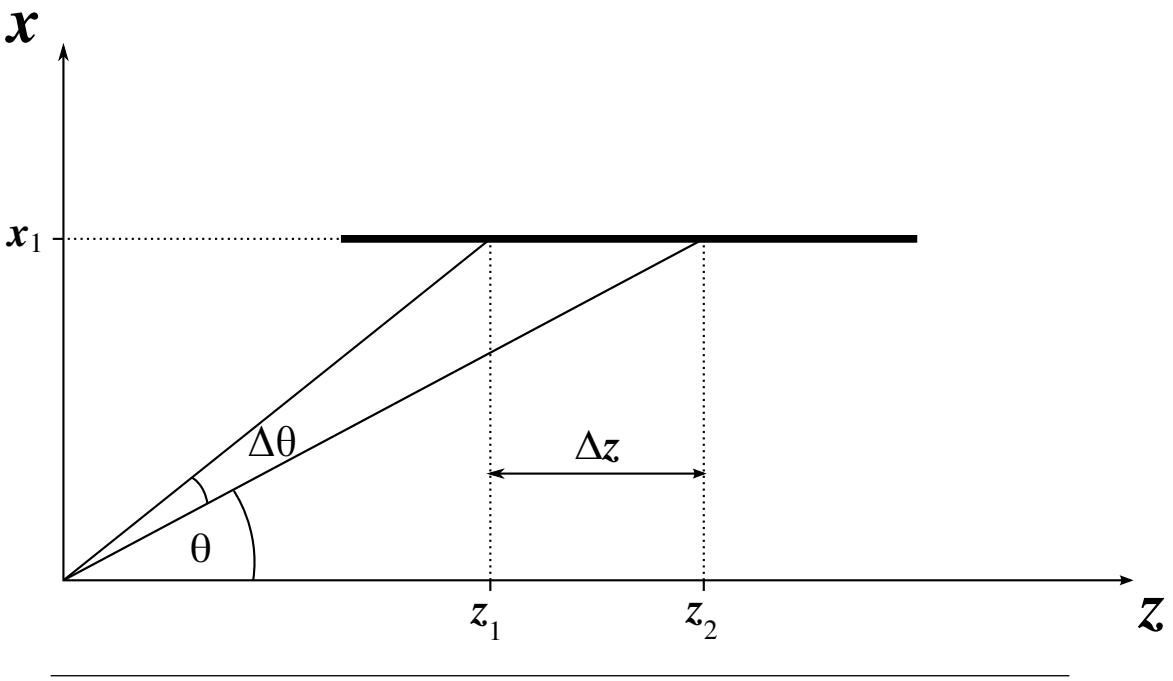

FIGURE 4.15: Depiction of the z-shift required to correct θ.

$$\Delta z = z_2 - \frac{x_1}{\tan(\theta + \Delta\theta)} \tag{4.19}$$

for the downstream box detector and

$$\Delta z = z_2 - \frac{x_1}{\tan(\pi - \theta - \Delta\theta)} \tag{4.20}$$

for the upstream box detector.

Equations 4.19 and 4.20 are both dependent upon the x (or y) coordinate of the DSSSD, which themselves may not be at their nominal values. Hence this method only provides an estimate for Δz. Under the assumption that the detector array is centred in the $x-y$ plane, where $x = \pm 40.8$ for the downstream detectors and ± 41.4 mm for the upstream detectors, it was found that each box detector was required to be sifted about 2 mm towards the target position.

4.2.2 Aligning the $x - y$ plane

The interaction point of the beam in the target is what is considered to be the target position during the analysis. This means that although checks where carried out during the set-up of the experiment that the target holder was correctly positioned at the centre,

there may still be an error in the alignment. These errors will occur if the beam spot is not centred at the centre of the target.

In an ideal scenario, each DSSSD should be positioned such that the target is equidistant from them in the $x - y$ plane. To find out whether this is the case, a plot showing the reaction data for each detector was plotted individually and overlayed on top of each other. This is shown for detectors ten and twelve in Figure 4.16, where it can be seen that there is still some discrepancy between detectors. The red band is clearly shown not to completely overlap that of the black band, even after a z-alignment correction has been applied.

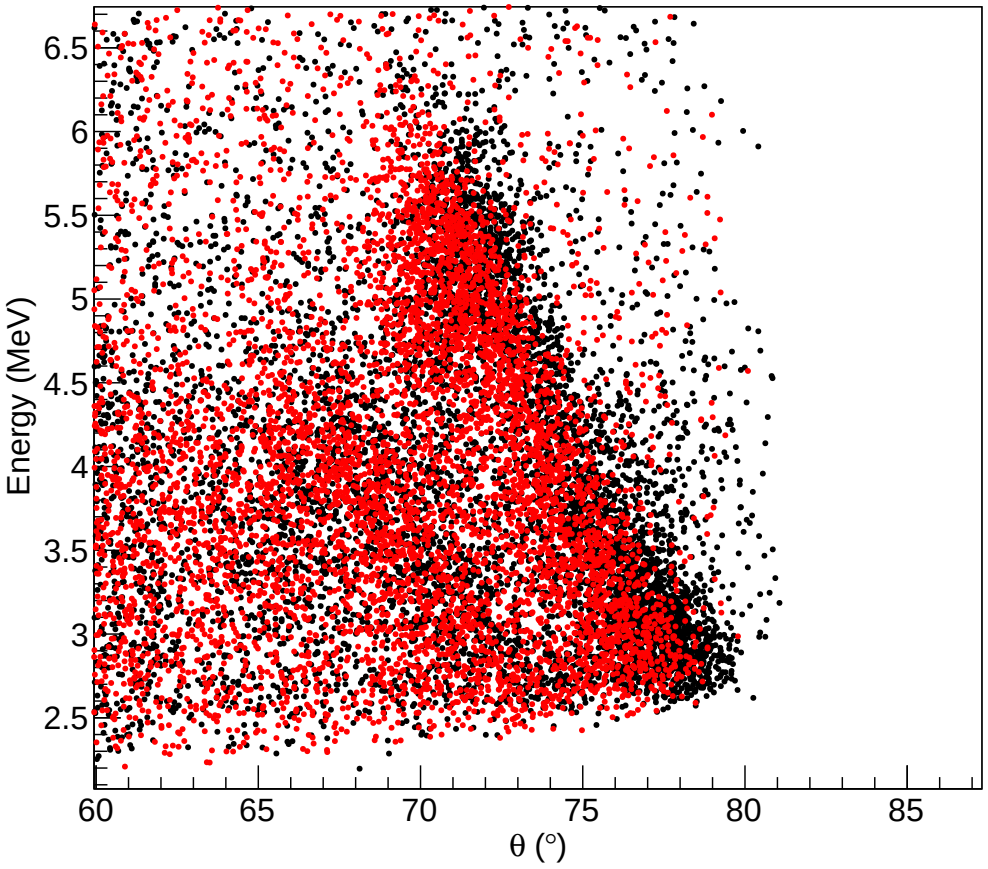

FIGURE 4.16: Kinematic lines plotted for detector 10 (black) and detector 12 (red).

The discrepancy between the detectors can be explained using Figure 4.17. If the target is not centred (case shown in red), then a particle that leaves the target at an angle θ_1 will be detected at a position z_1 in the detector. Likewise, a particle that emerges from the target at an angle of θ_2 will be detected at a position z_2. If these two particles are detected with the same energy, then θ_1 should equal θ_2. Since the target position was

initially assumed to be centred in the $x-y$ plane (case shown in black), the angles for particles detected with a certain energy have their value of θ evaluated incorrectly. A shift, Δx is required in order to meet the condition that $\theta_1 = \theta_2$. The magnitude of Δx is found by realising that $\tan\theta_1 = \tan\theta_2$ and therefore,

$$\Delta x = \frac{(z_1 - z_2)x}{z_2 + z_1}. \tag{4.21}$$

Both the alignment in the z-direction and in the $x-y$ plane can be performed to a first approximation in the ways described above, but it becomes near impossible to find the exact alignment by hand using these methods due to the dependency x, y and z have on each other. In order to find the best fit value to use for the position of the box relative to the target, a minimiser was coded and used to fit to the kinematic lines.

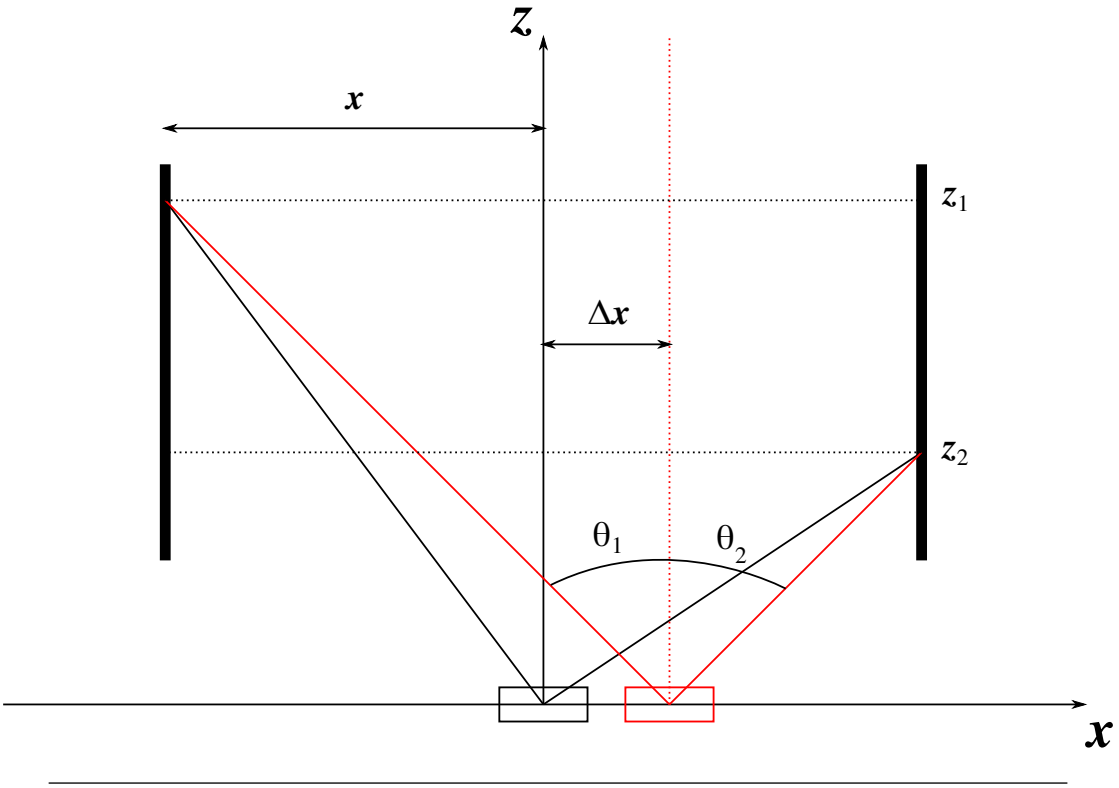

FIGURE 4.17: The x or y-shift required to correct θ.

4.2.3 Fitting to Kinematic Lines

The kinematics of the experiment are dependent on the reaction channel. The range of angles at which each type of reaction is seen is explained in Section 2.5.

For clarity, it should be noted that the ^{25}Na particles do not deviate greatly from the beam axis post reaction and so are not detected by SHARC. The kinematic lines shown

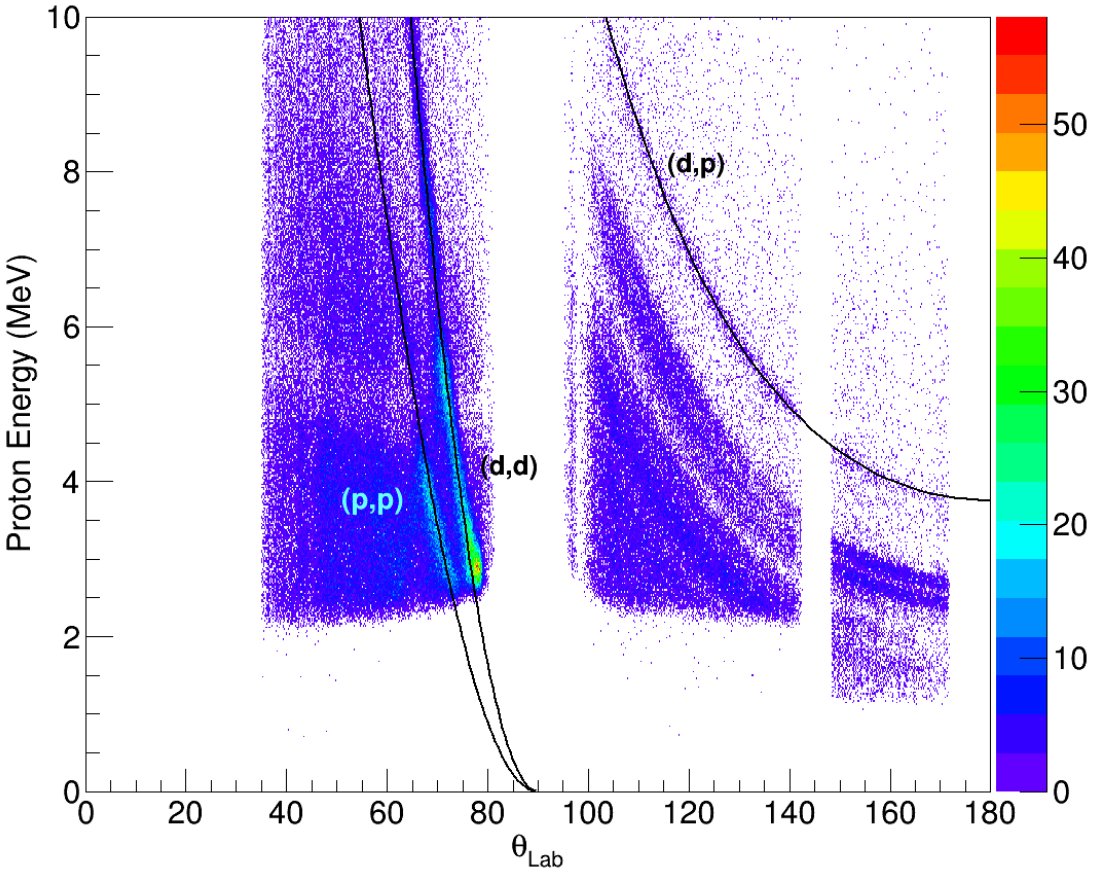

FIGURE 4.18: Kinematic lines over the whole range of the SHARC array are shown overlaid on top of the data. The calculated lines corresponding to the (p, p) and (d, d) elastic scattering data, and the protons from (d, p) leading to the ground-state of ^{25}Na are included.

in Figure 4.18 are therefore the kinematics of the protons produced in the reaction. Given that the energy and momentum the beam is known to be 8 MeV/A, and knowing that energy is conserved, the excitation energy of the ^{25}Na nuclei can be calculated using relativistic four vectors;

$$s_1 + s_2 = s_3 + s_4, \tag{4.22}$$

where s_n is the magnitude of the four vector containing the energy and momentum of the nth particle, P_n:

$$P_n = \begin{pmatrix} E_n/c \\ ip_{x,n} \\ ip_{y,n} \\ ip_{z,n} \end{pmatrix} \tag{4.23}$$

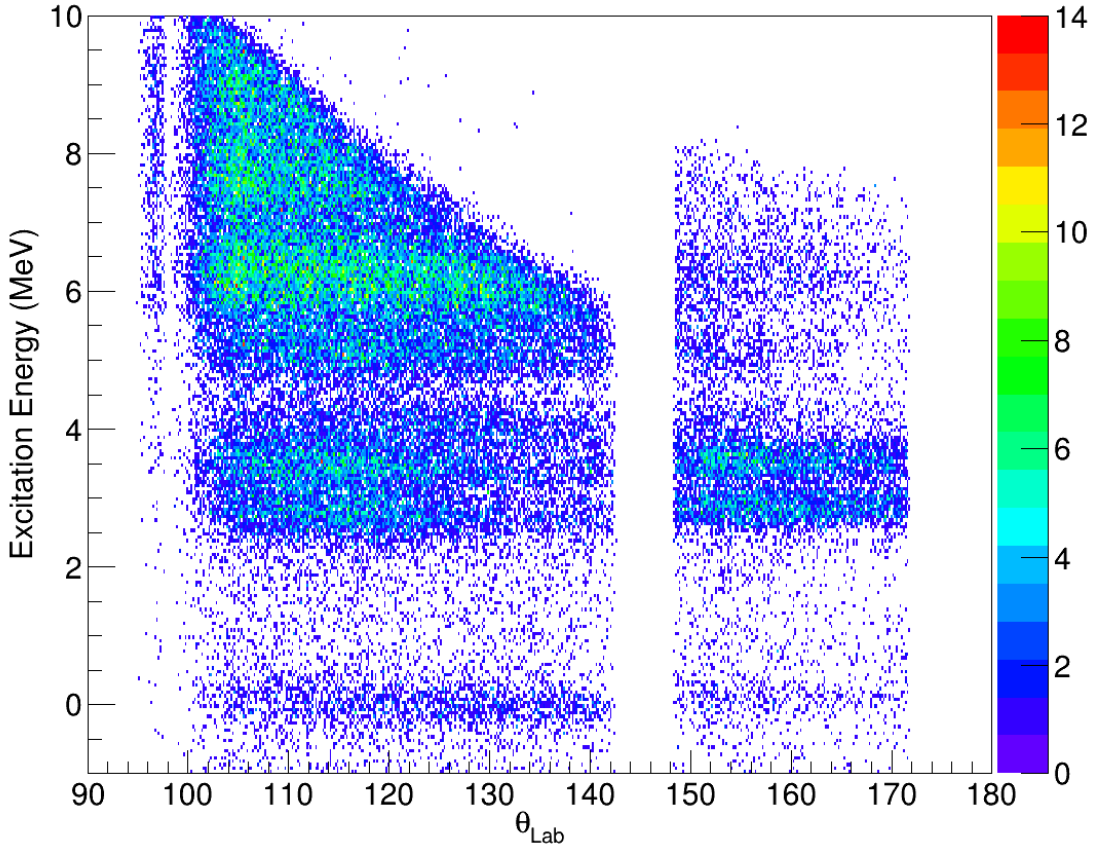

FIGURE 4.19: Excitation energy as calculated from (d, p) kinematics, shown as a function of angle for the upstream box and CD detectors. The horizontal bands represent energy levels populated in the experiment.

Figure 4.19 shows the result of this calculation for the upstream box. Figure 4.20 gives the projection of excited energy over this angular range and includes the markings showing the preliminary locations of the peaks that correspond to the states seen to be populated.

A large part of the analysis process is to find the position of the SHARC array so that the kinematic lines shown in the data match the theoretical kinematic lines. This is done by first estimating the x, y and z coordinates for the upstream and downstream boxes using the processes described in Sections 4.2.1 and 4.2.2. The procedure used to find an accurate position of the upstream box and CD detectors is described below. The procedure used to find an accurate position of the downstream box is described in Section 4.2.4.

Particles emerging from the target lose energy dependent on the thickness of the material it passed through. This means that a particle that is detected close to 90° will pass through more matter than a particle that is detected close to 0° or 180°. The effect this has on the kinematic lines is to reduce the energy of particles detected close to 90°. This

energy loss has to be corrected for in order to obtain good agreement with calculation, but this correction is not trivial since it is tied to the angle of the detected particle, which is dependent on the position of SHARC.

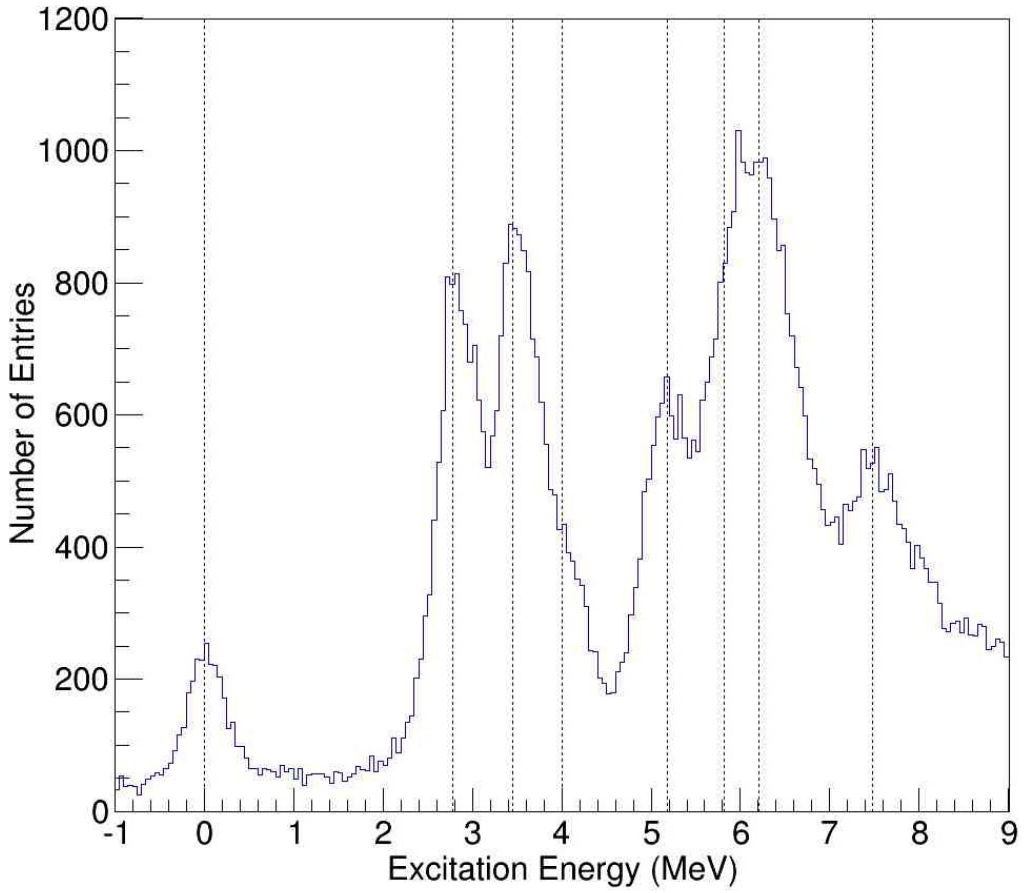

FIGURE 4.20: Excitation energy spectrum for ^{25}Na calculated using (d, p) kinematics for particles detected between 90° and 180°. The dotted lines show the initial estimated positions of excitation peaks.

The excitation energy spectrum (Figure 4.20) was needed in order to fit the kinematic lines more accurately than using the techniques described in Sections 4.2.2 and 4.2.1. A code was written to minimise the difference between the data and known excited states that were expected to be seen. An initial estimate for x, y, and z was provided for the target position using Equations 4.21 and 4.19. The estimate for the target thickness of 1 mg/cm^2, which was the manufacturers specification of the target, was also given and used to calculate the difference between the data and these known values. These values were then changed and the difference between theory and experimental data was again checked. This was repeated until a minimum was reached.

This procedure was performed with the ground-state data due to the simplicity of comparing the data to zero. However, the ground-state line is very faint – especially in the

CD detector (see figure 4.18), and so there were very few counts to base the alignment of the detector on. Repeating the process with a more visible state allowed for a more accurate measurement, but produces the problem of being able to identify the same state in the CD and the upstream box detector. This problem was solved using the γ-ray data and gating on a γ-ray that is associated with a known energy level.

Chapter 5 will describe in detail the clear evidence for the population of a state at 3.455 MeV in ^{25}Na. Gating on the γ-ray peaks associated with the decay of this state allows the protons detected at this energy to be identified in both the CD and box detectors. This means that the minimisation procedure can be applied to this state for both parts of the detector.

4.2.4 Aligning the Downstream Box Detectors

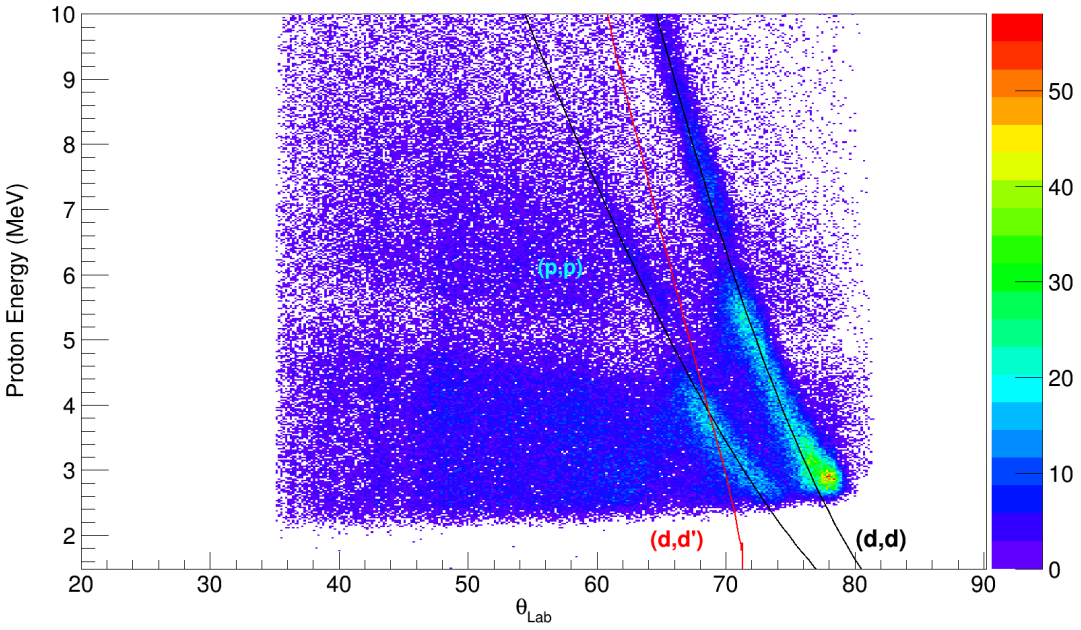

FIGURE 4.21: The kinematic lines for the downstream box detectors with the calculated kinematic lines for (d, d) and (p, p) elastic scatter.

Minimising the values for x, y, and z was much more problematic for the downstream box detector. Figure 4.21 shows the kinematic lines for the (p, p) and (d, d) elastic scatter data compared to the calculated kinematic lines. The calculated (d,d) kinematic line does not appear to follow the data perfectly, deviating slightly from the theory line close to the threshold and close to the punch through energy ($\approx$ 6 MeV). This deviation causes the data to appear slightly flatter than the theoretical kinematic line, which in turn causes the minimisation algorithm to fail. Omitting this energy region from the minimisation procedure left a very small selection of data that could be used to find the

detector positions. The solution was to analyse the counts detected by each pixel for the downstream box that covered the angles that were not affected by the high threshold or punch through.

Figure 4.21 shows also a kinematic line for a (d, d') inelastic scatter reaction (shown in red) where a ^{24}Na beam particle is left excited after a collision with a deuteron in the target. This line represents the 1.512 MeV excited states found in ^{24}Na and is depicted here because γ-rays depopulating this energy state were observed in the experiment. The energies populated in ^{24}Na are discussed in more detail in Section 4.4.1. It is clear that the inelastic data are well separated from the elastically scattered deuterons.

The elastically scattered deuterons are only detected over a small range of back strips in each DSSSD detector. Examining the energy of each back strip in this range against the front strip number gives the histogram shown in Figure 4.22. Taking the projection of each front strip value provides the energy spectrum seen for each pixel. A Gaussian fit was performed to find the centroid position in the (d, d) elastic peak. The number of counts minus background counts in the energy peak was also found at this stage, but were not utilised until the normalisation of the elastics in Section 4.2.5. The centroid energy for each pixel was then plotted against the position of the pixel for each back strip. The resultant graph (Figure 4.23) looks very similar to the histogram shown in Figure 4.22 except that the x-axis is given in millimetres from the target instead of strip number. Plotting the data in this fashion allowed for a direct comparison between the same back strip (same z) on detectors opposite one another in the detector array.

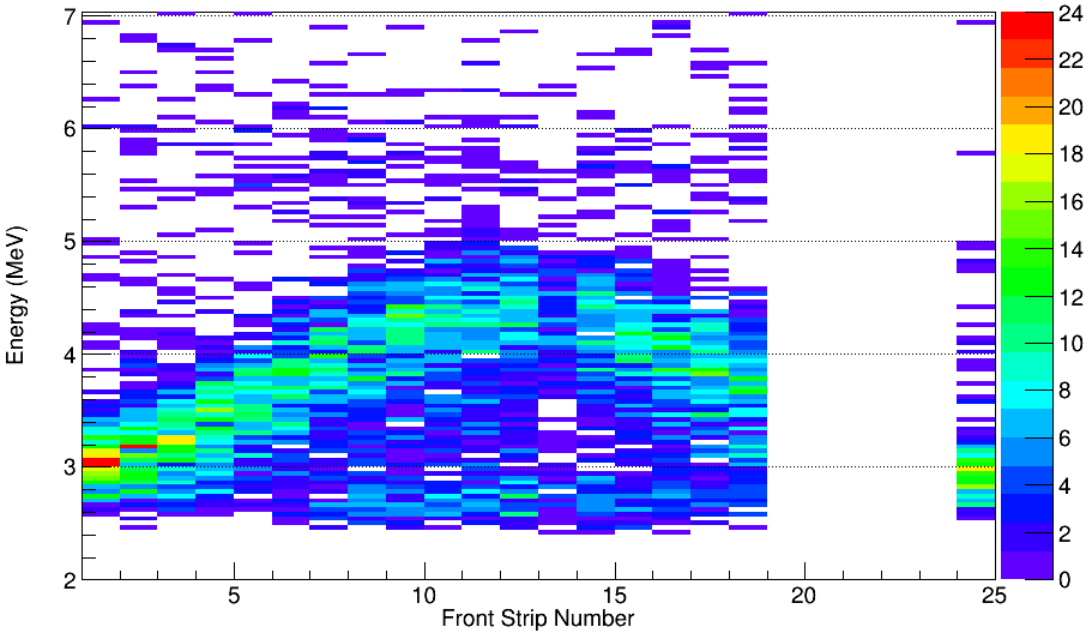

FIGURE 4.22: The energy of the elastic scattered particles at a constant z position.

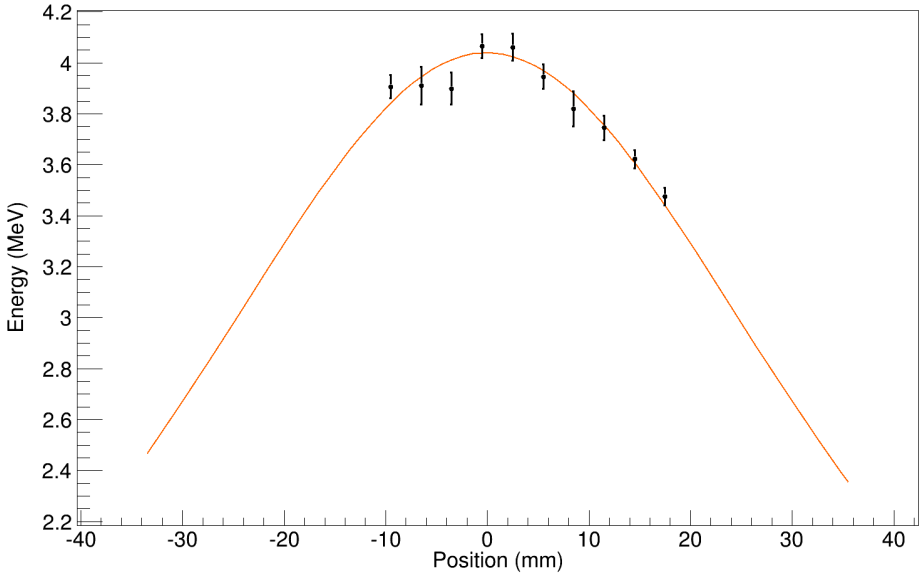

(A)

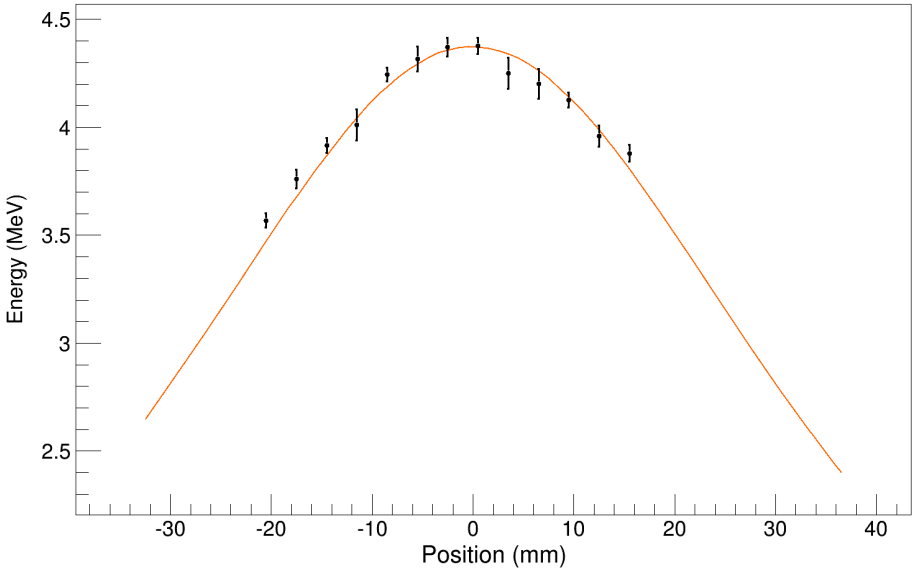

(B)

FIGURE 4.23: Energy plotted against the position of the 45th back strip for (A) detector 10 (B) detector 12.

For reasons described in Section 4.2.2 and shown in Figure 4.17, the maximum energy found for each back strip will vary, as the target position is changed. Moving the target position as shown in Figure 4.17 will result in the energy in one strip in one detector being different to its counterpart in the same strip in a different detector. This explains the small difference in the energies plotted in Figures 4.23a and 4.23b. A target shift in the $y - direction$ will result in the peaks' maximum energy plotted in Figure 4.23 occurring at a non-zero y position. The difference between 0 and the position at which the maximum energy is found gives the y-offset of the target. The x-shift and y-shift found with this method were -0.85 mm and 2.0 mm respectively, which are consistent

with the shifts found for the upstream box in Section 4.2.2. This y-shift has been applied in Figure 4.23 resulting in the peak occurring at $y = 0$.

The fit to the data points represents the theoretical values for the energy and is dependent on the centre-of-mass angle, θ_{cm}. The comparison between this theoretical line and the data points demonstrates the issue of trying to minimise the difference between theoretical kinematic lines and the elastic scatter data points as was done for the upstream box detectors described in section 4.2.3. Figure 4.24 shows two situations in which points deviate from the theoretical line in different ways. The angle compared to the z-axis, θ_{Lab}, varies slightly between the edge of a back strip and its centre. This means that the points with a more extreme x position in Figures 4.23 and 4.24 have a greater value for θ_{Lab} than at $x = 0$ mm. Therefore, some strips will be able to measure the full energy peak at the centre of the strip, but will have some – or all – of the peak cut off at the edges, resulting in a falsely high energy measurement. This can be seen at $x > 20$ mm in 4.24a which shows the 44th back strip in detector 10.

Figure 4.24b shows a deviation from the theory that is caused by the elastically scattered particle punching through the DSSSD detector. A combination of these two effects caused the (d, d) line shown in Figure 4.21 to be flatter than the theoretical kinematic line.

4.2.5 Normalising the Elastic Scatter

Normalising the data to the elastically scattered particles is crucial to obtaining the spectroscopic factors of the transfer reaction. The counts in the elastic energy peak were found per pixel in Section 4.2.4. The technique used was to calculate the counts per unit solid angle of the detector and compare it to the form of the theoretical $d\sigma/d\Omega$ for elastic scatter.

Theoretical calculations using the optical model were performed using the program DWUCK4 (Distorted Wave University Colorado Kunz), which calculates the the scattering for binary nuclear reactions using the Distorted Wave Born Approximation described in Section 2.3.2 [65]. Daehnick *et al.* [66] developed a potential which has a Woods-Saxon form and includes a Coulomb and a spin-orbit term. This potential was fitted to 4000 data points from experiments examining the elastic scatter of various stable and nearly stable nuclei at different energies [66]. The fits to these data points were used to determine the parameters required to reproduce the scattering potential for any target nucleus. This Daehnick potential was the input potential used in the DWUCK4 program to compute the elastic scattering theory predictions.

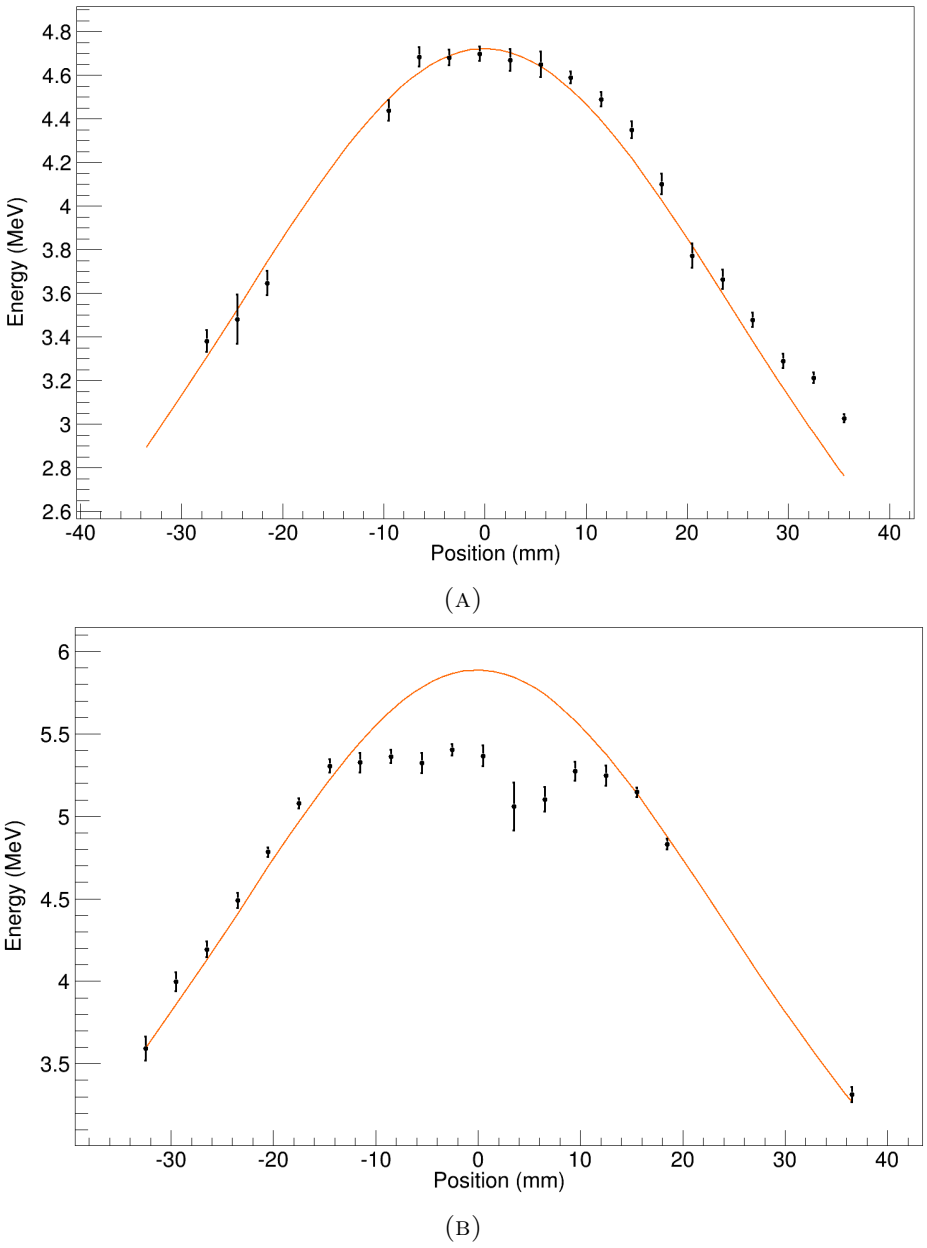

FIGURE 4.24: Threshold and punch through effects on elastic scatter seen in (A) detector 10 back strip 44, (B) detector 12 back strip 43.

The differential cross section of a beam consisting of a number of particles, I, onto a target comprised of t particles per cm^2 is defined by

$$\frac{\mathrm{d}\sigma}{\mathrm{d}\Omega} = \frac{N}{\varepsilon \mathrm{d}\Omega I t}, \tag{4.24}$$

were N is the yield in the solid angle range, $\mathrm{d}\Omega$, and ε is the detector efficiency. The thickness of the target was quoted as 1.0 mg/cm^2 by the manufacturer, however, the exact thickness is unknown as well as the ratio of protons to deuterons in the target.

Beam current measurements could not be taken due to the inclusion of the aluminium sheet in the Trifoil which stopped some particles reaching a Faraday Cup located in the beam dump. As a result, it was not possible to measure the cross sections of a reaction directly.

It is not actually necessary to know I, t and ε individually to calculate the differential cross section. Comparing the theoretical cross section of deuteron elastic scattering to the measured yield per pixel over the solid angle per pixel ($N/\mathrm{d}\Omega$) allows a scaling factor equal to $\varepsilon \cdot It$ to be found. This scaling factor cannot be used to scale the proton angular distributions for the downstream box detector since t does not remain the same for deuterons and protons.

For the SHARC array, the solid angle of one pixel is dependent on its position since the plane of the surface of each pixel is not perpendicular to the direction of travel of the detected particle. The solid angle for a specific pixel is given by Equation 4.6. Each value of $N/\mathrm{d}\Omega$ can now be calculated, plotted and scaled in order to get $\mathrm{d}\sigma/\mathrm{d}\Omega$, however, this is the differential cross section in the laboratory reference frame. The theoretical elastic cross section given by DWUCK4 outputs a differential cross section in the centre-of-mass frame and so a conversion from the lab reference frame to the centre-of-mass reference frame is needed. The Jacobian, $\mathrm{d}\Omega/\mathrm{d}\Omega'$ was used to convert the cross section of the data in the lab frame into the cross section of the centre-of-mass frame;

$$\frac{\mathrm{d}\sigma}{\mathrm{d}\Omega'} = \frac{\mathrm{d}\sigma}{\mathrm{d}\Omega} \cdot \frac{\mathrm{d}\Omega}{\mathrm{d}\Omega'}, \tag{4.25}$$

where the Jacobian is given by

$$\frac{\mathrm{d}\Omega}{\mathrm{d}\Omega'} = \frac{\gamma p' \left(p - \beta E \cos\theta\right)}{p^2}, \tag{4.26}$$

where primed quantities are the centre-of-mass variants and p is the momentum of the detected particle.

The data plotted for the elastic differential cross section reveal that the downstream box is sensitive to an area at which there is a minimum in the cross section. This minimum can clearly be seen in Figure 4.25. The minimum of the theoretical elastic scattering was shown to occur at a very specific angle in the centre-of-mass frame. Since the solid angle of the detector is dependent on the position of the detector relative to the target position, it was possible to establish the position of the downstream box detector by comparing the profile of the theoretical elastic scattering calculations to data.

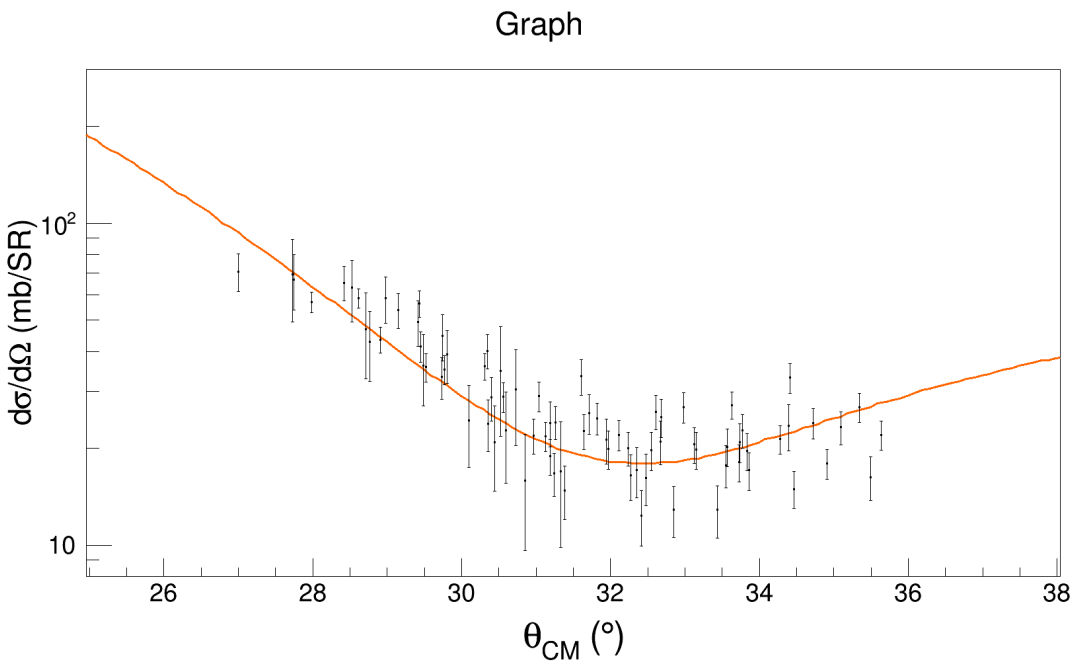

FIGURE 4.25: Elastic scattering cross section obtained by measuring the number of counts in the elastic scattering peak for each pixel. The data are scaled to fit theoretical values for the cross section and compared to the profile of this line.

4.3 Trifoil

The Trifoil is a simple detector primarily used to clean up the spectrum obtained from SHARC. It does not have the ability to distinguish the ^{25}Na particles after a reaction has taken place from the un-reacted ^{24}Na beam particles. The limited light collection from the trifoil means that it is not suited to energy measurements (and in any case it would only be a measure of $\mathrm{d}E/\mathrm{d}x$ which would not distinguish ^{25}Na and ^{24}Na). These factors, coupled with the fact that it is not position sensitive means that it is not suitable to be used as a primary detector for this experiment. Its use comes from the implementation of the aluminium foil placed in front of the detector and its ability to produce a logic signal that indicates when the foil has been penetrated.

The dimensions of the Trifoil are given in Section 3.5. Due to the distance the Trifoil is from the target, it is only sensitive to particles that are emitted at a maximum of 2.8° to the beam axis. This is not an issue with the set-up used in this experiment, since the Trifoil only needs to be sensitive to ^{25}Na particles that are associated with protons detected in SHARC. The NPTool software package was again useful here, as it allowed the angle calculation of the proton and ^{25}Na after the reaction using Lorentz transformations described in Section 4.2.3. Figure 4.26 shows the angle at which the ejected proton emerges versus the angle of the ^{25}Na nucleus in its ground-state. The

angles covered by the SHARC array are shown by the dashed lines travelling parallel to the y-axis and the angles covered by the Trifoil are shown by the dashed lines travelling parallel to the x-axis. The shaded regions represent the angles at which the experiment is sensitive to the (d,p) protons and the ^{25}Na nuclei.

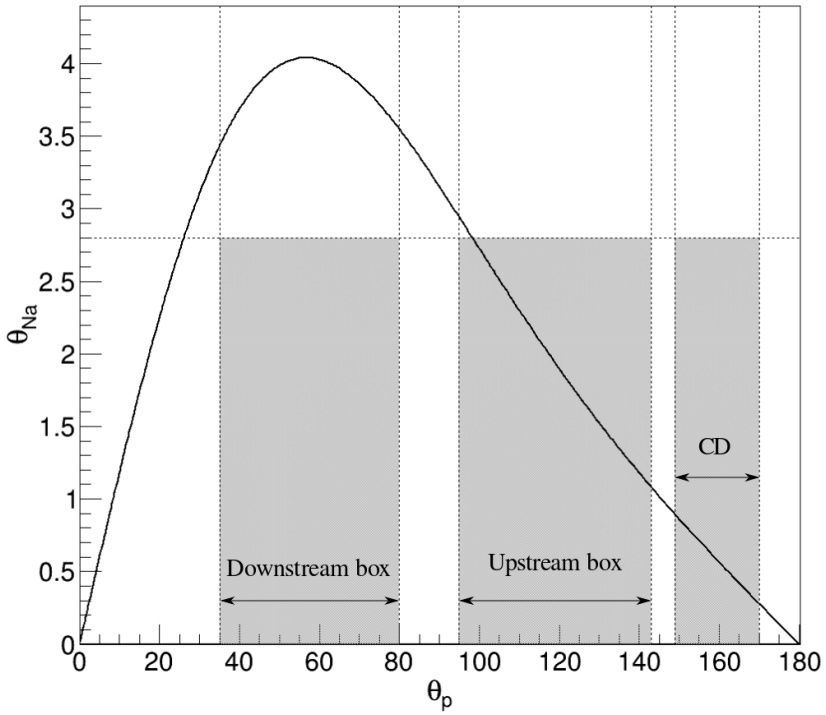

FIGURE 4.26: Angle of reacted ^{25}Na nuclei against the angle of the detected proton post reaction. The greyed regions show the anglular range at which the protons and the ^{25}Na nuclei are detected by both Sharc and the Trifoil respectively.

The foil placed in front of the scintillator is of a sufficient thickness as to stop higher Z particles created through fusion evaporation, but allows beam-like particles to pass through and be detected in the scintillator. This then gives a measurement that can be used to discriminate between good events detected in SHARC after a proton from a (d, p) reaction and events resulting from a fusion evaporation or other background process.

The compound nucleus that would be created in this experiment would be chlorine-36. Table 4.5 shows the fusion evaporation products created and the quantities in which they are produced, as calculated by the computer program PACE4 [67]. The energies of the evaporating nuclei have a statistical distribution and the energy quoted in Table 4.5 is the centroid of that distribution over all angles.

The thickness of aluminium needed to shield the Trifoil was calculated for these nuclei and displayed in Table 4.5. The kinematic lines for ^{25}Na in the ground-state and in an excited state of 10 MeV are shown in Figure 4.27. This shows the range of energies

Nucleus	%	Cross Section (mb)	Energy (MeV)	Stopping thickness (μm)
^{32}P	2.94	28	119	34.11
^{31}P	12.9	123	119	34.28
^{29}Si	23.8	227	119	38.56
^{29}Al	3.19	30.4	126	45.78
^{28}Si	13.2	126	105	33.51
^{28}Al	5.49	52.3	112	40.01
^{27}Al	4.44	42.2	105	37.31
^{26}Al	3.77	35.9	98	34.63
^{26}Mg	3.0	28.6	105	42.18
^{25}Mg	10.1	96.6	98	39.12
^{23}Na	3.19	30.3	91	41.12

TABLE 4.5: Highest yield fusion evaporation products, their energies and the thickness of aluminium required to stop them

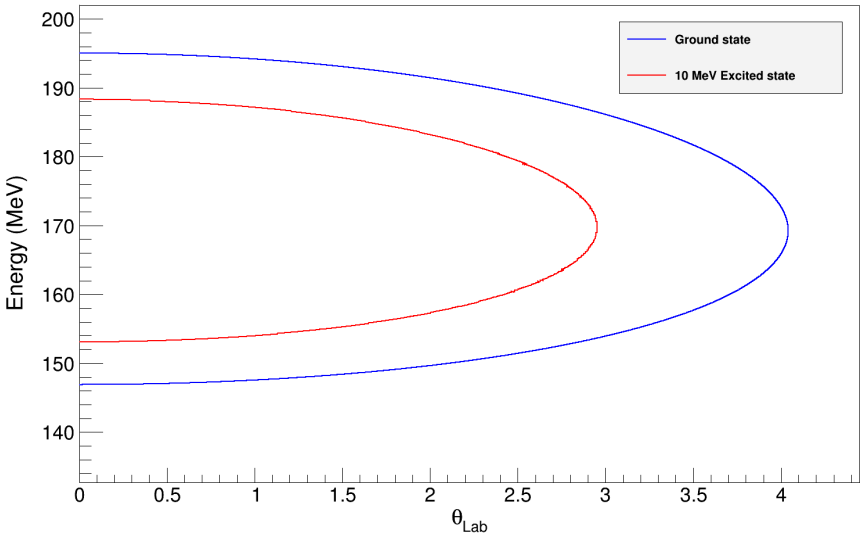

FIGURE 4.27: Kinematic plots the ^{25}Na at different energies. The figure is iintended to show how the kinetic energy of ^{25}Na changes as its kinetic energy increases.

at which the sodium nuclei are likely to be detected during the experiment (excited states above 8 MeV are not seen due to high energy thresholds). A ground-state nucleus emitted at zero degrees will have the lowest detected energy at 146.9 MeV, which relates to an aluminium stopping thickness of 74.66 μm. Many of the fusion evaporation products have very similar values of charge to that of ^{25}Na. This means that it is difficult to halt the fusion evaporation products whist still transmitting ^{25}Na through the foil. Aluminium-29 requires the most aluminium foil to stop at 45.78 μm and so a 50 μm (13.51 mg/cm^2) sheet of aluminium foil was used in front of the Trifoil during the experiment.

The waveform of the pulse detected by the Trifoil is digitised to find the time of the

pulse. This time is measured from a triggering event in SHARC and is measured in units of 1/16 (0.625 ns) of a clock cycle in the Tig-10 front end cards [55]. Because the front of the Trifoil is shielded by a foil that prevents any fusion evaporation products from being transmitted, the majority of events detected by the Trifoil will be caused by ^{25}Na nuclei or particles from the beam; the latter of which are limited to a focused dead spot at the centre of the scintillator. The histogram in Figure 4.28 shows the amount of counts detected at different times. The peak represents the reacted ^{25}Na nuclei. Gating on events between a time of 40 and 52 on the histogram when looking at γ and particle excitation spectra reduces noise caused by the fusion evaporation protons.

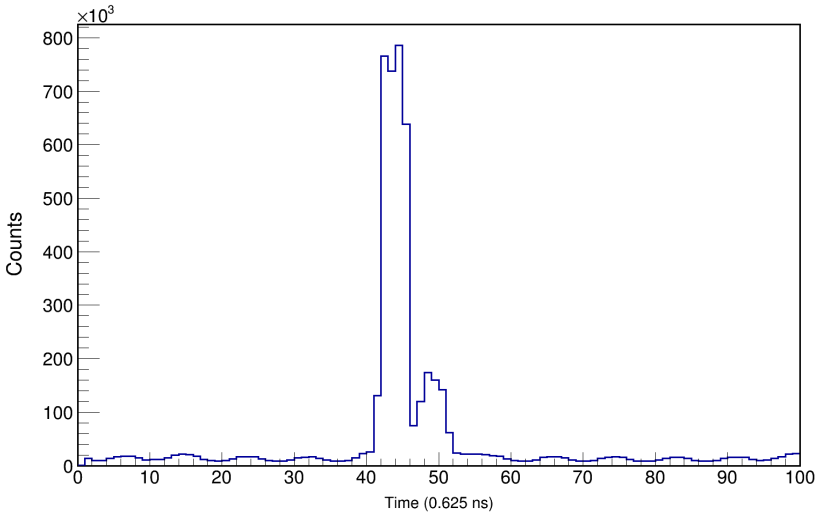

FIGURE 4.28: Time at which ^{25}Na nuclei are detected in the Trifoil.

4.4 Establishing the Excitation Energy Spectrum

The energy of ^{25}Na against the γ-ray energies were plotted in Figure 4.29. The high density of counts grouped together in narrow horizontal lines represent events where a well defined γ-ray is detected in coincidence with a proton in SHARC. This figure reveals some preliminary information to the structure of ^{25}Na because it shows the γ-rays associated with each excited state, and gives an early indication as to which photon energies to expect when analysing a particular excited state. This early look at the data provided information which was used to create the start of a level diagram of the nucleus. The process of building up a level scheme is described in detail in this section.

4.4.1 Gamma Spectra

The first obvious characteristic of the histogram in Figure 4.29 is the widths of the grouped data. The energy resolution of SHARC is significantly worse than that of TIGRESS, and so any measurement of the energy of a particle in the silicon detectors will be significantly less precise than the energy of a detected photon in the germanium detectors. For this reason, the γ-rays are particularly useful in determining the excitation energy of the nucleus.

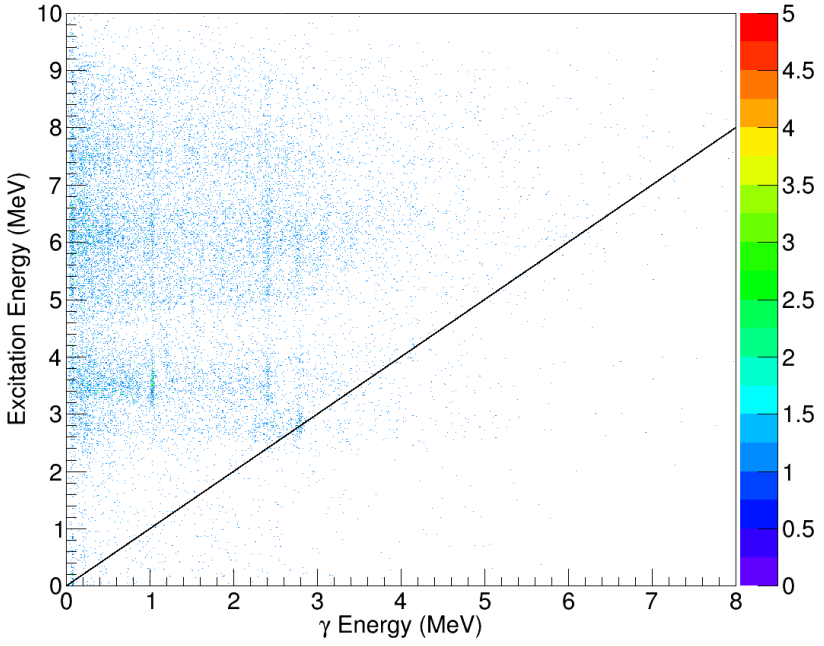

FIGURE 4.29: Excitation energy as calculated from the energy and angle of the detected proton vs γ-ray energy. The line indicates decays directly to the ground-state($E_x = E_\gamma$).

A γ-ray lying on the $x = y$ line means that an excited state at this energy decays directly to the ground-state because the emitted γ-ray has the same energy as the source particle. Groups of data within the region $y > x$ occur when a state decays through a lower excited state. Photons with the same y co-ordinate (same E_{Ex}) occur in a cascade event as a ^{25}Na nucleus decays to the ground-state via another excited state. The γ-rays with the same x co-ordinate give an indication that the excited states are linked by a possible decay chain.

There only appear to be two occurrences where an excited state decays directly to the ground-state in Figure 4.29. One occurrence is close to the origin and so is difficult to see on this plot. The other is around an excitation energy of 2.5 MeV - 3.0 MeV. Gating on this energy range to examine the γ-ray allowed the value of the excited state to be found. The γ peaks that were detected as part of a cascade were identified by gating on the excitation energy of ^{25}Na in steps of 0.5 MeV. The γ-rays with a summed energy lying

within the gate on excitation energy were noted as belonging to a cascade from an energy state within that region. This did not allow all γ-rays at each excitation energy range to be identified; peaks that did not sum to the total energy of the excited region were noted and a spectrum of excitation energy gated on these peaks was produced. An example of one of these spectra is shown in Figure 4.30 for the peak found at 2.788 MeV. Creating spectra like this gave information regarding the actual excitation energies associated with the γ-ray emission, which allowed a more accurate excitation energy window to be used for gating upon.

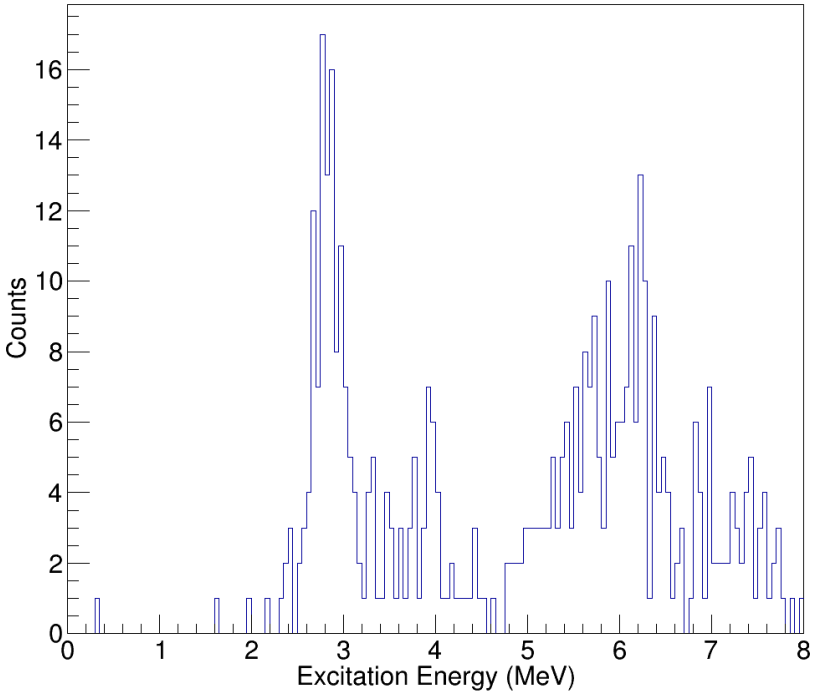

FIGURE 4.30: Excitation energy gated on the γ-ray at 2.788 MeV.

This iterative procedure helped to establish excitation energies that appeared to correspond to the states in ^{25}Na. The γ-ray emissions associated with the energies were examined in more detail. Figures 4.31 to 4.42 show the γ-rays observed while gating on a mean excitation energy $\pm$0.2 MeV. This energy range of $\pm$0.2 MeV is equal to $\pm\sigma$ for the average σ value representing the experimental widths of the excitation energy peaks (the process of obtaining σ is described in Section 4.4.3). In some instances, weakly populated states in ^{25}Na are overshadowed by close neighbours that are strongly populated. This causes difficulty in examining the γ-rays that are emitted from the weak state because γ-rays from the strong state will always contaminate the γ-ray energy spectrum. This problem is remedied somewhat by exploiting the angular distributions of the populated states. States of different spins and parities will have different angular distributions (see Section 5.1) which affect the relative population of peaks for different

excitation energies at different angles. Gating on an excitation energy region and a specific angular region where the ratio between the strong and weak peak is minimised allows the γ-rays associated with the weak state to be seen more clearly. An example of this occurs between the strong 3.455 MeV peak and the weak 3.995 MeV peak. The ratio of the strength of the peak at 3.455 MeV compared to the 3.995 MeV peak reaches a minimum between 119° and 143°, as can be seen in Figure 4.45.

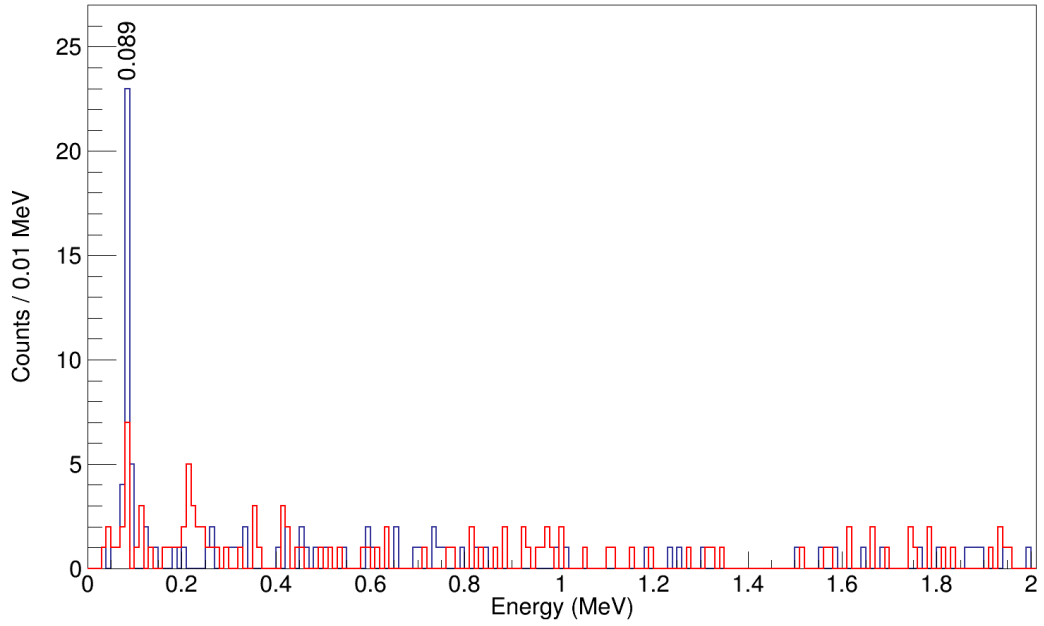

FIGURE 4.31: The γ-ray spectrum when gated on the excited energy spectrum at 0.089 ± 0.2 MeV (blue) (extending below zero allows for resolution effects). Background (red) gated by 0.5 ± 0.2 MeV.

Gating on the excitation region around 0.089 MeV showed a γ-ray at 0.089 MeV, as shown in Figure 4.31, which proves that there is a state at this energy that decays to the ground-state. Also shown in Figure 4.31 is the background spectrum (red) taken at the energy region at 0.5 ± 0.2 MeV. This is an empty energy region where no state is apparent in ^{25}Na This background shows a second peak at ~ 0.2 MeV which is caused by a fusion evaporation product that has not been completely filtered out by the Trifoil.

The state at 2.416 MeV was previously known to exist [11], but is predicted to be weakly populated during the transfer reaction by the shell-model. This results in a low count rate when gating on the 2.416 MeV excitation energy. Figure 4.32 shows a γ peak at 2.416 MeV as well as another peak at 2.788 MeV. This second peak is caused by the width of the gate overlapping with an adjacent excitation peak at 2.788 MeV.

The 2.788 MeV gated spectrum has a very clear peak when examining the excitation spectra (see Figure 4.20). The peak to the ground-state is clearly seen at 2.788 MeV, shown in Figure 4.33.

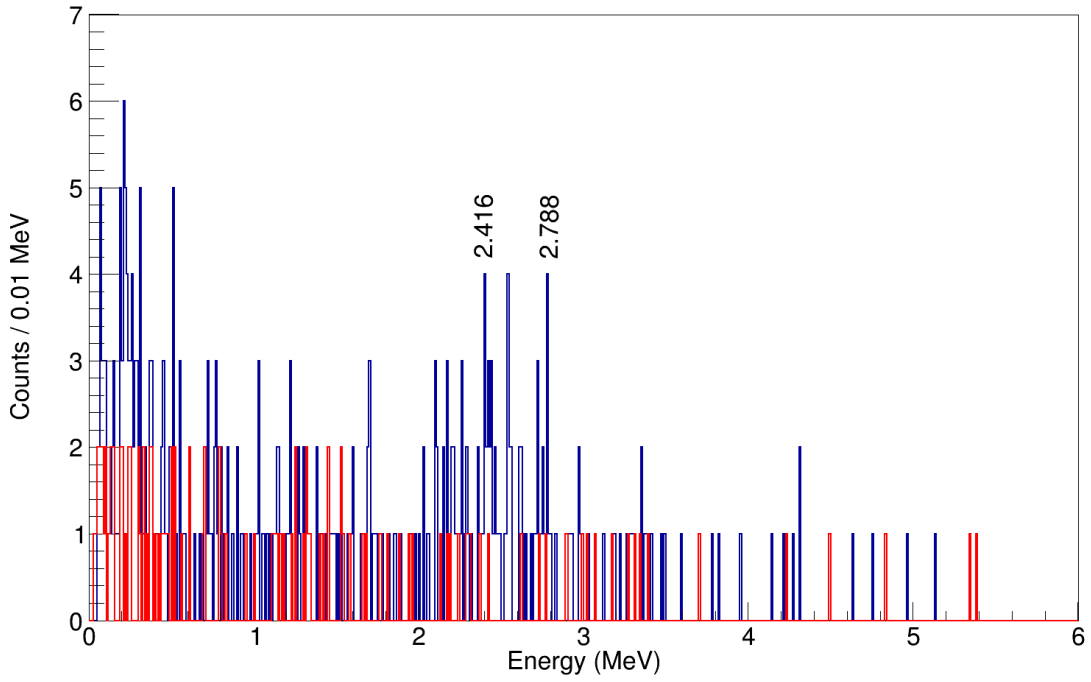

FIGURE 4.32: The γ-ray energy spectrum when gated on 2.416 ± 0.2 MeV (blue). Background (red) is for the 1.7 ± 0.2 MeV gate.

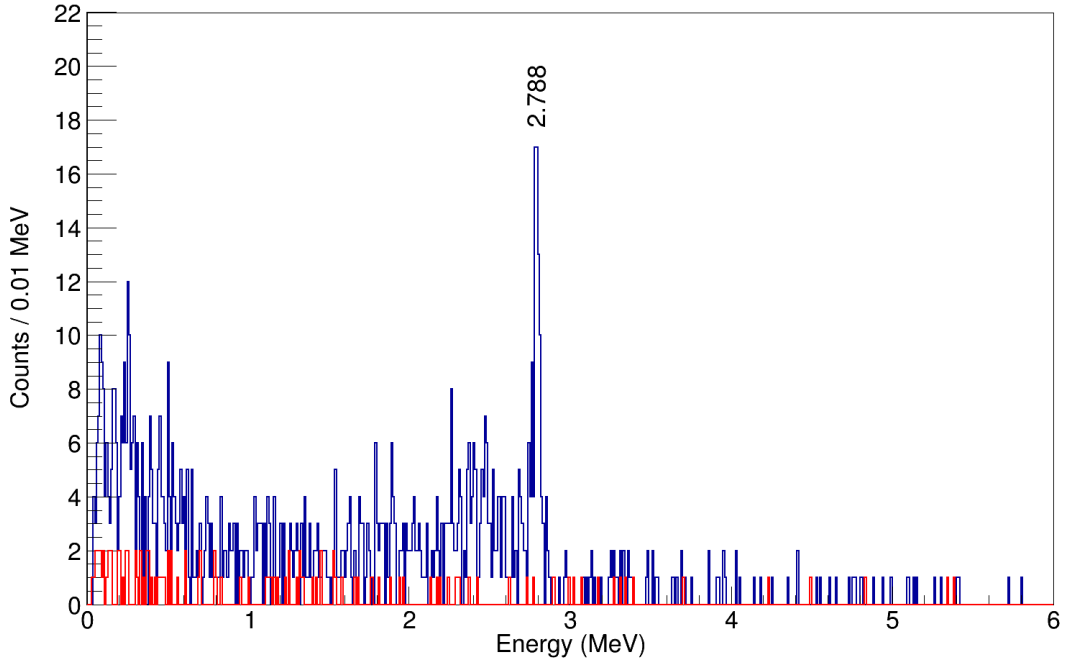

FIGURE 4.33: The γ-ray energy spectrum when gated on 2.788 ± 0.2 MeV (blue). Background (red) is for the 1.7 ± 0.2 MeV gate.

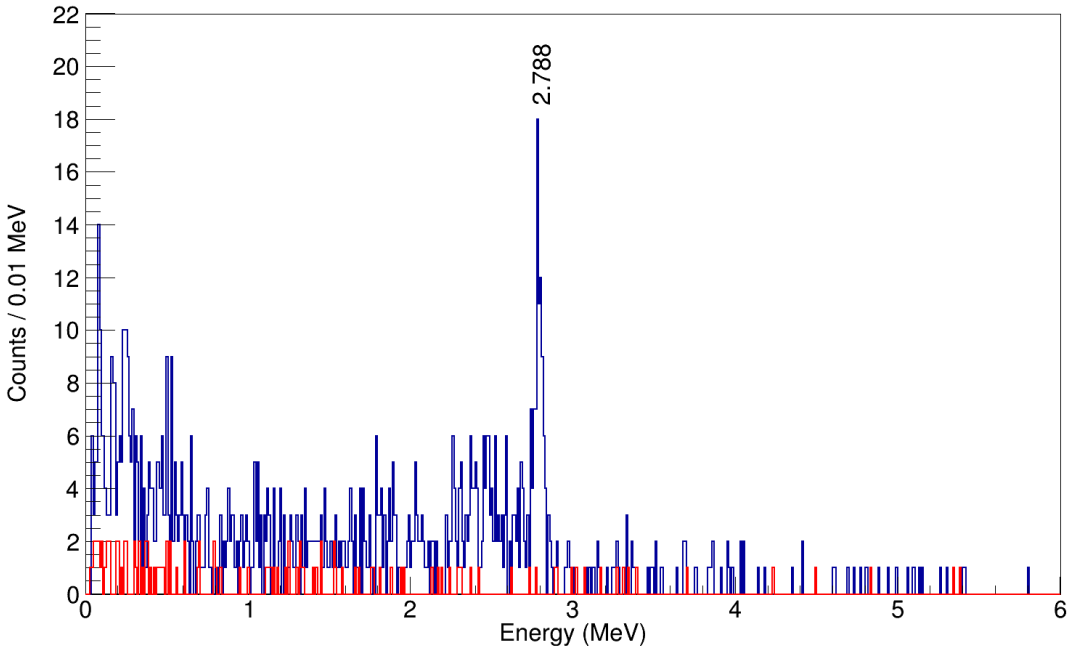

FIGURE 4.34: The γ-ray energy spectrum when gated on 2.914 ± 0.2 MeV (blue). Background (red) is for the 1.7 ± 0.2 MeV gate.

The state at 2.914 MeV is included in the analysis because that state had already been seen to exist. The state is known to decay through the 0.089 MeV energy level to the ground-state meaning that the γ-rays of energy 2.825 and 0.089 MeV are expected to be seen [11]. However, Figure 4.34 shows there is no evidence for these γ-rays, suggesting that this state was not populated during this experiment. There is an overlap in the energy range used to gate on the 2.914 MeV state and the nearby 2.788 MeV state which results in the observation of the 2.788 MeV γ-ray shown in the figure. Figures 4.33 and 4.34 also show the the Compton edge of the 2.788 MeV peak at $E_\gamma \sim 2.554$ MeV. These Compton scattered γ-rays are not suppressed because they are scattered out of the front face of the detector and so are not detected by the BGOs surrounding clover detectors. Additionally, back scatter peaks are also seen at low energies.

As with the 2.788 MeV state, there is a state that is strongly populated at 3.455 MeV. The γ-ray spectrum found when gating on this energy is shown in Figure 4.35 and clearly shows γ-rays at 1.039 and 2.416 MeV showing that the excited state decays through the 2.416 MeV state.

Figure 4.36 shows the spectrum when gating on the 3.995 MeV energy region and by gating on the angular range between 117° and 145°. Despite losing counts by adding the additional angle gate, two peaks are still visible at 1.207 and 2.788 MeV showing that the 3.995 state decays via the 2.788 MeV state to the ground-state. The inset shows the spectrum obtained when no angle gate is applied and shows the γ peaks associated

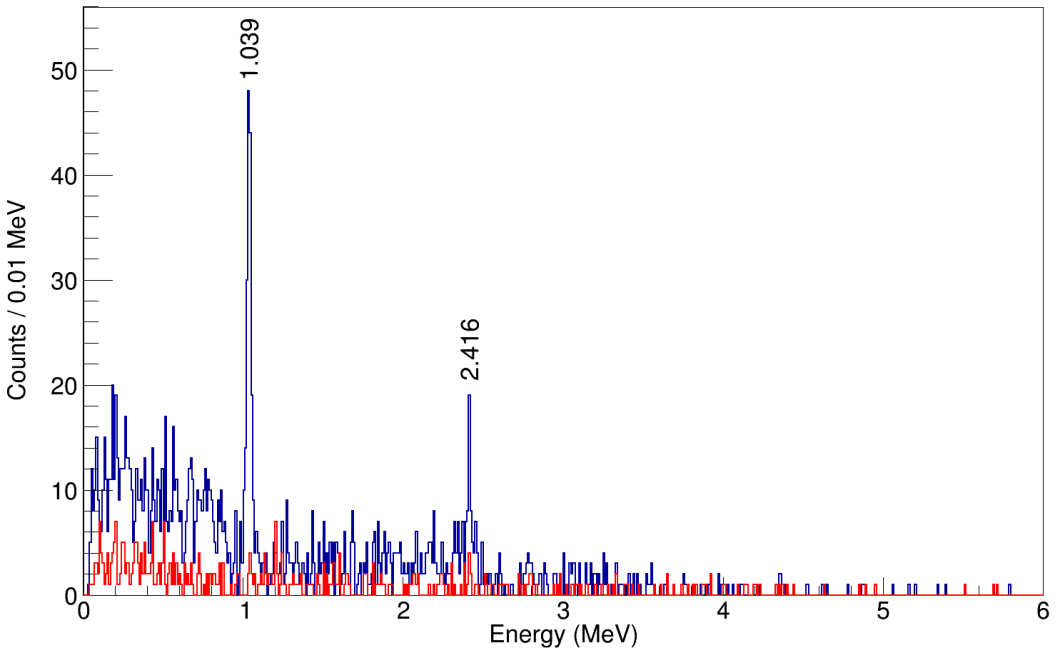

FIGURE 4.35: The γ-ray energy spectrum when gated on 3.455 ± 0.2 MeV (blue). Background (red) is for the 4.5 ± 0.2 MeV gate.

with with the 3.455 MeV state. This figure demonstrates the effectiveness of using the angular resolution provided by the SHARC array to distinguish between different states that are close together.

Figure 4.37 shows the γ-ray energy spectra gated at an excitation energy of 4.132 MeV. At this energy there is some evidence for a γ-ray with $E_\gamma = Ex$ suggesting there may be a state at this energy that decays directly to the ground-state. However, the efficiency of the HPGe detectors is low at these energies and so the count rate is not much higher than the background level (displayed in red) making it hard to determine with certainty that a state at this energy was seen in this experiment.

Figure 4.38 shows the γ-ray energy spectrum for the 5.22 MeV state gating on the angular range of $\theta = 113 - 137$. This angular range was used to try and minimise the contribution of any γ-rays that might be seen from the nearby state at 5.85 MeV. The inset shows a spectrum gated angular range of $\theta = 90 - 180$ and shows evidence for peaks at 2.416 and 2.804 MeV, which suggests that the 5.22 MeV state decays to the ground-state via the 2.416 MeV state. However, the 2.804 MeV peak is only visible in the inset, which looks at the whole angular range. The 2.804 MeV γ-ray is included in Figure 4.43 as a dashed line to indicate that it has been seen, but its connection to the 5.22 MeV state is uncertain since it disappears at $113° - 137°$.

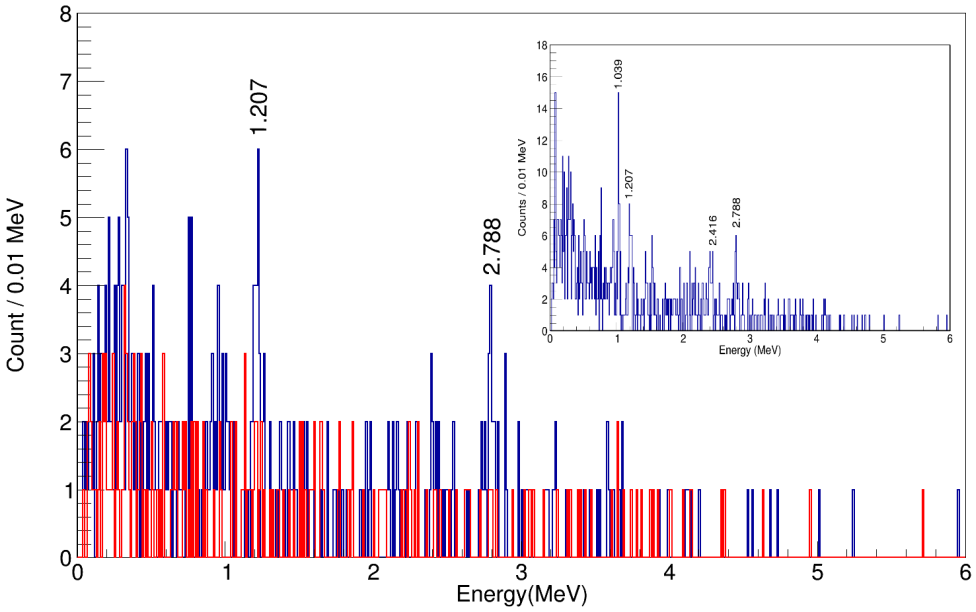

FIGURE 4.36: The γ-ray energy spectrum when gated on 3.995 ± 0.2 MeV and angular region of $\theta = 117 - 145°$ (blue). Background (red) is for the 4.5 ± 0.2 MeV gate. The inset shows the γ-ray energy spectrum gated on $\theta > 90°$.

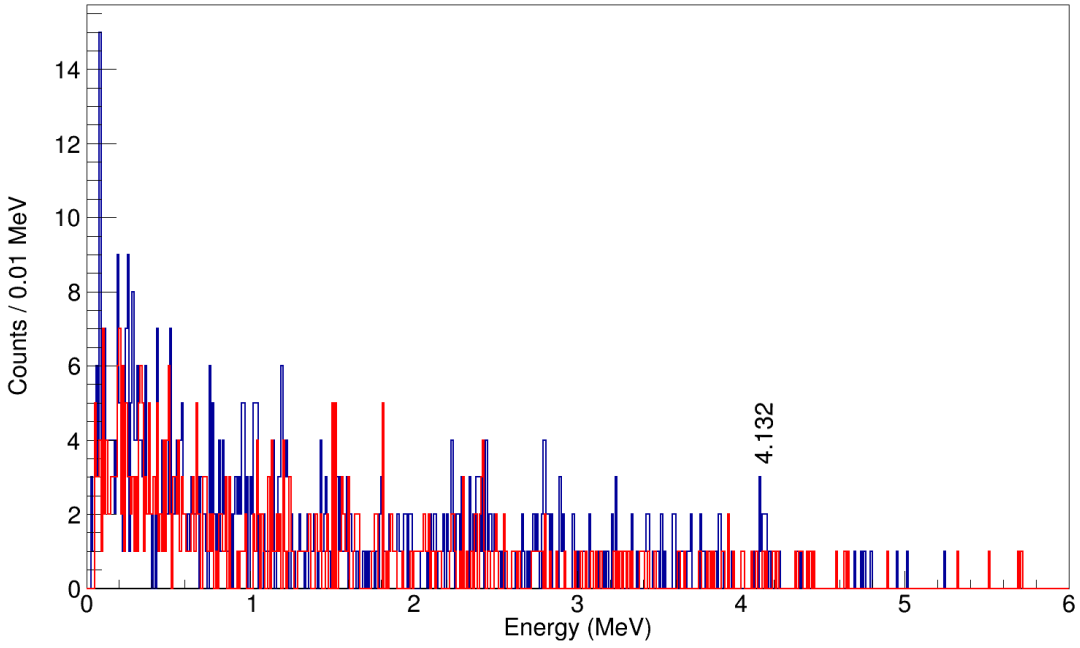

FIGURE 4.37: The γ-ray energy spectrum when gated on 4.132 ± 0.2 MeV (blue). Background (red) is for the 4.6 ± 0.2 MeV gate.

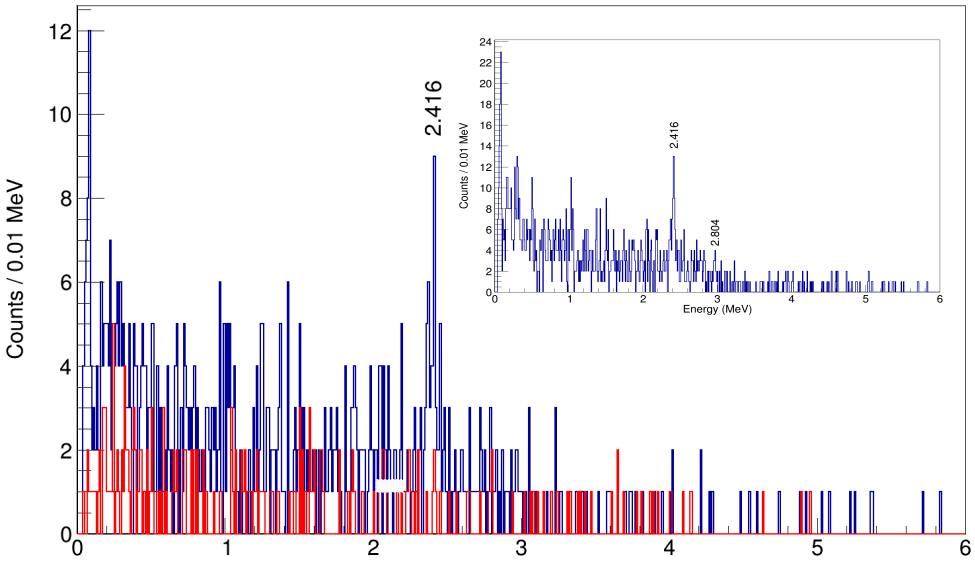

FIGURE 4.38: The γ-ray energy spectrum when gated on 5.22 ± 0.2 MeV and angular region of $\theta = 113 - 137°$ (blue). Background (red) is for the 4.5 ± 0.2 MeV gate. The inset shows the γ-ray energy spectrum gated on $\theta > 90°$.

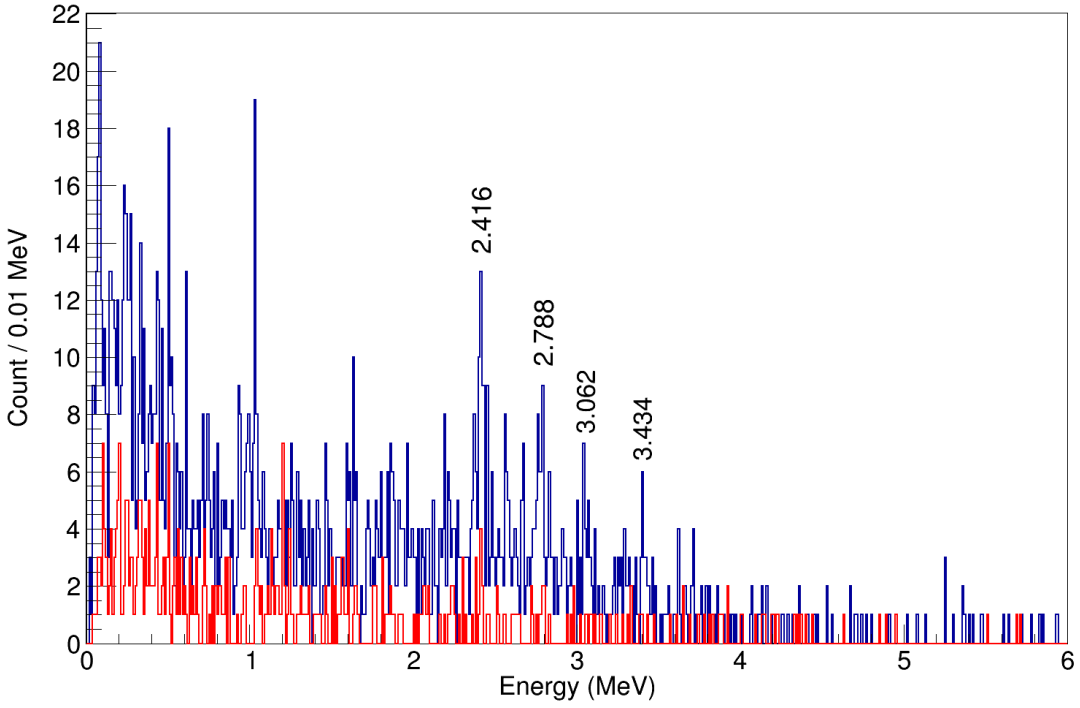

FIGURE 4.39: The γ-ray energy spectrum when gated on 5.85 ± 0.2 MeV (blue). Background (red) is for the 4.5 ± 0.2 MeV gate.

The γ-ray energy spectrum when gated around an excitation energy of 5.85 MeV is given in Figure 4.39. Two γ-ray chains can be observed in this spectrum: one decaying to the ground through the 2.416 MeV state and emitting a γ-ray at 2.416 and 3.434 MeV, and a second decay branch through the 2.788 MeV state which emits 2.788 and 3.062 MeV γ-rays.

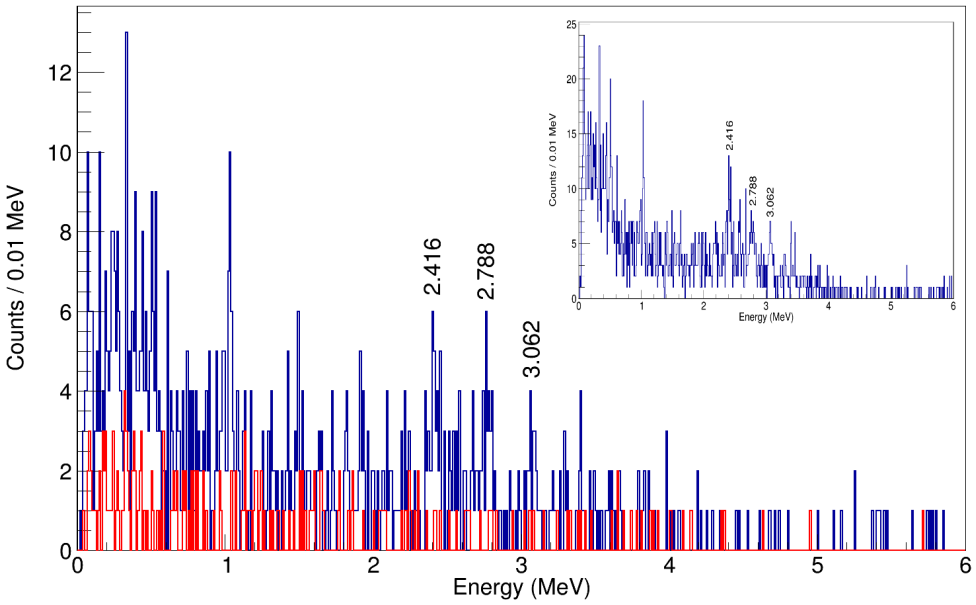

FIGURE 4.40: The γ-ray energy spectrum when gated on 6.005 ± 0.2 MeV and angular region of $\theta = 103 - 119°$ (blue). Background (red) is for the gate 4.5 ± 0.2 MeV. The inset shows the γ-ray energy spectrum gated on $\theta > 90°$.

A state at an energy of 6.005 MeV was used in order to fit the excitation spectrum as described in Section 4.4.3. However, Figure 4.40 does not reveal any γ-rays at this energy region apart from those also seen for the 5.85 MeV state as shown in Figure 4.39. This remains true even when the contamination caused by the 5.85 MeV state is minimised by gating on the angular range between 103° and 119°.

Gating on the excitation energy around 6.55 MeV yields the γ-ray energy spectrum shown in Figure 4.41. Four γ-ray peaks are identified in this spectrum at 1.039, 2.416, 3.095 and 4.134 MeV. This indicates two decay chains taken by the state at 6.55 MeV to the ground-state via the 2.416 MeV state (emitting the 4.134 MeV γ-ray to the 2.416 MeV state, and then decaying to the ground-state), and via the 3.455 MeV state (by emitting the 3.095 MeV γ-ray and then following the same decay path observed for the 3.455 MeV state).

The state at 7.48 MeV was included in the analysis in order to provide an adequate fit at that energy in the excitation energy spectrum as is described in section 4.4.3. However,

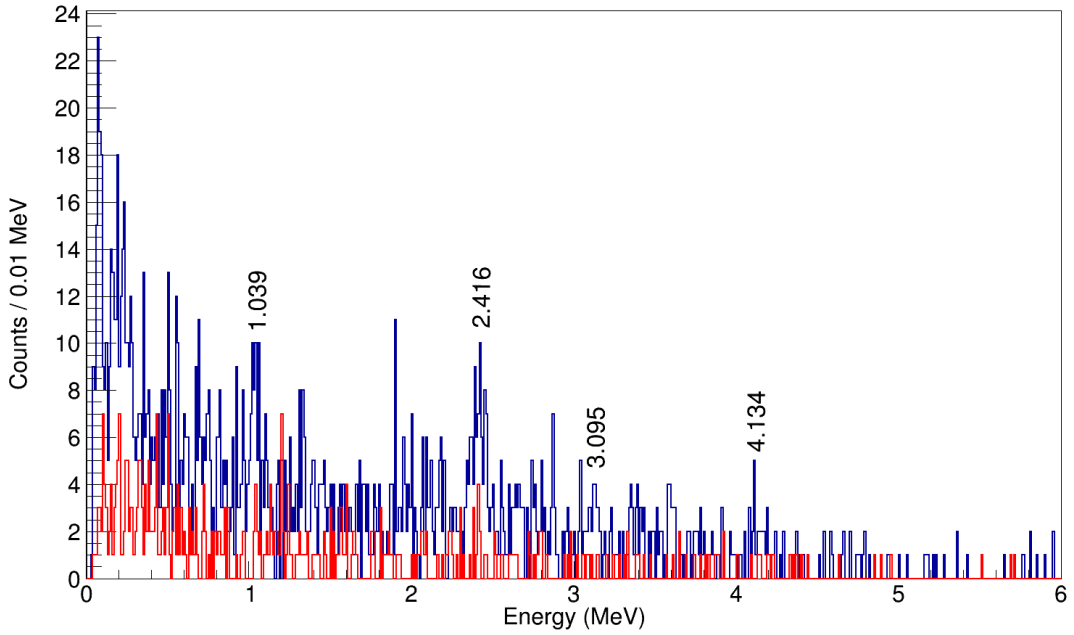

FIGURE 4.41: The γ-ray energy spectrum when gated on 6.55 ± 0.2 MeV (blue). Background (red) is for the 4.5 ± 0.2 MeV gate.

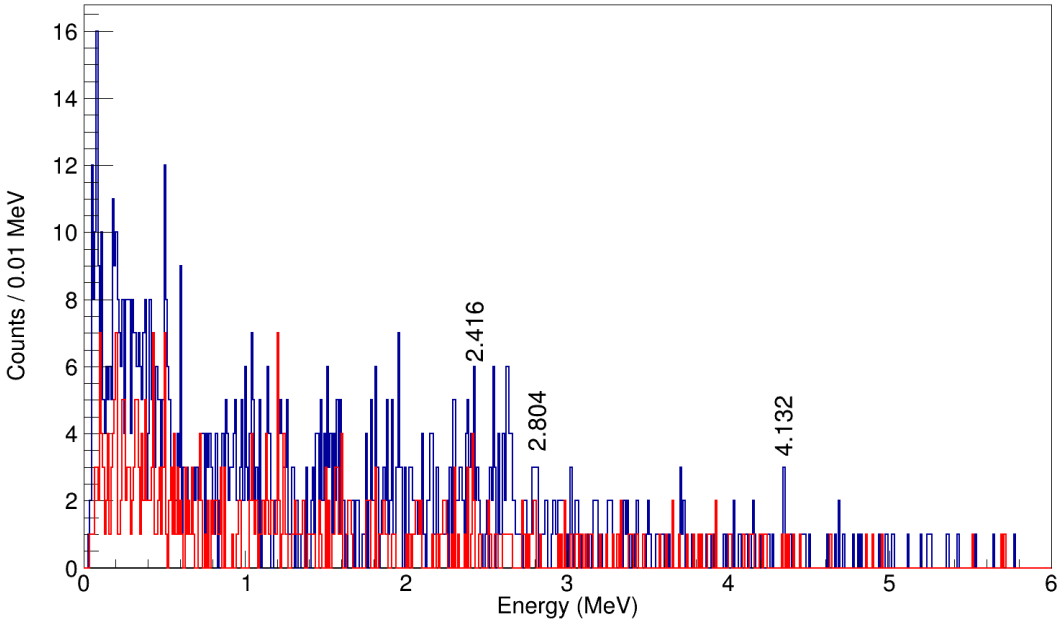

FIGURE 4.42: The γ-ray energy spectrum when gated on 7.48 ± 0.2 MeV (blue). Background (red) is for the 4.5 ± 0.2 MeV gate.

Figure 4.42 does not show any γ-rays that total 7.48 MeV. As a result, it is difficult to specify the energy of this state with precision; 7.48 MeV is therefore an approximation of the energy of this state and is deduced simply from the excitation energy fitting. Although Figure 4.42 does not show direct evidence of a state at 7.48 MeV, it does show γ-rays at 2.416 and 2.804 MeV, which could suggest a decay through the 5.22 MeV state. A peak at 4.132 MeV is also seen, adding to the credibility of the state at 4.132 MeV existing.

Some peaks were difficult to place because they came from relatively weakly populated states, or they came from states that were fairly close in energy to an already identified state, but decayed via a different pathway. These γ-rays were identified while examining a smaller subset of the data. While perfoming the fits on the excitation energies, as described in Section 4.4.3, the data were examined as a function of angle. Some peaks grew in strength relative to surrounding peaks at certain angles, allowing for those γ-rays to be identified more clearly when compared to surrounding peaks.

A final energy scheme was determined using the data collected from the γ spectra and is shown in Figure 4.43.

The γ spectra at angles $\theta_{Lab} < 90°$ were also examined. The spectrum over this range is shown in Figure 4.44. These gamma-rays are not associated with the ^{24}Na$(d,p)^{25}$Na reaction because SHARC is not sensitive to protons from this reaction between 0° and 90°.

These peaks originate from ^{24}Na particles that are inelastically scattered and decay in flight. The peak at 1.512 MeV is the γ-ray emission from the 5^+ state at the same energy in ^{24}Na, which decays to the ground-state. Also shown is a peak at 0.869 MeV which is associated with the γ-ray cascade from the 2^+ state at 1.341 MeV to the 1^+ state at 0.472 MeV. The γ-ray emission from the $1-+$ state to the 4^+ ground-state is not seen because because the half life of the state is long and so the particle does not decay until after it has passed through the detector. The peak seen in this region is therefore not caused by the decay of the 1^+ state, but is instead the result of the 0.511 MeV peak associated with an electron being Doppler shifted when detected in the 135° detector ring in TIGRESS.

4.4.2 Particle Spectra

Figure 4.20 shows the excitation energy spectrum of the ^{25}Na nuclei. The dashed lines represent the positions of the initial estimates of the main energy states that are populated during the (d,p) reaction. These estimates were used as starting values as to which

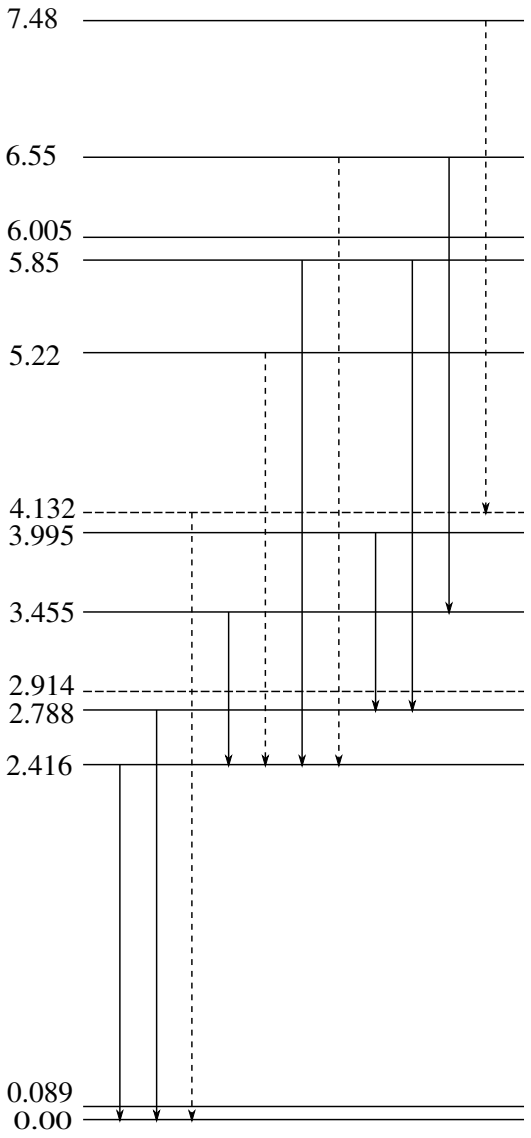

FIGURE 4.43: Final level scheme of ^{25}Na and the γ-ray cascades. Dashed lines represent transitions that remain tentative due to lack of statistics.

energies should have gates placed to look at the γ-ray energy spectrum. Observing the γ peaks in these gated spectra allowed for a more accurate estimate as to the energy observed. This iterative process, coupled with the previously known information about the shell structure of ^{25}Na [8] gave enough information to allow an attempt at fitting the excitation spectra in Figure 4.20. The degree to which this fit correctly reproduces the shape of the excitation energy spectrum gives more information as to whether or not an energy peak is missing from the fit.

Viewing the particle spectra when gated on a γ-ray provided information about a particle that was detected in coincidence with the the gated γ event. An example is shown in

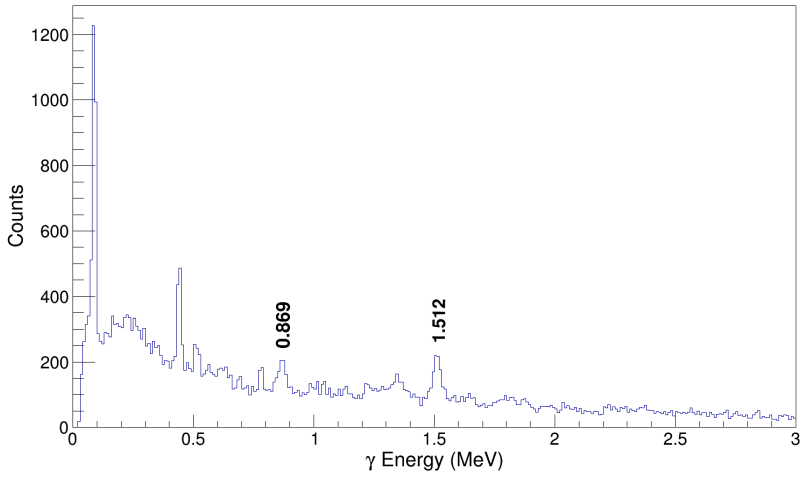

FIGURE 4.44: Gamma-ray energies when gated on protons detected at $\theta < 90°$.

Figure 4.30 which shows the particle excitation energy spectrum gated on the 2.788 MeV γ peak. Here it can be seen that the γ-ray is associated with an excited state of 2.788 MeV meaning that this state decays directly to the ground-state (as was seen in Fingure 4.29). There also appears to be a peak at ~ 4 MeV and evidence of several less clearly defined peaks at > 5 MeV. Some peaks exist at an energy higher than that of the γ-ray used for gating, suggesting that there are excited states that decay through the 2.788 MeV state. This information is used to try and find other γ-rays arising from these higher excitation energies.

Using both the particle and γ energy spectra, a level scheme was constructed. This is shown in Figure 4.43. Here states and γ-rays which have some evidence of existing, but could not be confirmed due to a lack of statistics are represented as dashed lines. The excitation energies identified for states in ^{25}Na were then used as the basis for the fitting algorithm implemented in Section 4.4.3.

4.4.3 Fitting the Excitation Energy Spectra

The energy values of the peaks seen in Figure 4.20 were discerned with the help of the γ-ray analysis described in Section 4.4.1. However, in some cases, it was difficult to conclude which energy states were being populated using the γ spectra alone. The fitting of the excitation spectrum therefore took place in tandem with the analysis performed on the γ-ray data in order to cement the understanding of the states.

Performing a simple Gaussian fit on each of the peaks that can be seen is not an appropriate method for this task as it allowed the fitting program too much freedom to adjust the parameters to match the histogram. That is, the statistics and the resolution

Excited State (MeV)
0.000
0.089
2.41
2.788
2.914
3.455
3.995
5.22
5.39
5.85
6.005
6.55
7.48

TABLE 4.6: Final excited states used in fitting particle spectra data.

were not sufficient to fit the spectrum reliably without further constraints. Instead, the equation used to fit was,

$$f(E) = \sum_{i=1}^{n} \left(a_i \exp\left(-\frac{1}{2} \frac{(E - (\Delta E + E_i))^2}{\sigma_i^2} \right) \right) + h(E), \tag{4.27}$$

where E_i is the energy of the peak, $h(E)$ is a linear background of the spectrum, and a_i is the amplitude of the ith peak. The values of the energy of each peak were adjusted over the course of this analysis as and when it became clear that these peaks were not needed in the fit, or if a peak was discovered to be missing. The final values for E_i are listed in Table 4.6.

Equation 4.27 is an adjusted Gaussian equation which allows some parameters to be fixed while allowing for some small variation needed to perform the fit. The ΔE represents a small shift allowed in the position of the peak. This shift was not fixed, but was limited to ± 0.1 MeV and was constant over each peak, meaning that the resulting fit was forced to place a peak close to the estimated values, but was allowed to compensate for a systematic error that might have occurred in a previous stage of the analysis. The value of σ of each peak was limited to be a function of energy, such that

$$\sigma_i = g(E_i) = mE_i + c. \tag{4.28}$$

The linear term, m, was forced to be positive in order to represent the decrease in energy resolution as energy increases due to the energy loss in the target.

The constants, a_i, determine the heights of the fitted peaks. This parameter was set to be greater than 0 since allowing the value to be negative was non-physical. Allowing the fitting program to do so gave it the freedom to artificially reduce the width of a neighbouring peak by subtracting counts. As a result, a requirement for a_i to be positive was placed on the parameter. The addition of this meant that the fit could assign a value of zero to the peak, inferring that the state at this energy was not being populated, but not allowing the program to change the shape of the function to create a falsely appropriate fit.

The evidence seen for the previously known states in ^{25}Na below 4.5 MeV was fairly strong when considering the γ-ray data. There was also little evidence to suggest that there were any previously unknown states occurring in this energy region. These two factors meant that the peaks below this energy could be used as a test to ensure that this part of the analysis was working as intended before analysis on the higher – and less well understood – energy states was carried out. Once the process for fitting the peaks seen below 4.5 MeV had been perfected, the entire observed energy range was fitted.

Figure 4.20 shows the data for the excited states over the entire angular range of the box and CD detectors. Since finding the angular distribution of individual states is important for finding the spectroscopic factors of those states (as described in section 5.2), it is not useful in this work to fit these data without first separating the data into different angle bins. The fitting algorithm was therefore applied several times for different angles. The original angle bins where set to a width of 8° which spanned the angular range covered by the box detectors ($95° - 143°$) and the CD detectors ($148° - 172°$). The fits produced with this are shown in Figure 4.45.

This first step in fitting the excitation spectra allowed for the value for σ to be dependent on energy. This assumption was checked by examining the values of m and c in Equation 4.28 at different angles. This revealed an average energy coefficient of ~ 0.005 and a value of c with a typical value of ~ 0.2 which decreased as the angle increased (Figure 4.46). The large difference in magnitude between m and c and the fact that there was a clear relationship between σ and the angle of detection suggested that the energy does not play a key role in the widths of the peaks in the particle spectra.

The relationship between σ and angle was investigated by substituting the appropriate values of m and c into Equation 4.28 and using $x = 3.1$ at various values of θ and fitting the results. This value of x was used because the peaks at 2.788 MeV and 3.455 MeV were well defined at every value of θ. It is therefore reasonable to assume that the fits of the histograms around this energy will be the most reliable. A σ that is a function of angle is likely to have a differential of zero at 180° for reasons of continuity. The data

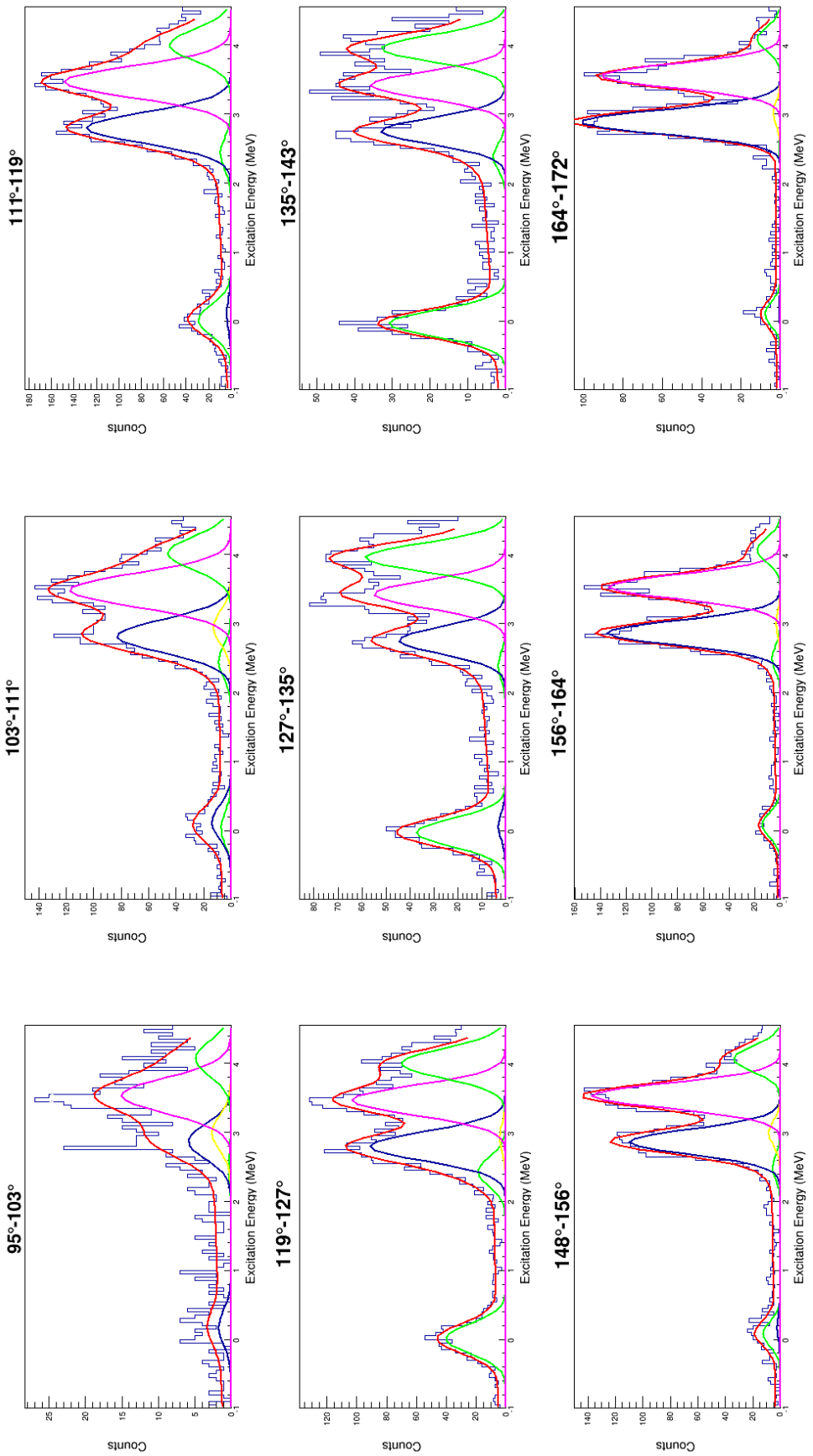

FIGURE 4.45: First attempts at fitting the excitation spectra for different angle bins before the restraint on peak widths was refined. The overall fit (red line) and the contributing peaks are shown.

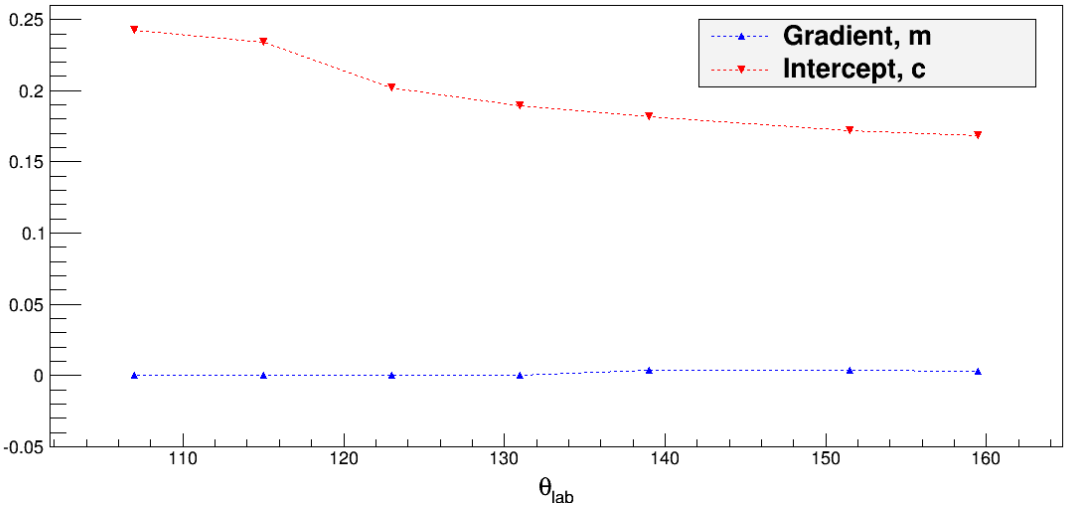

FIGURE 4.46: Comparison between the magnitude of the two parameters used to describe the energy dependence of σ (Equation 4.28).

appear to confirm this as the intercept line in Figure 4.46 flattens out as θ_{Lab} approaches 180°. An equation with this continuity condition was used to fit the data,

$$\sigma = a(\theta - 180)^2 + b, \tag{4.29}$$

where $a = 0.0000128$ and $b = 0.171$ and θ is the lab angle. The physical reason that the energy peak broadens at values close to 90° is related to the target material traversed by protons from reactions at the back of the target. An argument could be made that the function to describe the data should be trigonometric in form, but the quadratic function in Equation 4.29 was used instead because it fit the data perfectly well.

The shift parameter, ΔE, used in Equation 4.28 was used to allow the fitting algorithm freedom to shift the input values for the peaks. The peaks being fitted at this stage in the analysis (between 0 MeV and 4.5 MeV) have already been documented in literature. This is important to note because it means that the energies of these peaks are not in dispute. Therefore, if the fitting algorithm returns a non-zero result for ΔE, it would suggest that there was an error in the fitting equation or that there is a systematic error included in the analysis prior to this stage (for example, an error in the assumed thickness of the target). This shift was constrained to be constant over all peaks for each angle. The amplitudes of the shifts are listed in Table 4.7 and plotted in Figure 4.47. There is a clear trend in the shift parameter for both the Box and CD detectors. This suggests that there is in fact a small but identifiable systematic error in the analysis and that it is a different error for both the CD and the Box detectors. The inclusion of this

Detector	θ_{Lab} (°)	ΔE (MeV)
Box Detectors	101	0.08 (5)
	105	0.04 (2)
	109	0.03 (2)
	113	0.02 (2)
	117	0.008 (14)
	121	0.02 (1)
	125	0.01 (1)
	129	0.007 (2)
	133	−0.05 (1)
	137	−0.06 (3)
	141	−0.03 (2)
CD Detectors	152	0.078 (8)
	160	0.080 (7)
	168	0.097 (8)

TABLE 4.7: Values of the fitted shift parameter, correcting for systematic errors, as a function of angle in the upstream Box and CD detectors. There are plotted in Figure 4.47.

shift parameter in the fitting process compensates for any small error that has occurred in the analysis, without the need to identify the source of the error.

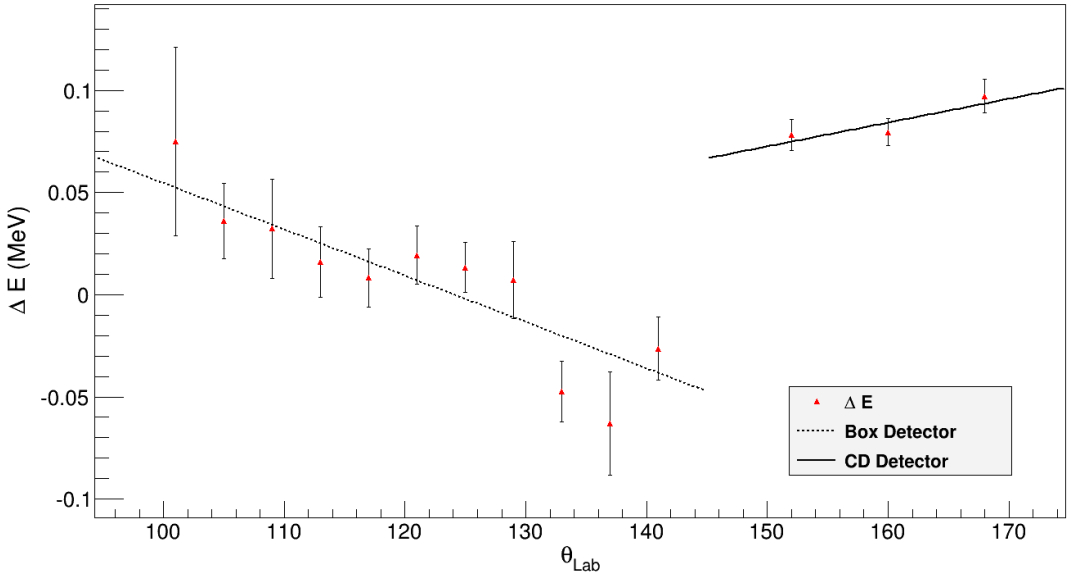

FIGURE 4.47: Values of the fitted shift parameter, correcting for systematic errors, as a function of angle in the upstream Box and CD detectors.

The number of counts under the fitted peak is required in order to calculate the differential cross sections of each peak. The integral of each peak can be calculated after the fit has been performed, but the errors in the fitting parameters could not give the error in the area without a modification. Equation 4.27 has to be modified in order to make the area one of the variables in the fitting equation.

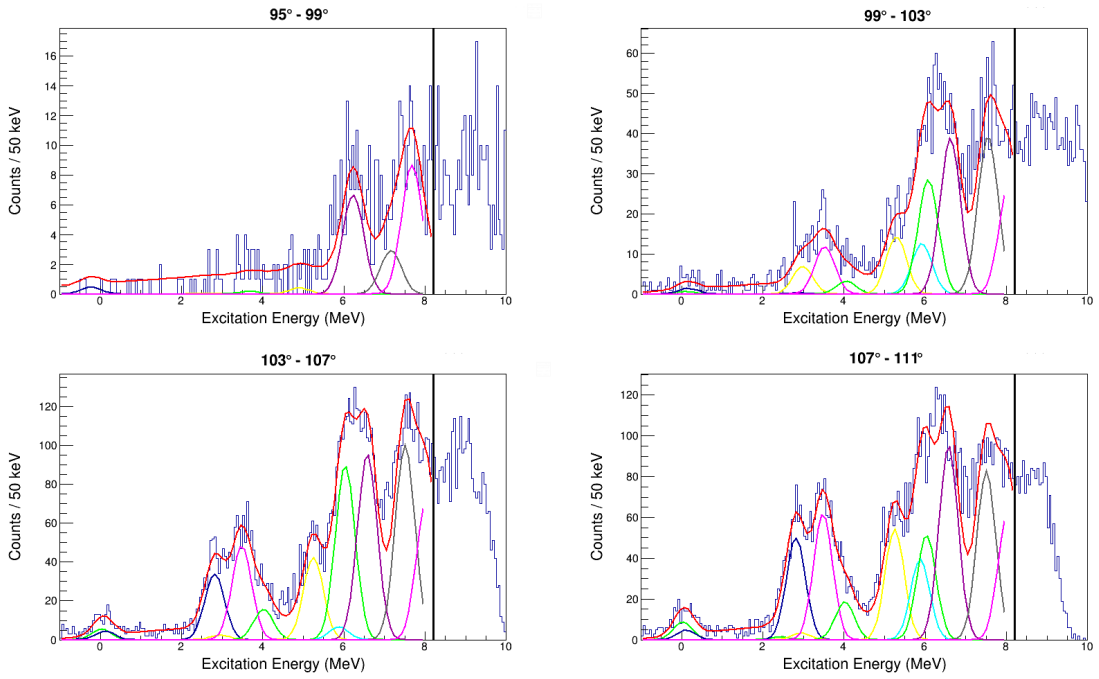

FIGURE 4.48: Final fits between 95° and 111° for the downstream box detector. The total fit (red) and the contributing peaks are shown.

The area, A, of a Gaussian peak is given by

$$A = a\sigma\sqrt{2\pi}, \tag{4.30}$$

where a is the amplitude and σ is the standard deviation of the Gaussian peak. Rearranging this and substituting into Equation 4.27 gives:

$$f(E) = \sum_{i=1}^{n} \left(\left(\frac{A_i}{\sigma\sqrt{2\pi}} \right) \exp\left(-\frac{1}{2} \frac{(E - (\Delta E + E_i))^2}{\sigma^2} \right) \right) + h(E) \tag{4.31}$$

Making A_i in Equation 4.31 an adjustable parameter in the fitting equation allows the number of counts under a peak and the error in this value to be extracted directly.

Once the fitting process had been perfected for this range of energies, the fit range was increased to include the whole energy range seen in this experiment. The shifts shown in Table 4.7 were fixed so that they would be included for higher energy peaks. If the fit failed to represent the histogram at higher energies, it suggested that the inputs for the centroid positions of peaks above 4.5 MeV are incorrect, and could then be adjusted in order to fit the data more accurately.

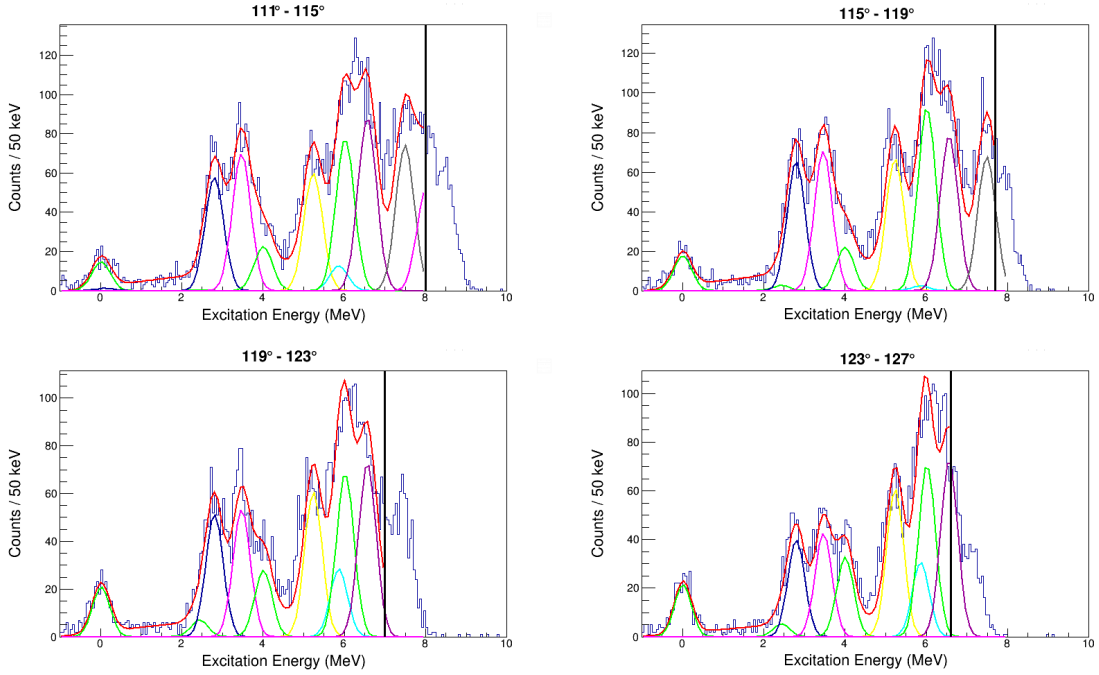

FIGURE 4.49: Final fits between 111° and 127° for the box detector. The total fit (red) and the contributing peaks are shown. The vertical line shows the maximum energy range used in the fit. The value of this energy is discussed in Section 4.4.4.

The first analysis employed 8° binning for the Box and CD detectors as described above, and shown in Figure 4.45. Once the fitting methods were optimised, 4° bins for the Box detector still gave enough counts to give a satisfactory fit to the histogram. The final fits produced for the box detectors at each angle are shown in Figures 4.48, 4.49 and 4.50. The final fits for each bin are shown in Figure 4.51. The vertical lines in each of these figures shows the maximum of the energy range used in the fit. These maximum energies derive from the lower threshold on energy as set in the silicon detectors and are discussed in Section 4.4.4.

4.4.4 DSSSD Thresholds

The threshold energy of the SHARC detectors was mistakenly placed at a higher setting than optimum during the experiment. The effect of this can be seen in Figure 4.18, where there is an obvious cut-off in the data below 2 MeV for the box detectors. This threshold cut-off effect is also seen in Figure 4.19 where energy states at high levels are progressively cut off as the angle increases. This is also seen in the CD detectors, where the thresholds were set to 2 MeV for three of four detectors, with the threshold for the remaining detector being set to 1.5 MeV. This means that there is limited angular distribution data for higher lying energy states.

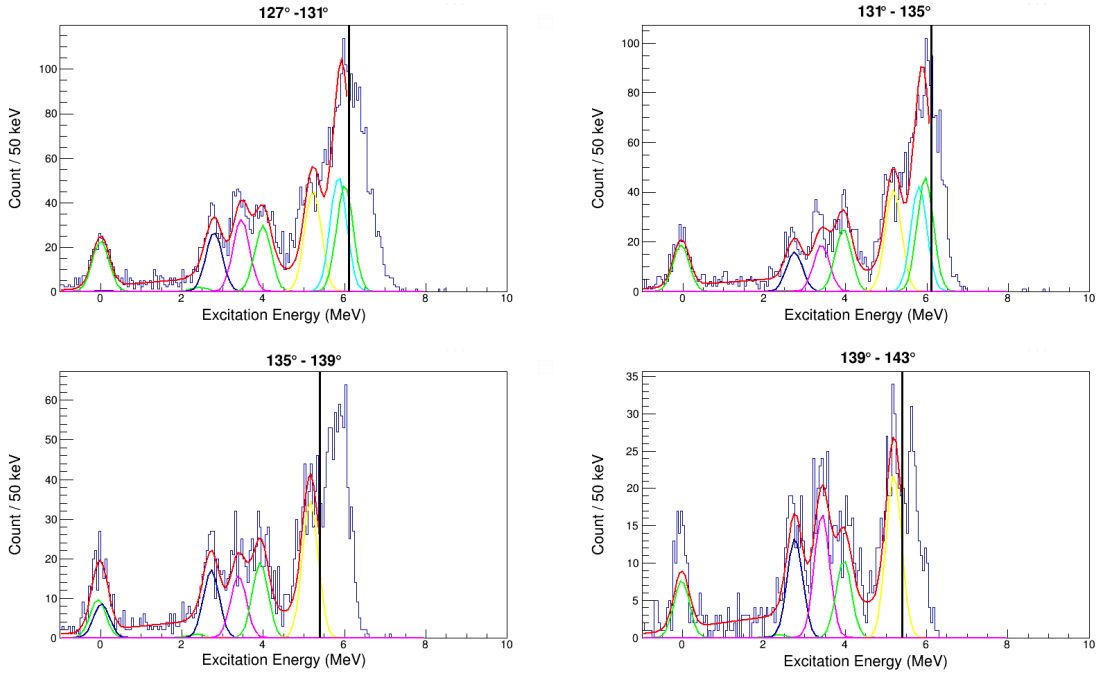

FIGURE 4.50: Final fits between 127° and 143° for the box detector. The total fit (red) and the contributing peaks are shown. The vertical line shows the maximum energy range used in the fit. The value of this energy is discussed in Section 4.4.4.

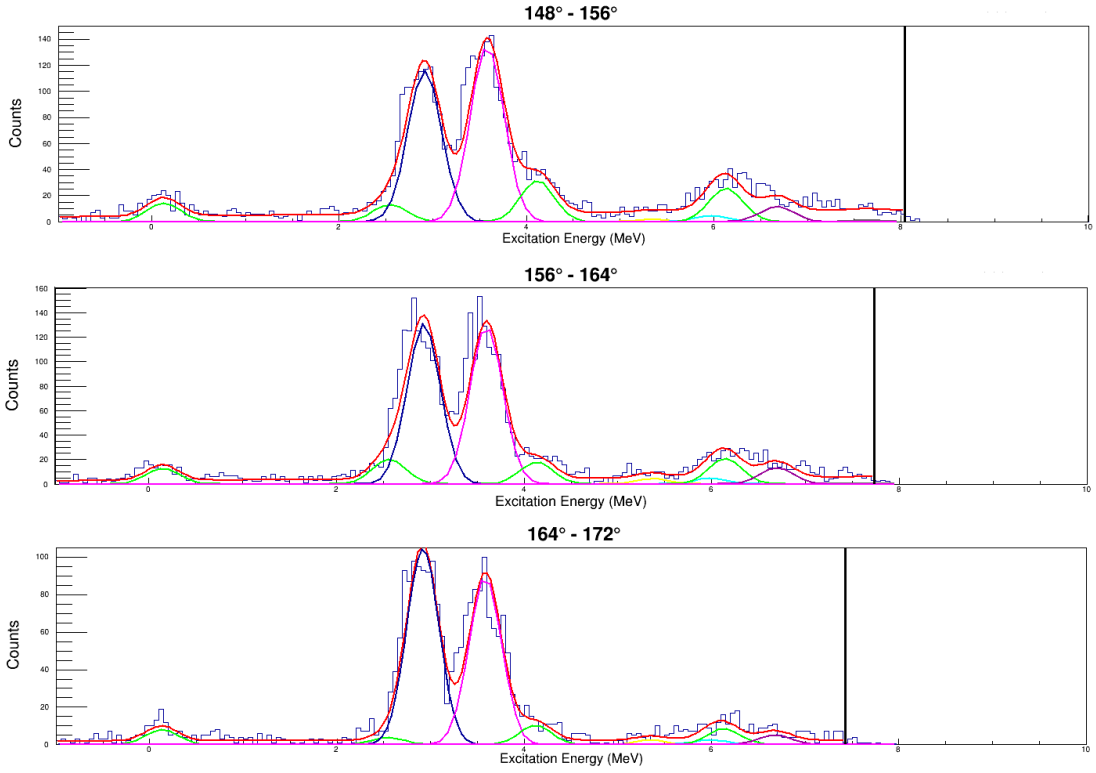

FIGURE 4.51: Final fits found for the entire range of the CD detector. The total fit (red) and the contributing peaks are shown. The vertical line shows the maximum energy range used in the fit. The value of this energy is discussed in section 4.4.4

The excited energy peaks near the cut-off are affected by the drop off in effective solid angle (see Figure 4.7) since the detector rapidly becomes less efficient at detecting particles as angle increases. This rapid change means that the measured number of counts in an excited state peak near the threshold cut-off is unreliable and should not be used in further analysis to determine the spectroscopic factor of the state. A protocol was devised for the case of the upstream box detector and the CD detectors in order to determine which energy peaks were suitable to continue to be included in the analysis.

The protocol decided for the box detectors will be discussed first, since it is the most complicated. A function for how the threshold cut-off energy, $E_{Threshold}$, varied with angle was established by measuring the angle at which the energy efficiency of the detector started to drop off appreciably for each energy level. The position at which this happens can be seen visually in Figure 4.7, and

$$E_{Threshold} = a\theta^2 + b\theta + c, \tag{4.32}$$

where $a = 0.001788$, $b = -0.5618$ and $c = 0.1756$. An energy peak will have a distribution of 2σ where σ is given in Equation 4.29. For example, consider a peak with an energy, E_1, and a width, $2\sigma_1$. If E_1 is less than $2\sigma_1$ above $E_{Threshold}$ at a given θ, it will contribute counts to the excitation spectra. In this situation, it is impossible to know how many counts are being contributed to the spectrum because there is no information available as to the height of the peak at E_1. This means that if a second peak with a centroid energy E_2 has the conditions $E_2 < E_{Threshold}$ and $E_2 > E_1 - 2\sigma_1$, then there will be an indeterminate number of extra counts of in peak E_2. In this case, peak E_2 cannot be included further in the analysis because it is not possible to obtain a reliable value for counts in the peak. The boundary at which peaks will fail to be applicable to be used in the analysis, which shall hereby be referred to as the 'analysis limit function', is shown in Figure 4.52. The value of the highest energy level not excluded by the analysis limit function for each angle bin is given in Table 4.8, which shows that peaks below 5.22 MeV never get excluded from the angular distribution analysis.

This reasoning, however, creates a problem: if peak E_2 is excluded, then any peak that has a peak value greater than $E_2 - 2\sigma_2$ must also be excluded from further analysis for the same reasons. To avoid this, peaks were excluded from the analysis, but not from the fitting range used to fit the excited peaks. Extending the fit range past the analysis limit line in Figure 4.52 gives the fitting algorithm freedom to fit the counts measured for the E_2 peak, and therefore allows the next lowest to be fitted without being affected by any unknowable counts.

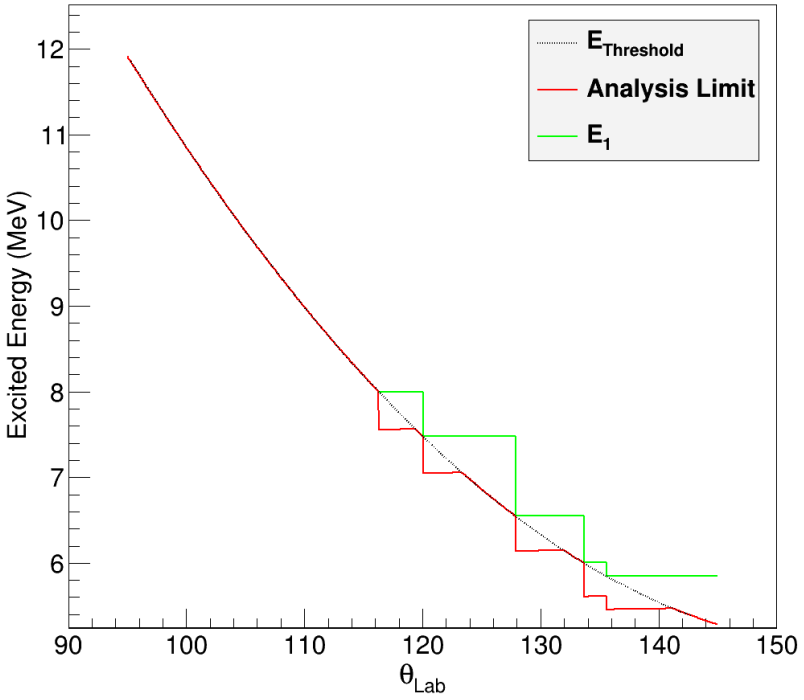

FIGURE 4.52: Limit on which peaks can be used in the analysis (red). This limit is always 2σ below the first state energy state above $E_{Threshold}$ (green).

Angle, θ_{Lab} (°)	Highest excited state accepted for further analysis (MeV)	Highest excited state included in the fit range (MeV)	Upper limit of fit range (MeV)
97	7.48	8.0	8.2
101	7.48	8.0	8.2
105	7.48	8.0	8.2
109	7.48	8.0	8.2
113	7.48	8.0	8.0
117	7.48	7.48	7.7
121	6.55	6.55	7.0
125	6.55	6.55	6.6
129	6.005	6.005	6.1
133	5.22	6.005	6.1
137	5.22	5.22	5.4
141	5.22	5.22	5.4

TABLE 4.8: Comparison between the final peaks included for further analysis, and the peaks included in the fits for the spectra given in Figures 4.49, 4.50 and 4.51.

The choice of the upper fitting limit of the graphs produced a new problem. If the value of the limit contained the tail end of a peak, the program would try and fit a Gaussian to this small subset of data in the tail. As a result, the program might misrepresent the strengths of the peaks used in the analysis used to find the spectroscopic factors. Three fit ranges where discussed and used to examine the stability of the fit: the first range extended from -1 to the analysis limit function; the second extended from -1 to $E_{Threshold}$; and the third had a range that was based on a visual examination of the excitation spectra shown in Figure 4.45, and could extend beyond $E_{Threshold}$.

This third method aimed to use as much information available from Figure 4.45 as possible to fit the data. This method does not have a definitive way in which to pick the fit range. Instead it judged the appropriate range bassed on whether or not certain criteria where met. It was decided that if 50% of a peak was within the fitting region then the fitting program should be able to adequately fit a Gaussian to it. In the instance where the centroid position of a peak lands below $E_{Threshold}$ and above the energy given by the analysis limit, then it can be used in the fit, but rejected for further analysis. The fit range used for each angular bin is given in Table 4.8.

Comparing the three fitting methods (Figure 4.53) showed that each fit gave the same results within errors for the majority of points. An exception to this is seen when observing the 5.85 MeV and 6.005 MeV (4.53b) state at 129°. The discrepancy at these points between the 'threshold' upper limit, and the other fitting limits was caused by the tail end of the 6.55 MeV peak being included in the fit which distorted the 5.85 MeV and 6.005 MeV peaks. The other two methods agreed with each other, suggesting that the fitting algorithm was stable. The 'individual' method was used because it used a fit range tailored for each angle bin. In summary, the setting of an a unusually high discriminator threshold caused some difficulty in fitting the region excitation energies close to the threshold, but a robust procedure was developed for dealing with the angle-dependent cut-off in excitation energy that resulted.

Fitting the excitation energy spectrum at different angles in the CD detector was a simpler task. This was essentially because the energy of protons for a given excitation energy has only a weak angular dependence in the CD region. Three of the four CD detectors were set with a threshold of 2 MeV prior to the experiment, causing a cut off effect similar to that described for the box detectors. However, one CD has a threshold of 1.5 MeV, which covers the whole excited energy spectrum for most of the detector (counts can be seen over the whole CD range in Figure 4.19). Only the data from this CD detector were used to fit the excitation spectra above 4.7 MeV (4.7 MeV marking an obvious gap between excited state peaks). Peaks below 4.7 MeV were fitted using all

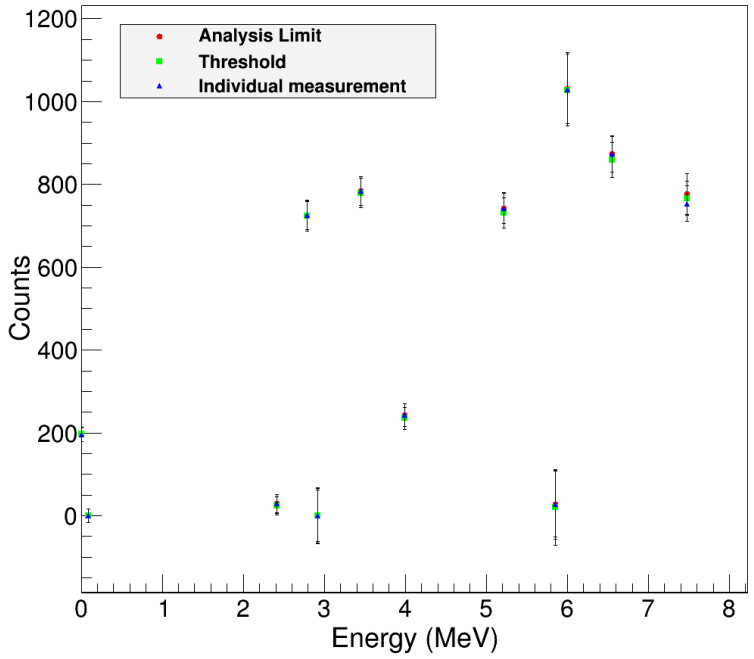

(A)

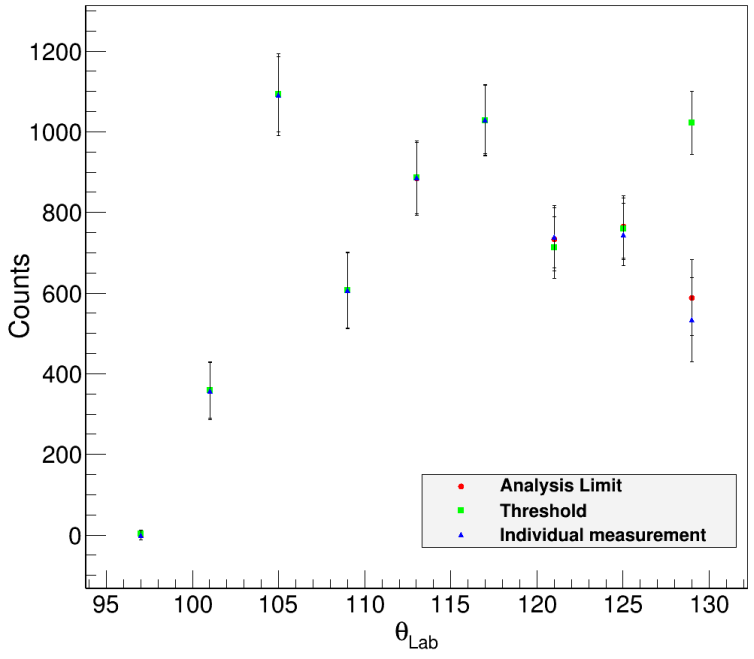

(B)

FIGURE 4.53: (A) Comparison of fitting methods at 117°. (B) Comparison of fitting methods for the 6.005 MeV state.

CD detectors. This required a new value for the solid angle coverage for one CD only, which was calculated using Equation 4.8.

The switch from using all four CD detectors to only using one results in a discontinuity in the graphs being fit because the number of counts detected above 4.7 MeV drops by a factor of four. This drop in counts can be seen in Figure 4.54, which shows the spectrum found for $\theta = 152°$.

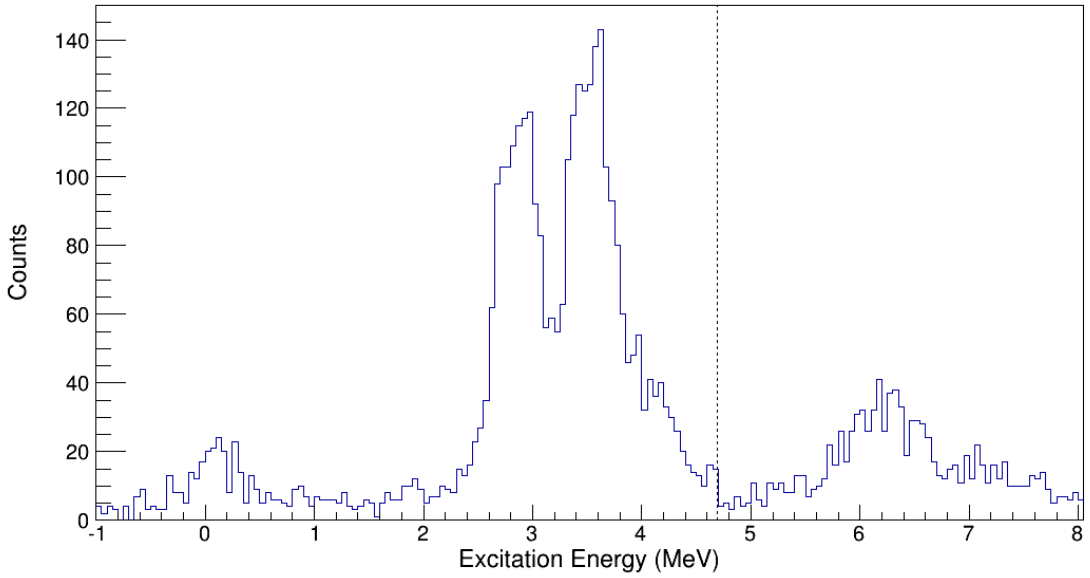

FIGURE 4.54: Discontinuity of counts in the CD detector at the transition between using all of the CD detectors (Energy < 4.7) and only using one detector (Ex > 4.7).

The sudden drop in counts in this region causes the background to be underestimated, which affects the number of counts found in any weak peak close to the 4.7 MeV transition. However, this underestimation of counts was considered the most desirable option for proceeding in the analysis since only using one CD detector for the entire energy range would result in a drop in statistics.

4.4.5 Angular Distributions

The data normalisation was discussed in Section 4.2.5 where a scaling factor was derived that was proportional to the beam current and number of particles in the target. The angular distributions of the differential cross section were found by multiplying this scaling factor by $\frac{N_E}{\mathrm{d}\Omega}$ where N_E is the number of counts in the fitted excited peak at energy E and $\mathrm{d}\Omega$ is the solid angle calculated using Equation 4.8. The graphs showing the angular distributions (differential cross sections) for the energy states observed in the experiment are shown in Figures 4.55 and 4.56.

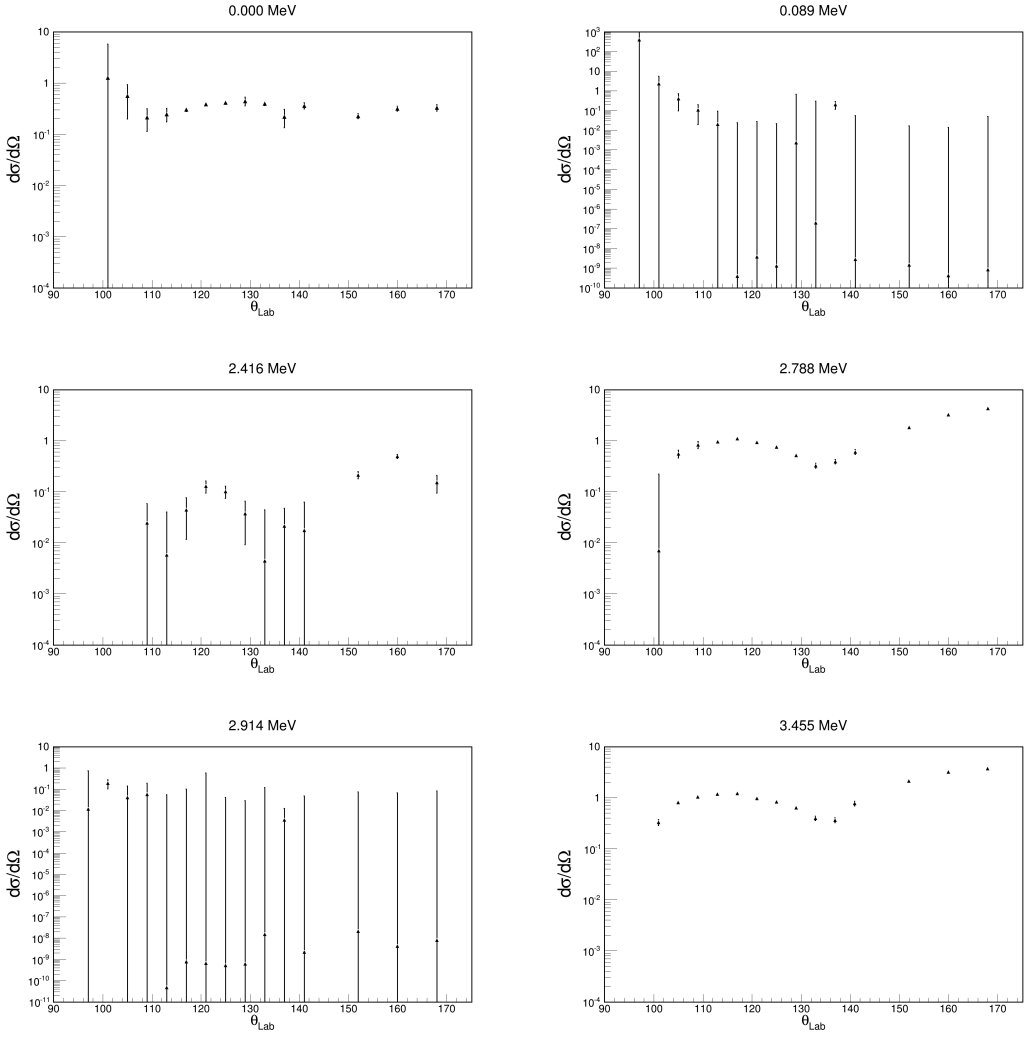

FIGURE 4.55: Differential cross sections of states up to the 3.455 MeV energy state.

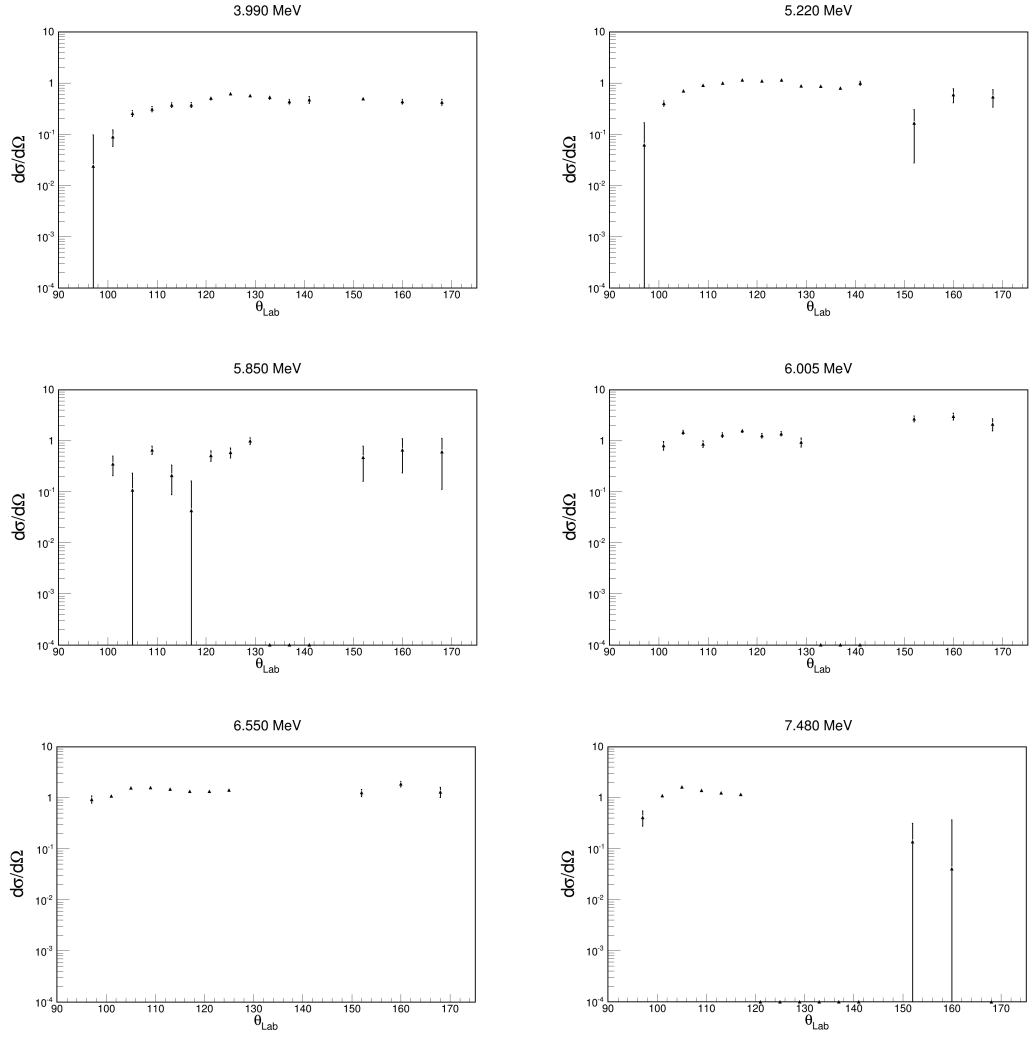

FIGURE 4.56: Angular distributions of states above the 3.455 MeV energy state.

Chapter 5

Results

5.1 Identification of States in ^{25}Na

5.1.1 TWOFNR

The theoretical cross sections for a single-particle state were calculated using the code TWOFNR [68] which used the zero-range ADWA method for different l-transfers at different energies, spins and parities. The input parameters used for the calculations matched those of this experiment: the cross sections were calculated for the ^{24}Na$(d,p)^{25}$Na reaction at 8 MeV/A with a ground-state of ^{24}Na being 4^+. The reaction Q-value for ^{25}Na was given as 6.786 MeV with higher level energy states having Q-values which vary accordingly as the excitation energy increases. The excitation energies used to calculate the Q-values are the excitation energies found from fitting the data as described in Section 4.4.3 and are listed in Table 4.6. The default integration range of $0-30$ fm with steps of 0.1 fm was used with 70 partial waves in the nucleon single-particle radial wave function. Non-locality corrections were not performed. The ADWA Johnson-Soper potential was used for the initial state potential, and the Chapel-Hill optical potential for the out-going proton. The default value for the $\langle p|d\rangle$ vertex constant of $D_0 = -122.5$ MeV fm$^{3/2}$ was implemented, which was treated as zero-range. The parameters for radius, R, and diffuseness, a, in the Wood-Saxon potential (Equation 2.3) were set to 1.25 fm and 0.65 fm respectively, and the spin-orbit strength of l-sigma is 6 MeV. Both the bound state non-locality and the spin-orbit radius parameter were set to zero.

The code outputs four data files containing the points on a graph showing the differential cross section angular distributions for a single-particle state in: a) the centre-of-mass frame, b) the lab frame, c) the centre-of-mass frame for the heavy particle in inverse kinematics, and d) the centre-of-mass frame for the light particle in inverse kinematics.

The profile of the graphs outputted only changed significantly when different values of l were input. Changing input parameters such as the final energy of the reaction alters the scale of graph, or the relative height of the peaks, but does not alter the angle at which the peaks (and troughs) occur in the angular distributions. The general shape of these angular distributions for $l = 0, 1, 2$, and 3, is shown in Figure 5.1 between 90° and 180°, which is the angular range studied in the experiment.

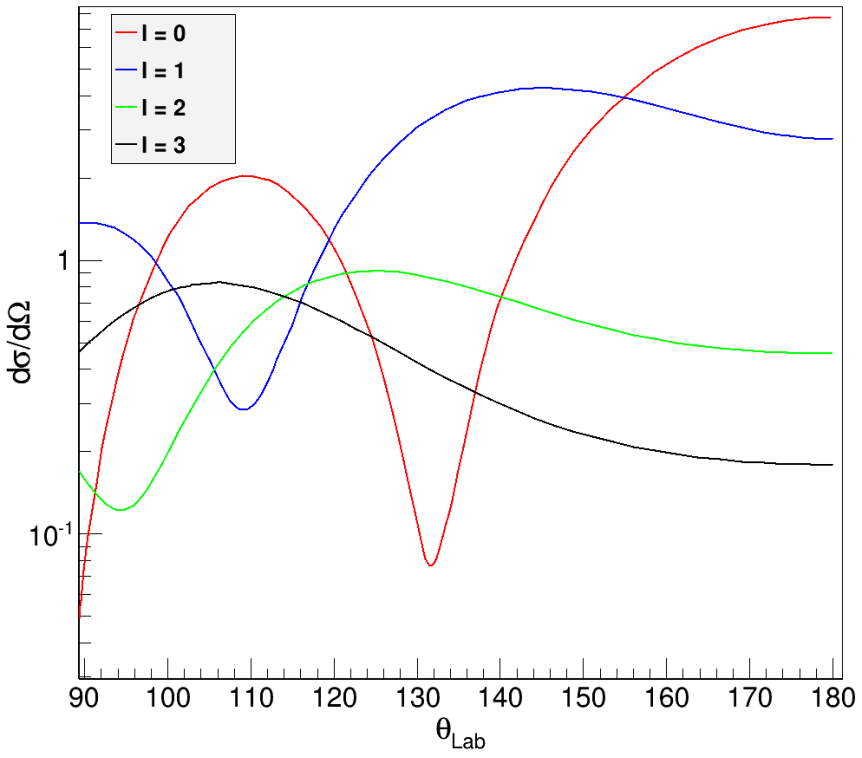

FIGURE 5.1: Angular distribution for different l values between 90° and 180°. These lines are all calculated using the same TWOFNR input parameters using an excitation energy of 4 MeV.

TWOFNR was used at various times in order to obtain the results found in this work. Its initial use is to determine the dominant transfer into each state by identifying which l, shown in Figure 5.1, best matches the profile of the experimental data for any given energy state. Later, once the spin and parity of each energy state has been determined, the TWOFNR code was used again using the specific values of excitation energy and spin and parity input parameters to calculate the state specific s, p, d, f-wave angular distributions and use them to find the spectroscopic factors. These processes will be described in more detail in the following sections.

5.1.2 Identifying the Dominant l Transition

Each populated energy is described by considering the superposition of two potential states that may be populated by the transferred neutron. If it is significantly more likely for an energy state to be populated via the transfer of a neutron of an $l = 0$ spin, for example, than it is to be populated with a neutron of spin $l = 2$, then the differential cross section of that state will look much more like the differential cross section of a fully $l = 0$ transfer. The differential cross sections found experimentally can be compared to the TWOFNR outputs for different energy states.

At this stage, the spin of the final state is not known, and so it is not possible to correctly input this parameter into the TWOFNR code. A final spin, J, of the energy state was therefore chosen that could be obtained using any value of l. The spin $J = 9/2$ was used which meant that it was assumed, for the purposes of this stage in the identification process, that each energy was achieved by populating the $s_{1/2}$, $p_{3/2}$, $d_{3/2}$, or $f_{7/2}$ shells.

The profile of the experimental data should, in some cases, have some similarities to the profile of the theoretical results. Finding these similarities can provide insight as to which l contributes the most to the energy state in question. For clarity, the theory calculations are not expected to be scaled correctly to fit the data at this stage; that will occur when the spectroscopic factors are found in Section 5.2. The important factor to take into account when considering Figures 5.2 to 5.13 is therefore not how close the data is to the theory, but how closely the shape of the data matches the shape of one of the theoretical lines.

A common feature of all of these graphs is how the points at 97° and 101° diverge from the general trend shown for the rest of the points in the graph. This inaccuracy is caused by the drop off in solid angle of the SHARC detector at these angles (Figure 4.7). This rapid decrease in solid angle causes a drop off in counts, as is seen in Figures 4.18 and 4.48.

Figure 5.2 shows good agreement with the $l = 2$ (green) line, suggesting that this state has a positive parity and is dominated by a d-wave transfer.

The data obtained for the 0.089 MeV state do not appear to fit any of the theory calculations shown in Figure 5.3 well. The differential cross section appears to drop below 10^{-6} at specific angles, suggesting the fit that was performed on the data as described in Section 4.4.3 did not require this energy state in order to recreate the energy spectrum. As a result, it does not appear possible to discern an information about the 0.089 MeV state at this stage.

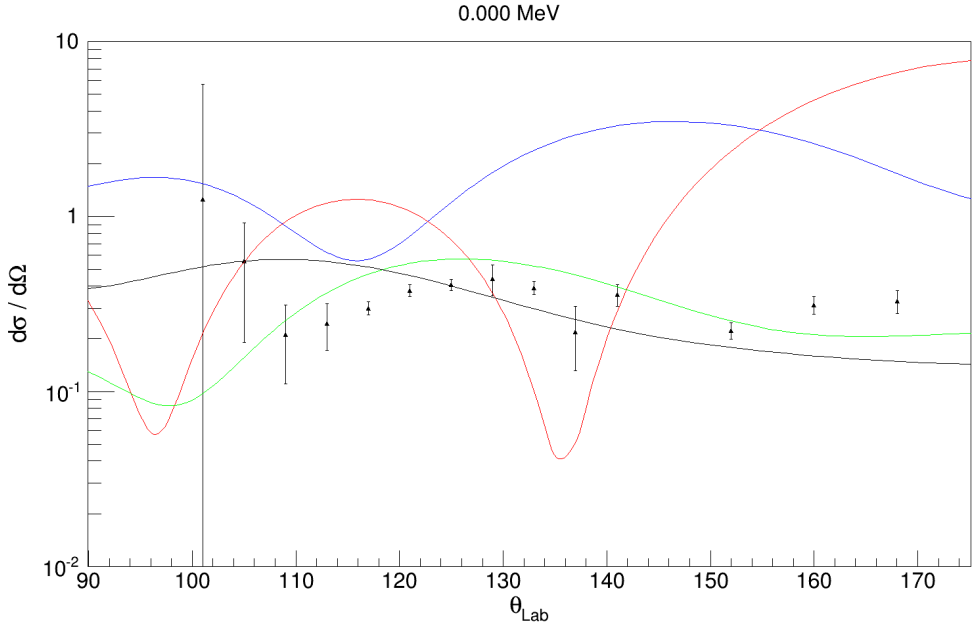

FIGURE 5.2: Comparison between experimental data and theoretical calculations for differential cross section using different values for l at 0.0 MeV. The l represented by each line is colour coded in the same way as is shown in Figure 5.1.

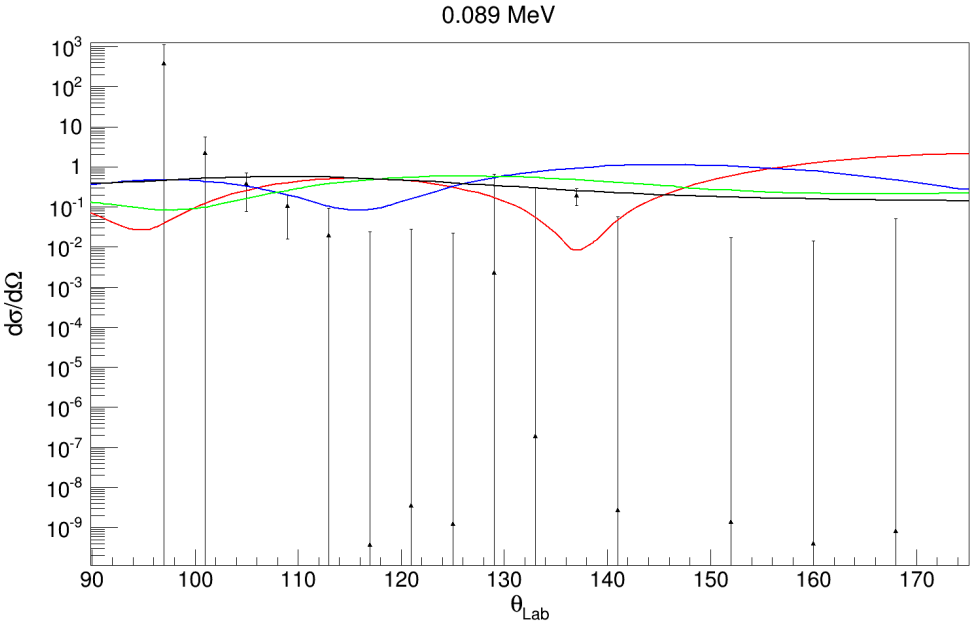

FIGURE 5.3: Comparison between experimental data and theoretical calculations for differential cross section using different values for l at 0.089 MeV. The l represented by each line is colour coded in the same way as is shown in Figure 5.1.

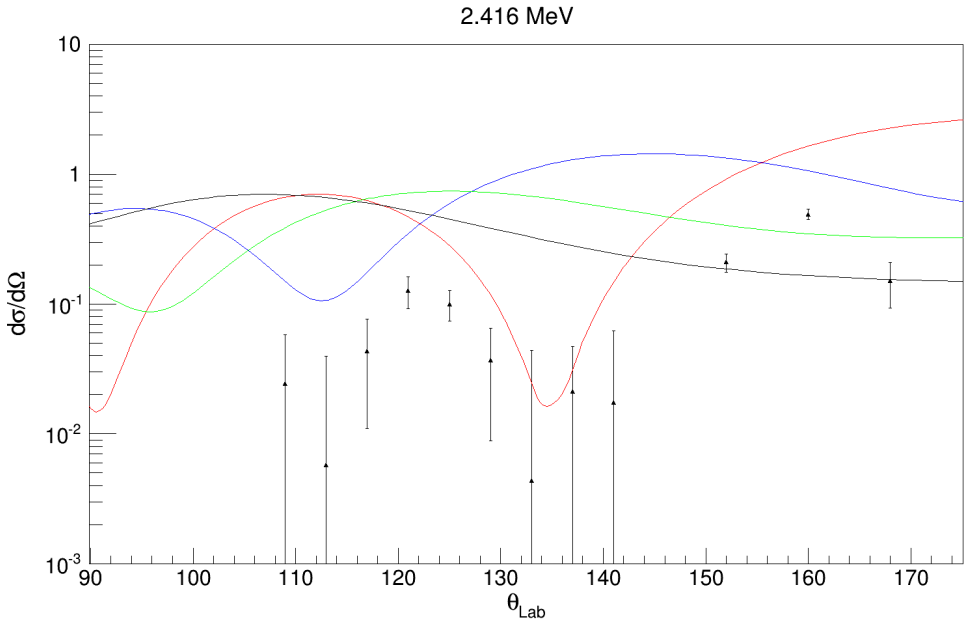

FIGURE 5.4: Comparison between experimental data and theoretical calculations for differential cross section using different values for l at 2.416 MeV. The l represented by each line is colour coded in the same way as is shown in Figure 5.1.

The 2.416 MeV state also does not appear to be strongly populated in the reaction and so does not have a very prominent peak in the fits described in Section 4.4.3. This gives the data points shown in Figure 5.4 to having large associated errors, however, the data points do appear to follow the same trend as the $l = 0$ (red) line, suggesting that the s-wave dominates the transfer reaction to this state and that the state has a positive parity.

Figure 5.5for the 2.788 MeV level clearly shows the data following the same trend as the $l = 0$ (red) theoretical line, suggesting that the s-wave transfer is the dominant transition and that the state has a positive parity.

The differential cross section of the 2.914 MeV state, shown in Figure 5.6, shows that the state was not strongly populated due to the low cross sections found at most angles. Because of this, it seems unwise to try and decipher the dominant $l-$wave for this state based on so few counts.

The data shown in Figure 5.7 for the 3.455 MeV state clearly show a dip at the same angle that the dip in the $l = 0$ (red) theoretical line occurs, demonstrating that this state is dominated by the s-wave transfer and suggesting that this state has a positive parity.

The data for the 3.995 MeV state shown in Figure 5.8 appear to have quite a flat profile. This would suggest that two $l-$waves play an equally strong role in populating this state.

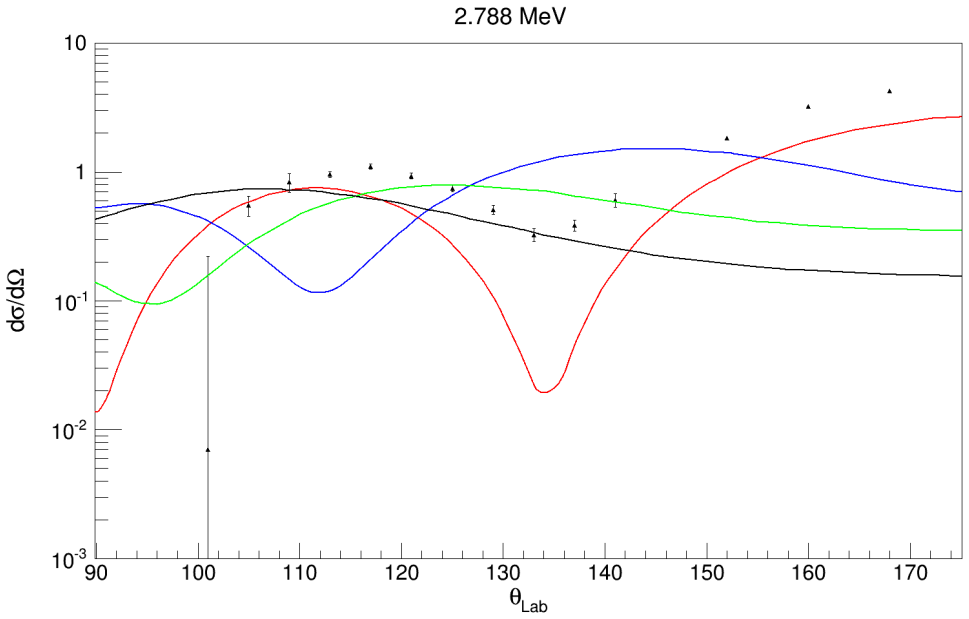

FIGURE 5.5: Comparison between experimental data and theoretical calculations for differential cross section using different values for l at 2.788 MeV. The l represented by each line is colour coded in the same way as is shown in Figure 5.1.

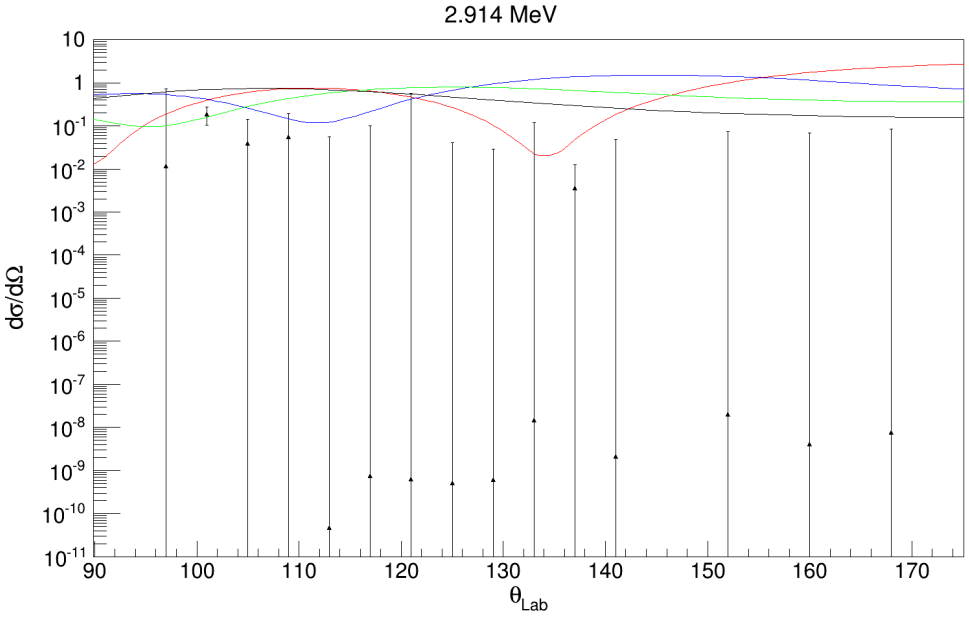

FIGURE 5.6: Comparison between experimental data and theoretical calculations for differential cross section using different values for l at 2.914 MeV. The l represented by each line is colour coded in the same way as is shown in Figure 5.1.

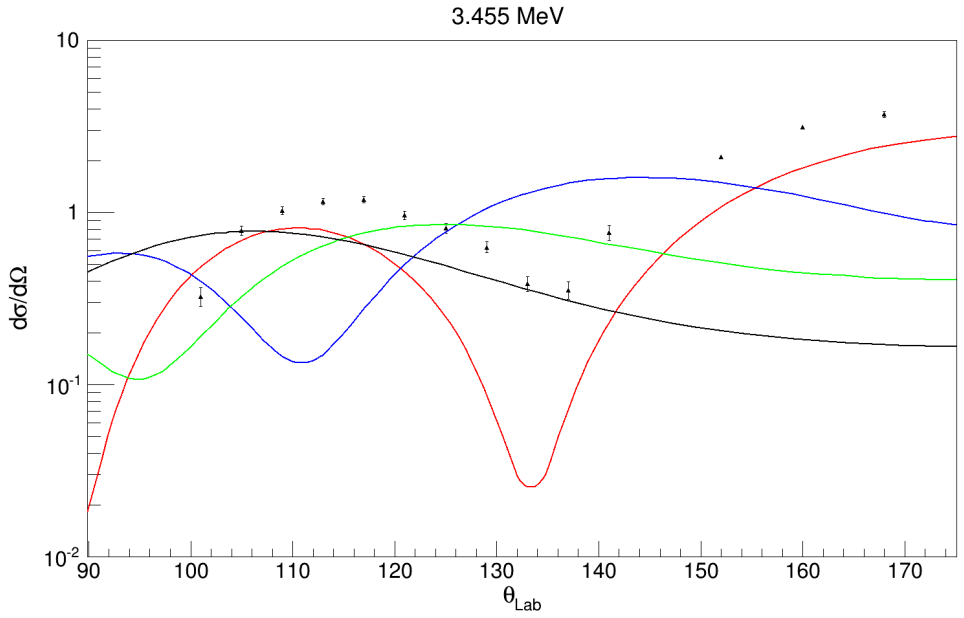

FIGURE 5.7: Comparison between experimental data and theoretical calculations for differential cross section using different values for l at 3.455 MeV. The l represented by each line is colour coded in the same way as is shown in Figure 5.1.

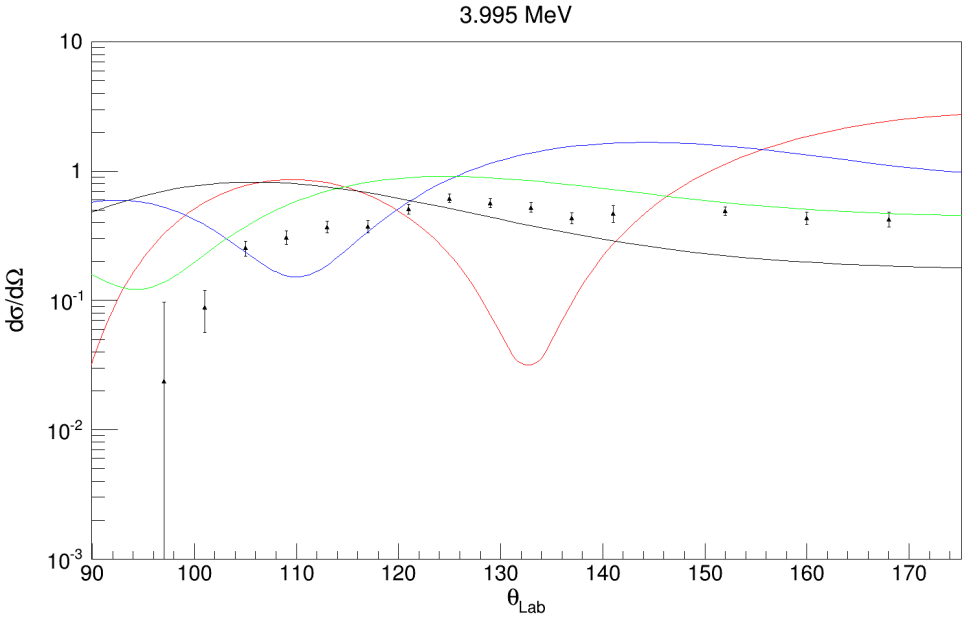

FIGURE 5.8: Comparison between experimental data and theoretical calculations for differential cross section using different values for l at 3.995 MeV. The l represented by each line is colour coded in the same way as is shown in Figure 5.1.

Despite this observation, the data do appear to exhibit similarities to the $l = 2$ (green) theoretical line since this line and the data rise into a peak at $\theta_{Lab} \sim 120°$. This implies that the parity of this state is positive.

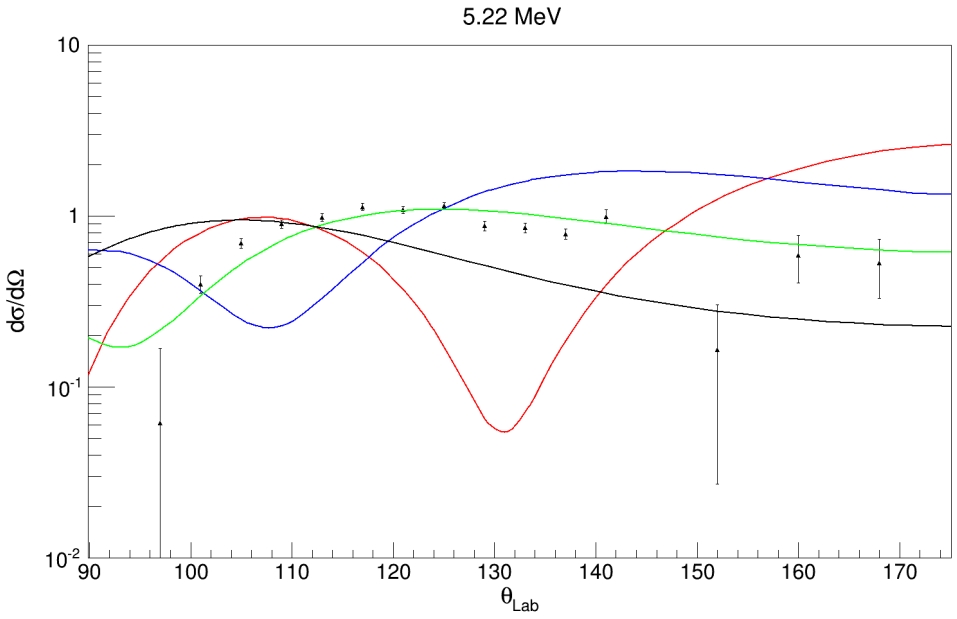

FIGURE 5.9: Comparison between experimental data and theoretical calculations for differential cross section using different values for l at 5.22 MeV. The l represented by each line is colour coded in the same way as is shown in Figure 5.1.

The data for the 5.22 MeV state, shown in Figure 5.9 clearly show similarities with the $l = 2$ (green) theoretical line, giving a strong indication that this state is populated via the d-wave and suggests a positive parity.

The data for the 5.85 MeV state shown in Figure 5.10 do not show any clear similarities with any of the theoretical lines shown. The difficulty in identifying the shape of the data is caused by the discontinuity of the points seen at $\theta_{Lab} = 105°$, 113° and 117°. Ignoring these points gives the impression that the data increases to a peak at $\theta_{Lab} \sim 120°$, giving a tentative identification of the d-wave (green) being dominant in the transfer to this state. The data obtained at this energy state and above start to suffer from the fact that high angles of the box detectors are cut off due to the threshold of the detectors. This may make it difficult to identify a s-wave transfer if there are no data points past 130° to show the associated secondary peak.

As with the 3.995 MeV state, the 6.005 MeV state shown in Figure 5.11 appears to have a rather featureless profile, making it difficult to identify. Two different l-wave might combine to give the total profile that is shown by the data. It is easy to see that there are multiple ways to combine two of the l-waves shown in Figures 5.2 to 5.13 that might

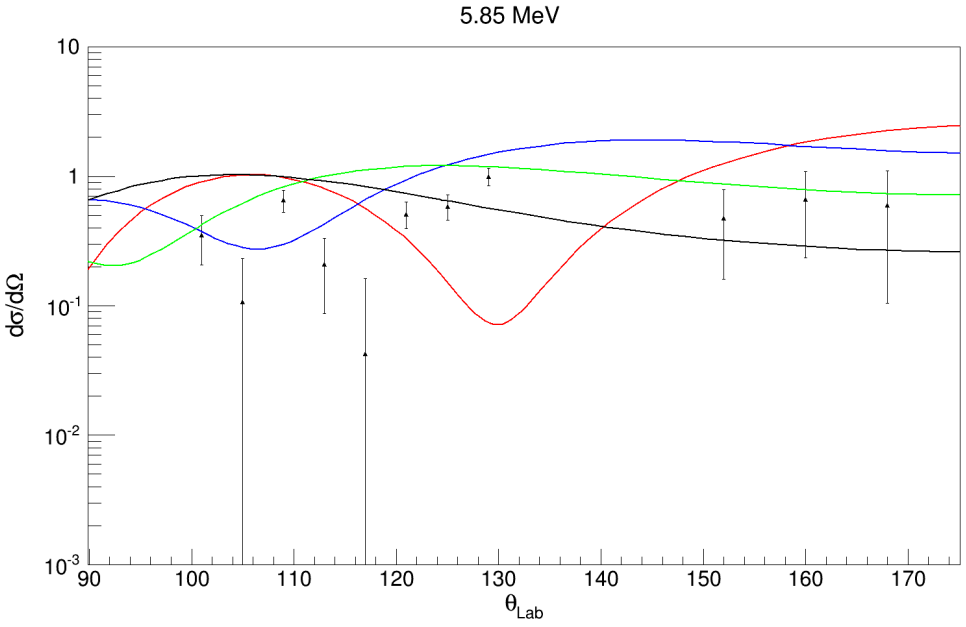

FIGURE 5.10: Comparison between experimental data and theoretical calculations for differential cross section using different values for l at 5.85 MeV. The l represented by each line is colour coded in the same way as is shown in Figure 5.1.

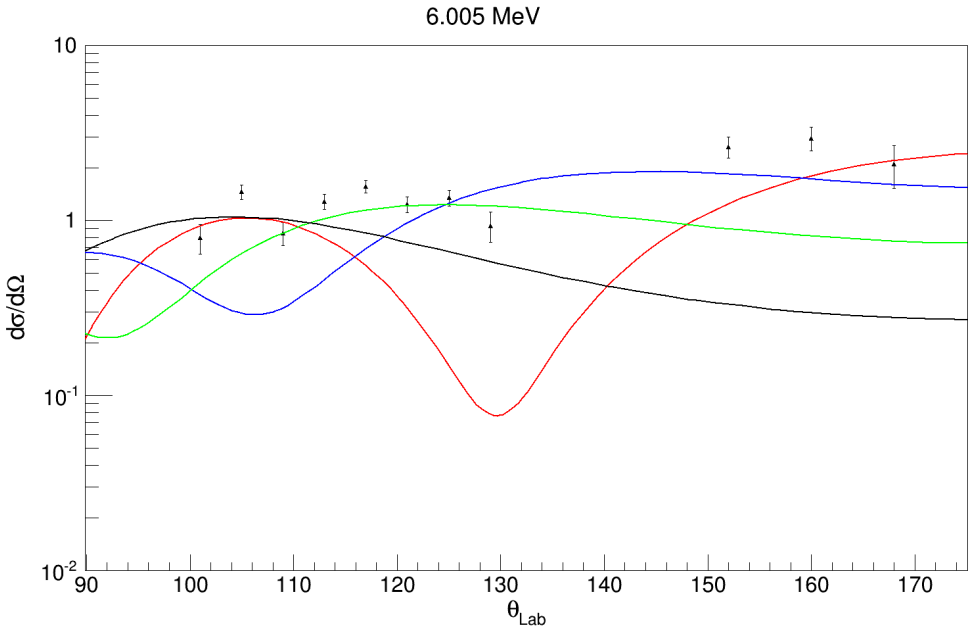

FIGURE 5.11: Comparison between experimental data and theoretical calculations for differential cross section using different values for l at 6.005 MeV. The l represented by each line is colour coded in the same way as is shown in Figure 5.1.

result in a total differential cross section that is relatively flat. Figure 5.12, showing the data for the 6.55 MeV state, is similarly featureless, making it difficult to identify.

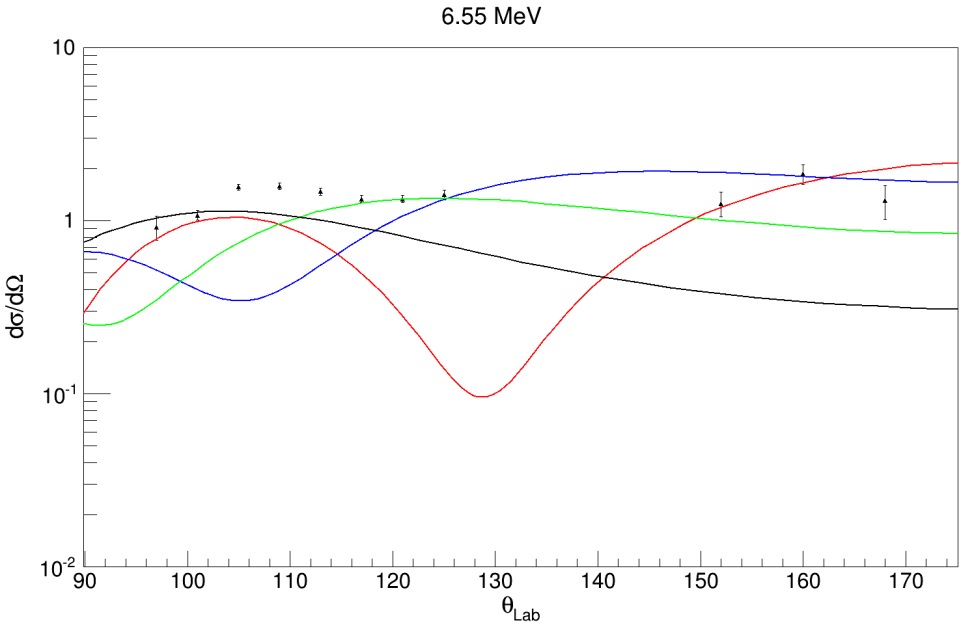

FIGURE 5.12: Comparison between experimental data and theoretical calculations for differential cross section using different values for l at 6.55 MeV. The l represented by each line is colour coded in the same way as is shown in Figure 5.1.

The data for the 7.48 MeV state in particular suffers from lack of data at higher angles in the box detector due to the high thresholds. The small amount of points makes it difficult to correctly identify, but tentative evidence suggests that the state could be dominated by the f-wave transition (black), suggesting that the state has a negative parity. This early conclusion is reached using the downward trend exhibited by the four points from the box detector at $\theta = 105°$, $109°$, $113°$ and $117°$

5.1.3 Gamma-ray Transitions

The shell-model also provides predictions of the γ-ray decay transitions that may occur between the predicted states. Some of the states given by the shell-model and their γ-ray transmissions are shown in Figure 5.17.

The γ-rays seen in the experiment have already been described in Section 4.4.1 (and a level scheme depicting the γ-ray transitions is given in Figure 4.43). Finding similarities between the observed γ-ray decay scheme and the decay scheme predicted by the shell-model provides evidence for assignment of the spin and parity to the experimentally observed energy states. The final assignment of each energy is fully described in Section

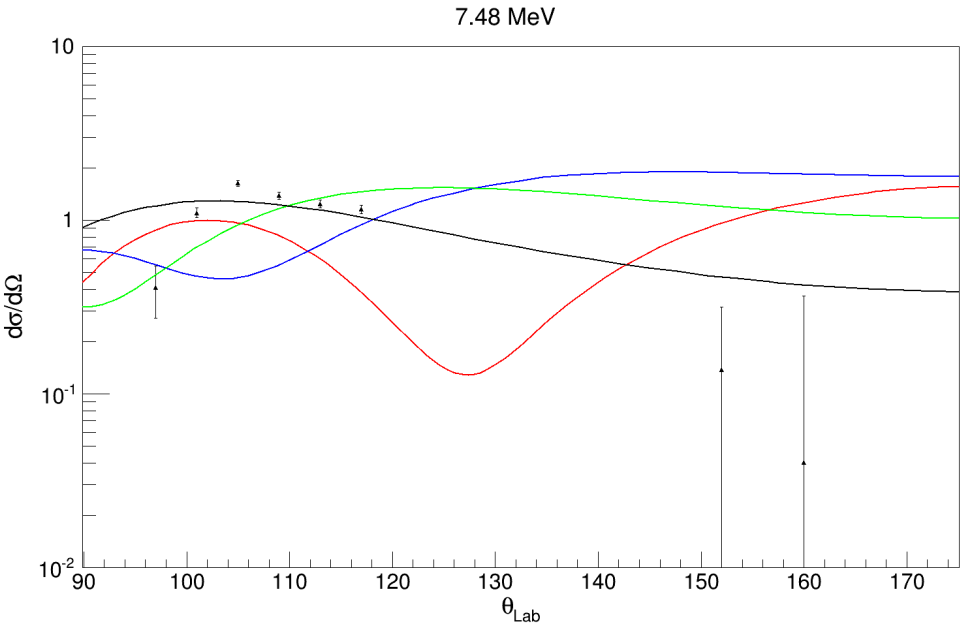

FIGURE 5.13: Comparison between experimental data and theoretical calculations for differential cross section using different values for l at 7.48 MeV. The l represented by each line is colour coded in the same way as is shown in Figure 5.1.

5.1.5, but for ease of comparison, the energy scheme obtained from the experiment with the final spin/parity assignments is displayed in Figure 5.15.

The shell-model is not perfect; it does not correctly give the true values of the energy states that are possible, nor will it give completely accurate predictions as to the transitions of the γ-rays. However, it has shown success in describing the structure of the nucleus, as described in Section 2.1. Therefore, not all the transitions that are predicted and shown in Figure 5.14 are seen in the experiment. The transition strengths might be the cause of discrepancies between theory and experiment; a weak transition may result in the γ-ray not being detected in the experiment, even though it is really emitted. It is also possible there is a problem with the experiment that keeps some γ photons from being detected. An example of this is would be in the efficiency of the TIGRESS clovers; high energy γ-rays are less likely to be detected by TIGRESS, and so some γ-ray transitions might be missed. The result of all these points is to conclude that the absence of a γ-ray does not invalidate the identification of a state. Instead, the similarities between the shell-model transition predictions and the experimentally observed transitions are used to provide evidence - not proof - of a state's spin and parity.

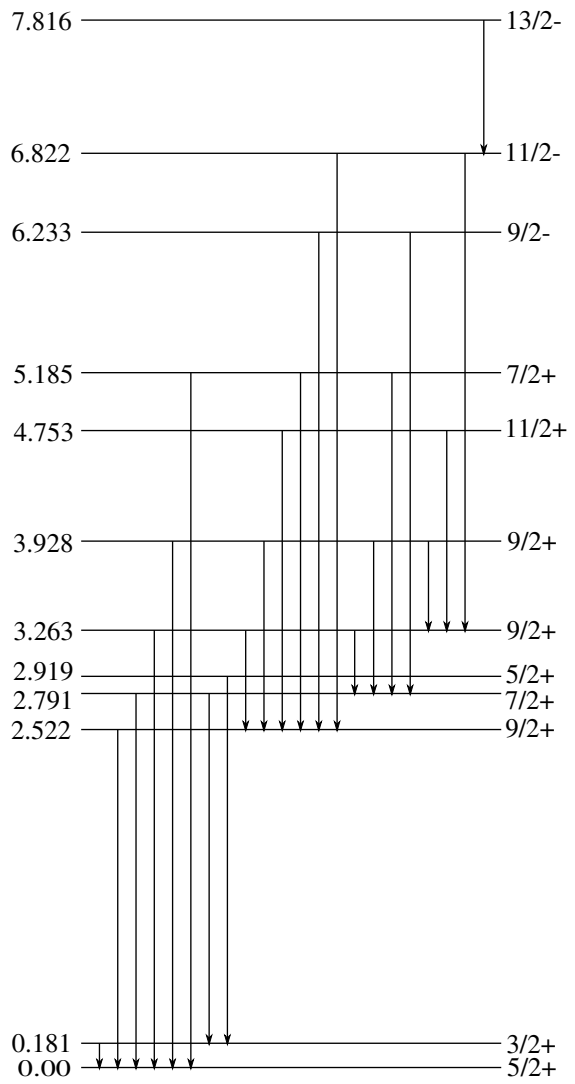

FIGURE 5.14: shell-model energy level scheme and γ transitions.

5.1.4 Strengths of the Populated States

Of the low energy states already known in ^{25}Na, only three have a spin and parity that are confirmed and are also detected in this experiment (see Table 1.1). The spins of the unidentified states were identified by finding the theoretical 'reaction strength' of the state, i.e. the strength of a reaction taking into account the Spectroscopic Factors and spin designations from the shell-model, and the theoretical cross sections, σ, and comparing with the number of counts for that state detected in the experiment.

To find the theoretical reaction strengths, the cross section, σ, needed to be found for different values of l. TWOFNR was used for this purpose. Using a target nucleus spin of 4^+ and a spin value of $9/2$ for the final nucleus state, the differential cross sections, $\mathrm{d}\sigma/\mathrm{d}\Omega$, were calculated for a transferred nucleon of spin $s_{1/2}$, $p_{3/2}$, $d_{3/2}$ and $f_{7/2}$. The

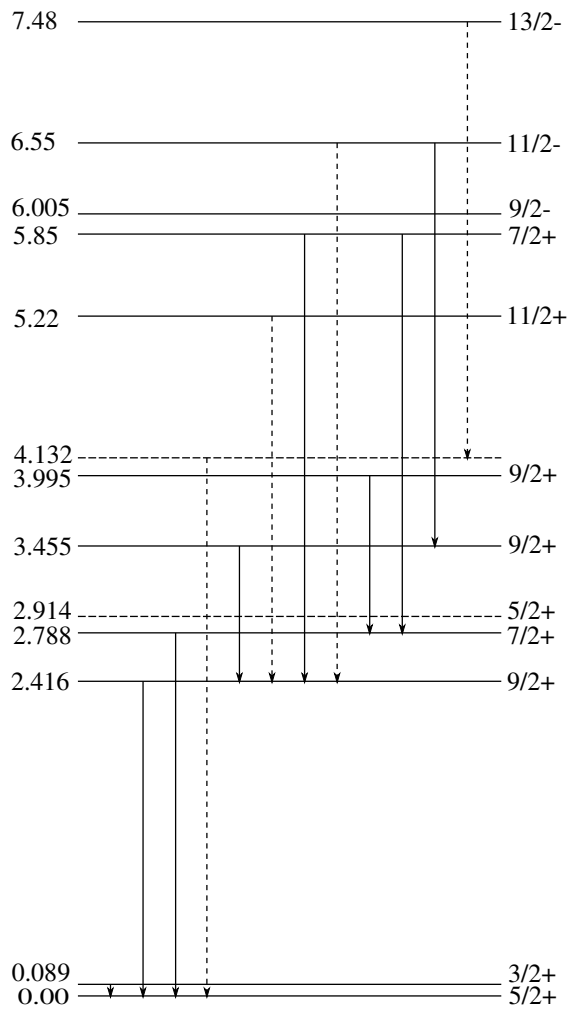

FIGURE 5.15: Experimentally obtained level scheme including γ transitions and spin/-parity designation.

other parameters input into TWOFNR were the same as those described in Section 5.1.1. The value of σ was found by integrating $\mathrm{d}\sigma/\mathrm{d}\Omega$ over the coverage given by the Box and CD detector as in Equation 5.1,

$$\sigma = \int_{Box} \frac{\mathrm{d}\sigma}{\mathrm{d}\Omega} 2\pi \sin\theta \mathrm{d}\theta + \int_{CD} \frac{\mathrm{d}\sigma}{\mathrm{d}\Omega} 2\pi \sin\theta \mathrm{d}\theta, \tag{5.1}$$

where $2\pi \sin\theta \mathrm{d}\theta$ is the value for $\mathrm{d}\Omega$ given in Equation 4.5. The cross section, σ, was found this way for several energies ranging from 0 MeV to 8 MeV. Plotting these values showed how the theoretical values of cross sections for different l varied over the energy range of the peaks detected in the experiment. The points for each l were then fitted in order to be able to find a value of σ for any given energy. This is shown in Figure 5.16.

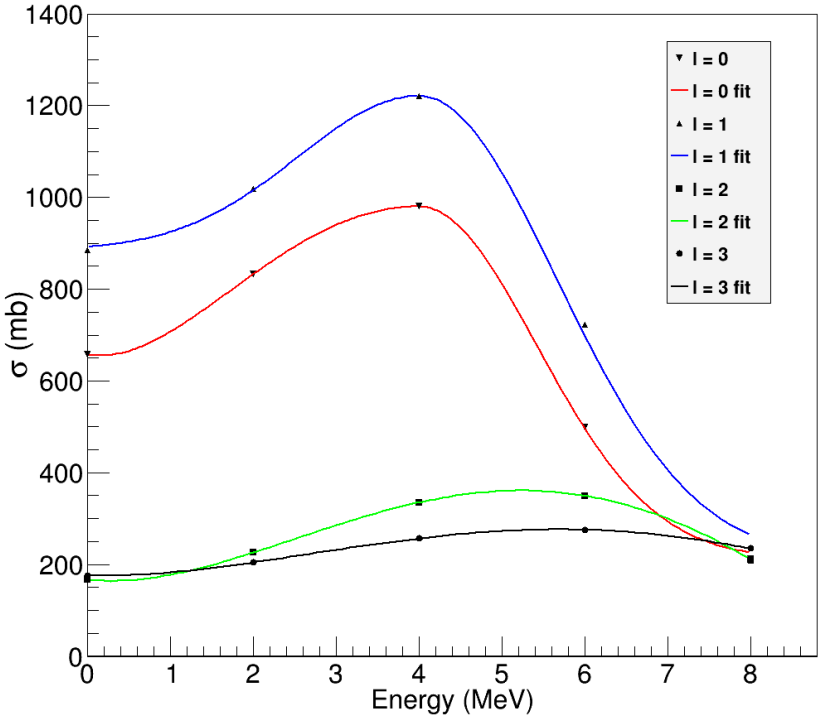

FIGURE 5.16: Variation of cross section as energy increases at different values of l.

Energy (MeV)	Threshold Angle, θ (°)	
	Box	CD
0	143.0	172.0
2	143.0	172.0
4	143.0	172.0
6	133.6	172.0
8	116.2	153.1

TABLE 5.1: Threshold cut off at various energies.

The value of σ is dependent on the angular coverage of the Box and CD detectors. At $\sim$ 6 MeV, the experiment was subject to the threshold effects described in Section 4.4.4. The angular coverage of the Box and CD DSSSDs had to be adjusted in order to be a true comparison between the theoretical results and the experiment. The upper angular limits of both the Box and CD detectors are caused by the high thresholds are given in Table 5.1 at various energies.

The constant 2π in Equation 5.1 was obtained by assuming full coverage in ϕ (see Equation 4.5). Even though this assumption is not completely accurate given the experimental set-up, it is a close approximation to it at most energies and angles. However, at energies greater than 4.7 MeV, only a quarter of the CD detector is used, meaning that the integral over the CD detector becomes

Energy (MeV)	Spectroscopic Factors			
	$l = 0$	$l = 1$	$l = 2$	$l = 3$
0			0.53861	
0.181			0.7311	
2.552	0.04687		0.03866	
2.791	0.64902		0.09495	
2.919			0.01554	
3.263	0.36835		0.32253	
3.928	0.03433		0.20302	
4.097	0.00184		0.15766	
4.753			0.2899	
5.185	0.01638		0.42662	
6.154		0.2313		0.1058
6.233		0.3963		0.2793
6.822		0.2225		0.4709
7.044			0.1535	
7.322		0.0929		0.0863
7.816				0.4877
8.105		0.0856		0.0478
8.617		0.069		0.01
8.982				0.3048

TABLE 5.2: Spectrocopic factors given by the shell-model per l.

$$\sigma_{CD} = \int_{CD} \frac{\mathrm{d}\sigma}{\mathrm{d}\Omega} \frac{\pi}{2} \sin\theta \mathrm{d}\theta. \tag{5.2}$$

These modifications occur at high energies and cause the values of σ shown in Figure 5.16 to be lower than they would have been otherwise. Below 4.7 MeV, σ increases for every l as energy increases.

The theoretical cross sections of the states listed in Table 5.2 were found using the fit lines for each value of l in Figure 5.16. However, this is still not an accurate comparison to the number of counts obtained in the experiment because it does not address the occupancy of the state being populated. For instance, for ^{25}Na, the ground-state is known to have a spin of 5/2. The degeneracy of this state, i.e. the number of quantum states that have the same energy, is given by $2J + 1$, which equals 6 in the case that $J = 5/2$. This means that the probability of a neutron being deposited in the ground-state is six times more likely due to the degeneracy of the state.

The spectroscopic factors, S, given by the shell-model also play a roll in what is expected to be seen in the experiment. The values for S for each excited state is given in Table 5.2. The final value of the reaction strength predicted by the theory is then given by

$$\mathcal{R} = S(2J + 1)\sigma. \tag{5.3}$$

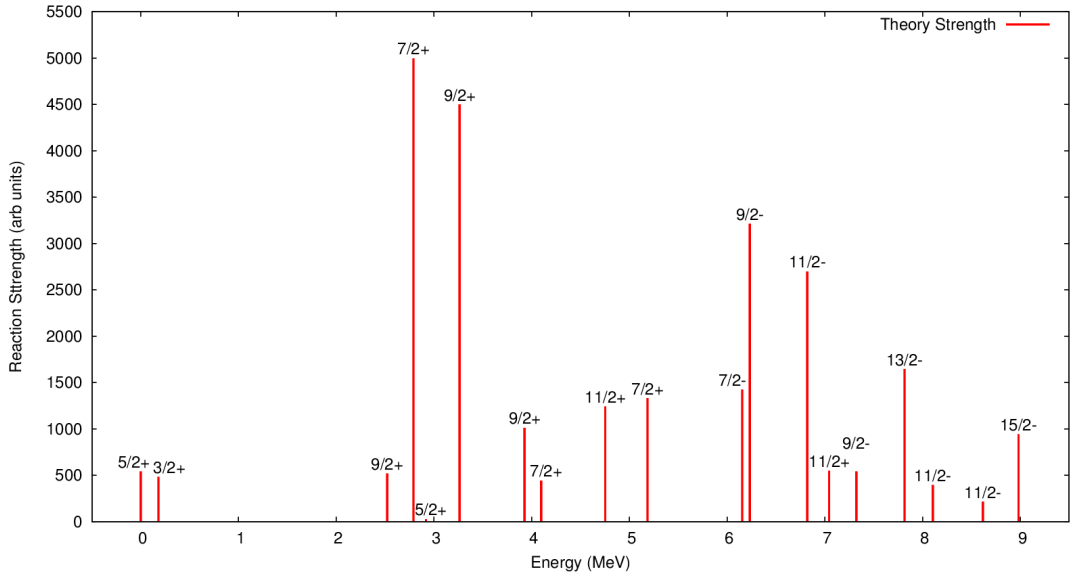

FIGURE 5.17: Strengths and the spins and parities of states predicted by the shell-model.

The values of $\mathcal{R}$ are shown graphically in Figure 5.17 for all the energies listed in Table 5.2.

5.1.5 Assigning Spin and Parity to States in ^{25}Na

Finally assigning the spin and parity to the states observed in the experiment requires combining all the information obtained in sections 5.1.2 to 5.1.3. Figure 5.18 shows the total counts of each energy state that was seen in the experiment. The final spin and parity designations for each state are also labelled. The process used to find these labels is described here.

Consider the $7/2^+$ and $9/2^+$ states at 2.791 MeV and 3.263 MeV in Figure 5.17. The reaction strength, $\mathcal{R}$, is the highest of all the states shown in this figure, suggesting that there will be a high count rate of these states in the experiment. Table 5.2 shows that the s-wave contributionr is predicted to be strong in both of these states. These facts produce a strong argument that these states are the experimentally observed states found at 2.788 MeV and 3.455 MeV. These experimental energies both have a strong s-wave dependence, as can be seen in Figures 5.5 and 5.7, and have a high count rate, as is shown in Figure 5.18. The 2.788 MeV and 3.455 MeV states are therefore assigned a spin and parity of $7/2^+$ and $9/2^+$ respectively.

This provides a starting point that can be used to identify other experimentally observed energy states. The 2.788 MeV state that was just identified is fed by the 3.995 MeV

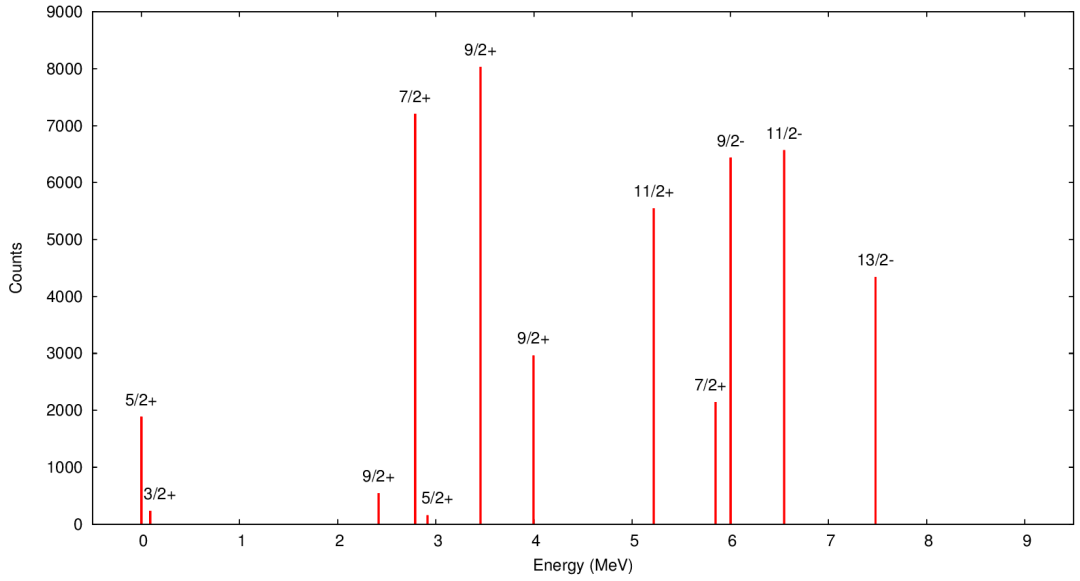

FIGURE 5.18: Strengths and the spins and parities of experimentally observed states.

state as is shown by Figure 5.15. The 3.995 MeV state has a d-wave dependence as is shown in Figure 5.8. In the shell-model, there are four states that are predicted to feed into the corresponding $7/2^+$ state at 2.791. The 3.263 MeV $9/2^+$ state has already been established to correspond to the 3.455 MeV experimental state. Of the three other states that feed into 2.791 MeV, only two are predicted to have a strong d-wave dependence: 3.928 MeV and 5.185 MeV with spins and parities of $9/2^+$ and $7/2^+$ respectively. The $7/2^+$ MeV is dismissed due to the large difference between the observed energy of 3.995 MeV and the predicted energy of 5.185 MeV. Therefore, the 3.995 MeV is identified to be the $9/2^+$ state.

The experimentally observed state at 3.455 MeV (now identified as $9/2^+$) is seen to decay through the state at 2.416 MeV and then to the ground-state. The 2.416 MeV is weakly populated, but has an s-wave dependence as shown in Figure 5.4. Comparing this information to the data given by the shell-model gives evidence for the 2.416 MeV being the $9/2^+$ state at 2.522 MeV. This state also appears to be dependent on the s-wave, is predicted to be relatively weakly populated when compared to the strongly populated state at 3.263 MeV (Figure 5.17), and is the only state that is fed by the 3.263 state and also decays to the ground-state (Figure 5.14). Therefore, it is concluded that the experimental state at 2.416 has a spin and parity of $9/2^+$.

Now consider the experimental state found at 5.85 MeV. It was not possible to identify which l was dominant in the transition of this state (see Figure 5.10), so the only method available to identify the corresponding state predicted by the shell-model is by using the observed γ-ray decay scheme. The experimental data show that the 5.85 state decays

through the states at 2.416 and 2.788 MeV, which have already been identified to have spin and parity assignments of $9/2^+$ and $7/2^+$ respectively. The only state that exhibits this same decay pattern as predicted by the shell-model is the 5.185 MeV, $7/2^+$ state. Based on this, the observed 5.85 state is assigned the spin and parity of $7/2^+$.

The experimental state found at 5.22 MeV was shown using Figure 5.9 to have a strong d-wave dependence, and was seen to decay through the 2.416 MeV, $9/2^+$ state. When applying this information to the shell-model predictions, there are three states that pass through the equivalent $9/2^+$ state that are also dominated by the d-wave transition. These are the 3.928 MeV, $9/2^+$ state, the 4.753 MeV , $11/2^+$ state, and the 5.185 MeV, 7/2+ state. The states at 3.928 and 5.185 MeV already correspond to the experimentally observed states at 3.995 and 5.85 MeV respectively, and so can not be considered in the assignment of the 5.85 MeV energy level. This leaves the $11/2^+$ state at 4.753 MeV. Therefore, it is concluded that the state at 5.22 MeV is has the spin and parity of $11/2^+$.

The highest three states observed in the experiment are difficult to identify; it was not possible to determine which l-wave was dominant in the transfer reaction because the differential cross section obtained from the data was too flat to be able to compare to the profiles given by TWOFNR. The γ-ray decays seen for these levels offer little help because only the state at 6.55 MeV has a γ-ray associated with it that decays through an energy level that has already been identified. In comparison, the state at 6.005 MeV has no γ-rays associated with it, and the γ-rays associated with the 7.48 MeV follows a decay chain that is independent to the decay chains that have been taken by every other state discussed thus far. The only other clues as to the spin and parity of the states that are available is the reaction strengths of the predicted energy levels shown in Figure 5.17 and how they compare to the counts seen in the experiment for these three states. Figure 5.18 shows that there is quite a high count rate for these three energy states. This high count rate appears to be reflected in the reaction strength given to the states predicted by the shell-model at 6.233, 6.822 and 7.816 MeV with a spin and parity of $9/2^-$, $11/2^-$ and $13/2^-$ respectively. Based solely on this observation, the experimental states at 6.005, 6.55 and 7.48 MeV where identified as a $9/2^-$, $11/2^-$ and $13/2^-$ state respectively. This designation is supported for the 6.55 MeV state by the γ-ray that is associated with its decay. Since the state decays through the 2.416 MeV energy level, which mirrors the shell-model prediction that the $11/2^-$ state will to the ground-state via the two $9/2^+$ states.

The final states that have not yet been discussed are at 0.089 MeV and at 2.914 MeV. Both theses states are very weak, as can be seen when looking at Figures 5.3 and 5.6. There are no data that allows these energies to be assigned to a specific parity and spin. However, these states have already been seen and their spins are already known [69].

They are therefore labelled here as $3/2^+$ for the 0.089 MeV state, and $5/2^+$ for the 2.914 MeV state.

The difference in the energy of the experimentally observed states compared to those predicted in theory is shown in Figure 5.19 with the newly assigned spins and parities labelled.

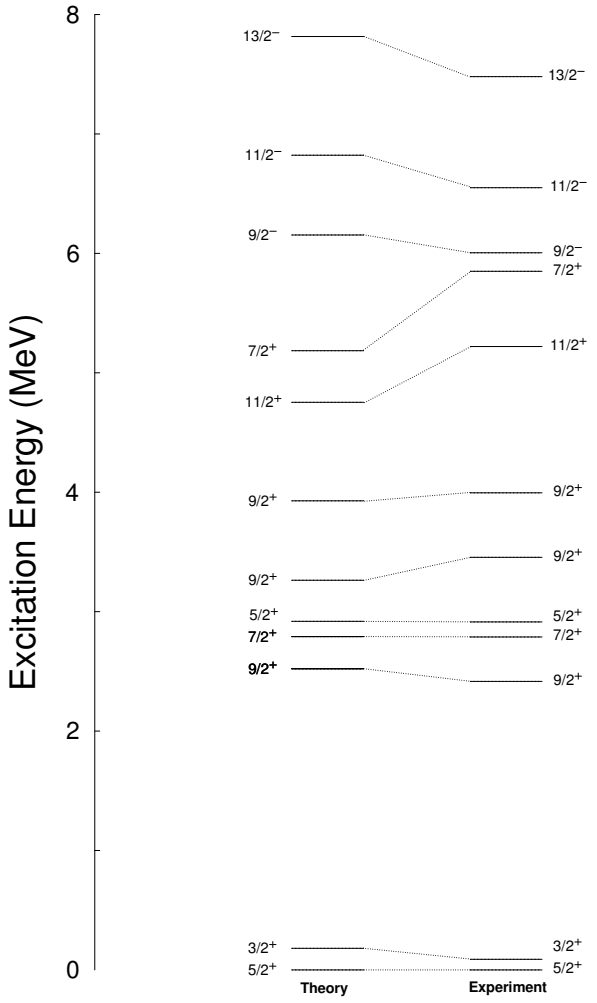

FIGURE 5.19: Comparison between the energy levels found in the experiment and those predicted by theory.

5.2 Spectroscopic Factors

The spectroscopic factor (SF) of a reaction describes how much like a single-particle state the final reacted state corresponds to. A simple description of the transfer reaction describes an unpaired nucleon being placed into an unoccupied shell, creating an energy state that has a specific spin and parity. This 'single-particle state' is described as such because it is the one transferred nucleon that determines the spin of the state. However,

it is possible for a nucleon to be placed into a completely different nuclear shell and still produce an energy state with the same spin and parity as the single-particle state. This happens when two nucleons in the same shell couple together to a spin other than zero. If a state is formed purely by the single-particle transfer reaction, then the state has a SF of one. However, if the state is formed by two or more particles coupling to a state of the same spin and parity at the same energy, then the SF is reduced.

The shell-model predictions for the SF have already been used to calculate the reaction strength for each of the predicted energies and are listed in Table 5.2. However, at this stage, it was not important to know the J value of the transferred nucleons since only the total SF per l was required. Table 5.3 gives the predicted energy of the states along with the SFs of the state for each J.

Multiplying the appropriate theoretical lines given by TWOFNR by the predicted magnitudes of each SF given in Table 5.3 gives the final theoretical predictions for each excited energy. The single-particle states that contributed the most to the cross section of the reaction, as predicted by the shell-model, were used to provide the comparison between theory and data. This comparison is shown in Figures 5.20 to 5.23.

It can be seen here that the shell-model predicts the spectroscopic factors with varying success. Some energies, such as the ground-state and 5.22 MeV excited state appear to have relatively good agreement with theory. Other states, such as the 2.788 MeV, 2.416 MeV and 3.455 MeV appear to have had the magnitudes of each SF over estimated, resulting in a theoretical line that is greater than the data. The 6.005 MeV and 6.55 MeV states show a difference in the predicted magnitude of the spectroscopic factors found and the relative proportion between the single-particle state that make the total theoretical line. This is demonstrated by the calculated lines having a different form compared to the data.

5.2.1 Minimising Chi squared

The values for the spectroscopic factors predicted by theory does not give satisfactory results for all the energy states observed. The outputs from TWOFNR must have a χ^2 minimisation performed on them in order to obtain the final values for the spectroscopic factors for each state.

The angular distribution of a state is given by the sum of the single-particle state angular distributions multiplied by the spectroscopic factors of those single-particle states,

$$\left(\frac{\mathrm{d}\sigma}{\mathrm{d}\Omega}\right)_{Total} = a\left(\frac{\mathrm{d}\sigma}{\mathrm{d}\Omega}\right)_1 + b\left(\frac{\mathrm{d}\sigma}{\mathrm{d}\Omega}\right)_2, \tag{5.4}$$

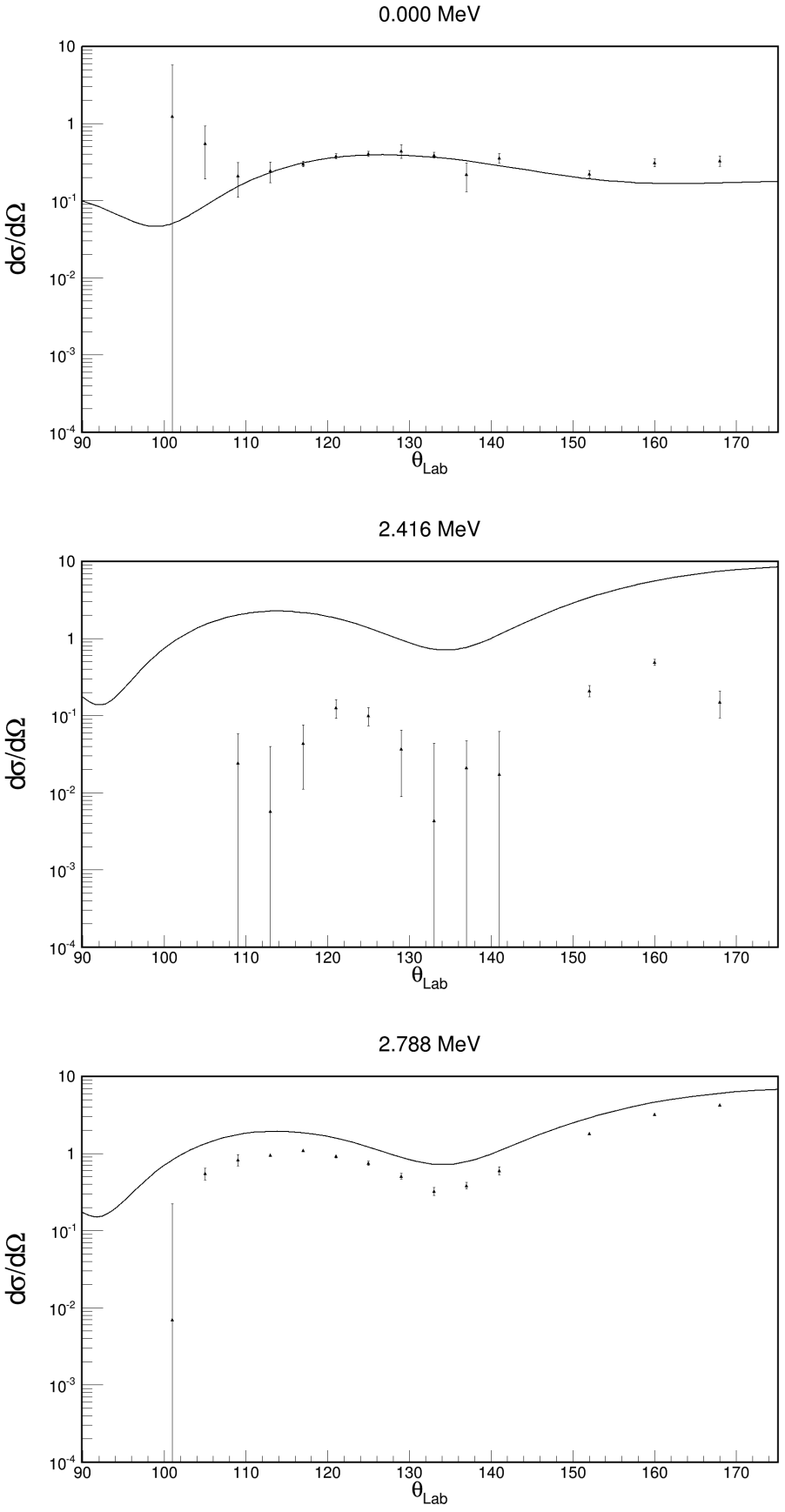

FIGURE 5.20: Comparison between theory and data for various energy levels.

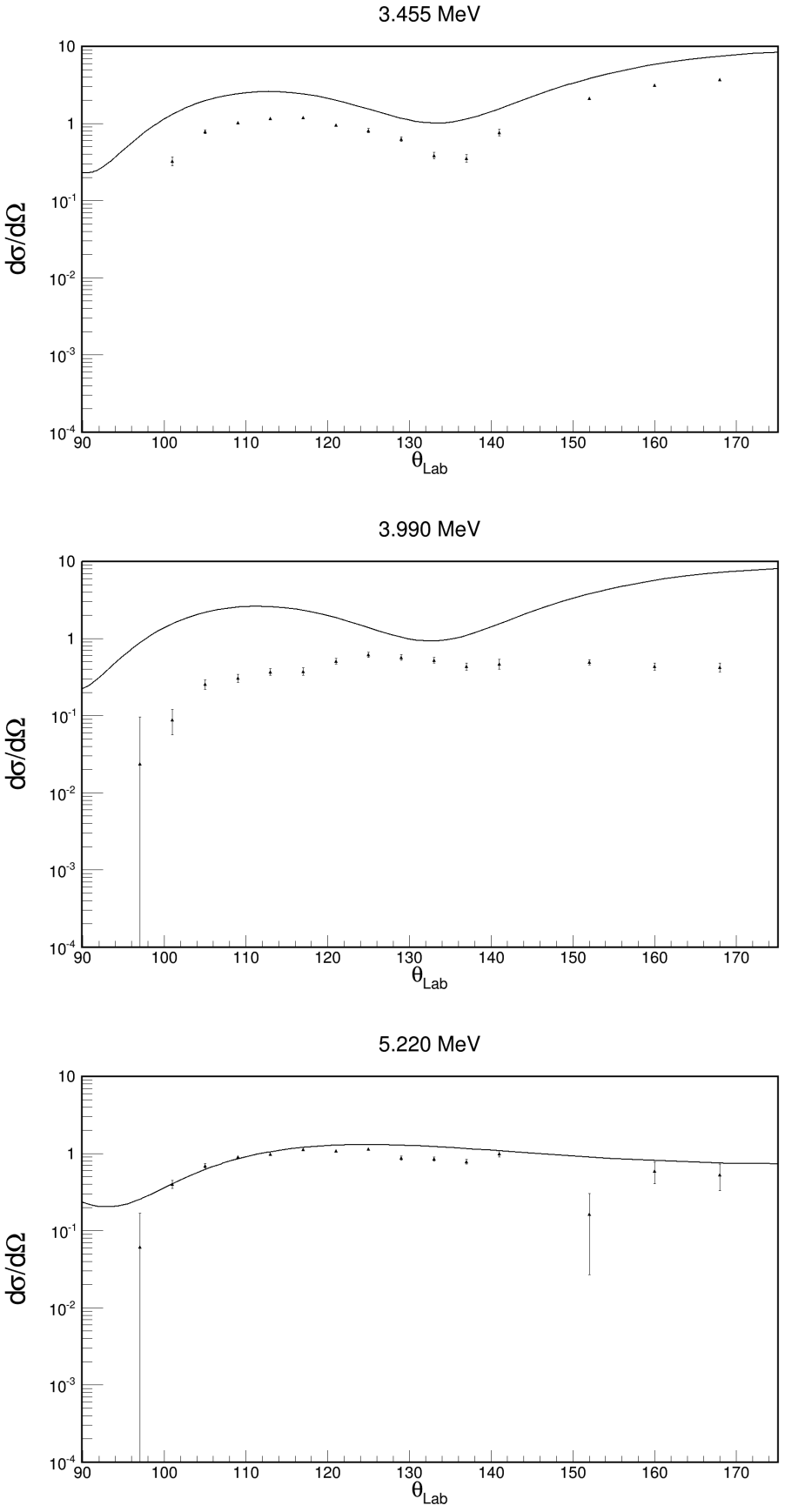

FIGURE 5.21: Comparison between theory and data for various energy levels.

Spin / Parity	Excitation Energy (MeV)	Spectroscopic factor s1/2	p3/2	d3/2	d5/2	f7/2
5/2+	0.0			0.0034	0.53521	
3/2+	0.181				0.7311	
9/2+	2.522	0.04687		0.03194		
7/2+	2.791	0.64902			0.08391	
5/2+	2.919				0.01519	
9/2+	3.263	0.36835			0.17443	
9/2+	3.928	0.03433		0.17516		
11/2+	4.753			0.21832		
7/2+	5.185	0.01638		0.41194		
9/2−	6.154		0.2025			0.0969
11/2−	6.822		0.2225			0.4706
13/2−	7.816					0.4861

TABLE 5.3: Theoretical spectroscopic factors for each level.

where the subscript denotes the n^{th} single-particle state used in the calculation and a and b are the spectroscopic factors of these states. The unknown quantities, a and b, will be obtained using the following process.

A code was written which minimised the χ^2 value of $(\mathrm{d}\sigma/\mathrm{d}\Omega)_{Total}$ to the data points. The spectroscopic factors in Equation 5.4 were set as variable parameters that could have a value between 0 and 2. A spectroscopic factor greater than 1 is non-physical, however, the code was allowed this extra degree of freedom in order to see how much greater than 1 the code would want to set the parameters in order to appropriately minimise the theory to the data. Using an iterative process, different values of a and b were substituted into Equation 5.4. During each iteration, the value of $(\mathrm{d}\sigma/\mathrm{d}\Omega)_{Total}$ was evaluated at the centre angle of each angle bin and substituted into Equation 5.5. Subsequently, a value for χ^2 for these values of a and b were found using

$$\chi^2 = \sum_{\theta} \left(\frac{\left(\frac{\mathrm{d}\sigma}{\mathrm{d}\Omega}\right)_{Exp,\theta} - \left(\frac{\mathrm{d}\sigma}{\mathrm{d}\Omega}\right)_{Th,\theta}}{\Delta\left(\frac{\mathrm{d}\sigma}{\mathrm{d}\Omega}\right)_{Exp,\theta}} \right)^2, \tag{5.5}$$

where $(\mathrm{d}\sigma/\mathrm{d}\Omega)_{Exp,\theta}$ and $(\mathrm{d}\sigma/\mathrm{d}\Omega)_{Th,\theta}$ are the differential cross sections from the experimental data and theory respectively at a lab angle θ, and $\Delta\,(\mathrm{d}\sigma/\mathrm{d}\Omega)_{Exp,\theta}$ is the error in the differential cross section of the experimental data.

Due to the high threshold, and other hindrances such as dead strips causing fewer counts to be detected at certain angles, some values of θ were excluded from the measurement of χ^2 so not to skew the final result. The excluded angles at different energies are listed in Table 5.4.

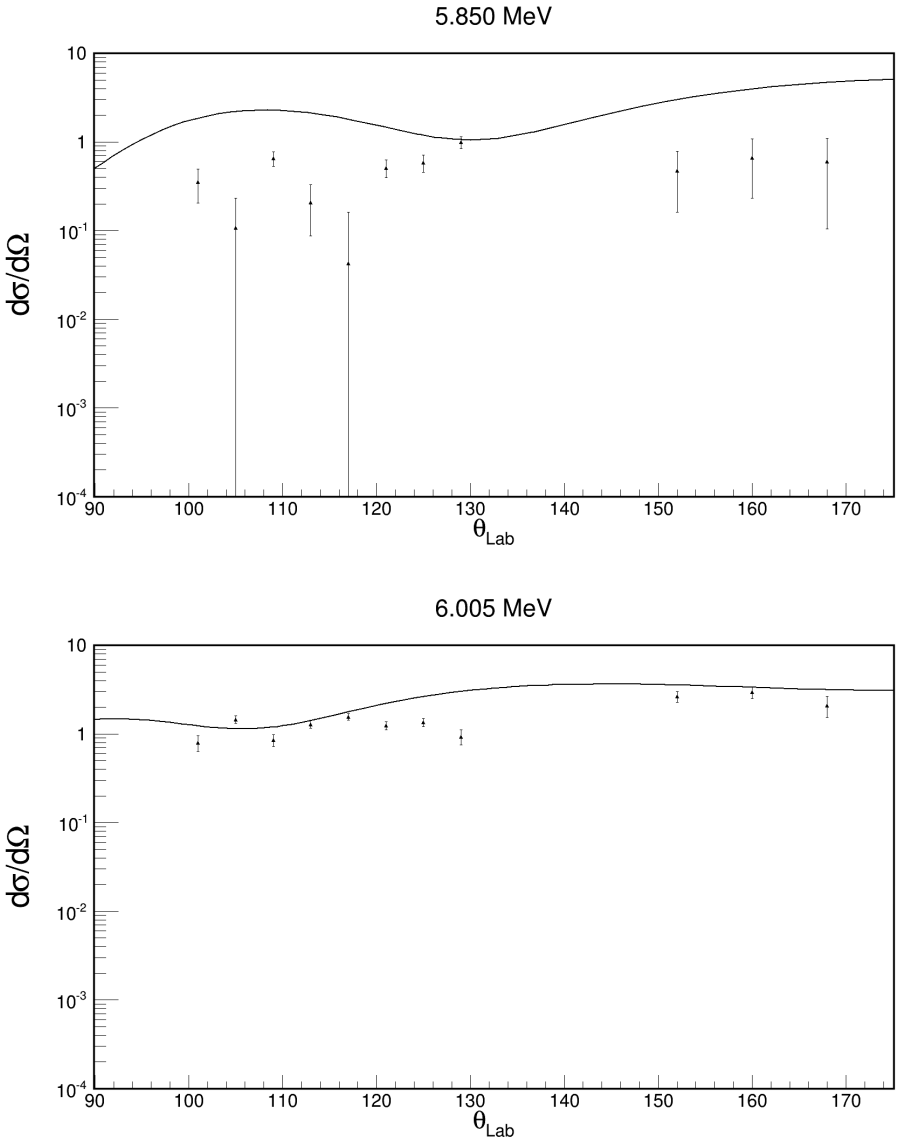

FIGURE 5.22: Comparison between theory and data for various energy levels.

In some instances, a state is created by the transfer of a particle with the same l, but different j values. An example of this is shown in 5.3 for the ground-state, which is predicted to have a spectroscopic factor of 0.0034 and 0.53521 for the $d_{3/2}$ and $d_{5/2}$ levels respectively. The method used to obtain the experimental values of the spectroscopic factors described above is not able to distinguish between the angular distributions of the $d_{3/2}$ and $d_{5/2}$ levels, and so it can only find the spectroscopic factors for states the are a superposition of different l values. In the instance where l is the same, as is the case with the ground-state, variable b in Equation 5.4 is set to 0 and the value found for a is quoted in Table 5.5 as the spectroscopic factor of the l with the largest theoretically predicted value.

The final values for the spectroscopic factors for each single-particle state at every energy

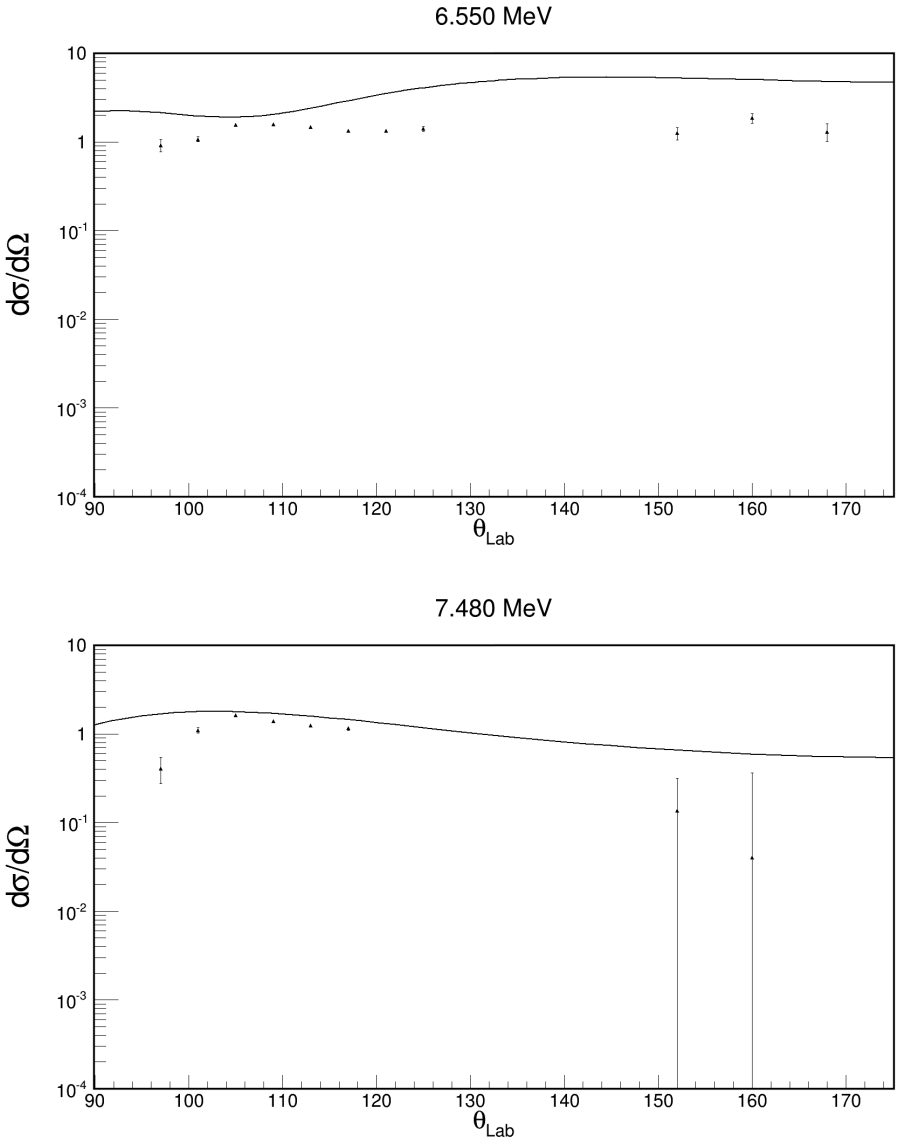

FIGURE 5.23: Comparison between theory and data for various energy levels.

examined in this analysis are listed in Table 5.5. The fits that these spectroscopic factors give are shown in Figures 5.24 to 5.33. Also shown in these figures are the contributions of the each single-particle state to the final fit. Graphs for the 0.089 and 2.914 MeV states are not shown because the minimisation program failed due to the lack of counts observed for these states.

The ground-state of ^{25}Na seems to be a pure d-wave transfer as shown in Figure 5.24. The shell-model predicts that the state is made up of two d-wave components in the transfer reaction (Table 5.3). The $d_{3/2}$ component does not contribute much to the total state compared to the $d_{5/2}$, and so it was not used to fit the data.

Excitation Energy (MeV)	Omitted Angles (°)
0.0	97, 101, 141
0.089	97, 101, 141
2.416	97, 101, 141
2.788	97, 101, 141
2.914	97, 101, 141
3.455	97, 101, 141
3.995	97, 101, 141
5.22	97, 101, 141
5.85	97, 101, 133 137, 141
6.005	97, 101, 133 137, 141
6.55	97, 101, 129 133, 137, 141
7.48	97, 101, 121 125, 129, 133 137, 141, 168

TABLE 5.4: Angles omitted when applying χ^2 minimisation scheme.

Spin/ Parity	Excitation Energy (MeV)	Spectroscopic factors s1/2	p3/2	d3/2	d5/2	f7/2
5/2+	0.0				1.08 (4)	
3/2+	0.089				0.02 (5)	
9/2+	2.416	0.028 (4)		0.01 (2)		
7/2+	2.788	0.66 (1)			0.46 (3)	
5/2+	2.914				0.006 (16)	
9/2+	3.455	0.51 (2)			0.41 (2)	
9/2+	3.995	0.024 (6)		0.56 (2)		
11/2+	5.22			0.83 (2)		
7/2+	5.85	0.00 (4)		0.52 (6)		
9/2−	6.005		0.38 (5)			1.3 (1)
11/2−	6.55		0.15 (2)			1.07 (3)
13/2−	7.48					0.83 (2)

TABLE 5.5: Experimental spectroscopic factors for each level.

The state at 2.419 MeV was not predicted to be strongly populated in the transfer reaction. The inclusion of the state in the fitting of the excitation spectra given by SHARC was based on the knowledge that it had been detected previously [69]. Previously known information about the state was limited to the energy of the state, and its decay path. The energy did not have a spin associated with it. Figure 5.25 shows the final fit found for the energy level. The total fitted angular distribution does not appear to deviate greatly from the s-wave contribution to the reaction. The d-wave contribution is also show, though it appears to to be several orders of magnitude weaker than the s-wave component.

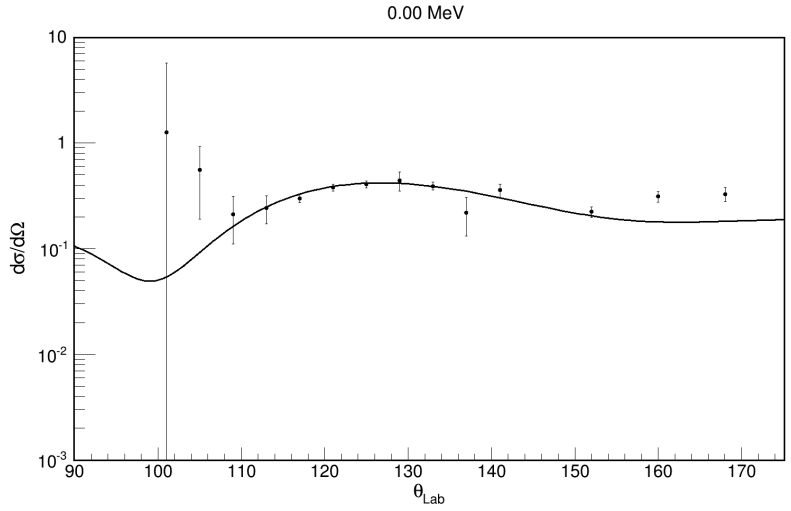

FIGURE 5.24: Fitted angular distributions for 0.00 MeV. Contributions of the d-wave to the total fit are shown.

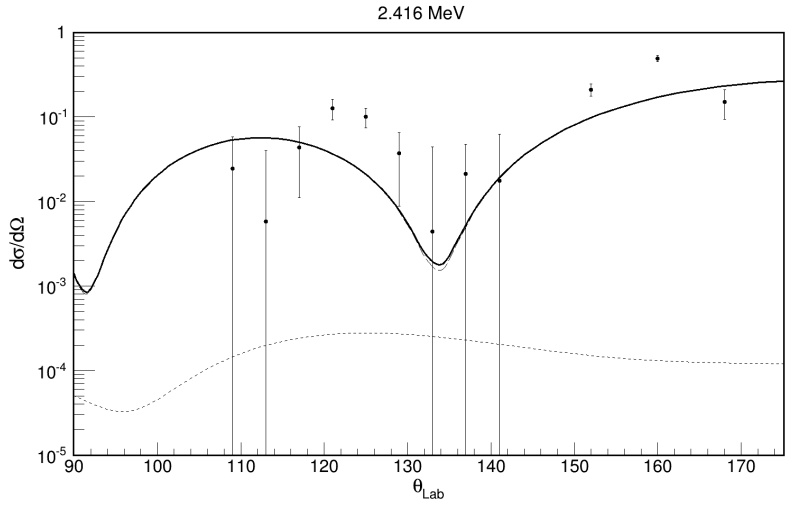

FIGURE 5.25: Fitted angular distributions for 2.416 MeV. Contributions of s-wave and d-wave to the total fit are shown.

The state at 2.788 MeV was also known prior to the experiment, however, the spin and parity values were uncertain, being thought to be one of: $1/2^+$, $3/2$ or $5/2^-$[69]. Figure 5.26 demonstrates a clear s and d-wave dependence on the shape of the angular distribution, eliminating the possibility of the state having a negative parity. The state has been identified, with strong evidence, as a $7/2^+$ state (different from what was previously thought). The figure shows that the s-wave component dominates for most of the angular range provided, with a d-wave dependency at $\sim 125^\circ - 135^\circ$.

The spin and parity of the state at 3.455 MeV was previously unknown. It was identified in this experiment as a $9/2^+$ state. As with the 2.788 MeV state, Figure 5.27 shows a

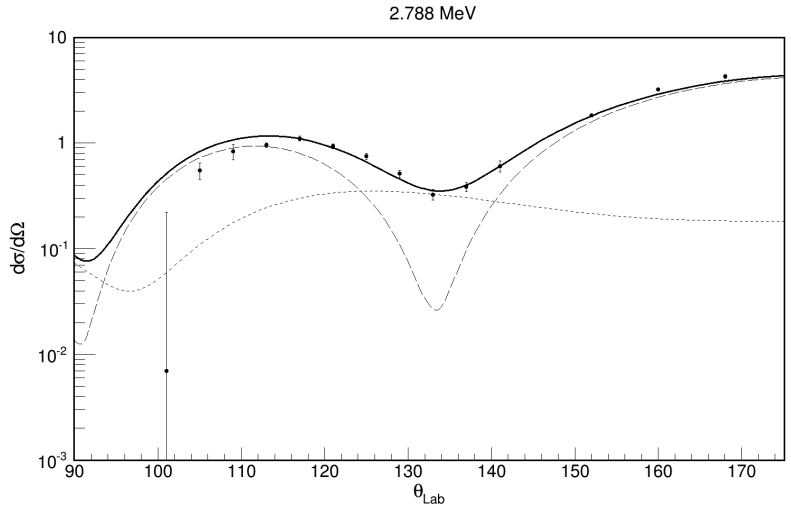

FIGURE 5.26: Fitted angular distributions for 2.788 MeV. Contributions of s-wave and d-wave to the total fit are shown.

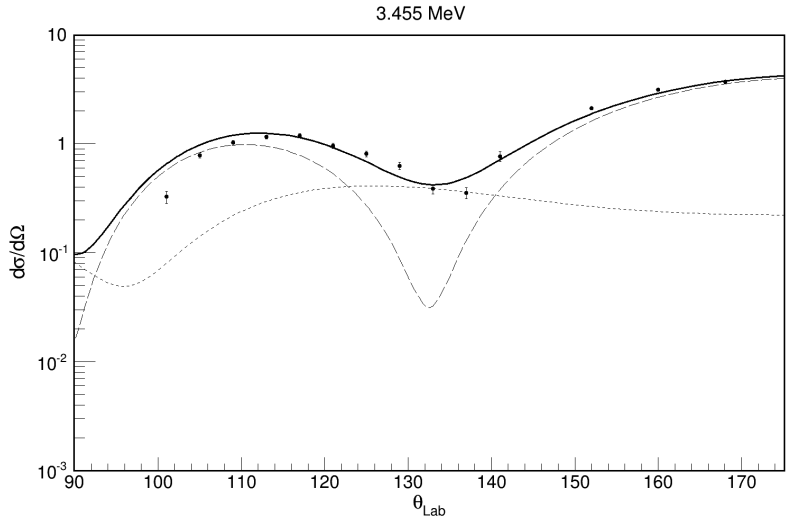

FIGURE 5.27: Fitted angular distributions for 3.455 MeV. Contributions of s-wave and d-wave to the total fit are shown.

strong s-wave dependence, with a d-wave component that become dominant within the angular range of $\sim 125° - 135°$.

Literature gives the the spin and parity of the state at 3.995 MeV to be $1/2^-$ [69]. However, the fit to the angular distribution in Figure 5.28 shows a strong d-wave transfer (and a weaker, but still important s-wave transfer), confirming a positive parity. The d-wave dominates the reaction. The s-wave does not contribute much to the total shown, but does become significant above $150°$.

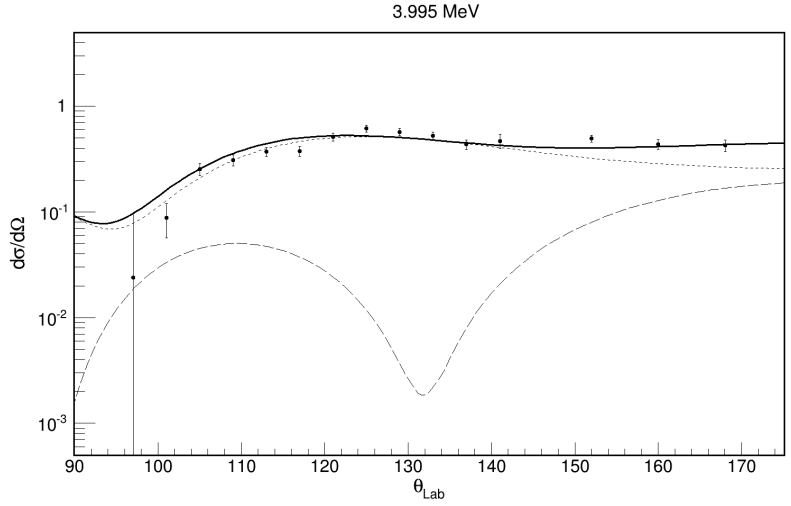

FIGURE 5.28: Fitted angular distributions for 3.995 MeV. Contributions of s-wave and d-wave to the total fit are shown.

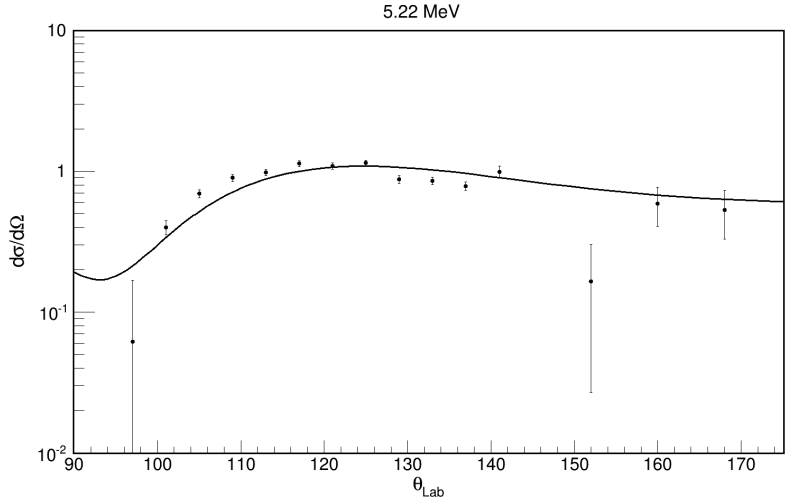

FIGURE 5.29: Fitted angular distributions for 5.22 MeV. Contributions of the d-wave to the total fit are shown.

Prior to this experiment, the 5.22 MeV energy level did not have a known spin or parity. It was identified to be an $11/2^+$ state in this work. Table 5.3 shows that spectroscopic factor of the state at 5.22 MeV consists of a pure d-wave transfer. Figure 5.29 supports this. Unlike the state at 3.995 MeV, at which the data diverges from the $l = 2$ line at 150° when the s-wave becomes significant, the data for the 5.22 MeV state seems to follow the $l = 2$ line though out the entire angular range suggesting that there is no other significant l contributing to the state.

The state at 6.005 MeV has previously been established to have a negative parity [69], but the spin of the state has not been decisively established. Figure 5.31 shows the

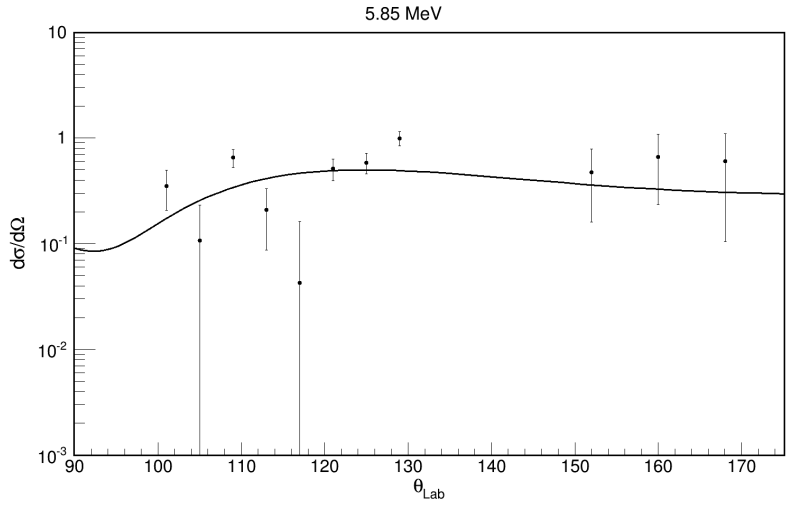

FIGURE 5.30: Fitted angular distributions for 5.85 MeV. Contributions of the d-wave to the total fit are shown.

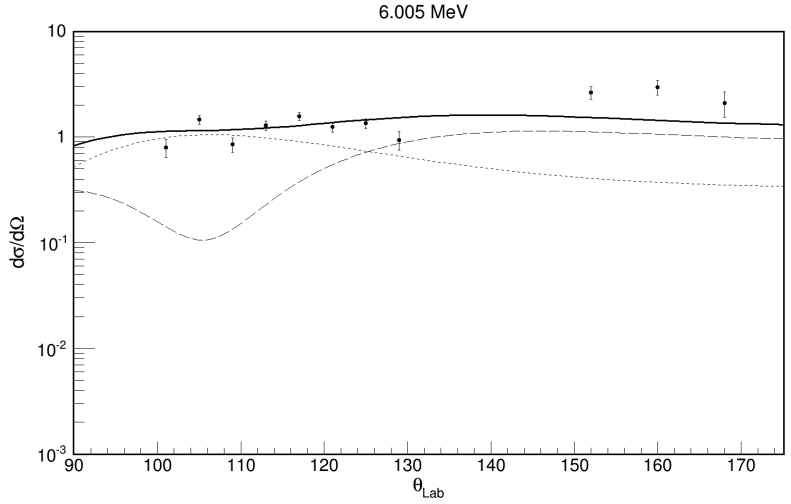

FIGURE 5.31: Fitted angular distributions for 6.005 MeV. Contributions of p-wave and f-wave to the total fit are shown.

contributions of the $l = 1$ and 3 waves produce good fits to the data, thus adding to the conclusion that this state does have a negative parity. The spin was found to be 9/2, though this was based solely on the comparison between the counts seen in the state during the experiment and the expected reaction strength.

The state at 6.55 MeV was presumed to have a spin and parity of $3/2^-$ [69]. Figure 5.32 does assume a negative parity due to the good fit produced by the $l = 1$ and 3 lines, but identified the state to have an 11/2 spin based on a comparison to the theoretical reaction strength.

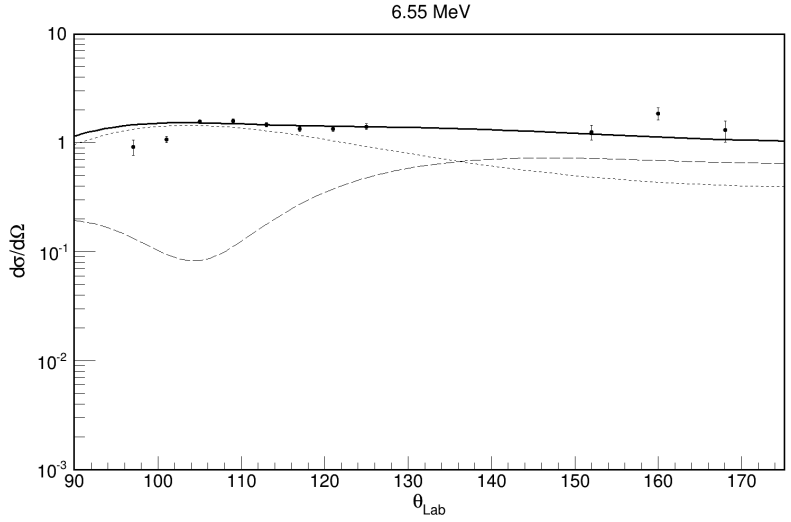

FIGURE 5.32: Fitted angular distributions for 6.55 MeV. Contributions of p-wave and f-wave to the total fit are shown.

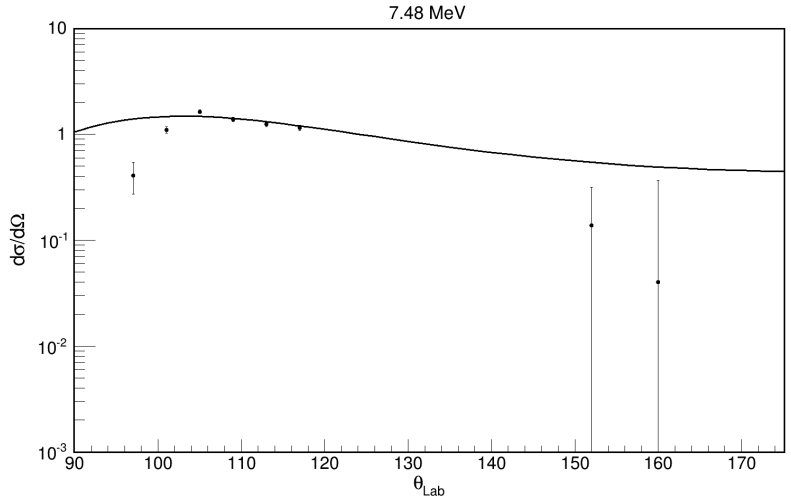

FIGURE 5.33: Fitted angular distributions for 7.48 MeV. Contributions of the f-wave to the total fit are shown.

The state at 7.48 MeV was not previously known, so no data exist for it. Figure 5.33 shows an f-wave contribution to the state which demonstrates some agreement to the data, though there are not many data points to fit due to threshold issues encountered during the experiment. The state was tentatively labelled as a $13/2^-$ state.

Some comments about Figures 5.24 to 5.33 follow. The ground-state angular distribution shown in Figure 5.24 has been fitted using a purely d-wave transfer. This fits the data well between 109° and 141°, but undershoots the data points above 152°. This same characteristic is also seen in Figure 5.28 in which the three data points above 145°

do not follow the d-wave angular distribution. In the case of the 3.995 MeV state, the divergence of these points can be accounted for by considering the s-wave angular distribution, which becomes more prominent at high lab angles. However, there is no s-wave in the ground-state because it is not possible to create a $5/2^+$ state in ^{25}Na by coupling the spin of a neutron in the $s_{1/2}$ sub-shell the the 4^+ ground-state of ^{24}Na. Figure 5.24 then, could show evidence for higher order contributions playing a small but noticeable role in the population of the ground-state.

The states that were identified with negative parities during the experiment consistently fail to match the spin values seen in literature. These states were identified using the predicted reaction strengths calculated in Section 5.1.4, a process that depends upon the accuracy of the predictions of the spectroscopic factors given by the shell-model. Figures 5.20 and 5.21 were created using these predictions and highlight the reliability of the shell-model. The identification of other states took the reaction strength into account, but used a host of other evidence to come to a conclusion as to what the state was. The only evidence that was available to identify the negative parity states was the reaction strength.

A comparison of the SF predicted by the shell-model and found in this experiment is shown in Figure 5.34.

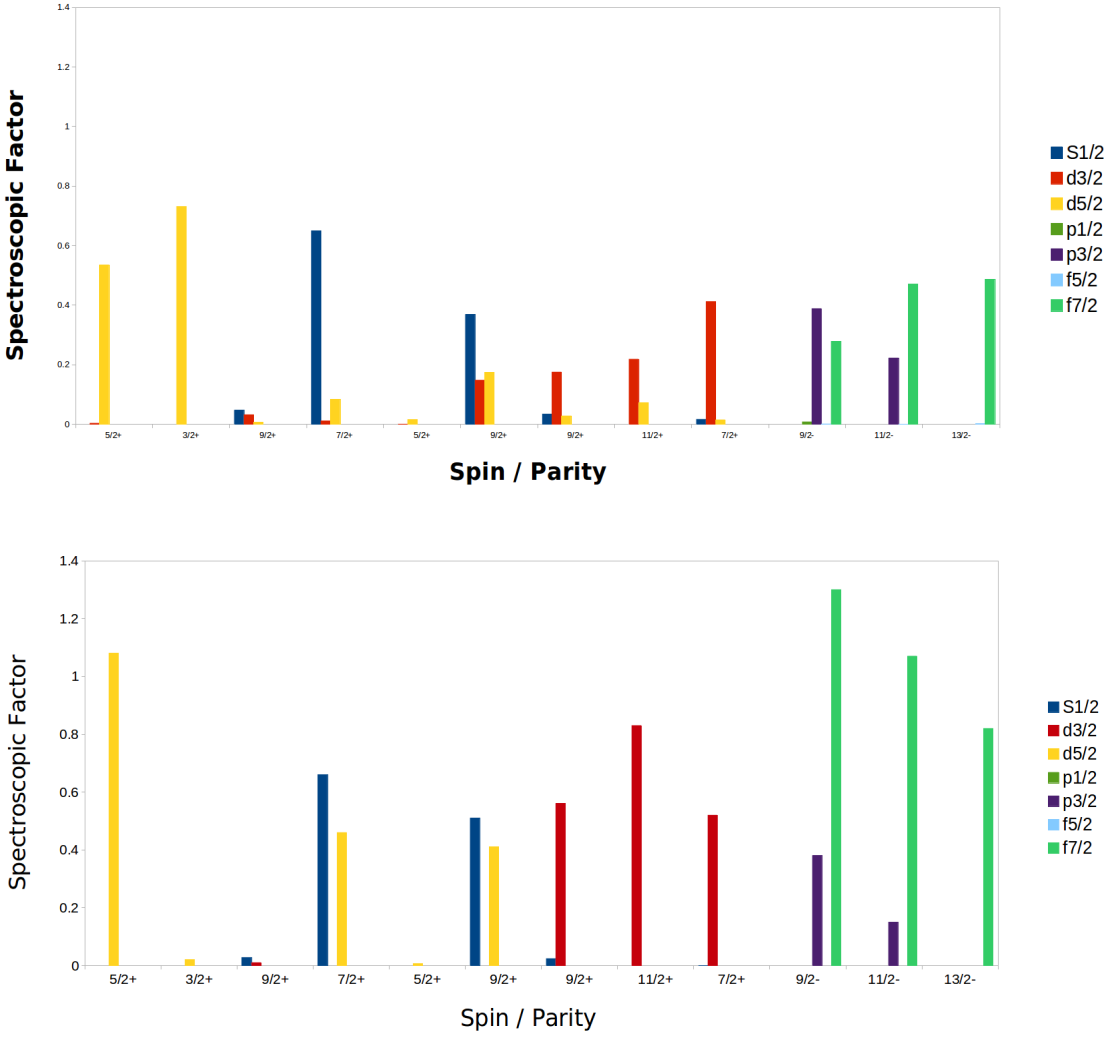

FIGURE 5.34: Spectroscopic factors predicted by the shell-model (top panel) compared to those found in the experiment (bottom panel).

Chapter 6

Discussion

The experiment discussed in this work aimed to examine the shell structure of ^{25}Na, in particular, the excitation energies between 3.4 and 4.0 MeV. This energy range is within 0.6 MeV of the proton threshold of ^{25}Na's mirror nucleus, ^{25}Si. Due to a weak beam intensity, during the experiment, some of the weakest states predicted by the shell-model (which could still be important astrophysically) were not able to be studied, but the more strongly populated states, including two states that are relevant to the energy region of interest, could be studied in detail.

This chapter will discuss the results in two parts: the first will compare the observed structure of ^{25}Na to the structure predicted by the shell-model, the second will discuss the states relevant to the $^{24}\mathrm{Al}(p,\gamma)^{25}\mathrm{Si}$ reaction. The shell-model predictions for energy and spectroscopic factors were taken from WBC calculations, which incorporates USD-A shell-model calculations. The occupancies of each state were obtained from WBP-M calculations, which derives from USD calculations. The reason for taking values from different shell-models is simply that there is currently no algorithm to calculate the occupancies in the newer WBC model and so WBP-M is used when it is not possible to use WBC.

6.1 The Structure of ^{25}Na

6.1.1 Positive Parity States

States with a positive parity have no p or f-wave contribution to the wave functions since the nucleons all remain in the sd-shell (and so $l = 0, 2$) for the low-lying states in ^{25}Na. The average occupancies, n, of the sub-shells in these positive parity states (Tables 6.1,

J^{π}_{n}	SF $(d_{5/2})$	SF $(s_{1/2})$	SF $(d_{3/2})$	n$(d_{5/2})$	n$(s_{1/2})$	n$(d_{3/2})$
$7/2^{+}_{1}$	0.08	0.65	0.11	6.77	1.46	0.78
$7/2^{+}_{2}$	0.02	0.01	0.00	6.68	1.49	0.83
$7/2^{+}_{3}$	0.05	0.00	0.11	6.89	1.23	0.88
$7/2^{+}_{4}$	0.00	0.02	0.01	6.60	1.39	1.01
$7/2^{+}_{5}$	0.01	0.02	0.41	6.62	1.00	1.38
$7/2^{+}_{6}$	0.01	0.00	0.03	6.28	1.39	1.32
$7/2^{+}_{7}$	0.00	0.01	0.00	6.56	1.29	1.15

TABLE 6.1: The spectroscopic factors for each sub shell in the sd-shell for $7/2^{+}$ states as calculated by the WBC shell-model. The average occupancies for each sub shell in the sd-shell for $7/2^{+}$ states as calculated by the WBP-M shell-model.

J^{π}_{n}	E_{Exp} (MeV)	E_{WBC} (MeV)	E_{WBP-M} (MeV)	Shift (keV)
$7/2^{+}_{1}$	2.788	2.791	2.730	+61
$7/2^{+}_{2}$		3.421	3.019	+402
$7/2^{+}_{3}$		4.097	4.003	+94
$7/2^{+}_{4}$		4.694	4.657	+37
$7/2^{+}_{5}$	5.85	5.185	4.940	+245
$7/2^{+}_{6}$		5.644	5.361	+283
$7/2^{+}_{7}$		6.107	5.974	+33

TABLE 6.2: A comparison between the WBC, WBP-M shell-model predictions and the experimentally seen energies for $7/2^{+}$ states. The shifts between the different shell-model energies are also shown.

6.3 and 6.5) will all sum up to nine because there are three protons and six neutrons coupling together to create the state.

As discussed in Chapter 1, the coupling of the three protons in ^{25}Na make up the first $5/2^{+}$, $3/2^{+}$ and $9/2^{+}$ states when the neutrons fill up the $d_{5/2}$ shell and are coupled to 0^{+}. The WBC shell-model calculates the spectroscopic strengths of the $5/2^{+}$ ground-state and the first $3/2^{+}$ state to be dominated by the $d_{5/2}$ wave function in both cases. This prediction is not observed within the experimental results (Figure 5.34) which shows a large $d_{5/2}$ contribution to the ground-state, but gives a near zero spectroscopic strength for the $3/2^{+}$ excited state. This discrepancy between theory and experiment is likely caused by the experimental limitation to resolve the ground-state from the $3/2^{+}$ state at 0.089 MeV. This poor resolution caused the fitting algorithm used to fit the excitation spectra to put all the strength into the ground-state and ignore the $3/2^{+}$ state. This resulted in the large spectroscopic factor of 1.08 ± 0.04 for the ground-state, an a small spectroscopic factor of 0.02 ± 0.04 for the $3/2^{+}$ state.

The details of the first seven $7/2^{+}$ states predicted by the shell-model are given in Table 6.2. Of these listed states, only two are observed experimentally during this work. A difference of less than 200 keV between experiment and theory is generally considered to be acceptable for excitation energies. The first observed $7/2^{+}$ state at 2.788 MeV is well

J^{π}_{n}	SF $(d_{5/2})$	SF $(s_{1/2})$	SF $(d_{3/2})$	n$(d_{5/2})$	n$(s_{1/2})$	n$(d_{3/2})$
$9/2^{+}_{1}$	0.01	0.05	0.03	7.46	0.77	0.76
$9/2^{+}_{2}$	0.17	0.37	0.15	6.94	1.14	0.92
$9/2^{+}_{3}$	0.03	0.03	0.18	6.91	1.22	0.87

TABLE 6.3: The spectroscopic factors for each sub shell in the sd-shell for $9/2^{+}$ states as calculated by the WBC shell-model. The average occupancies for each sub shell in the sd-shell for $9/2^{+}$ states as calculated by the WBP-M shell-model

within this range since the difference between this energy and that given by the WBC calculation is 3 keV. The second observed $7/2^{+}$ state observed differs quite dramatically from the theoretical prediction, as can be seen in Figure 5.19. The observed energy of this state is 5.85 MeV, and corresponds with the theoretical energy of 5.185 MeV, and so the difference between the two is -665 keV. However, as is seen in Table 6.2, the $7/2^{+}_{6}$ state has an energy of 5.644, which is -206 keV from the experimental energy. It is therefore possible that the experimentally observed energy has been misidentified as the $7/2^{+}_{5}$ state when it is in fact the $7/2^{+}_{6}$ state and the shell-model has failed to obtain the correct phases or other properties in the wave functions. This argument is supported by the average occupancies of the sub-shells of the $7/2^{+}_{5}$ and $7/2^{+}_{6}$ states shown in Table 6.1, which are very similar to each other.

The comparison of the spectroscopic factors between theory and experiment is shown graphically in Figure 5.34. The $s_{1/2}$ component of the wave function for the first $7/2^{+}$ state is shown here to give a similar value for both the theory and the experiment (0.65 and 0.66 ± 0.01 respectively). In comparison, the differences between the experimental and theoretical values for the $d_{5/2}$ portion of the wave function for this state are very different, with the experimental value being found to be 0.46, approximately six times larger, than the predicted value of 0.08.

The same information for the $9/2^{+}$ states are given in Tables 6.4 and 6.3. The lowest of these states has an almost zero spectroscopic factor, which is reflected in the results shown in Figure 5.34. The occupancies for this level (and indeed, for all other $9/2^{+}$ states) shows that the transferred neutron is most likely to be found in the $d_{5/2}$ sub-shell, which completes a pair. When the neutron is found in this level, then the spin of the neutrons will couple to zero, and so the $9/2^{+}$ will be created by the coupling of the protons in the $d_{5/2}$ sub-shell. The protons are only expected to be coupled to $9/2^{+}$ 3% of the time. In a single-step direct reaction, which is assumed to be dominant in a (d, p) reaction, it is inherent that the lowest $9/2^{+}$ will be weakly populated for this reason.

The second $9/2^{+}$ state is very strongly populated in the data. The comparison between theoretical and experimental spectroscopic factors for the $s_{1/2}$ portion of the wave function remains the biggest contribution to the wave function, but has a value of 0.51 ± 0.02

J_n^π	E_{Exp} (MeV)	E_{WBC} (MeV)	E_{WBP-M} (MeV)	Shift (keV)
$9/2_1^+$	2.416	2.522	2.542	-20
$9/2_2^+$	3.455	3.263	3.155	$+108$
$9/2_3^+$	3.995	3.927	3.918	$+9$

TABLE 6.4: A comparison between the WBC, WBP-M shell-model predictions and the experimentally seen energies for $9/2^+$ states. The shifts between the different shell-model energies are also shown.

J_n^π	SF $(d_{5/2})$	SF $(s_{1/2})$	SF $(d_{3/2})$	n$(d_{5/2})$	n$(s_{1/2})$	n$(d_{3/2})$
$11/2_1^+$	0.07	0.00	0.22	6.93	1.05	1.02
$11/2_2^+$	0.01	0.00	0.08	6.85	1.12	1.04
$11/2_3^+$	0.00	0.00	0.08	6.81	1.12	1.07
$11/2_4^+$	0.00	0.00	0.15	6.81	1.04	1.15

TABLE 6.5: The spectroscopic factors for each sub shell in the sd-shell for $11/2^+$ states as calculated by the WBC shell-model. The average occupancies for each sub shell in the sd-shell for $11/2^+$ states as calculated by the WBP-M shell-model.

experimentally and 0.37 theoretically. The theory predicts the d-wave contribution to the wave function to be divided fairly evenly between the $d_{5/2}$ and $d_{3/2}$, with the spectroscopic factors being 0.17 and 0.15 respectively. Experimentally, the $d_{5/2}$ state was found to have a spectroscopic factor of 0.41. It should be pointed out, however, that fitting the d-wave angular distributions to the data was the method for discerning the experimental spectroscopic factors. This method does not distinguish between the $d_{5/2}$ and $d_{3/2}$ states, and so the experimentally obtained value could be a mix of the $d_{5/2}$ and $d_{3/2}$ contribution to the wave function. If the d-wave contribution is split evenly between $d_{5/2}$ and $d_{3/2}$, as the shell-model predicts, then the spectroscopic factors for each state will be approximately ≈ 0.21, which is close to the theoretical value.

Only the first $11/2^+$ state was observed in the experiment. The WBC model fails in assigning the correct spectroscopic strength and energy to this state. The energy of the state predicted by the shell-model is given in Table 6.6. The difference between the experimental energy and what is predicted by the WBC model is 467 keV, which is much larger than is usually expected. This could mean that the observed state is the second $11/2^+$ state and that the spectroscopic strength obtained from the WBC model is weighted incorrectly.

With regard to the spectroscopic strength, if the observed state is the first $11/2^+$ state, then the theory predicted a value of 0.07 and 0.22 (Table 6.5) for the $d_{5/2}$ and $d_{3/2}$ states respectively. The experimental value obtained for $d_{3/2}$ was 0.83, which is significantly higher than the theoretical value.

J_n^π	E_{Exp} (MeV)	E_{WBC} (MeV)	E_{WBP-M} (MeV)	Shift (keV)
$11/2_1^+$	5.22	4.753	4.540	+210
$11/2_2^+$		5.394	5.587	-193
$11/2_3^+$		6.177	5.919	+258
$11/2_4^+$		7.043	6.940	+103

TABLE 6.6: A comparison between the WBC, WBP-M shell-model predictions and the experimentally seen energies for $11/2^+$ states. The shifts between the different shell-model energies are also shown.

6.1.2 Negative Parity States

For ^{25}Na, a negative parity state is primarily formed by inserting a neutron into the pf-shell and so these states are generally seen at higher energy levels than positive parity states. The average occupancies for each sub-shell in Table 6.7 equates to a value less than one because it is possible to create a negative parity state by exciting a neutron from the p-shell to the in the core of ^{25}Na to the sd-shell in addition to creating a negative parity state by placing a neutron in the pf-shell. This is appears to be especially true in the case of the $7/2_1^-$ and $9/2_1^-$ states shown in Table 6.7.

The first negative parity states with significant spectroscopic factors predicted by the shell-model does not occur until 5.804 MeV (Table 6.8), however, the first energy level seen experimentally is the $9/2^-$ state at 6.005 MeV. The energies of the $9/2_2^-$, $11/2_1^-$ and $13/2_1^-$ states where observed to have a lower energy than predicted by the WBC by 228, 272 and 336 keV respectively. This degree of agreement is reasonable for the relatively high excitation energy of the state. A similar shift could place the $7/2_2^-$ state at 6.4 MeV, which would be difficult to resolve from the $11/2_1^-$ state in this experiment. If this is the case, then the γ-ray transition from the $7/2_2^-$ level, which is heavily dominated by the transition to the ground-state of ^{25}Na, would not be observed due to the low γ detection efficiency at 6.4 MeV. Thus, some of the p-wave strength attributed to the $11/2_1^-$ may come from the unidentified and unresolvable $7/2_1^-$ state.

The spectroscopic factors found in this work and quoted in Table 5.5 for the f-wave component of the wave function for the negative parity states are greater than one for the $9/2_2^-$ and $11/2_1^-$ states. The experimental errors derived from uncertainties in the data are quoted, but do not take into account the errors that are associated with the theory used to describe the reaction. Reference [70] quantifies this error for nuclei in the range of $Z = 8 - 28$ to be $\pm 40\%$, which reduces the observed spectroscopic factors for these states to a reasonable value.

Overall, The WBC shell-model is seen to provide an acceptable model of structure and relative energy of the negative parity states in ^{25}Na.

J_n^π	SF $(f_{7/2})$	SF $(p_{3/2})$	SF $(p_{1/2})$	n$(f_{7/2})$	n$(p_{3/2})$	n$(p_{1/2})$
$7/2_1^-$	0.07	0.03	0.00	0.16	0.04	0.01
$7/2_2^-$	0.10	0.20	0.03	0.21	0.25	0.05
$9/2_1^-$	0.03	0.03	0.01	0.12	0.03	0.01
$9/2_2^-$	0.03	0.39	0.01	0.37	0.43	0.04
$11/2_1^-$	0.47	0.22	0.00	0.52	0.37	0.02
$13/2_2^-$	0.49	0.00	0.00	0.65	0.27	0.01
$15/2_1^-$	0.30	0.00	0.00	0.78	0.15	0.01
$15/2_2^-$	0.20	0.00	0.00	0.61	0.08	0.01

TABLE 6.7: The spectroscopic factors for each sub shell in the pf-shell as calculated by the WBC shell-model. The average occupancies for each sub shell in the pf-shell as calculated by the WBP-M shell-model.

J_n^π	E_{Exp} (MeV)	E_{WBC} (MeV)	E_{WBP-M} (MeV)	Shift (keV)
$7/2_1^-$		5.804	5.778	+26
$7/2_2^-$		6.154	6.154	+0
$9/2_1^-$		5.875	5.819	+38
$9/2_2^-$	6.005	6.233	6.206	+27
$11/2_1^-$	6.55	6.822	6.797	+25
$13/2_1^-$	7.48	7.816	7.783	+33
$15/2_1^-$		8.982	8.940	+42
$15/2_2^-$		10.331	10.396	-65

TABLE 6.8: A comparison between the WBC, WBP-M shell-model predictions and the experimentally seen energies. The shifts between the different shell-model energies are also shown.

The difference between the spectroscopic factors predicted using the WBC shell-model and the experiment is shown in Tables 5.3 and 5.5. Aside from a tendency to reduce the strength of the $f_{7/2}$ level in lowest negative parity states and some other minor differences in spectroscopic strengths described in this and the preceding section, the WBC shell-model is able to describe the energy scheme of ^{25}Na reasonably well.

6.1.3 Comparison to Literature

The current knowledge of ^{25}Na was described in the Introduction with a summary of the energies, spins and parities given in Table 1.1. A comparison between the results found in this work to the results found in previous studies is given in Table 6.9.

The spin assignments assigned from the current work do not always agree with those from the literature. The most serious discrepancy between literature and this work is for the 3.995 MeV excited state which was reported to be a $1/2^-$ state in reference [12] which populated ^{25}Na using the (d,t) reaction. The angular distribution reported for the 3.995 in [12] is not dramatically different to that given for the $5/2^+$ ground-state, which could indicate the pick up of a $d_{5/2}$ proton. There is some disagreement about which

spin and parity should be assigned to the state at 2.788 MeV. As stated in reference [69], the literature spin value of this state is assumed, in part, because of the γ decay of the 3.995 MeV energy through the 2.788 MeV energy level, which then decays to the ground-state. Hence, the incorrect spin for the 2.788 MeV energy is derived from the incorrect spin assignment of the higher energy state. The 2.788 MeV excited energy level was very strongly populated in this experiment, and so there is strong evidence for it being $7/2^+$, and the present work confirms the state at 3.995 MeV as having a $9/2^+$ spin and parity. The WBC shell-model predicts the lowest $1/2^-$ to lie closer to 3.0 MeV than 4.0 MeV, which could relate to a state that has not yet been observed, or could be the spin assignment of a state at 3.353 MeV (Table 1.1).

6.2 Astrophysical Relevance - the ^{25}Si Nucleus

The ^{25}Si nucleus is the mirror partner of ^{25}Na. It is proton bound and is expected to have a level scheme very similar to ^{25}Na. States between the proton separation energy of 3.414 MeV and $4MeV$ are of astrophysical relevance. For ^{25}Na, this energy region is bound since the neutron separation energy is $S_n = 9.011$ MeV, hence, information gained about the states in this region in the present work can provide information about the certain unbound states in ^{25}Si.

The Coulomb barrier heavily hinders the proton channel in the $^{24}\mathrm{Al}(p,\gamma)^{25}\mathrm{Si}$ reaction, and so the preferred decay mode of the resonance is through γ-ray emission. Equation 2.29 shows that the resonance strength is proportional to $\Gamma^{(+)}\Gamma^{(-)}/(\Gamma^{(+)} + \Gamma^{(-)})$. In a (p,γ) reaction, $\Gamma^{(+)} = \Gamma_p$ and $\Gamma^{(-)} = \Gamma_\gamma$. If $\Gamma_p \ll \Gamma_\gamma$ then $\Gamma_\gamma \approx \Gamma_p + \Gamma_\gamma$, and so

Excitation Energy (MeV)	J^π (Present Work)	J^π (Literature)[33]	J^π [5]
0.00	5/2+	5/2+	5/2+
0.089	3/2+	3/2+	3/2+
2.416	9/2+		9/2+
2.788	7/2+	(1/2+, 3/2, 5/2−)	7/2+
2.914	5/2+	5/2+	5/2+
3.455	9/2+		3/2+
3.995	9/2+	1/2−	
5.22	11/2+		
5.85	7/2+		
6.005	(9/2−)	(1/2, 3/2)−	
6.55	(11/2−)	3/2−	
7.48	(13/2−)		

TABLE 6.9: Comparison between spins and parities from the current work and literature. The third column gives the spins from NNDC [33]. The fourth column gives the spins from Herndl et al [5].

the reaction rate is effectively proportional to Γ_p for resonances in ^{25}Si. The ratio of σ/σ_{SPM} gives the spectroscopic factor of a reaction (Equation 2.20). Since $\sigma \propto \omega\gamma$, then this also means that the ratio of the proton width to the single-particle proton width also gives the spectroscopic factor. By applying this method in reverse, the value of the proton width, Γ_p can be estimated from the measured spectroscopic factor obtained from studying ^{25}Na.

Experiments show that many pairs of mirror nuclei at $A \approx 25$ share a similar energy structure to each other [33] except for when the $s_{1/2}$ sub-shell is populated. In these instances, the large rms radius of the $s_{1/2}$ nucleons and the associated change in Coulomb interaction with the core protons causes a shift in the energy level [5]. The change in the Coulomb potential between the mirror pair causes a downward shift in the energy of the state for the proton rich nucleus due to matching of the proton wave function before and after the reaction takes place. This shift is known as the Thomas-Ehrman shift which is described in detail in reference [71].

The few energy levels of ^{25}Si that have been determined experimentally were obtained using the ^{28}Si(^{3}H,^{6}He)^{25}Si reaction [72]. Figure 6.1 shows the energy scheme obtained from this experiment and compares it to the energy scheme of ^{25}Na. The lines that tentatively link the states are taken from reference [72] except for the uppermost state where the line connects to the 3.995 MeV state that was observed during this experiment whereas the original connection was to the 3.928 MeV energy in ^{25}Na. The only information available for the states in ^{25}Si are their energies, and so the only basis for these connections is the similarity between the energies of the states. Matching the 3.820 MeV state in ^{25}Si to the 3.995 MeV state in ^{25}Na is therefore reasonable.

Regarding the energy range of astrophysical relevance. Only two states observed in this experiment are observed between 3.414 and 4.000 MeV: the $9/2^+_2$ state at 3.455 MeV, and the $9/2^+_3$ state at 3.995 MeV. Of these, the state at 3.455 MeV is very strongly populated, but is only 41 keV over the 3.414 MeV threshold which means that the Coulomb barrier will greatly suppress the population of this state. In addition to this, the state also has a strong s-wave contribution to its wave function, as is shown in Figure 5.27, and so will experience a large Thomas-Ehrman shift to below 3.414 MeV. This means that the $9/2^+_2$ state is likely a bound state in ^{25}Si, and therefore not relevant to the astrophysical *rp*-process. However, it may still be useful to consider the results gained in this work for this state and compare to results presented by Herndl et al. [5]. Table 6.10 gives the spectroscopic factors for the states examined by Herndl et al. and compares them to the spectroscopic factors found in this work.

The most significant result in Table 6.10 is the agreement between the s-wave spectroscopic factor found from the experiment and given by the shell-model used by Herndl et

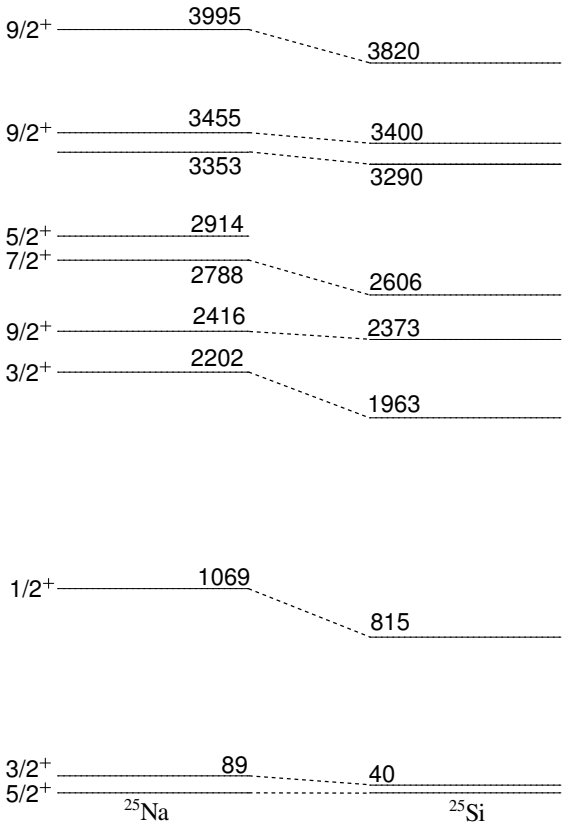

FIGURE 6.1: Comparison of ^{25}Na and ^{25}Si energy levels. The lines connecting states are tentative and are based purely on the similarity of the energy levels between the nuclei.

J^π_n	E_{WBC} (MeV)	E_{Exp} (MeV)	$\mathrm{SF}_{\mathrm{Herndl}}$			$\mathrm{SF}_{\mathrm{Exp}}$		
			$d_{5/2}$	$s_{1/2}$	$d_{3/2}$	$d_{5/2}$	$s_{1/2}$	$d_{3/2}$
$9/2^+_2$	3.263	3.455	0.18	0.33	0.17	0.41	0.51	
$5/3^+_3$	3.813		0.02		0.01			
$9/2^+_3$	3.927	3.995	0.03	0.02	0.144		0.02	0.53
$7/2^+_3$	4.097		0.04	0.01	0.16			
$5/2^+_4$	4.153		0.04		<0.01			
$5/2^+_5$	4.416		<0.01		<0.01			

TABLE 6.10: Comparison of spectroscopic factors calculated by Herndl et al. and observed in experiment. All experimental errors for the spectroscopic factors equate to ± 0.02 except for 0.02 which is ± 0.01.

al. The absence of experimental results for the other states listed in the table confirms that these state in the energy region of interest are too weak to be observed.

The reaction rates for each of the resonant states for p+^{24}Al calculated by Herndl et al. are shown in Figure 2.5. The lowest energy plotted is for $E_R = 0.19$ MeV, which corresponds to the $5/2^+_3$. The resonance at $E_R = 0.41$ MeV corresponds to the $9/2^+_3$ state which is measured during this experiment. The s component of the wave function found from experiment for this state matches the value used by Herndl et al. which is relevant because s-transfers are usually the dominating reaction channel in astrophysical reactions due to their zero angular momentum. The $E_R = 0.50$ and 0.51 MeV resonances correspond to the $7/2^+_3$ and $5/2^+_4$ states respectively, and were not measured during this experiment, and so it can be deduced that the shell-model gives the correct order of magnitude for their spectroscopic factors.

Chapter 7

Conclusion

New knowledge has been obtained about the structure of ^{25}Na. The use of the TIGRESS HPGe detector array in conjunction with the SHARC DSSSD array demonstrates the benefits of simultaneous particle and γ-ray detection. Silicon detectors such as those used in SHARC tend to have poor energy resolution when compared to the HPGe detectors used in TIGRESS. Using both types of detector allows for the efficient detection of particles which is necessary in order to determine the excited energies populated during the (d, p) reaction while simultaneously being able to resolve energy doublets using the coincident γ-rays that are emitted from these states. This feature of the experimental set-up allowed for the identification of the the excited sate appearing at 0.089 MeV, which was otherwise unresolvable from the ground-state.

A thick 1.0 mg/cm^2 target was used in order to increase the probability of a reaction occurring given the low beam intensity of 10^4 pps. The decision to do this caused the energy resolution in SHARC to decrease due to a greater spread of energies with which the protons will emerge from the target. However, this drop in resolution proved to be necessary in order to utilise TIGRESS effectively since it was very difficult to identify some of the energy peaks seen in the γ-ray spectra. Using a 0.5 mg/cm^2 target, as originally planned, would have made some of the γ-ray peaks indistinguishable from background. This observation leads to the conclusion that the 10^4 pps is the limit of this technique's effectiveness to measure the spectroscopic factors of the $d(^{24}\mathrm{Na}, p)^{25}\mathrm{Na}$ reaction.

The position of SHARC relative to the target was required to calculate the excitation energies of the ^{25}Na nucleus. Previous experiments using the SHARC and TIGRESS arrays to find the structure of ^{26}Na [57] [63] acquired the detector positions by fitting kinematic lines to the data. Due to issues with the threshold during this work, it was discovered that the kinematic lines for inelastic scatter did not follow the value that

theory dictated close to the threshold cut-off energy. Additionally, particles that punch through the DSSSDs only deposit a fraction of their total energy in the detector. These combined effects cause the kinematics from the data to have a shollower gradient than the theoretical kinematic line. These effects are small and therefore do not usually affect the fit of the data to theory. During this work, the threshold of the detectors was set to 2 MeV for all but one of the DSSSDs, making a fit to the theoretical kinematic lines impossible. A technique was developed in order to correctly position SHARC that did not rely on fitting the kinematic data to theory. Spectra from individual pixels in the DSSSDs were analysed in order to determine the shift required to position the array at the correct position.

The state at 2.416 MeV was overshadowed by the nearby 2.788 MeV peak. The state at 2.416 MeV was very weakly populated in this experiment due to the fact that it arose from proton excitation, which is unlikely to occur in a (d, p) reaction. The energy level had been identified previously, but no spin/parity value had been assigned to it. The spin/parity values were obtained for each state observed by analysing the γ-rays detected by TIGRESS and by comparing the expected "Reaction strength", $\mathcal{R} = S(2J + 1)\sigma$, to the yield of each energy level obtained experimentally. Using this method, the levels with previously unknown spins and parities at 2.416, 3.455, 5.22 and 5.85 MeV where assigned $9/2^+$, $9/2^+$, $11/2^+$ and $7/2^+$ respectively. Negative parity states were also identified using this technique, though the results are less conclusive due to a lack of γ-ray statistics and the fact that the angular distributions appear to be very flat.

The third $9/2^+$ state was shown to be at an excited energy of 3.995 MeV. This energy level had previously been identified to have a spin and parity of $1/2^-$, which lead to the state at 2.788 MeV to be given an incorrect spin/parity value shown in Table 6.9 based on the observed decay pain through this state. The 2.788 MeV state was very clear in this experiment, which led to strong evidence of it being the first $7/2^+$ state. The γ-ray decay scheme, coupled with the angular distribution obtained for the excited state at 3.995 MeV confirm that this state should be identified as the third $9/2^+$ state.

The spectroscopic factors found in this experiment generally support those predicted by the WBC shell-model with a few exceptions: the spectroscopic factors for the ground-state and $3/2^+$ state appear to be under and over estimated respectively. This is probably due to the experiment's inability to resolve these two states which results in the strength of the state being assigned to the ground-state while the $3/2^+$ first excited state is ignored. There also appears to be a tendency for the $f_{7/2}$ level to dominate the structure of low-lying negative parity states in the experiment, compared to predictions made by the shell-model. In general, however, the WBC calculations are a good guide to the strongly populated states, as is shown graphically in Figures 5.17 and 5.18.

Astrophysically, the only observed state that is expected to contribute to the *rp*-process that is in the energy region of interest is the $9/2^+$ state at 3.995 MeV. The spectroscopic factor for the s-component of the wave function of this state matches the value predicted by Herndl et al. [5]. The inability to detect any other state within the energy region of interest is also in keeping with what was predicted by Herndl, suggesting that their reaction rate calculations do not need to be greatly modified. The $9/2^+$ state at 3.455 MeV appears at an energy that would be unbound in ^{25}Si, but is expected to be Thomas-Ehrman shifted below threshold and so is not expected to contribute to astrophysical reaction rates.

Bibliography

[1] W. N. Catford et al. Nucleon transfer via (d,p) using TIARA with a ^{24}Ne radioactive beam. *Journal of Physics G: Nuclear and Particle Physics*, 31(10):1655–1661, (2005).

[2] S. M. Brown, W. N. Catford et al. Low-lying neutron fp-shell intruder states in ^{27}Ne. *Phys. Rev. C*, 85:011302, (2012).

[3] G. L. Wilson and W. N. Catford et al. Towards ^{26}Na via (d,p) with SHARC and TIGRESS and a novel zero-degree detector. *Journal of Physics: Conference Series*, 381(1):012097, (2012).

[4] N. K. Timofeyuk, R. C. Johnson and A. M. Mukhamedzhanov. Relation between Proton and Neutron Asymptotic Normalization Coefficients for Light Mirror Nuclei and its Relevance to Nuclear Astrophysics. *Phys. Rev. Lett.*, 91:232501, (2003).

[5] H. Herndl, J. Görres, M. Wiescher, B. A. Brown, and L. Van Wormer. Proton capture reaction rates in the *rp* process. *Phys. Rev. C*, 52:1078–1094, (1995).

[6] C. Iliadis, A. Champagne, J. José, S. Starrfield and P. Tupper. The Effects of Thermonuclear Reaction-Rate Variations on Nova Nucleosynthesis: A Sensitivity Study. *The Astrophysical Journal Supplement Series*, 142(1):1–75, (2002).

[7] H. E. Gove, G. A. Bartholomew, E. B. Paul and A. E. Litherland. Properties of low lying levels in Mg^{25}. *Nuclear Physics*, 2(2):132–146, (1956).

[8] H. Marchant S. Hinds and R. Middleton. Some energy levels of F^{21} and Na^{25}. *Nuclear Physics*, 31:118–127, (1962).

[9] K. Yagi, Y. Nakajima, K. Katori, Y. Awaya and Manabu Fujioka. Energy-level structure of O^{19}, O^{18} and O^{17} investigated by (d, p) reactions with 15 MeV deuterons. *Nuclear Physics*, 41:584–603, (1963).

[10] I. Talmi and I. Unna. THEORETICAL INTERPRETATION OF ENERGY LEVELS IN LIGHT NUCLEi. *Ann. Rev. Nucl. Sci*, 41:353–408, (1960).

[11] J. A. BECKER, R. E. MCDONALD, L. F.CHASE, and D. KOHLER. Low-Lying Levels in Na^{25}. *Phys. Rev.*, 188:1783–1791, (1969).

[12] G. Mairle E. Krämer and G. Kaschl. Proton pick-up from the magnesium isotopes: ^{24,25,26}Mg(d, τ)^{23,24,25}Na. *Nuclear Physics A*, 165(2):353–383, (1971).

[13] J. Jänecke. The Reaction $^{26}Mg(d,\tau)^{25}Na$ and the Structure of ^{25}Na. *Nuclear Physics*, A204:497–515, (1973).

[14] H. T. Fortune, R. Middleton, J. D. Garrett and R.M. Dreizler. Jπ assignments in ^{25}Na from ^{23}Na(t, p). *Physics Letters B*, 79(1):55–57, (1978).

[15] R. D. Woods and D. S. Saxon. Diffuse Surface Optical Model for Nucleon-Nuclei Scattering. *Phys. Rev.*, 95:577–578, (1954).

[16] J. S. Lilley. *Nuclear physics: principles and applications.* J. Wiley, illustrated, reprint edition, (2001).

[17] M. G. Mayer. Nuclear Configurations in the Spin-Orbit Coupling Model. I. Empirical Evidence. *Phys. Rev.*, 78:16–21, (1950).

[18] B. L. Cohen. *Concepts of Nuclear Physics McGraw-Hill series in fundamentals of physics.* Tata McGraw-Hill, (1971).

[19] K. S. Krane. *Introductory Nuclear Physics.* Wiley, revised edition, (1988).

[20] K. F. Riley, M. P. Hobson and S. J. Bence. *Mathematical Methods for Physics and Engineering.* Cambridge University Press, Third edition, (2006).

[21] B. A. Brown and B. H. Wildenthal. Status of the Nuclear Shell Model. *Annual Review of Nuclear and Particle Science*, 38(1):29–66, (1988).

[22] B. H. Wildenthal. Empirical strengths of spin operators in nuclei. *Progress in Particle and Nuclear Physics*, 11:5–51, (1984).

[23] B. A. Brown, and W. A. Richter. New "USD" Hamiltonians for the *sd* shell. *Phys. Rev. C*, 74:034315, (2006).

[24] E. K. Warburton, and B. A. Brown. Effective interactions for the $0p$ $1s$ $0d$ nuclear shell-model space. *Phys. Rev. C*, 46:923–944, (1992).

[25] A. Brown. WBC. Private communication, (2016).

[26] G. R. Satchler. *Introduction to Nuclear Reactions.* Macmillan Education LTD, second edition edition, (1990).

[27] N. K. Glendenning. *Direct Nuclear Reactions*. World Scientific Publishing Co., (2004).

[28] C. Barbieri. On the meaning and usefulness of spectroscopic factors. In Proceedings of Reaction Mechanisms for Rare Isotope Beams, editor, *Ed. A. Brown*, volume 57 of *791*. MSU, AIP Conf. Proc, (2005). AIP 0-354-0280-9/05.

[29] A. Poves. Shell Model and Spectroscopic Factors. http://www.cenbg.in2p3.fr/heberge/EcoleJoliotCurie/coursannee/cours/CoursPoves.pdf Accessed 17/04/2016. Accociated with Ecole Internationale Joliot Curie (C.E.N.B.G.) institue website.

[30] A. M. Moro. Isolde nuclear reaction and nuclear structure course. Lecture Course, (2014).

[31] S. S. M. Wong. *Introductory Nuclear Physics*. John Wiley and Sons Inc., Second Edition edition, (2008).

[32] J. C. Camacho and A. M. Moro. A Pedestrian Approach to the Theory of Transfer Reactions: Application to Weakly-Bound and Unbound Exotic Nuclei. In *The Euroschool on Exotic Beams*, volume IV. Springer, (2014).

[33] NNDC data tables. http://www.nndc.bnl.gov/chart/. Accessed: 22/07/16.

[34] R. C. Johnson, and P. J. R. Soper. Contribution of Deuteron Breakup Channels to Deuteron Stripping and Elastic Scattering. *Phys. Rev. C*, 1:976–990, (1970).

[35] C. E. Rolfs and W. S. Rodney. *Cauldrons in the Cosmos: Nuclear Astrophysics*. University of Chicago Press, (1988).

[36] W. E. Ormand and B. A. Brown. Empirical isospin-nonconserving hamiltonians for shell-model calculations. *Nuclear Physics A*, 491(1):1–23, (1989).

[37] R. B. Firestone. Nuclear Data Sheets for A = 24. *Nuclear Data Sheets*, 108(11): 2319–2392, (2007).

[38] W. N. Catford. Nucleon transfer studies with radioactive beams. *Nuclear Physics A*, 701(1):1c–6c, (2002).

[39] G. F. Knoll. *Radiation Detection and Measurement*. Wiley, Third edition, (2000).

[40] D. J. Morrissey and B. M. Sherrill. In-flight separation of projectile fragments. In *The Euroschool Lectures on Physics with Exotic Beams*, volume I. Springer, (2004).

[41] P. Van Duppen. Isotope Separation On Line and Post Acceleration. In *The Euroschool Lectures on Physics with Exotic Beams*, volume II. Springer, (2006).

[42] M. Pasini, R.E. Laxdal and P.N. Ostroumov. BEAM DYNAMICS STUDIES ON THE ISAC-II POST-ACCELERATOR AT TRIUMF. In *Proceedings of EPAC 2002, Paris, France*, pages 933–935, (2002).

[43] R. E. Laxdal. ISAC-I AND ISAC-II AT TRIUMF: ACHIEVED PERFORMANCE AND NEW CONSTRUCTION. In *Proceedings of LINAC2002, Gyeongju, Korea*, pages 294–298, (2002).

[44] https://www.triumf.info/wiki/exp-prog/index.php/ISAC_(Isotope_Separator_and_ACcelerator), . Accessed: 01/09/16.

[45] http://www.triumf.ca/research-program/research-facilities/isac-facilities, . Accessed: 01/09/16.

[46] C. A. Diget, S. P. Fox, A. Smith and S. Williams et al. SHARC: Silicon Highly-segmented Array for Reactions and Coulex used in conjunction with the TIGRESS gamma-ray spectrometer. *Journal of Instrumentation*, 6(02):02005, (2011).

[47] Micron Semiconductor 2009 Catalogue. www.micronsemiconductor.co.uk, (2009).

[48] P. E. Garrett, A. Andreyev and R. A. E. Austin et al. The TRIUMF nuclear structure program and TIGRESS. *Nuclear Instruments and Methods in Physics Research Section B: Beam Interactions with Materials and Atoms*, 261(1–2):1084–1088, (2007).

[49] M. A. Schumaker, and C. E. Svensson et al. Optimization of Compton-suppression and summing schemes for the TIGRESS HPGe detector array. *Nuclear Instruments and Methods in Physics Research Section A: Accelerators, Spectrometers, Detectors and Associated Equipment*, 573:157–160, (2007).

[50] C. E. Svensson et al. TIGRESS: TRIUMF-ISAC gamma-ray escape-suppressed spectrometer. *Journal of Physics G: Nuclear and Particle Physics*, 31:S1663–S1668, (2005).

[51] C. E. Svensson et al. Position sensitivity of the TIGRESS 32-fold segmented HPGe clover detector . *Nuclear Instruments and Methods in Physics Research Section A: Accelerators, Spectrometers, Detectors and Associated Equipment*, 540(2–3):348–360, (2005).

[52] https://www.triumf.info/wiki/tigwiki/index.php/Suppression_Shield_Gain_Matching, . Accessed: 01/09/16.

[53] B. Davids and C. N. Davids. EMMA: A recoil mass spectrometer for ISAC-II at TRIUMF. *Nuclear Instruments and Methods in Physics Research Section A:*

Accelerators, Spectrometers, Detectors and Associated Equipment, 544(3):565–576, (2005).

[54] W. N. Catford. What Can We Learn from Transfer, and How Is Best to Do It. In *The Euroschool on Exotic Beams*, volume IV. Springer, (2014).

[55] Triumf tigwiki. https://www.triumf.info/wiki/tigwiki/index.php/TIGRESS_Event_Bank_Format. Accessed: 22/07/16.

[56] Spesification of the Phillips Scientific Quad Majority Logic Unit, NIM Model 755. http://www.phillipsscientific.com/pdf/755ds.pdf. Accessed: 22/07/16.

[57] G. Wilson. Investigating the Evolution of the Nuclear Magic Numbers via Single-Neutron Transfer Populating ^{26}Na, (2012). PhD Thesis. University of Surrey.

[58] A. Matta, P. Morfouace, N. de Séréville, F. Flavigny, M. Labiche and R. Shearman. NPTool: a simulation and analysis framework for low-energy nuclear physics experiments. *Journal of Physics G: Nuclear and Particle Physics*, 43(4):045113, (2016).

[59] M. D. Ziegler J. F. Ziegler and J. P. Biersack. SRIM – The stopping and range of ions in matter (2010) . *Nuclear Instruments and Methods in Physics Research Section B: Beam Interactions with Materials and Atoms*, 268(11–12):1818–1823, (2010). 19th International Conference on Ion Beam Analysis.

[60] J. F. Ziegler. INTERACTIONS OF IONS WITH MATTER. http://www.srim.org/ Accessed 08/07/2016.

[61] A. Matta. Study of the neutron-rich ^{10}He by one-proton transfer reaction ^{11}Li$(d,^3He)$, (2012). PhD Thesis. De l'Université Paris Sud.

[62] M. Labiche et al. TIARA: A large solid angle silicon array for direct reaction studies with radioactive beams. *Nuclear Instruments and Methods in Physics Research Section A: Accelerators, Spectrometers, Detectors and Associated Equipment*, 614: 439–448, (2010).

[63] I. C. Celik. A particle-γ coincidence study of ^{26}Na using the transfer reaction $^{25}Na(d,p\gamma)^{26}Na$, (2014). PhD Thesis. University of Surrey.

[64] Radware software package. http://www.radware.phy.ornl.gov.

[65] P. D. Kunz. Zero Range Distorted Wave Born Approximation. http://spot.colorado.edu/~kunz/dwba/dw4_doc.pdf, (2002). Accessed: 22/07/16.

[66] W. W. Daehnick. Global optical model potential for elastic deuteron scattering from 12 to 90 MeV. *Phys. Rev. C*, 21:2253–2274, (1980).

[67] O. Tarasov and D. Bazin. PACE4. http://lise.nscl.msu.edu/download/. Accessed: 14/09/2015.

[68] J. A. Tostevin. TWOFNR version 12 (of M. Toyama, M. Igarashi and N. Kishida) and code FRONT (private communication).

[69] R. B. Firestone. Nuclear Data Sheets for A = 25. *Nuclear Data Sheets*, 110(8): 1691–1744, (2009).

[70] M. B. Tsang and J. Lee et al. Survey of Excited State Neutron Spectroscopic Factors for $Z = 8 - 28$ Nuclei. *Phys. Rev. Lett.*, 102:062501, (2009).

[71] R. G. Thomas. An Analysis of the Energy Levels of the Mirror Nuclei, C^{13} and N^{13}. *Phys. Rev.*, 88:1109–1125, (1952).

[72] W. Benenson, J. Driesbach, I. D. Proctor, G. F. Trentelman, and B. M. Preedom. Energy Levels of ^{25}Si from the Reaction ^{28}Si(^{3}He, ^{6}He)^{25}Si at 70.4 MeV. *Phys. Rev. C*, 5, (1972).